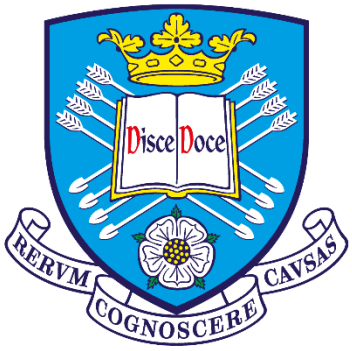

The University Of Sheffield.

Biophysical studies on a novel family of iridium polypyridyl complexes

By

Sasha Michelle Stimpson

A thesis submitted for the degree of Doctor of Philosophy

The University of Sheffield

Department of Chemistry

September 2018

"Science, for me, gives a partial explanation for life.
In so far as it goes, it is based on fact, experience and experiment"

Rosalind Franklin, Chemist

Abstract

This thesis presents a new series of iridium polypyridyl complexes that have been synthesised; $[Ir(bpy)_2(dppz)]^{3+}$ **1**, $[Ir(phen)_2(dppz)]^{3+}$ **2**, $[Ir(phen)_2(C\text{^}N\ dppz)]^{2+}$ **3** (where bpy = 2,2' bypyridine, phen = 1,10-phenanthroline, dppz = dipyrido[3:2- *a*:2',3'-*c*]phenazine). This library of structurally related complexes vary in steric and charge properties. Photophysical studies show that the complexes are all emissive having metal-to-ligand charge-transfer bands ~500 nm. All three complexes were found to possess long-lived luminesce lifetimes of ~500 ns and above. Further biophysical studies with the three iridium complexes and CT-DNA were carried out. Viscometry measurements indicate that the dppz derivatives clearly intercalate between DNA base pairs. Spectroscopic techniques show all three complexes bind to DNA with binding affinities ~ 10^6 M^{-1} – values similar to their ruthenium-dppz analogues. DNA "light-switch" behaviour is not observed upon interaction with nucleic acids, in fact, a substantial decrease in steady-state luminescence occurs in the presence of CT-DNA. Follow up titrations with guanosine-5'-monophosphate shows redox quenching, which could cause a decrease in luminescence. The photonuclease activity of these complexes were investigated using supercoiled plasmid DNA, with complexes **1** and **2** producing photo-oxidation products that cleaved the plasmid DNA by producing scissions in the supercoiled structure. Transient absorption spectroscopy provided a way to measure the intramolecular excited state processes. The kinetics of the complexes in the presence of DNA were quite different to that of the free complex in solution. Proving that there is an electron transfer reaction between the complexes and the guanine bases.

The later part of this thesis aimed to investigate the cellular uptake of the complexes **1-3.** Upon reversible binding the DNA there is a decrease in MLCT steady state emission, which during quenching and gel electrophoresis experiments produced redox-quenching and photocleavage of nucleic acids. Research became focused in this area because such complexes offer many advantageous as luminescent probes of DNA structure, however have a major drawback of poor cellular uptake which restricts their uses in live cells. Confocal laser scanning microscopy of the metallo-intercalator **1**-**3** showed that they were internalised by the MCF-7 breast cancer cell line. Further colocalisation studies showed specific organelle targeting, with **1** and **3** highlighting the lysosomes, and **2** the mitochondria. Cell viability studies of **2** alongside the highly potent cis-platin showed no/low cytotoxic activity as such. However, upon photo-

irradiation the complex became more cytotoxic. Inductively coupled mass spectrometry showed that the complex displayed increased cellular uptake in serum free conditions. This work has established novel iridium complexes, reported DNA binding interactions and preliminary cellular studies.

Publication

Directly originating from this thesis:

Chapter 3 – DNA binding studies

"Tuning the excited state of water soluble Ir^{III}-based DNA intercalators that are isostructural with $[Ru^{II}(NN)_2(dppz)]$ light-switch complexes"

Stimpson, S.; Jenkinson, D. R; Sadler, A.; Latham, M.; Wragg, A.; Meijer, A. H. M.; Thomas, J. A., *Angew. Chem.*, ***2015***, *127, 3043-3046.*

Declaration

Except where specific references have been made to other sources, the work in this thesis is the original work of the author. It has not been submitted, in whole or in part, for any other degree. Certain results have already been published in a peer reviewed journal.

Sasha Michelle Stimpson

September 2018

Acknowledgements

I would firstly like to thank my supervisor Professor Jim Thomas for his continued support, enthusiasm, and providing opportunities for me to travel all around the world during this PhD. I would like to thank the Molecular-scale Engineering Doctoral Training Program directors Giles Davies, Graham Leggett, Christoph Wälti, and Jamie Hobbs for accepting me as a research student at both the Universities of Sheffield and Leeds. The interdisciplinary nature of this scheme allowed me to have a head-start to my project and contributed to many collaborations. I am forever grateful to EPSRC for funding and enabling me to carry out my PhD.

I am thankful for the grant received from The Royal Society, which allowed me to set up a collaboration with The University of New South Wales, Australian Defence Force Academy. The experiences and memories gained during those months with Professor Grant Collins and the rest of his amazing group will stay with me forever. Special thanks to my mentor, and friend Professor Richard Keene, for your hospitality in Adelaide and on-going support during my time in Oz – I must owe you about 100 dinners out and many more gin and tonics.

Not just the Aussies, I would like to thank all my collaborators here in the U.K. Prof. Julia Weinstein and the rest of her group for letting me use their laser facilities. Thanks to Dr. Andrea Rawlings for having to show me the gel electrophoresis procedure countless times – I have finally got the hang of it now! Prof. Anthony Meijer for his help with computational modelling of all my compounds. Big big thanks to Dr. Paul Jarman for taking me under his wing in BMS and showing me the ways of cell biology. The skills you have taught me will no doubt shape my career in the future.

A special thanks to Denise in accounts for always being there to help with payments, conference booking, orders, and more importantly WINE! Thanks to the original stores boys Pete and Nick, nothing better than a bit of banter while collecting your deliveries. Pete as I write this I am sitting in the sun but it is going to take me a lifetime to be as tanned as you! Dan the glassblower, thank you for helping create my Schlenk line, I think it was 4th time lucky that it was fitted without smashing!!

To all the Thomas group members past and present Mike, Ash, Cazza, Hiwa, Paul, Tom, Stuart, Sam, Rach, Si, Kirsty and Shahryar – A massive thanks for help, and constant lab fun! The formation SKS – Sasha Kirsty Simon – when then all the group went on holiday to Italy and we dominated the lab. Shout out to my fave masters boys George Guy, Josh Birch and Liam Darling for all the lab laughs, Kisstory take over, entrance music, and pub booth blogging. Special thanks to Dr. Mike Walker, you've been there with me since day one and I feel like we both went on a journey together during our time in the Chemistry department. Desk buddy and fume cupboard neighbour we were joint at the hip and had more ups and downs than a married couple. I thank you for helping me throughout my whole project – it was not the same when you left. You should see the state of your pristine desk now Mike – Simon sits there!!!

My original Chem mates Andy and Luke for countless pub visits and diva antics. My Springvailer Wailers (Otis, Goons and Stirly B) and my party pakoras (Nat/ Paul). You guys were always there to help me through the tough times lots of love to you all. I would finally like to thank all of my family and friends outside of the Chemistry department, especially my sister little Lea (she actually understands what I'm doing)– I will be milking being called a doctor with you lot! Lots and lots of love! My Grandad Stimpson always said I got my brains from him so I'm making you proud - as my dad would say "The force is strong in our family".

I am very grateful to have such a great support network – I could not have done it without any of you.

Contents

Chapter 1
Introduction

Introduction

DNA is the universal blueprint for life as it is the heredity material in humans and almost all other organisms. It is an instruction manual giving cells the ability to store, retrieve, and translate genetic information. In all eukaryotic and prokaryotic organisms, DNA is the chemical repository of genetic information and for long-term storage. Not only does DNA provide the genetic code to cellular life, it contains all that is needed to construct other components of the cells such as RNA and proteins.[1] As DNA acts as a template for its own replication allowing genetic information to be duplicated, it allows organisms to make copies of themselves. The flow of biological information begins with DNA being transcribed into RNA, which in turn, is translated into proteins. This vital sequence has been formalised by Crick as the "*central dogma of molecular biology*".[2] By the term biological "*information*" Crick meant the precise order of units along a nucleic acid or protein chain i.e. its sequence. This flow of information is unidirectional: although proteins contain the information encoded in DNA, they do not have influence over the sequence of nucleic acids or other proteins. Thus, nucleic acids are always prior to proteins in the flow of biological information and are often considered the most important component of the cell (*Figure 1.1*). For these reasons, the geneticist George Beadle described nucleic acids as "a recipe for constructing a person".[3]

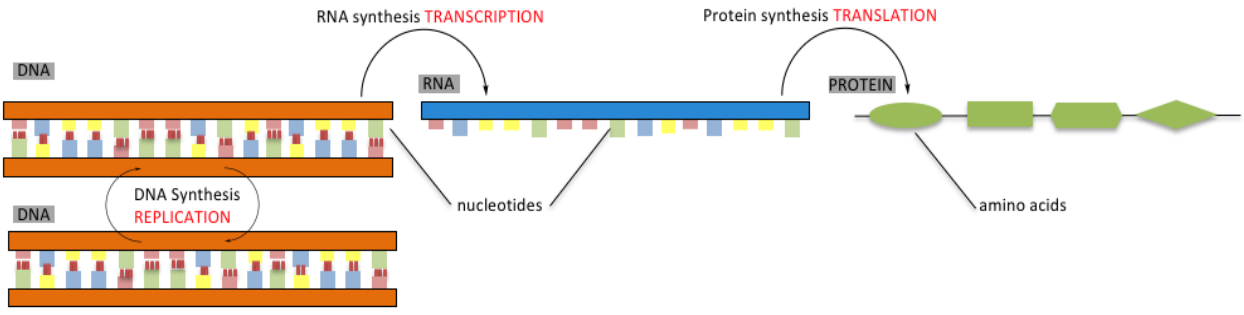

Figure 1.1: The central dogma of molecular biology illustrating the pathway from DNA to protein in which the flow of genetic information passes from DNA to RNA (transcription) and from RNA to protein (translation) in all living cells.

DNA is the library of the cell, simultaneously storing and dispensing information required for life, therefore the structure of DNA is of great importance and is intrinsically linked to essential biological processes. DNA is a large biopolymer comprised of, code-dependant, alternating nucleotide base building blocks. Nucleosides are comprised of a nitrogen heterocyclic base and a pentose sugar. When nucleosides are bonded through a 5' Phosphate-ester linkage to a phosphoric acid they form a nucleotide. The nucleotides of DNA contain one of four heterocyclic nitrogen bases, Adenine (A), Guanine (G), Thymine (T) and Cytosine (C). It is through sequences of these nucleotide bases that the genetic code, holding the biological information needed for all living organisms, is formed. C and T are smaller pyrimidine molecules containing a single nitrogen ring, whereas G and A are larger purine moieties with double nitrogen rings. In physiological conditions DNA forms a highly stable, anti-parallel, negatively charged, double helical biopolymer. Typically DNA forms two chains that follow right-handed helices with the sequence of atoms running in opposite directions. The bases are on the inside of the helix and the phosphates on the outside with each sugar being roughly perpendicular to the attached base. There is a residue on each chain every 3.4 Å in the *z*-direction (*Figure 1.2*).

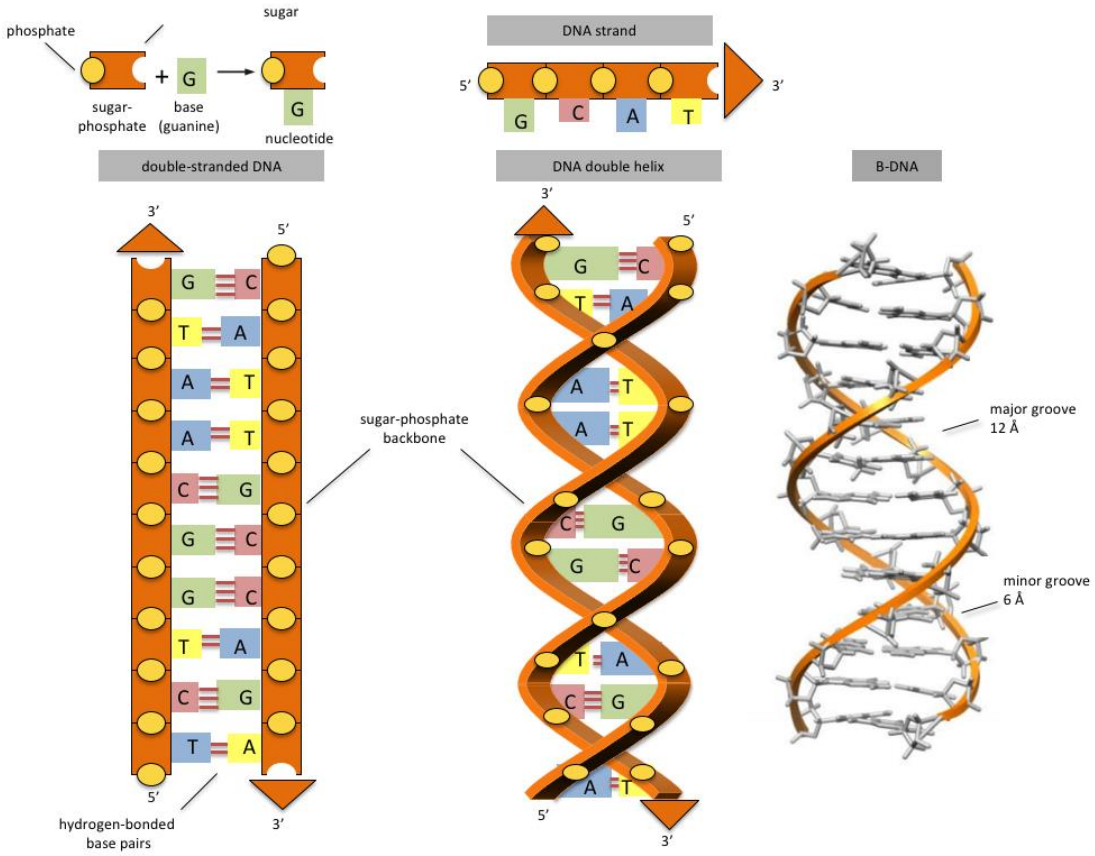

Figure 1.2: DNA and its building blocks.

This exact model of DNA helical structure was described by Watson & Crick in 1953,[4] which greatly improved the model previously proposed by Pauling & Corey also in 1953.[5] Pauling hypothesised that DNA was likely to be a three-chain helix where the large base groups face outwards and the phosphate groups stacked to the core. As a result of insufficient structural data this theory was discarded. Watson and Crick discovered that the two phosphate-sugar right-hand helical chains arrange themselves from 5'-3' around the same axis in an anti-parallel fashion i.e. each chain runs in the opposite direction to the other. These two ends are chemically and biologically quite distinct, and gives each strand of DNA polarity (hydroxyl group at the 3' end, 3'OH and a single phosphate group at the 5' end (5'PO_4). The process of DNA replication is directional and occurs *via* the addition of a 5' nucleoside. The structure of DNA physically protects the all-important atoms of the bases from chemical modification of the environment. Numerous hydrogen bonds, π- π aromatic stacking and hydrophobic intermolecular forces between the horizontal pyridine and purine bases hold the two chains together. The hydrogen bonds hold the nitrogenous bases together and are base specific, leading to the familiar Watson & Crick base pairing where A (adenine) can only form hydrogen bonds with T (thymine) and C (cytosine) can only form hydrogen bonds with G (guanine) (*Figure 1.3*).

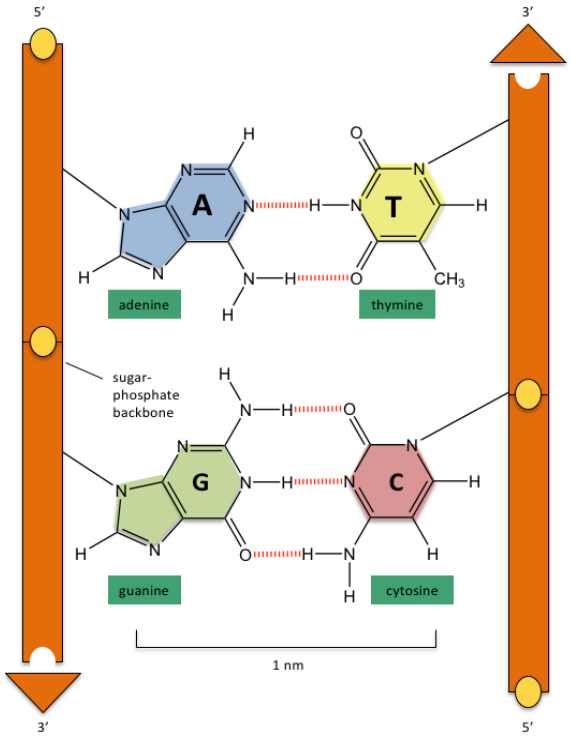

Figure 1.3: Watson and Crick complementary base pairing within the DNA double helix. Hydrogen bonds forming efficiently between A and T, G and C.

These aromatic base pairs are planar and can therefore reside on top of one another like a stack of coins. The position of a single coin is stablised in the stack by the coins above and below it. The individual forces that contribute to the formation of DNA are weak. However the combined sum of the weak interactions cooperatively produce a stable helix.[6]

1.1.1 DNA Confirmation

The DNA double helix is inherently flexible, back in the 1960s when the first single-crystal x-rays of protein molecules began emerging, homogeneous DNA crystal structures were not available. Instead attention was focussed on the diffraction pattern of DNA with varying ambient environments (salt, alcohol, and humidity concentrations). Following these studies, it was concluded that double-helical DNA could be categorised into two families; A and B, each possessing fundamental differences in the way that base pairs are stacked and orientated around the phosphate backbone. Later studies - led by the growth of crystals suitable for x-ray analysis - uncovered an unexpected left-handed z-form of DNA.[7] These polymorphs are interrelated by the differences in the displacement and orientation of the Watson-Crick base pairs from the central helix axis.

In vivo, DNA is most commonly found as the canonical duplex right-handed helical structure first described by Watson & Crick and now known as B-DNA. It is the most prevalent form found in cellular conditions consisting of highly hydrated DNA fibres. When humidity levels are low (<75%) sequences can adopt an A-DNA structure, which is much wider than B-DNA because base pairs stack slightly off centre instead of on top of each other. The bases stack this way due to the puckering of the ribose units, which causes A-DNA to be tilted rather than perpendicular to the helix axis. The A-form is favoured in low humidity concentrations because fewer water molecules are bound to this structure. A-form helices are common for DNA-RNA hybrids, as well as for double stranded RNA.[8] One of the first DNA sequences to be crystallised was, surprisingly, a left-handed helix with a characteristic zigzag phosphate backbone, hence the name Z-DNA. The Z- form is narrow in comparison to the other two forms due to the bases alternating between *anti*- and *syn*- conformation (*Figure 1.4*).[9]

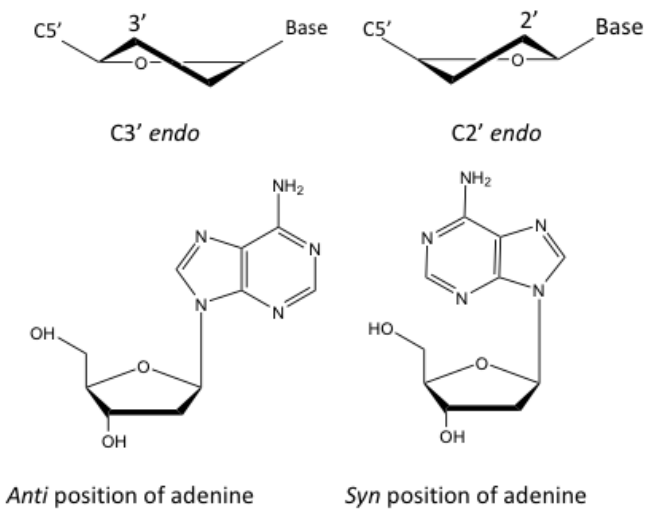

Parameter	*A*-DNA	*B*-DNA	*Z*-DNA
Helix sense	Right	Right	Left
Base pairs per turn	11	10	12
Axial rise (nm)	0.26	0.34	0.45
Helix pitch (°)	28	34	45
Base pair tilt (°)	20	-6	7
Twist angle (°)	33	36	-30
Diameter of helix (nm)	2.3	2.0	1.8

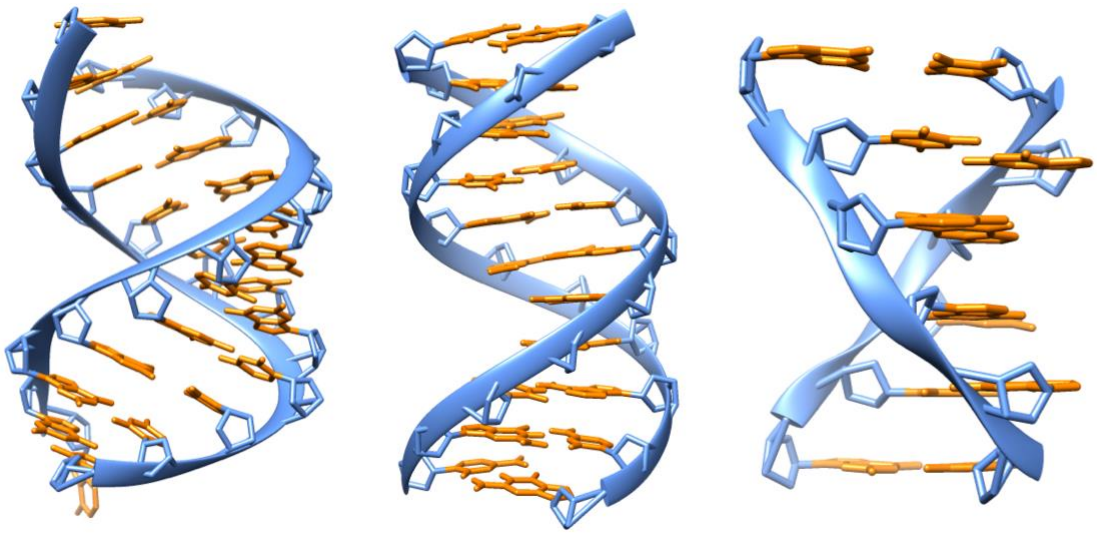

Figure 1.4: Top- The different sugar and nucleoside conformations. 'Syn' and 'anti' refer to the orientations of the N-glycosidic bond between the base and the deoxyribose. Middle- Table comparing the different helical parameters for A-, B-, and Z-DNA. Bottom – The A- B- and Z- structures from left to right (PBD ID: 1ZJE, 1KB1, 400D).

1.1.2 The major and minor groove

The asymmetry of the attachment of the phosphodiester backbones to the base pairs results in two repeating and alternating indentations called the major and minor grooves. The grooves act as base pair recognition and binding sites for small molecules such a proteins or drugs. The major groove contains base-pair specific information while the minor groove is usually base-pair non-specific. This means that species can interact with the DNA either in a specific or non-specific manner. Their dimensions depend on base pair orientation and displacement, for averaged-sequence B-form DNA (for inter-strand phosphate•••phosphate distances)

(1) Width: major groove, 11.6 Å; minor groove, 6 Å

(2) Depth: major groove, 8.5 Å; minor groove, 8.2 Å

These measurements are derived from fibre-diffraction studies on natural DNAs, which cancel out any sequence effects, so local values in specific sequences of genomic DNA may show variations from these values.[10] The patterning along the DNA helices allows binding substrates such as proteins to recognise specific sequences of bases, without having to open the double helix (*Figure 1.5*).

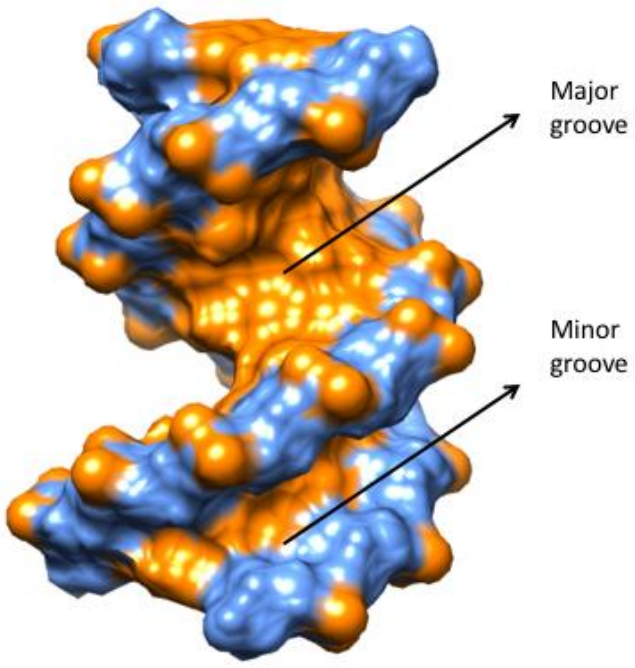

Figure 1.5: Surface representation of B-DNA featuring a narrow minor groove and a broad major groove (PDB ID: 1KB1).

1.1.3 DNA binding

The sequence and structure of DNA is intrinsically linked to many biological processes that are essential for life. Its unique structure mean that small molecules and proteins can bind to it either reversibly or irreversibly. An understanding of how these events occur are important; as more information is gathered on how small molecules specifically bind to DNA, the design of compounds for diagnostic and therapeutic processes will improve.

1.1.3.1 Irreversible binding to DNA

Molecules can irreversibly bind to the phosphodiester backbone, sugar residue, or bases of the DNA helix, this disrupts the activity of the DNA and can lead to permanent damage. "Classic chemotherapy" is based on this mechanism, as disrupting genetic and cellular processes such as transcription, gene expression, or replication, can lead to cell death. Due to their genetic instability, cancer cells are incapable of normal cell cycle processes, the resultant response to any damage being cell death.[11] From the 50s - 70s, researchers produced a series of cytotoxic agents with interesting antitumor activities. These included 5-fluorouracil (1957), Cytoxan (1958), vinblastine (1960), adriamycin (1970) and perhaps the best-known molecule that binds to DNA, is cis-diammine-dichloro-platinum (II) (1971), a simple square planar complex that gained international recognition under the name cisplatin.[12]

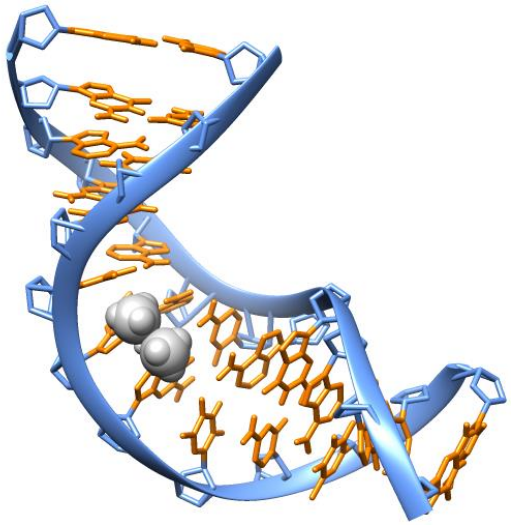

Figure 1.6: NMR solution structure of B-DNA containing a cis-platin d(GpG) intrastrand crosslink, the major adduct of the anticancer drug (PDB ID: 1A84).

The development of cisplatin marked a watershed moment in the treatment of cancer, being used to treat testicular, bladder, ovarian, oesophageal, lung, and stomach cancers.[12] Following its serendipitous discovery by Barnet Rosenberg, and later clinical trials, cisplatin had positive activity against cancers in patients considered terminal and unresponsive to prior therapies.[13] Cisplatin's mode of action is governed by irreversibly binding to DNA through guanine sites. These adducts form intrastrand bonds with the DNA, disrupting the structure and altering the shape of the helix. This change in sugar confirmation restricts the flexibility of the DNA backbone and produces a large bend in the duplex structure. Thus, interfering with the cells repair mechanism leading to cell death (*Figure 1.6*).[14]

1.1.3.2 Reversible binding to DNA

As well as forming irreversible covalent bonds/adducts, small molecules are also able to reversibly bind to DNA. There are possible medical/biotechnological applications of molecules that can reversibly bind to DNA. These include new diagnostic agents for testing specific sequences, medical probes for specific structures of DNA for genetic diseases or perhaps even gene modulation. The 3 principle ways for small molecules to interact with the double helix are:

Electrostatic: In physiological conditions, DNA molecules exist as a polyanion. This involves cations and ligands (*e.g.* Na^{+}, Mg^{2+}, or polyamides) forming complementary electrostatic interactions with the sugar-phosphate backbone. This type of binding leaves little scope for specificity.

Groove binding: As mentioned previously, the winding of the DNA double helix asymmetrically, produces major and minor grooves. This mode of binding involves molecules that make direct interactions with the edges of base-pairs in either of these DNA grooves.

Intercalation: Insertion of a planar aromatic moiety which slides between the base pairs perpendicular to the helical axis.[15] This results in the DNA helix unravelling to compensate and a change in the hydrodynamic properties of the system.

1.1.3.2.1 Electrostatic binding

DNA is a polyelectrolyte, the cations which surround the negatively charged double helix are usually inorganic and hydrated. Additionally, positively charged amino acid side chains of proteins and polyamines may neutralise DNA charges. Cationic metal species can therefore interact with the DNA double helix *via* electrostatic interactions between opposing coulombic charges. The stability of folded DNA conformations requires interaction with metal cations in solution such as Na^{+} or Mg^{2+} through a process called counterion condensation.[16] Net charges on DNA are simplified to just one negative charge per phosphate group. Upon interaction with metal cations, the polyanionic duplex is neutralised. This promotes the release of condensed counter-ions to stabilise the overall charge and entropy of the system. This effect is weak for monocationic and small species, however, as illustrated by highly charged species such as polyamines, it can greatly contribute to binding affinities. For example, solution phase studies on naturally occurring polyamines like spermine and spermidine using techniques such as equilibrium dialysis, calorimetry, and NMR measurements on ^{23}Na, ^{14}N and ^{1}H nuclei reveal that these species bind to B-DNA through these non-specific interactions.[17] These experimental findings are strongly supported by the counterion condensation theory. Thus, the cationic polyamines interact with the DNA phosphates non-specifically by forming a condensed layer near the DNA surface (*Figure 1.7).*

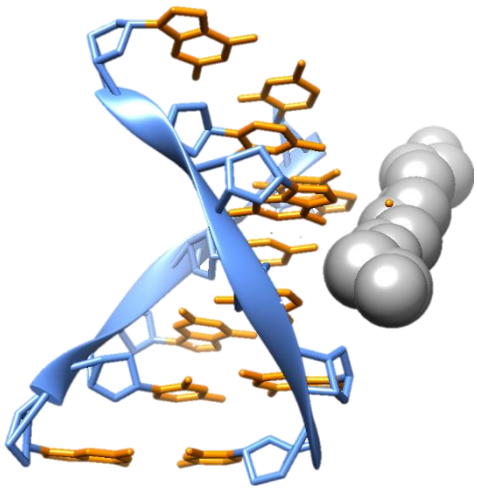

Figure 1.7: Structure showing spermine electrostatically binding to DNA (PDB ID: 1F6C).

In the past, their cellular function was not known with any certainty however recent findings show they slow down autoxidation processes and inhibit oxidative damage caused by free radicals. Thus it seems the primary function of these polyamines is to protect DNA from damage by the long lived, highly reactive excited state of oxygen known as singlet oxygen $^1O_2^*$. The direct interaction of these compounds with nucleic acids[18] is confirmed by physico-chemical studies demonstrating that they increase DNA melting temperatures T_m upon stoichiometric complexation.[17]

1.1.3.2.2 Groove Binding

The double helix of DNA is of great length and short diameter. The patterns of the hydrogen bonds between the complimentary base-pairs cause the formation of the two grooves as they cause the sugar groups to be held at a 120° angle from each other. Molecules of specific shape and size can then approach DNA and reside within a groove due to Van der Waals interactions, hydrophobic, and hydrogen bonding. As outlined previously these grooves provide DNA sequence information as the edge of each base pair presents a distinctive pattern of hydrogen-bond donors and acceptors and also hydrophobic patterns. Proteins and small molecules therefore do not require direct access to the interior of the double helix to distinguish between one DNA sequence and another as they can interact directly with the edges of the base pairs of the polynucleotide. Minor groove binding molecules are usually constructed of heterocyclic or aromatic hydrocarbon rings that possess rotational freedom. This means they are usually crescent shaped molecules that are of complimentary size to reside in the minor groove. The molecule fits within the groove with the displacement of water.[19] Therefore, the smaller minor groove produces hydrophobic interactions which are crucial to ensure the position of the molecule is optimally maintained and this can only occur when the groove is narrow.[20] On the other hand, as the strand backbones are wider apart in the major groove compared to the minor groove, it is generally easier for DNA binding proteins to interact with the bases on the major groove side.

1.1.3.2.2.1 Distamycin and Netropsin

Drugs that target DNA with high sequence specificity have gained increasing attention for their potential medicinal applications. Netropsin and close relative distamycin are antiviral, antitumor, antibiotics, that although are too toxic for clinical use, have received extensive study. Structural studies have shown that netropsin binds to DNA by deep penetration into the minor groove along AT-rich domains (*Figure 1.8*).[21]

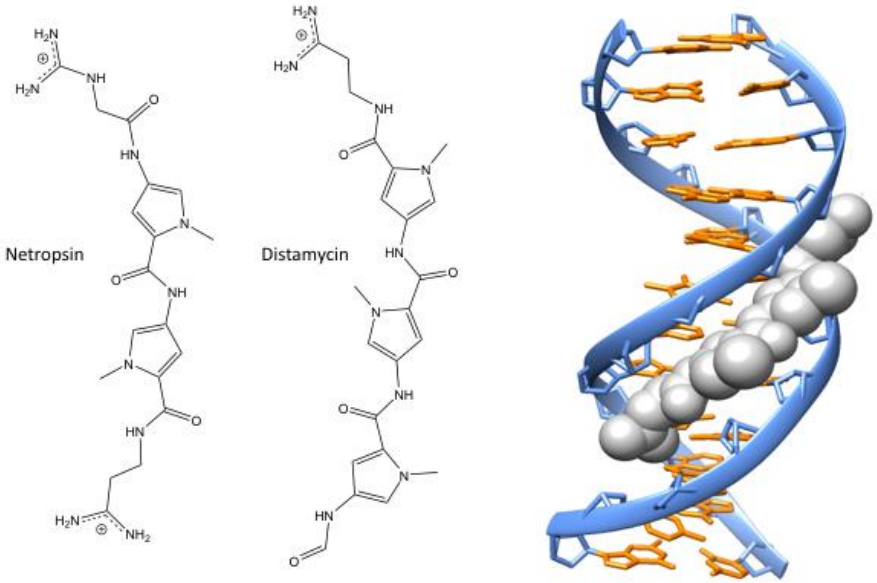

Figure 1.8: Left- Chemical structures of netropsin and distamycin. Right- Structure showing netropsin binding within the minor groove of B-DNA (PDB ID: 121D).

As there is no DNA conformational transition required for this groove binding the subsequent condensed cation ion release results in Netropsin interacting with DNA in an entropically favoured event.[22,23] The drug molecule is planar, with a small cross-section such that it fits into the narrow minor groove in 5'-AATT regions of the structure, with the walls of the groove in close contact with the pyrrole and amide groups. The crescent-shaped ligand fits into the minor groove with little steric hindrance with little perturbation of the DNA structure. Due to the molecules torsional freedom, Netropsin can bend to maximise these isohelical contacts. The Netropsin drug molecule has a large set of hydrogen bond donors, which complement the bonding between the A/T base pair edges. Each amide group is pointing inwards providing a point of contact with two consecutive A:T bases[10]. Steric interactions between the pyrrole methyl groups prevent irreversible binding of the drug. Distamycin is the tris-*N*-methylpyrrole analogue of Netropsin, possessing one more cationic guanidium group and therefore one more

DNA binding site due to this increased length. This antiviral compound also binds to AT rich DNA bases with high affinity.

1.1.3.2.2.2 Hoechst 33258

Hoechst 33258, H33258, is one of a series of compounds developed by the Hoechst Pharmaceutical Company for potential clinical use. However, the major use of H33258 is as a fluorescent cytological stain for DNA both *in vivo* and *in vitro*.[24] Following the criteria needed for a groove-binding drug, Hoechst is crescent shaped and consists of flat hydrophobic aromatic rings (*Figure 1.9*).[25]

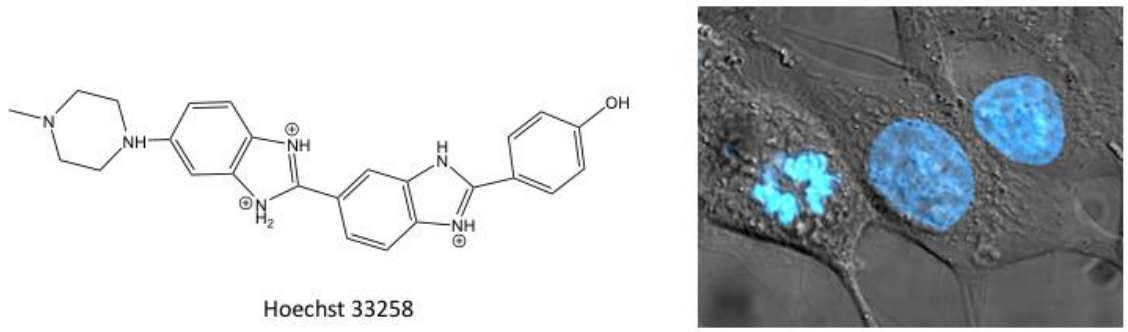

Figure 1.9: Left - Chemical structure of Hoechst 33258. Right- Transmission image of HeLa cells with an overlay of Hoechst 33258 staining (blue).[25]

This results in a snug fit within the hydrophobic sugar walls in the minor groove. H33258 preferably binds to AT rich domains of double stranded DNA, a feature in common with all three minor groove binders. It is particularly useful in quantitative determination of DNA in biological materials as fluorescence increases with addition of DNA.[26] The dye binds to all nucleic acids, but AT-rich DNA duplexes enhance fluorescence two-fold greater than GC –rich sequences.[27] This inherent sequence selectivity, in even the simplest of minor groove ligands, can be used to probe DNA structure and dynamics and finds application in imaging and therapeutics.

1.1.3.2.3 Intercalation

Intercalative interactions were first reported by Lerman, *et al.* in 1961, during an investigation of the hydrodynamic properties of calf thymus DNA with a series of Acridines.[28] The results showed that these small molecules did not interact with the DNA simply on the basis of aggregation or electrostatic effects and were found to intercalate within the double helix. As DNA is a twisted ladder structure with aromatic base pairs being held together by a large network of hydrogen bonds, compounds that interact reversibly with DNA in this way are inserted between adjacent nucleotide-pair layers, extending and unwinding the double helix. These hydrodynamic changes are the consequence of the DNA undergoing structural rearrangements to compensate for the insertion of a foreign moiety between the base pairs in which bending between the layers is diminished and there is concomitant increase in length. DNA intercalation represents an invasive, yet reversible, mode of DNA-ligand binding. This intercalative mode of action is known to play a role in disease emergence and drug treatment as it can disrupt essential DNA- associated processes such as replication, transcription and repair. An example of an intercalating molecule is Ethidium Bromide, which is used as a nucleic acid stain (*Figure 1.10*). The high affinity DNA binding of Ethidium Bromide greatly enhances its fluorescence intensity and lifetime. Also it has been reported to show significant anti-tumour and anti-viral properties. Electrostatics complement this mode of reversible binding as it is driven by aromatic interactions of overlapping π orbitals. The dimensions of Ethidium Bromide are comparable to a nucleotide base-pair and so its interaction with DNA is driven by the means of π-π hydrophobic *p*-orbital overlap. Another favourable structural feature is the partial positive charge, as this enhances electrostatic and hydrogen bond interactions with the DNA.[28]

Ethidium Bromide

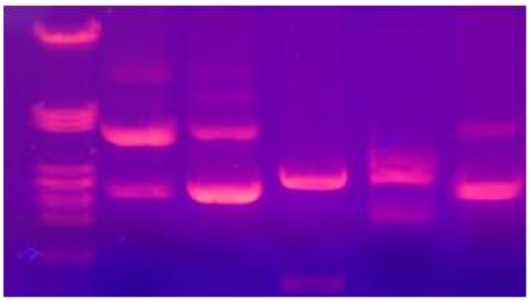

Figure 1.10: Left - Chemical structure of ethidium bromide. Right - DNA sample separated using gel electrophoresis of nucleic acids and stained with ethidium bromide that emits orange light after binding to DNA.[28]

1.1.4 Transition metal complexes

The design of small molecules that interact with DNA is of great importance as they monitor/ interfere with cellular genetic processes resulting in possible diagnostic probes, reactive agents and therapeutics. DNA replication, RNA transcription, and protein translation, can all be initiated or disrupted by small molecules binding to DNA. Although DNA is a therapeutic target, due to the varied complexity and the polymorphic nature of its structure a variety of small molecules can potentially interact with it and, as mentioned previously, there are also various modes that the small molecules can bind to the DNA helix both irreversibly and reversibly. In this context, transition metal complexes that bind with DNA have become an area of considerable interest. Initially, transition metal complexes may seem an odd choice for DNA molecular recognition, as organic molecules have been used as substrates to interact with the DNA helix and the study of transition metal complexes has been confined to coordination sites in proteins.[29] However, as mentioned previously, the interactions of heavy metal complexes with nucleic acids has led to successful applications in chemotherapy, *i.e.* cisplatin and platinum derivatives. Both the well-explored spectroscopy and chemical reactivity of transition metal complexes can also be exploited to obtain a potentially vast range of reagents to probe nucleic acids. Metal complexes provide well-defined coordination geometries that also provide distinct and highly researched electrochemical or photophysical properties.[30] By simply varying the chemical synthesis of these compounds, the size, charge distribution, stereochemistry, redox potential and other physical properties of the metal can used as a pharmacological toolbox to study cellular functions within the cell.[31] In such complexes, the metal-ion itself acts as a scaffold to anchor ligand architectures together and add functionality for specific applications. This research has mainly focused on d^8 square planar and d^6 octahedral transition metal geometries. Due to well-developed and designed substitution chemistry and chemical inertness, these metals are ideal candidates for the central atom of these nucleic acid probes. By matching the shapes and symmetries of metal complexes to particular variations in the complex structure of DNA families of molecules for these applications have been developed.[32] In particular, the photophysical properties of these systems make then particularly attractive as probes and phototherapeutics. The following section provides a background to these properties.

1.1.4.1 Basic Principles of Luminescence

Luminescence is spontaneous emission of radiation from an electronically excited species, not in thermal equilibrium with its environment. The difference between the exciting and emitted wavelengths is known as the Stokes shift.[41] Fluorescence and phosphorescence are particular cases of luminescence and can be distinguished through a consideration of their excited states. When luminophores are in their ground state, spontaneous absorption of one or more photons can occur, causing an electronic transition to an excited state. The fate of the excited electron and emission processes can be understood by a diagram first conceived by Alexander Jablonski in the 1930s (*Figure 1.11*).[42] When a molecule is excited by the absorption of light it relaxes back to the ground state through various processes. There are two spin states relevant to the complexes discussed here, the singlet, S_0, S_1 S_2, etc. and the triplet, T_1, T_2, etc. The difference between these states are due to the arrangement of electrons in the orbitals of the molecule. In the emission from S_1 to S_0 there is no change in spin state of the electron during its transition. The difference between fluorescence and phosphorescence stems from the Pauli Exclusion Principle: "No more than two electrons may occupy any given orbital, and if two do occupy one orbital their spins must be paired".[43]

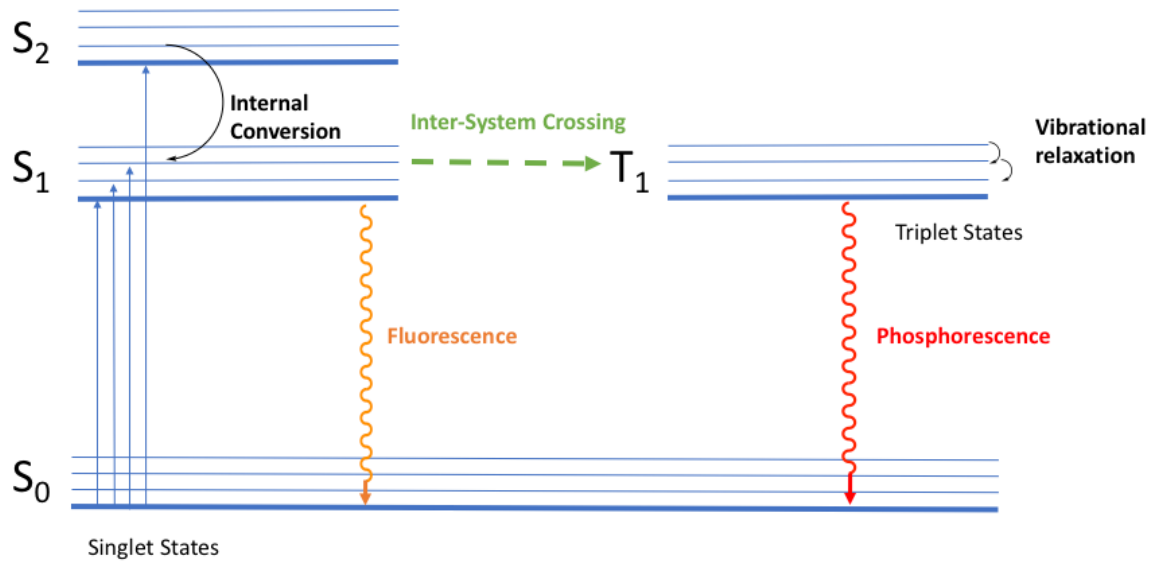

Figure 1.11: A Jablonski diagram showing the excitation and resultant possible decay pathways of fluorescence, intersystem crossing, vibrational relaxation and phosphorescence.

In an excited state where an electron is promoted in the same spin orientation as it was in the ground state this is a singlet state. Molecules in the S_1 state can also undergo a spin conversion to the first triplet state. Emission from this state is called phosphorescence, which is usually shifted to longer wavelengths/lower energies compared to fluorescence. Since the transition from singlet to triplet state required for phosphorescence is formally disallowed, this process is commonly less likely than the singlet-to-singlet-based transition of fluorecence.[44]

1.1.4.2 Fluorescence Lifetimes and Quantum Yields

When a photon of light is absorbed by a luminophore, the deactivation process back to the ground state is dependent upon its exact nature and surroundings. The main deactivation processes that can occur are fluorescence, internal conversion, vibrational relaxation (non-radiative loss of energy as heat to the surroundings), or intersystem crossing to the triplet manifold with subsequent non-radiative deactivation along with phosphorescence. Quantum yields are used to measure the probability of emission from a molecule; in other words, they are a measure of emission efficiency. For example, by definition, a quantum yield of fluorescence, ϕ_F, expresses the ratio of the number of emitted photons to the number of absorbed photons per time unit (*Equation 1.1*).[45]

$$\phi_F = \frac{No.\,of\ emittied\ photons}{No.\,absorbed\ photons}$$

Equation 1.1

The quantum yield is dependent on the lifetimes and subsequent rate constants for deactivation processes that can be radiative (k_r) and non-radiative (k_{nr}) (*Equation 1.2*).

$$\phi_F = \frac{k_r}{(k_r + k_{nr})}$$

Equation 1.2

1.1.5 Introduction to transition metal photophysics

The field of photophysics and photochemistry of transition metal complexes has grown rapidly. This area of research has been accelerated by the development of the ligand field theory, and

growing knowledge of the excited state electron transitions due to the rapid advances in high grade spectrophotometers and lasers.[46] There are structural prerequisites for photoluminescence. Many first-row transition metal complexes possess electronic structures with low energy gaps between ground and excited states that, upon excitation, result in radiationless loss of absorbed energy. This is because emission from an excited state requires a large energy gap between the ground state and the excited state - a phenomenon that is known as the "Energy Gap Law". This law shows that transition probability is determined by a Gaussian function of energy gap between the two electronic states and the Stokes shift. This produces an Arrhenius type temperature behaviour where upon the transition probability depends exponentially on the energy barrier for the intersection of the two potential energy surfaces.[47] Therefore, the non-radiative decay rate of a metal-ligand complex increases exponentially as the energy gap of emission energy decreases. A decrease in the ^{3}MLCT excited state energy may reduce the activated decay *via* higher energy states, and the non-radiate decay directly to the ground state can increase.[48–50] Moving down towards the second and third row transition metal series, this basic requirement is usually met by systems with d^6, d^8, and d^{10} electronic configurations. With this rule in hand, the properties of excited states can be revealed through investigation of the luminescent properties of such species.[51] An increasingly important class of luminescent metal complexes include those of Ru^{II}, Os^{II}, Re^{I}, Rh^{III}, and Ir^{III} metal centres coordinated to high field polypyridyl ligands.

1.1.5.1 Spectroscopic states of transition metal complexes

Beautiful colours and rich excited-state behaviour are prominent features of transition metal chemistry. Understanding the structure and dynamics of the electronic and excited state of these complexes is an important goal of current spectroscopic, photophysical, photochemical and theoretical research.[52] In these systems, it can be helpful to consider the energy levels of the metal ions and ligands separately from each other. Thus, the ground state, excited states, and redox species can be described in a sufficiently approximate way by localised molecular orbital configurations.[53] Transition metal complexes are characterised by partially filled *d*- orbitals, and the occupancy of these orbitals determines the emissive properties. To explain this phenomenon, an MX_6d^6 metal complex can be used where M is a metal centre and X is a ligand of an octahedral complex. There are 5 degenerate *d*- orbitals present in transition metals which are split by the octahedral crystal field of the ligands.

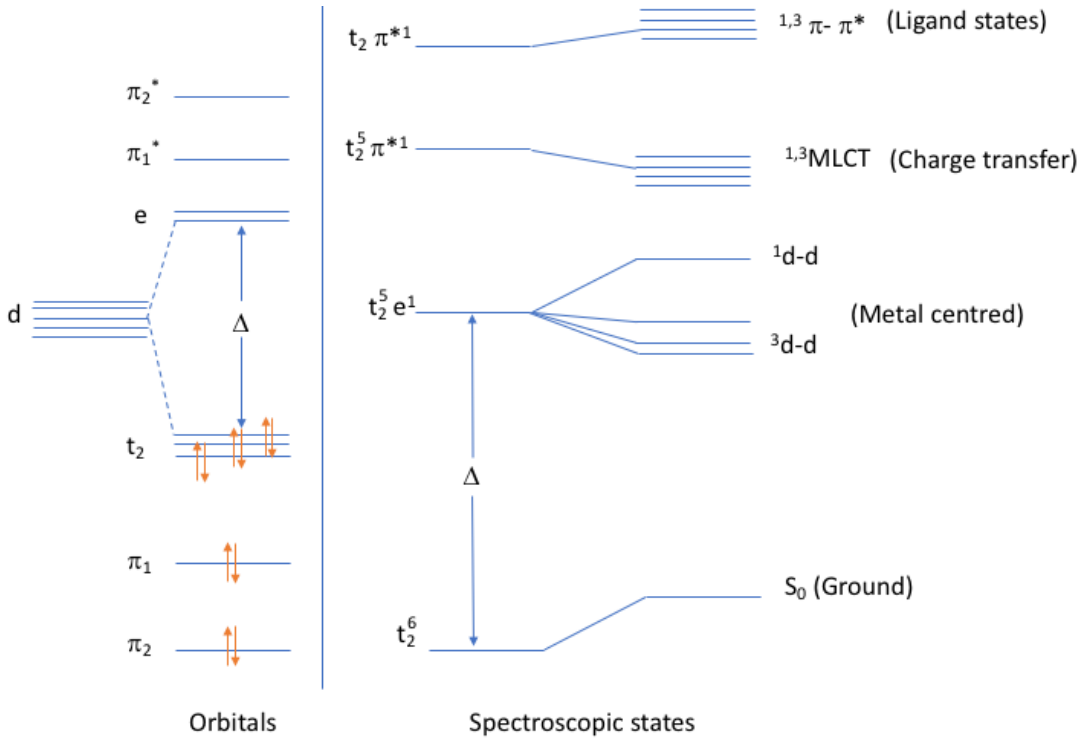

Figure 1.12: Simplified orbital and state diagrams for a d^6 metal in an octahedral environment showing d and π- bonding and π^* antibonding orbitals. Each arrow represents an electron with its associated spin. A strong crystal field is assumed.

This results in a triply degenerate t_{2g}, and a doubly degenerate e_g level. The crystal field splitting parameter is particularly important as it governs the magnitude of difference between the t_{2g} and e_g levels (*Figure 1.12*). In such a system, luminescent properties can be controlled by manipulation of the metal ion, ligand, and geometry.[54] The different classification of electronic transitions within a metal complex are determined by the original and final orbitals involved. Transitions predominantly localised on the central metal, eg *d-d* transitions, are usually *metal-centred* (MC). Transitions between molecular orbitals localised on the ligand are usually called *ligand-centred* (LC) or intraligand transitions. Finally, transitions between molecular orbitals of different localisation, which cause the displacement of the electronic charge are called *charge-transfer* (CT) transitions. More specifically, an excited state where there is charge transfer from a ligand to the metal is called *ligand-to-metal charge-transfer* (LMCT) while the reverse process is known as *metal-to-ligand charge-transfer* (MLCT). There are also some transitions that can occur which are less frequently encountered which are those from a metal-centred orbital to a solvent orbital (*charge-transfer to solvent*, CTTS), or between two orbitals predominately localised on two ligands on the metal centre (*ligand-to-*

ligand charge transfer, LLCT).[53] Luminescence spectroscopy is an important tool in photochemistry since it provides a deeper insight into excited state processes and emission behaviour of metal complexes.

1.1.6 Metallo-intercalators

As discussed earlier, there are three reversible DNA binding modes, although this section is largely based upon metal complexes that bind to DNA through intercalation. Intercalators are planar aromatic moieties which interact with the base-pairs within the hydrophobic helix by an overlap in *p*- orbitals and aromaticity. Metallo-intercalators are simply metal complexes, which have one or more intercalating group attached to the centre. Due to the rigidity of the metal complexes geometry the intercalating ligand unit can be orientated parallel to the base-pairs and protrude away from the metal centre. Metallo-intercalators can insert into the double helix from the groove and itself acts as a new base-pair (*Figure 1.13*).

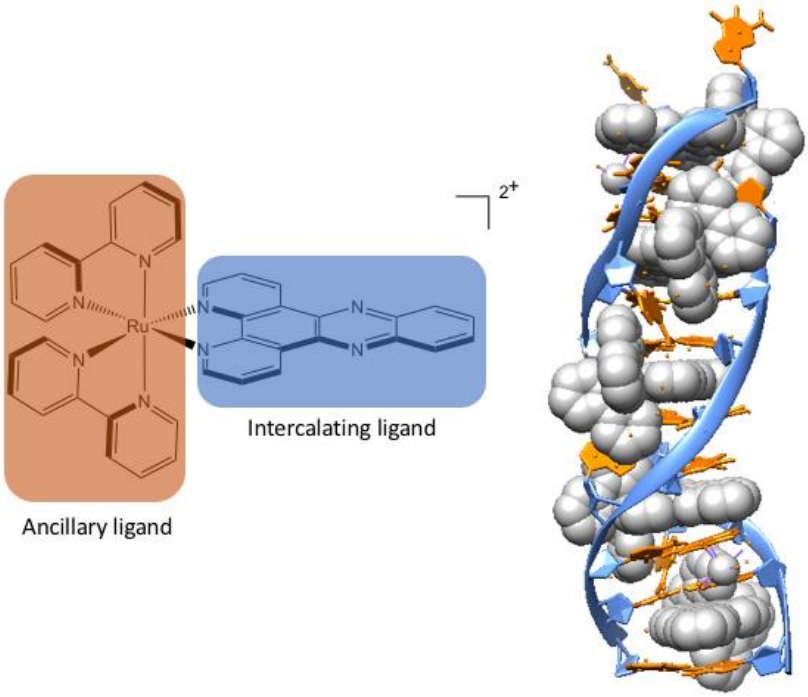

Figure 1.13: Left - The general form of a metallo-intercalator $[Ru(bpy)_2(dppz)]^{2+}$ (bpy = 2,2'-bipyridine and dppz = dipyrido[3,2-a:2',3'-c]phenazine. Right - Structure showing the complex intercalated within B-DNA (PDB ID: 4E1U).

This intercalative interaction, does not cause any perturbation within a base-pair, it only causes the opening of the phosphate angle. This next section will provide an insight to earlier work of metallo-intercalators and create a successive timeline of their progression

1.1.6.1 Early work

Transition metal complexes that could reversibly bind to DNA by intercalation were first prepared by Stephan Lippard and co-workers in the mid-1970's.[32] Their research was focussed on platinum complexes as biological probe reagents. They discovered that square-planar platinum(II) complexes containing the terpyridyl ligand bound to planar aromatic ligands can bind to DNA by intercalation with strong affinities.[33] This was carried out by looking at X-ray diffraction patterns of both DNA and the platinum complexes in the bound form. Leonard Lerman had previously found that stable complexes between intercalative dyes and duplex DNA showed a spectral shift and change in hydrodynamic properties of the system, *i.e.* viscosity. Lippard carried out similar studies on the platinum complexes and provided evidence to support the conclusion that these compounds are metallointercalators.[34] The group's studies showed that, although $[(phen)Pt(en)]^{2+}$ and $[(bpy)Pt(en)]^{2+}$ were shown to intercalate into the helix, $[(pyr)_2Pt(en)]^{2+}$ with pyridine ligands rotated out of the coordination plane could not (*Figure 1.14).*

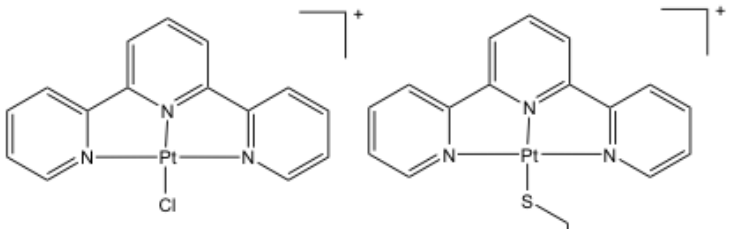

Figure 1.14: Chemical structures of chloroterpyrideineplatinum(II) 'PtTC' (left) and hydroxyethanethiolatoterpyridine(II) 'PtTS' (right).

1.1.6.2 Phenanthroline metal complexes

As the 1980's began, work was focussed on octahedral transition metals bound to phenanthroline units. The tris(phenanthroline) unit does not possess any hydrogen bond donors and interactions with DNA are simply from intercalative stacking. The earliest work by Barton and co-workers of metal chelates being used as DNA structural probes were with complexes involving cobalt,[35] rhodium,[36] and ruthenium.[37] It was not until 1986 that studies incorporating stereochemistry and chirality to ruthenium complexes burgeoned. Ru(II) complexes are of popular choice because of their chemical stability, high luminescence and metal-to-ligand

charge-transfer in the visible spectrum which perturbs when bound to DNA.[38] In addition, the complexes luminesce with high quantum yield.

Chiral metal complexes are of great interest as they have they have the potential to recognise different local structures within the DNA due to its asymmetry and shape. Work began in the Barton group investigating the enantiomeric selectivity of ruthenium complexes with DNA. As these complexes are chiral, their syntheses produce a mixture of Λ and Δ enantiomers. The Barton group investigated how the photophysical properties of various ruthenium(II) complexes differ as a function of DNA binding. The metal complexes employed in this initial study were bidentate ligands 2,2'-bipyridine (bpy), 1,10-phenanthroline (phen), and diphenyl-1,10-phenanthroline (DIP) (*Figure 1.15*).

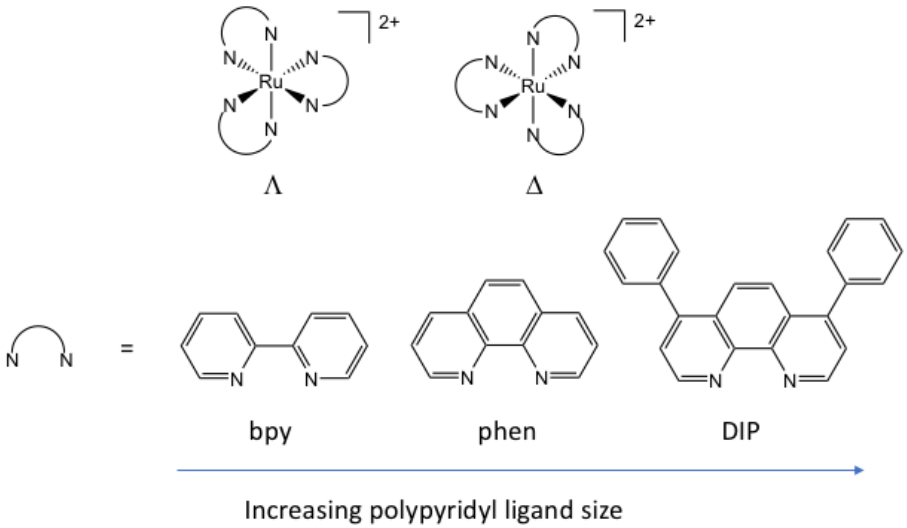

Figure 1.15 Octahedral Ru(II) tris(phenanthroline) complexes and derivatives.

It was concluded that the DNA binding of the $[Ru(bpy)_3]^{2+}$ complex was negligible, however for both complexes $[Ru(phen)_3]^{2+}$ and $[Ru(DIP)_3]^{2+}$ the results suggested high affinity binding. Upon further investigations the complex $[Ru(DIP)_3]^{2+}$ was found to have significant enantiomeric selectivity in intercalation with DNA. The Δ isomer appeared to bind preferentially to DNA in an intercalative way whilst the Λ isomer binds electrostatically. The Λ ligand opposes the helical groove and orientation of the double helix and due to steric constraints is unable to intercalate.[39] The sheer hydrophobicity and limited solubility of the salts of this complex which were examined (Cl^-, ClO_4, PF_6) required in a small amount of

organic solvent to be added. Thus, a later study on the chiral discrimination of the interaction of $[Ru(DIP)_3]^{2+}$ shows equal changes in the absorption spectrum for both enantiomers. Here a diacetate salt of the complex was prepared to increase solubility, and experiments carried out in acetate buffer to minimise precipitation complications. The group's conclusions were that the complexes are extremely hydrophobic and neither intercalates or binds stereoselectively to B-form DNA.[40]

1.1.6.3 The molecular light switch effect

Ruthenium complexes are ideally suited for the application as sensitive noncovalent probes for nucleic acid structures. These complexes are water-soluble, coordinatively saturated, and inert to substitution. Ruthenium(II) ions bound to polypyridyl units are intensely coloured due to their electronic substitutions within the complexes. The potential of substitutionally inert metal complexes as photochemical probes of nucleic acid structure has been explored extensively over the past decade. As mentioned previously, much work has focussed on the interactions between well-characterised ruthenium complexes and DNA duplexes. A case in point is provided by the complex first reported in 1990 by Friedman *et al* known as the molecular "light-switch" for DNA.[55] This probe is $[Ru(bpy)_2(dppz)]^{2+}$ (bpy = 2,2'-bipyridine, dppz = dipyrido[3,2-a:2',3'-*c*]phenazine) which shows a profound luminescence enhancement when bound to DNA (*Figure 1.16*).

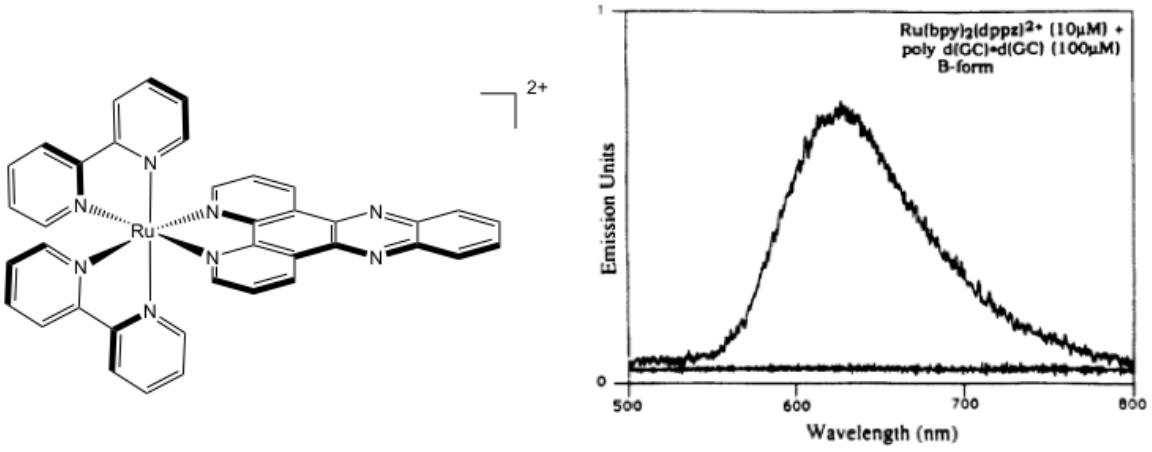

Figure 1.16: Left - Chemical structure of the molecular light-switch complex $[Ru(bpy)_2(dppz)]^{2+}$. Right - steady-state emission spectra of $[Ru(bpy)_2(dppz)]^{2+}$ in the absence and presence of B-DNA.[49]

The luminescence of this complex is environment dependant and the emission in aqueous solutions is switched on by the presence of DNA. The important structural feature of this complex is the dppz unit. This planar, aromatic ligand drives the complex to interact with DNA by stacking between the base pairs through intercalation. This molecular probe displays striking photophysical properties that were also investigated in 1990 by Sauvage *et al*. Electrochemical and spectroscopic measurements of its ground and excited states showed that the charge transfer is directed from the metal centre to the phenazine of the dppz ligand.[56] It was deduced that the light-induced charge transfer flows from ^{1}MLCT excited state then rapidly decays *via* intersystem crossing to a ^{3}MLCT excited state primarily localised on the phenazine nitrogen atoms. This directional metal-to-ligand charge-transfer (MLCT) onto the intercalating unit means that the luminescence of the bound complex provides a sensitive reporter of the DNA helical environment (*Figure 1.17*). The excited state of this complex is highly sensitive to its microenvironment, showing strong (MLCT) centred luminescence in organic solvents, ethanol, acetonitrile, isopropanol. However, in aqueous/protic solvents there is no MLCT as the major nonradiative deactivation pathway for the complex involves the protonation of the phenazine nitrogen atoms in the excited state.

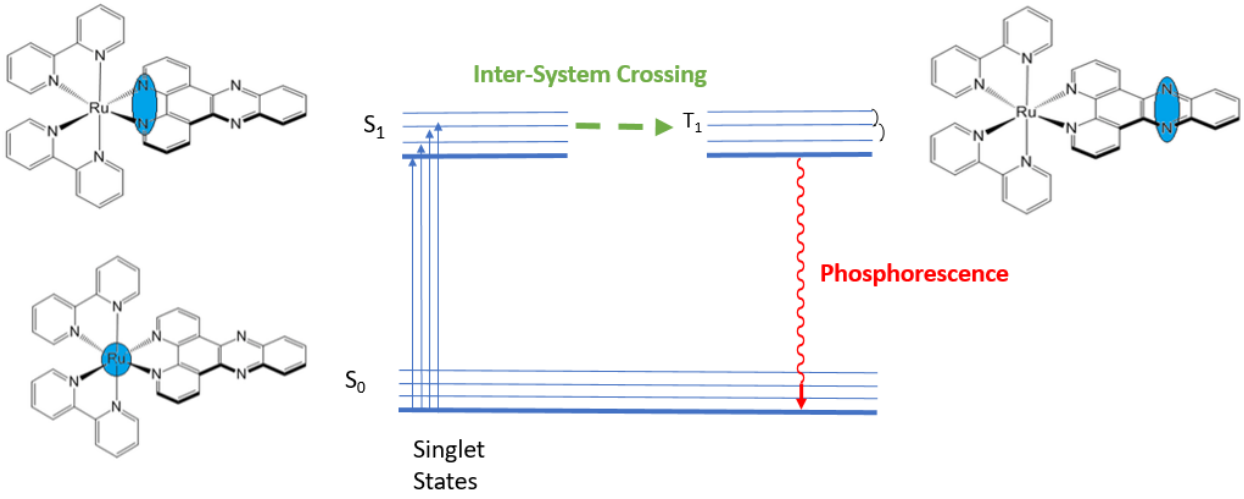

Figure 1.17: Jablonski diagram showing the excited states involved in the DNA light-switch effect. The blue areas on the molecule represent where the electron is localised.

These photophysical properties explain why the complex is known as the molecular light-switch. In aqueous environments the complex does not luminescence, but upon intercalating - in the hydrophobic environment between the stacked DNA base pairs - it is emissive as the nitrogens on the phenazine units are shielded from any water molecules which would deactivate its MLCT-based luminescence. Correlations between the extent of the protection within a DNA helix and luminescent parameters can be observed. As mentioned previously, binding interactions with complexes and DNA can be enantioselective (*Figure 1.18*). Per Lincoln *et al* synthesised pure enantiomers of the analogue $[Ru(phen)_2(dppz)]^{2+}$ and investigated luminescence, excited state lifetimes, isotropic absorption and linear dichroism data for each enantiomer to obtain detailed information about the binding of the respective complexes.[57] Their results showed the binding of the two enantiomers to be of similar strengths ($K_b=10^8$ M^{-1}) however the relative quantum yield of the Δ enantiomer is 6-10 times higher than that of the Λ, meaning that 85% of emission observed from the racemic mixture is as a result of the Δ. These investigations offer an excellent illustration of how science progresses. One structure at a time, the ability to understand, design, and produce complexes for biomedical purposes is getting closer.

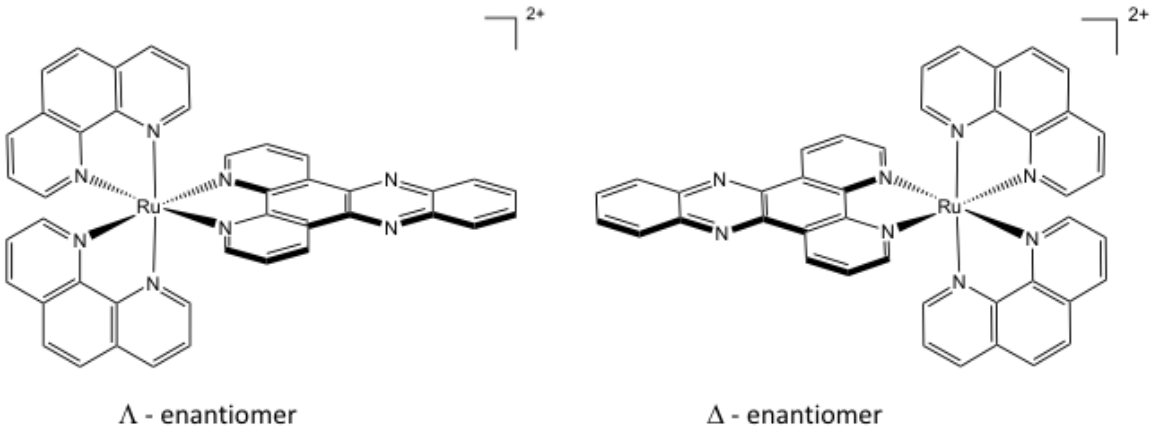

Figure 1.18: The different enantiomers of $[Ru(phen)_2(dppz)^{2+}$, Λ and Δ.

The distinct light-switch effect is generally considered to follow from the protection of the phenazine nitrogens from hydrogen bonding water when the dppz moiety is intercalated between the base pairs. Despite the extensive evaluation of the DNA binding and spectroscopic properties of numerous structural analogues of $[Ru(bpy)_2(dppz)]^{2+}$, there are still fundamental questions still to be answered regarding their emission properties in the presence of DNA. Early

work showed that the pure Λ and Δ enantiomers of both $[Ru(phen)_2(dppz)]^{2+}$ and $[Ru(bpy)_2(dppz)]^{2+}$ exhibit biexponential luminescence decay upon DNA binding. It was proposed that this was due to a difference in the location of the dppz ligand within the intercalation pocket. A later combined analysis of calorimetric and photophysical data for the binding of these complexes to $[poly(dAdT)]_2$ the biexponential data could be assigned.[58] The shorter lifetime is because complexes that are centred in the intercalation pocket and the longer lifetime is a result of a canted, side on binding geometry found only at the end of contiguous sequences of bound ligands. Other work by Lincoln *et al* combined studies of linear dichroism spectroscopy and emission anisotropy with a series of enantiomerically pure substitution-inert ruthenium(II) complexes containing phen and bpy ligands. The markedly weaker binding affinities observed when moving from $[Ru(bpy)_2(phen)]^{2+}$ to $[Ru(bpy)_3]^{2+}$ supports a stacking interaction with the phen ligand and the base pairs. Hydrodynamic studies show that $[Ru(phen)_2(dppz)]^{2+}$ and classical intercalation lengthen the DNA upon binding, however this phenomenon does not occur with $[Ru(phen)_3]^{2+}$. This data led to the introduction to two alternative binding modes; semi-intercalation (wedging an opening between adjacent base pairs) and quasi-intercalation (indenture of one base pair) (*Figure 1.19*).

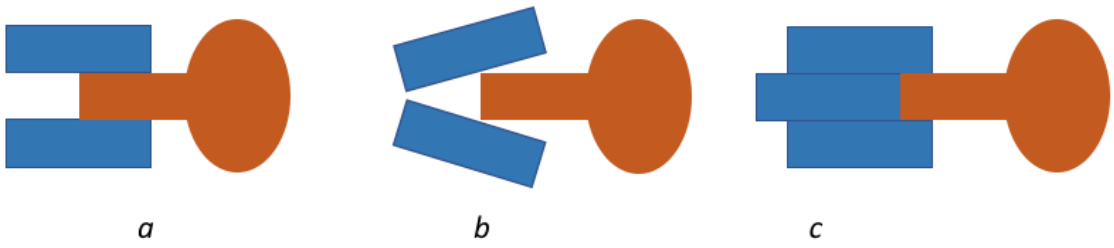

Figure 1.19: Schematics defining the concepts of intercalation (a), semi-intercalation (b) and quasi- intercalation (c).

1.1.6.4 X-ray crystallographic studies

It has only been within the last five years or so that there has been reported X-ray structures of dppz complexes with small DNA molecules.[59] Advances in time-resolved X-ray crystallography can lead to structural studies of excited state geometries of such compounds which can either complement or surpass previous spectroscopic studies reported in solution. The enormous improvement of technology, at the Diamond Light Source as well as other synchrotrons means that usable data can be obtained from a crystal as small as 10x10x10 μm.[60]

These predicted binding modes were first observed by X-ray crystallography by Cardin *et al* with $[Ru(TAP)_2(dppz)]^{2+}$.[61] It was shown by crystal structures that two binding modes were observed; each complex binds to d(TCGGCGCCGA) by intercalation of the dipyridophenzaine ligand and also by semi-intercalation of one of the orthogonal tetraazaphenanthrene ligands resulting in kinking of the DNA (*Figure 1.20).* This creation of a kink is similar to the platination of DNA observed with well-known antitumor agents such as *cis*-platin and oxaliplatin. There are marked similarities in the overall curvature and the alignment of the semi-intercalated ring. As it is known that transcription and gene expression is dependent on protein-induced distortion in DNA, this discovery suggests that such complexes might be effective in modulating such process.[62]

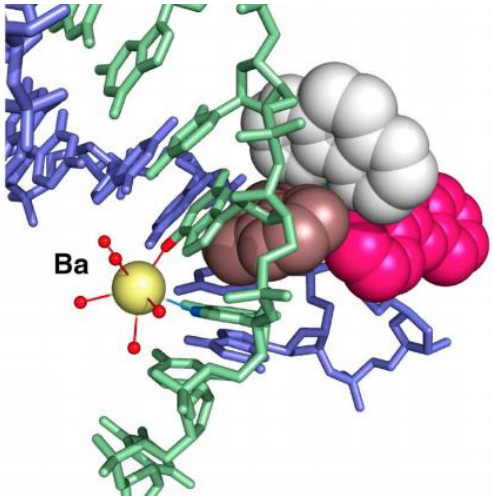

Figure 1.20: Kinking of DNA by semi-intercalation of an orthogonal TAP ligand with the oligonucleotide d(TGGCGCCGA) in the presence of barium ions.[59]

Successive crystallographic work within the Cardin group focused on the binding mode of Λ-$[Ru(phen)_2(dppz)]^{2+}$ and two oligonucleotide duplexes; $d(CCGGTACCGG)_2$ and $d(CCGGATCCGG)_2$.[63] Results showed a perpendicular intercalation of the dppz unit in the TA/TA step of the first oligonucleotide, which is not observed in the latter AT/AT step. T was concluded that specificity to TA/TA was a result of the packing of the phenanthroline ligands against the adenosine base pair. However, in both duplex sequences a second ruthenium complex, $[Ru(TAP)_2(dppz)]^{2+}$, links the duplexes through a combination of a shallower angled intercalation. Whilst a number of binary DNA-complex X-ray crystal structures are available, most include information based on Λ-$[Ru(phen)_2(dppz)]^{2+}$, until this work within the Cardin group, there had been no atomic coordinates of a crystal structure showing Δ-

$[Ru(phen)_2(dppz)]^{2+}$ binding to well matched DNA. It has been hypothesised that the reason behind the more intense luminescence observed with the Δ-$[Ru(phen)_2(dppz)]^{2+}$ is because of the stereoselectivity of the binding event. The asymmetric duplex structure serves as a template which discriminates in binding of small molecules by chirality. It was proposed that the twist of the Δ-enantiomer is a better fit to the right hand helix sense of the DNA backbone.[64] More recent predictions of new binding modes; semi-intercalation and quasi-intercalation, and more observations using X-ray crystallography have produced some interesting findings. This was observed with the aforementioned $[Ru(TAP)_2(dppz)]^{2+}$, where unexpectedly the Λ- enantiomer preferentially crystallised selectively to particular DNA sequences when starting with a racemic mixture, contradictory to previous assumptions. This was the driving force for this work within the Cardin group is to understand how the more difficult to crystallise Δ-$[Ru(phen)_2(dppz)]^{2+}$ bind to DNA. Using the two binding modes discovered in this study, and previously obtained results from other groups this Δ- enantiomer has been proposed to have 5 binding modes each with a different microenviroment around the complex.[65–68] It was suggested that the luminescence lifetime of the complexes in the binding sites presented would be in the following order Mismatch AA> well-matched non-CG sites with base flipping > canted intercalation> symmetrical intercalation > semi- intercalation. The story is not over with this enantiomer, due to its difficulty crystallising and limited results to date, it has not been fully characterised (*Figure 1.21*).

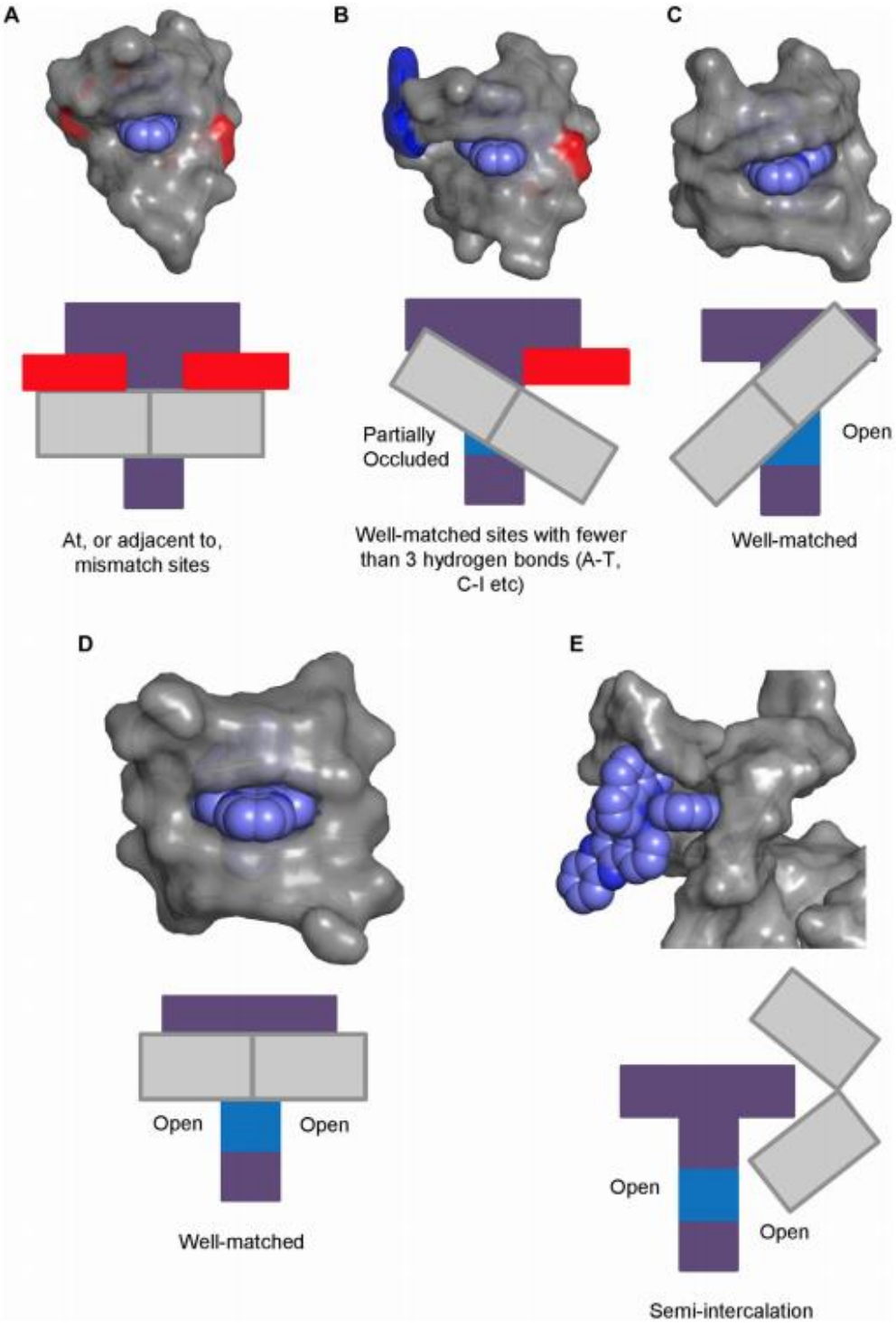

Figure 1.21: Five possible binding modes for Δ-[Ru(phen)$_2$(dppz)]$^{2+}$ to DNA. (a) The complex binds at, adjacent to, a mismatch site. The flanking adenine (or purine bases) stack on the ancillary ligands, reducing intercalation depth and preventing dppz nitrogen atoms from hydrogen bonding to solvent water molecules. (b) Insertion into well-matched sites with less than three H-bonds between the bases. The purine flips out and is able to π-stack onto an ancillary ligand. The pyrimidine also flips out but does not stack. This partially but not completely occludes one dppz nitrogen. (c) Canted (angled) intercalation into a well-matched base pair leaves one dppz nitrogen atom entirely exposed to solvent. (d) Model for intercalation by a Δ enantiomer at a 5'-AT/AT-3' step. Symmetrical intercalation into this step should expose both dppz nitrogens to the solvent. (e) Semi-intercalation by an ancillary ligand into the DNA duplex, exposing both phenazine nitrogen atoms to solvent. DNA is drawn in grey as a solvent-accessible surface, the carbon atoms of the complex are in purple with nitrogen atoms in blue. In the schematic diagram, the complex is drawn in purple with dppz nitrogen atoms as blue. DNA bases are represented as grey blocks with flanking adenine bases as red rectangles.[66]

1.1.6.5 Metallo-insertors and mismatches

The majority of complexes that bind to DNA non-covalently are either intercalators or groove binders. More recently another mode of binding called metallo-insertion has been reported. Unlike intercalation, where the aromatic planar unit of the complex slides in between the base pairs, resulting in the helix unwinding to compensate, metallo-insertors eject the bases of a single base-pair, with the planar aromatic unit of the complex acting as a π stacking replacement within the DNA double helix. No examples of this phenomenon were reported until the Barton group in 1997. Their research focussed on mismatch-specific DNA-binding agents which led on to the discovery of rhodium complexes that bind *via* this unique method.[69] Recent work has been focussed in the design of metal-complexes which can specifically interact with mismatched DNA preferentially. Base mismatches naturally occur in DNA as a result of genotoxic chemicals, ultra-violet radiation, and ionising radiation. Usually the body quickly corrects these with mismatch repair proteins, however failure to do so can lead to genetic mutations, spontaneous cancers, and heredity cancers.[70] Base-mismatch recognition poses a new challenge in the design and synthesis of DNA binding molecules. Barton and co-workers reported the first metallo-insertor DNA mismatch recognition agent $[Rh(bpy)_2(chrysi)]^{3+}$ (chrysi = 5,6-chrysenequinone diamine).[71] Molecular modelling investigations suggested that the broader four-ring chrysi ligand is too large to slide into the base pairs like in intercalation methods. However, it was the right size to fit into the locally perturbed site of a DNA mismatch. The racemic mixture was separated into enantiomerically pure Δ-$[Rh(bpy)_2(chrysi)]^{3+}$ and Λ-$[Rh(bpy)_2(chyrsi)]^{3+}$ and the binding properties of the enantiomers were measured on a set of 17-mer oligonucleotides all containing one DNA mismatch. This compound showed a dramatic enantiomeric effect with Δ binding to DNA mismatches extremely well, and Λ being almost completely inactive.[72] The width of the expansive aromatic system of the chrysi ligand exceeds the width of well-matched base pairs 11.3 Å versus 10.8 Å, as a result complexes bearing this ligand are preferentially accommodated at thermodynamically destabalised mismatch sites (*Figure 1.22*).

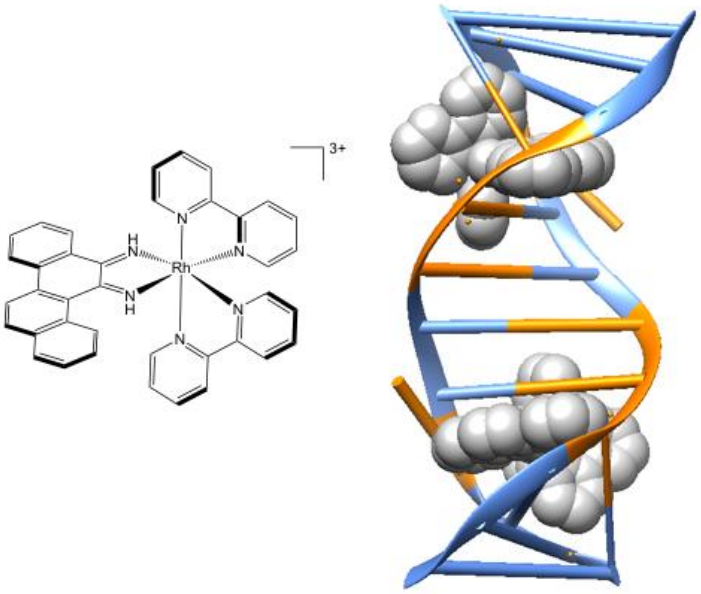

Figure 1.22: Chemical structure of the metallo-insertor Δ-[Rh(bpy)$_2$(chrysi)]$^{3+}$ (chrysi = 5,6-chrysenequinone diamine). Right - Structure of the bulky rhodium complex bound to an A-A DNA mismatch (orange) showing the general architecture of the metalloinsertion binding mode (PDB ID: 2O1I).

In the last few years the Barton group have investigated light switch complexes that recognize mismatches. They reported a crystal structure of Δ-[Ru(bpy)$_2$(dppz)]$^{2+}$ bound to mismatched DNA.[73] in which the complex is co-crystalised with a 12-mer oligonucleotide containing two adenosine-adenosine mismatches. Lack of DNA mismatch repair within the body has been linked to an increased rate of mutation and several types of cancer[74]. In an effort to develop new and selective probes for DNA mismatches attention was drawn to derivatives if [Ru(bpy)$_2$(dppz)]$^{2+}$ which are known to serve as molecular light-switches for DNA. Through ancillary ligand modification mismatch specificity was explored using [Ru(Me$_4$phen)$_2$(dppz)]$^{2+}$, (Me$_4$phen = 3,4,7,8-tetramethyl-1,10-phenanthroline).[75] The reasoning behind incorporating methyl groups on to the phenanthroline unit would disfavour binding to well-matched base pair sites due to steric clashing between the bulky ligand and the DNA backbone. The steady state luminescence response of the complex 2was explored using both a well-matched 27-mer DNA duplex and an analogous duplex containing a single CC mismatch. Subsequent DNA titrations produced relative binding affinities of 6.8×10^4 and 1.8×10^6 M^{-1} for well-matched and mismatched sites, respectfully. Thus, concluding that the complex is quite selective for binding to the single base mismatch. Further studies to test the specificity of this binding were carried out using well-matched GC and AT sequences compared to GG, AA, CT, TT, CA and CC mismatches. The greatest luminescent enhancement

was indeed by the most thermodynamically destabalised CC. To help explain the differential luminescence observed between the mismatched and well-matched DNA samples crystal structures were produced (*Figure 1.23*).

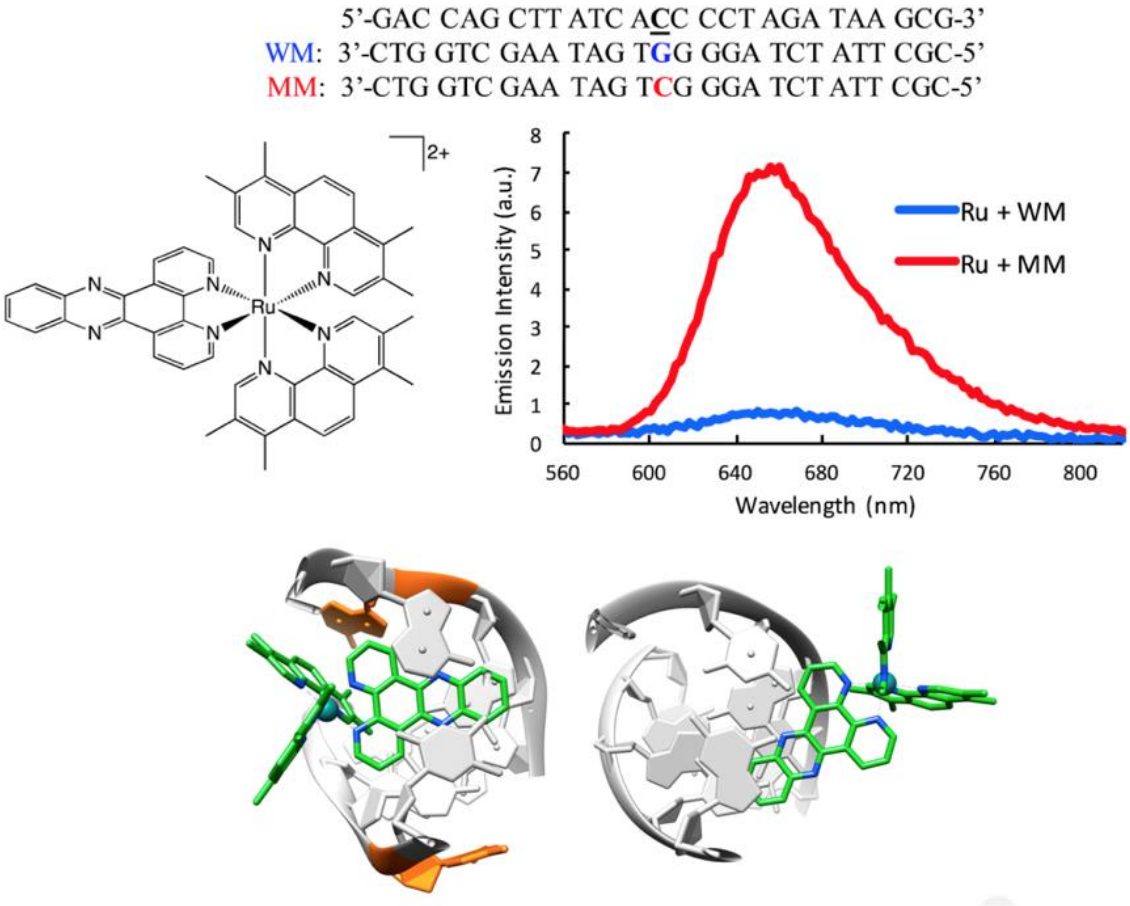

Figure 1.23: Top – DNA sequences used; Middle left – Schematic of $[Ru(Me_4phen)_2(dppz)]^{2+}$; Middle right – Steady-state luminescence spectra of rac-$[Ru(Me_4phen)_2(dppz)]^{2+}$ with the well-matched (blue) duplex and with the duplex containing a single base pair CC mismatch (red); Bottom – Views down the helix of Δ-$[Ru(Me_4phen)_2(dppz)]^{2+}$modelled into crystal structures of DNA duplexes. The ruthenium complex is shown in green with nitrogen atoms shown in blue. Bottom left – metalloinsertion at a mismatch site from the minor groove (the extruded mismatch bases are in orange); Bottom right – side-on intercalation at a well-matched site from the major groove.[65]

In the presence of a well-matched sequence a short complex excited state lifetime was observed at 35 ns, however in the presence of mismatched DNA the complex decays in a biexponential function with components of 33 and 160 ns. Given this short lifetime when bound to well matched DNA it was hypothesised that a side on intercalation is dominant.

1.1.7 Transition metal complexes as imaging agents

1.1.7.1 Principles of fluorescent cell imaging

Optical microscopy is one of the key biophysical methods in current life sciences research. Fluorescence microscopy, in particular, provides scientists with the ability to understand the complex spatiotemporal interplay of biomolecules on a molecular level.[76] Although the intrinsic fluorescence of biological species are weak, non-specific, and therefore limited for fluorescence microscopy organic fluorescent labelling agents can be used to enhance this such as synthetic dyes, nanocrystals, and proteins. In fluorescence microscopy, the high energy light irradiates and excites fluorophores in the sample. The excited fluorophore then emits lower energy fluorescent light, which is seen by the eye or another detector. Normal illumination results in the fluorescence of the entire specimen thickness, so that 90% of emitted light is out of focus resulting in a reduction in the final contrast and resolution. Unless the specimen is very thin then areas of the specimen above and below the focal plane still contribute to the image as "out of focus blur". Confocal fluorescence microscopy is one of the most powerful techniques in biological research and diagnostics as it avoids many of these pitfalls. Illumination of fluorophores causes photobleaching and subsequent cell damage, hence everything must be done to limit the duration and intensity of illumination. Confocal microscopy has the ability to shut off illumination light when not needed, meaning multiple probes can be imaged simultaneously.[77] Data acquisition rates of conventional scanning confocal microscopes are capable of rapid imaging of small samples. Laser scanning confocal microscopy also offers several advantages of conventional wide-field fluorescence microscopy including controllable depth of field, the elimination of out-of-focus information and the ability to collect serial optical sections from thick specimens (*Figure 1.24*).[78]

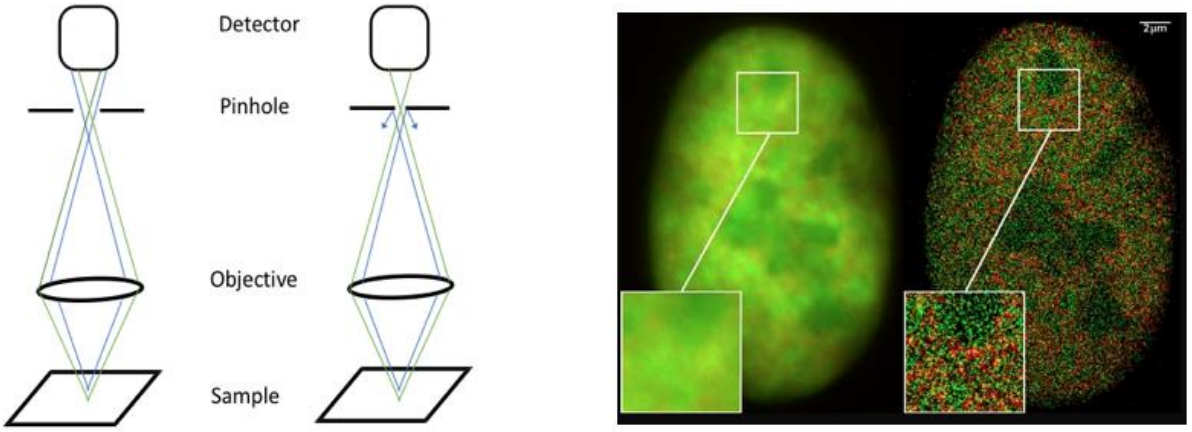

Figure 1.24: Left - Schematic showing a fluorescence microscope versus a confocal microscope. In a confocal microscope, the detector must be the same distance as the light source from the illuminated portion of the sample to effectively block out-of-focus light. Right – image showing the difference in resolution between wide-field and confocal microscopy of a bone cancer cell.[68]

The majority of fluorescent dyes used as cell probes are based on organic molecules such as fluoresceins, rhodamines, and cyanines. While some cell components are fluorescent, these commercially available dyes are usually used to allow imaging of areas which are non-fluorescent. Different dyes can accumulate in different areas of the cells, and due to emission at differing wavelengths, a multi-coloured reconstructed image can be obtained to simultaneously highlight several important structures within. General requirements that need to be met for a species to be used in bioimaging include that a probe should:[79]

(1) Be photostable and soluble in aqueous growth media suitable for biological applications.
(2) Be able to rapidly penetrate into a cell.
(3) Be non-toxic and non-phototoxic to the organism.
(4) Not interfere with metabolic activity.
(5) Show preferential localisation in a certain organelle of the cell.
(6) Be capable of being excited/emitted at wavelengths that can transmit through cellular structures (UV light penetrates the cells but leads to damage).
(7) Display a large enough Stokes shift to permit the use of optical filters that separate excitation light from emission light. This has two-fold importance: to prevent self-quenching and to distinguish the emission of the fluorophore from auto-fluorescence.

(8) Display a lifetime long enough to, distinguish the probe from the short auto-fluorescence lifetimes of endogenous fluorophores.

When considering these criteria, currently used organic fluorophores have some drawbacks, particularly photobleaching. Fluorescence emitted by almost all fluorescent dyes fades during observation. This is caused by photochemically driven chemical modification of the dye, resulting in the irreversible loss of ability to fluoresce (*Figure 1.25).*[80]

Some fluorophores have a very short lifetime, fading after the emission of only a few hundred photons, whereas other can emit millions of photons before being photobleached.

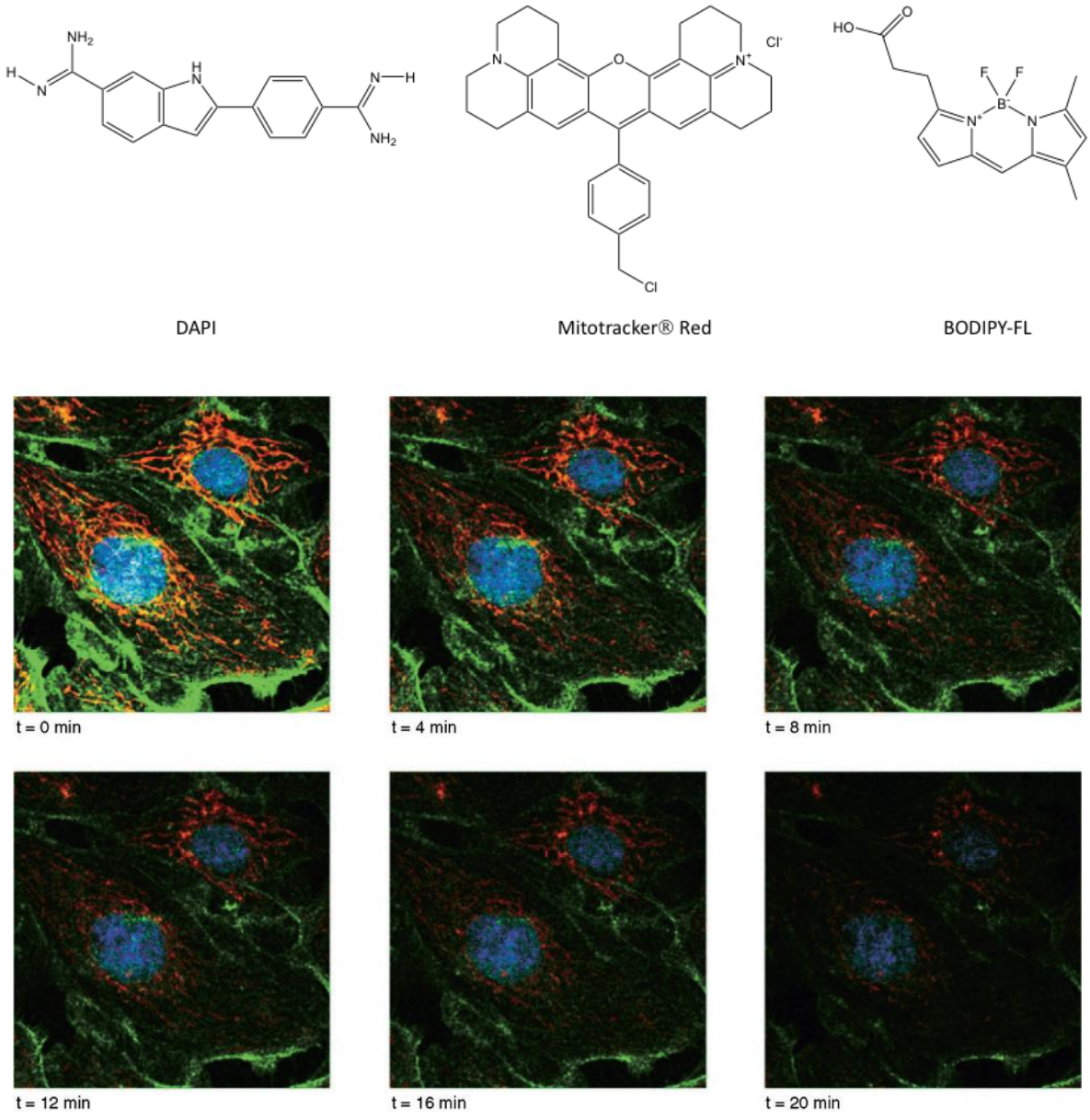

Figure 1.25: Top - Chemical structures of the common fluorescent dyes DAPI (nuclear stain), Mitotracker Red (mitochondria stain) and BODIPY-FL (actin filament stain). Bottom - Loss of fluorescence of DAPI (blue), Mitotracker Red (red), and BODIPY-FL (green) in fixed bovine pulmonary artery endothelial (BPAE) cells.[63]

1.1.7.2 Transition metal complexes as imaging agents

Recently there has been key developments in exploiting luminescent transition metal complexes for biological applications of optical imaging and targeted molecular probes.[81] The d^6- platinum metal group (ruthenium, rhodium, palladium, osmium, iridium and platinum) possess desirable properties for such applications including tunable emission throughout the viable and near-IR regions, long luminescence lifetimes (from 100s of nanoseconds to microseconds), good luminescent quantum yields, large Stokes shifts, good thermal, chemical, photochemical stability, and importantly they are kinetically inert.[82] They also possess well-developed substitution chemistry, this leads to a diverse range of metal-ligand architectures with a range of photophysical properties. These complexes have a combination of an easily oxidised d^6 metal centre and a strongly π- accepting polypyridyl ligand leading to MLCT-based excited states. A perfect example of this is the archetypical $[Ru(bpy)_3]^{2+}$. The central metal ion plays an important role as it facilitates intersystem crossing from shorter-lived fluorescence singlet states to longer lived triplet phosphorescent states. This is due to a phenomena called the heavy atom effect, which is the perturbation of the spin-orbit coupling in a molecule due to a nearby atom of a high atomic number.[83] It is known that in aromatic systems the heavy atom effect greatly influences singlet to triplet intersystem crossing rates, and thus phosphorescent lifetimes.[83] Spin-orbit coupling enables fast intersystem crossing, estimated to occur in tens to hundreds of femtoseconds. In contrast the ^{3}MLCT states produced have lifetimes of microseconds to milliseconds.[84] The energy lost in the conversion to the triplet state and geometric reorganisation results in a larger Stokes shift than that of classical fluorophores.[85] There is scope for colour tuning as the highest occupied molecular orbital (HOMO) and the lowest unoccupied molecular orbital (LUMO) are based on structures within the complexes. The HOMO is usually based on the metal centre and the LUMO is situated on the polypyridyl rings. Resulting in both molecular orbitals being independently tuned from one another. The relative ordering of the excited states and the energy gaps between them are the main influence of the photophysics. Thus, by controlling the stereoelectronic nature of the ligands attached to the metal centre the excited state properties can be tuned.[86]

1.1.7.3 Ruthenium(II) complexes for luminescent imaging

Ru^{II} complexes have rich photophyscial attributes which provide a basis to design responsive luminescence probes to selectively quantify and image biological samples. Despite being the parent compound in photochemistry and photophysics, ruthenium(II) *tris*-bipyridine,

$[Ru(bpy)_3]^{2+}$ is not well suited for live-cell luminescence imaging owing to poor cellular uptake. In fact, it is common for Ru^{II} complexes to show inefficient penetration across phospholipid bilayers of the live cell membranes as a result of their cationic charges and polarity.[85] One way to overcome these problems is to modify the polypyridyl ligands to increase lipophilicity.[87] Using confocal microscopy and flow cytometry, the uptake of $[Ru(DIP)_2(dppz)]^{2+}$ **Ru1** was found to accumulate in the cells more quickly in comparison to the molecular light-switch complex $[Ru(bpy)_2(dppz)]^{2+}$, despite the larger size. This complex was found to enter the cell through the mechanism of passive diffusion within an hour at micromolar concentrations (*Figure 1.26).*

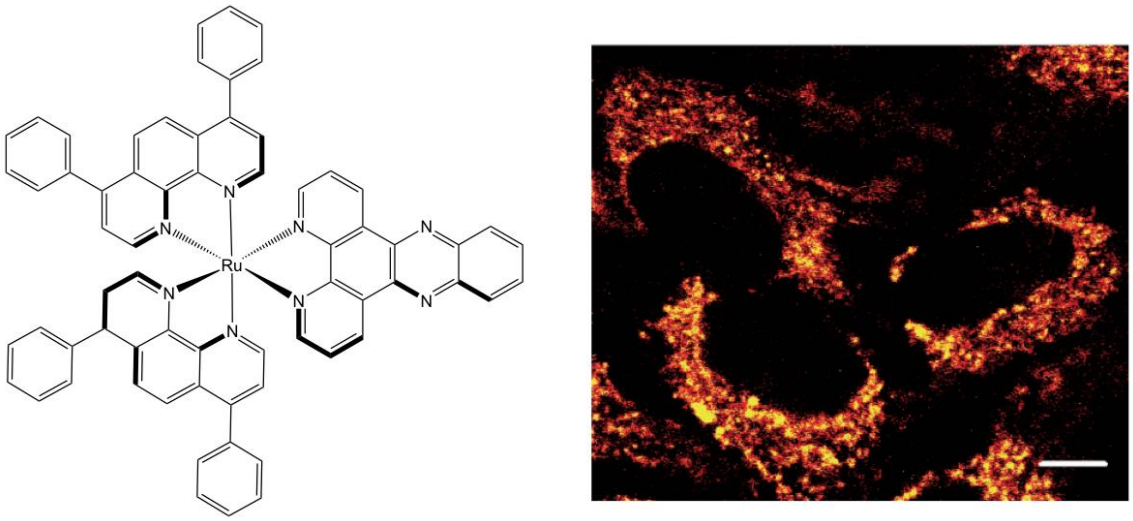

*Figure 1.26: Left - Chemical structure of $[Ru(DIP)_2(dppz)]^{2+}$ **Ru1** Right - HeLa cells incubated with 5 μM complex for 4 hours and imaged by confocal microscopy. Note that the cytoplasm is extensively stained with the Ru complex. Scale bar is 10 μm.[77]*

Cell-penetrating peptides can be conjugated to Ru^{II} complexes to increase their cellular uptake, such as the HIV tat peptides and oligoarginine. Studies were carried out by incorporating cell-penetrating peptides with dppz complexes of Ru^{II}. As mentioned previously, such complexes in aqueous solution luminesce brightly only when bound to DNA. An example of this is when the cellular uptake of the peptide conjugates of Ru(II) dppz with and without a fluorescent tag were compared.[88] Three Ru(II) dppz conjugates were synthesised: Ru-octaarginine (Ru-D-R8) **Ru2**, Ru-octaarginine-fluorescein (Ru-D-R8-fluor) **Ru3**, and Ru-fluorescein (Ru-fluor) **Ru4**. The complexes were incubated with HeLa cells, and as expected cellular uptake is strongly enhanced compared to unconjugated systems ($[Ru(phen)_2(dppz)]^{2+}$ and $[Ru(bpy)_2(dppz)]^{2+}$) proven by higher luminescence evident in cell samples even after shorter incubation times (*Figure 1.27*).

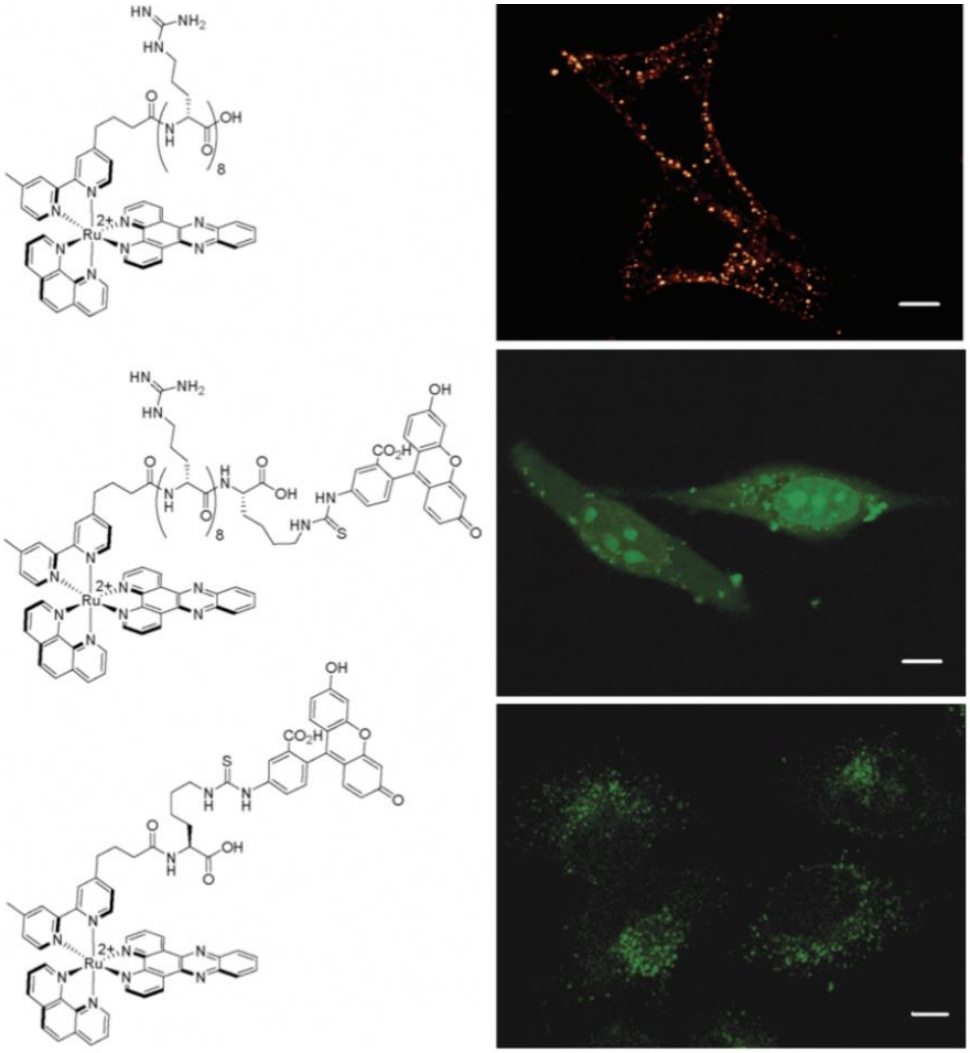

Figure 1.27: HeLa cells were incubated with 5 μM Ru-D-R8 ***Ru2*** *for 30 min (top), 5 μM Ru-D-R8-fluor* ***Ru3*** *for 30 min (middle) and 20 μM Ru-fluor* ***Ru4*** *for 41 hours (bottom) at 37℃ and imaged by confocal microscopy. Note that Ru-D-R8 is isolated to the cytoplasm while Ru-D-R8-fluor stains the cytosol, nucleus and the nucleoli. Ru-fluor only shows weak cytoplasmic staining. Scale bars are 10 μM.*[78]

In recent years, the use of nanoparticles, especially metal nanoparticles has expanded into biomedical research. Gold nanoparticles are extremely popular due to their small size to volume ratio, high thermal stability, amenability of synthesis and functionalisation and ease of detection.[89–91] Work in the Gunnlaugsson group combined Ru(II)-polypyridyl complexes with gold nanoparticles to create luminescent probes/imaging agents for various biological applications.[92] Upon microirradiation of the Ru(II) bispolypyridyl chlorides: $Ru(bpy)_2Cl_2$ **Ru5**, $Ru(phen)_2Cl_2$ **Ru6**, and $Ru(TAP)_2Cl_2$ **Ru7** (TAP = 1,4,5,8-tetraazaphenanthrene) were coupled 11-mercaptoundecanoic acid and 5-amino-1,10-phenanthroline and attached to gold nanoparticles. All three ruthenium complexes functionalised gold nanoparticles displayed high DNA binding affinities all in the region of ~ 10^7 M^{-1}. Using confocal fluorescence microscopy,

it was found that all three compounds undergo rapid cellular uptake within HeLa cells, localising within the cell cytoplasm and nucleus within a 4-hour time window (*Figure 1.28).*

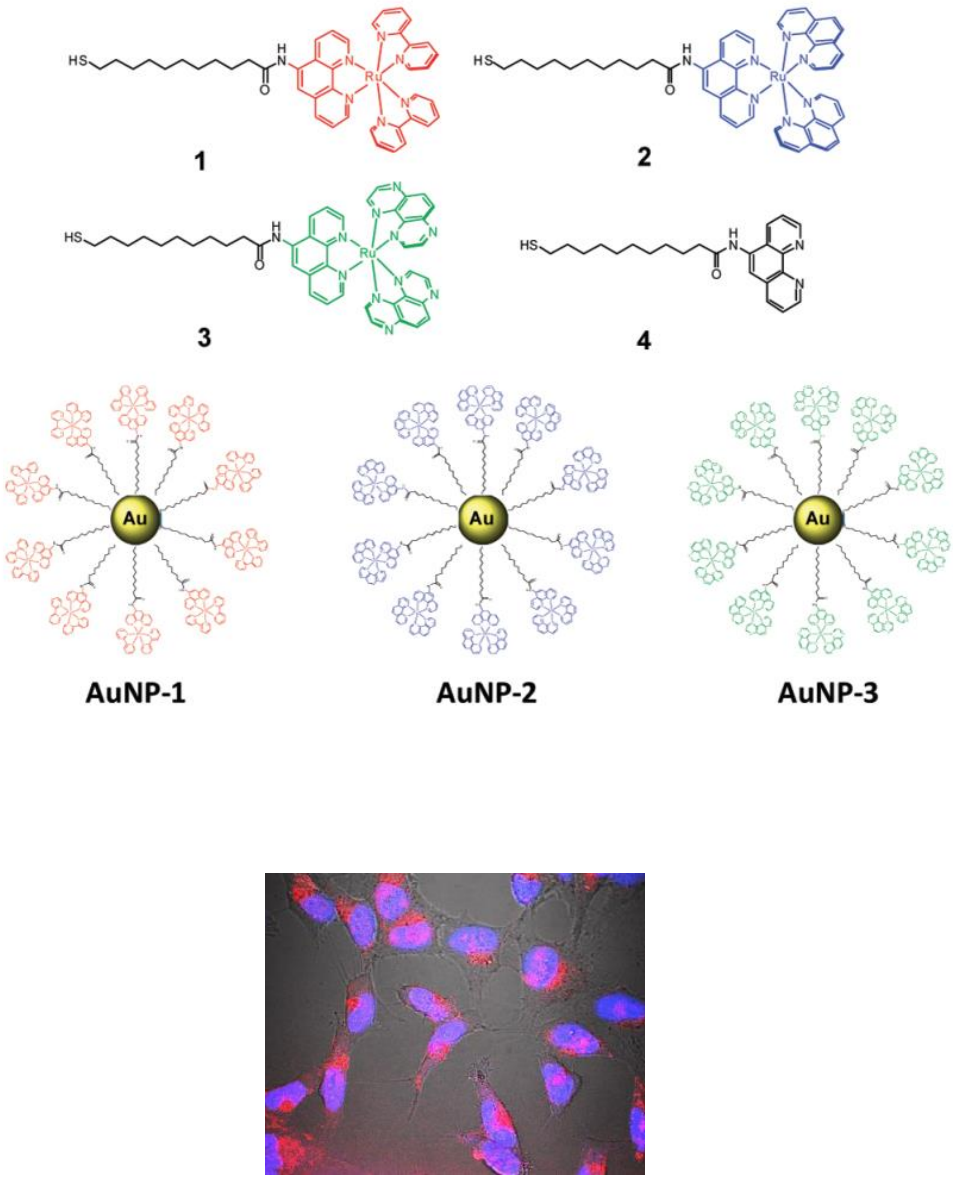

*Figure 1.28: Top - Structures of the complexes **Ru5, Ru6** and **Ru7** and the ligand; Middle- Cartoon representation of their corresponding Au nanoparticle systems: Bottom – live HeLa cell confocal imaging of nanoparticle* (red) and an overlay of nuclear co-stain DAPI (blue).[8]*

Ever since the discovery of the aforementioned molecular light-switch complex $[Ru(bpy)_2(dppz)]^{2+}$ there has been a great deal of interest in the potential of polypyridyl complexes as highly sensitive structure-specific DNA probes. Although much previous research in this area was hampered by poor cellular uptake restricting the use of these luminescent metal complexes.[93] Within the Thomas group, the use of a dinuclear ruthenium(II)

polypyridyl complex as a direct imaging agent for DNA structure in living cells was first developed by Dr Martin Gill.[94] Two complexes were investigated $[(phen)_2Ru(tpphz)Ru(phen)_2]^{4+}$ **Ru8** and $[(bpy)_2Ru(tpphz)Ru(bpy)_2]^{4+}$ **Ru9** (phen = 1,10-phenathroline, tpphz = tetrapyrido[3,2-1:2',3'-c:3",2"-h:2''',3'''-j]phenazine) (*Figure 1.29*).

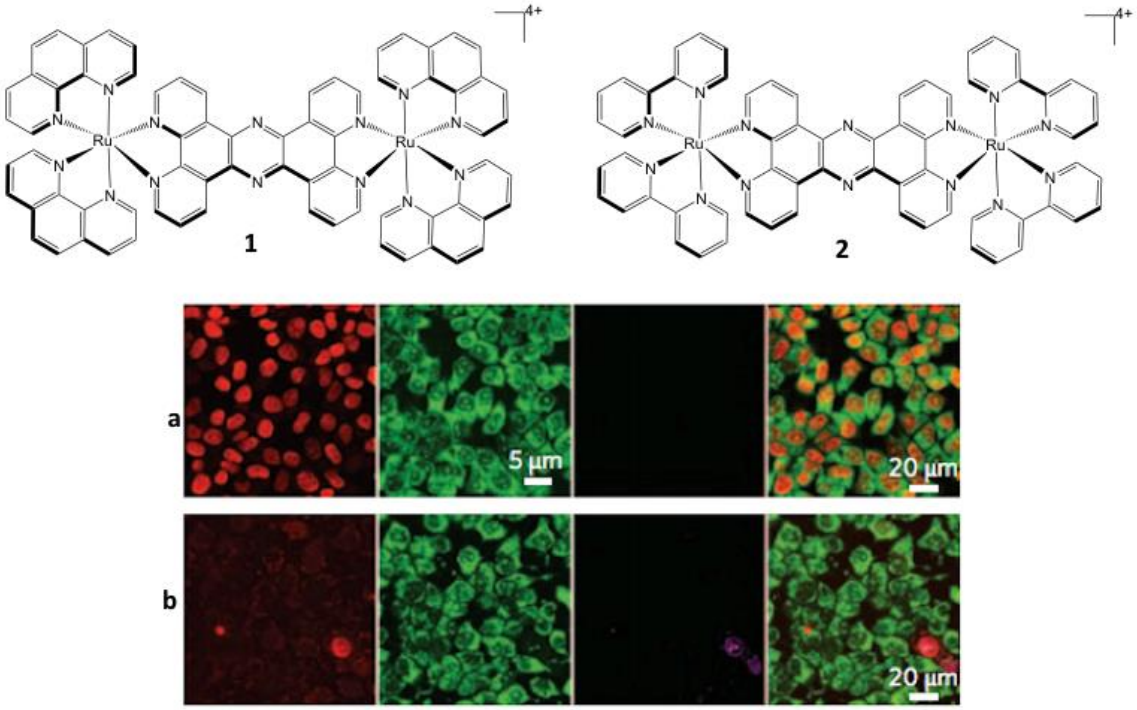

Figure 1.29: Top - Chemical structures of [(Ru(phen)2)2(tpphz]4+ ***Ru8*** *and [(Ru(bpy)2)2(tpphz)]4+* ***Ru9*** *Bottom - a) Uptake and nuclear staining of MCF-7 breast cancer cell line by 1 (500 µM, 1 hr). From left to right: luminescence emission of 1 (red), live stain SYTO 9 (green), dead cell stain propidium iodide (PI) (purple) and overlay image. B) Incubation with 2 (500 µM, 1 hr) shows no staining of live cells and the co-localisation with PI emission shows 2 to act as a dead cell stain.[94]*

Both of these complexes have emissive MLCT states upon DNA binding, similar to those of related dppz complexes. As expected, this light switch effect arises from the shielding of the phenazine nitrogen atoms on the tpphz unit from water upon binding to DNA resulting in the ^{3}MLCT state.[95] Neither complexes showed high toxicity over a 24-hour incubation with a breast cancer cell line MCF-7. (IC_{50} values of 138 µM and >500 µM respectfully, **1** being the more toxic of the two). In comparison to **Ru8, Ru9** showed no staining for live cells however further studies revealed it is an efficient fixed cell stain and is an indicator of cell mortality. Further investigations were then carried out with **Ru8** and **Ru9**. Apart from nuclear DNA, other cellular apparatus can be targeted by these metal complex imaging agents. Imaging of mitochondria is useful due to the mitochondrion's role in electron transport, oxidative phosphorylation and downstream effects in physiological cell death.[96] Follow-up work

demonstrated that dinuclear ruthenium (II) complexes can be specifically delivered to mitochondria by employing a biocompatible, pH-sensitive polymerosome vector (*Figure 1.30*).[97] **Ru8** and **Ru9** were encapsulated within polymerosomes and their subcellular location was investigated by costaining with fluorescent organelle dyes. These included Mitotracker Red (labels active mitochondria), Lysotracker Yellow (tracks acidic lysosomes in live cells) and SYTO 9 (cell viability cell). Surprisingly both complexes delivered in this way localise within mitochondria; even **Ru9** which previously showed no cellular uptake as a free complex.

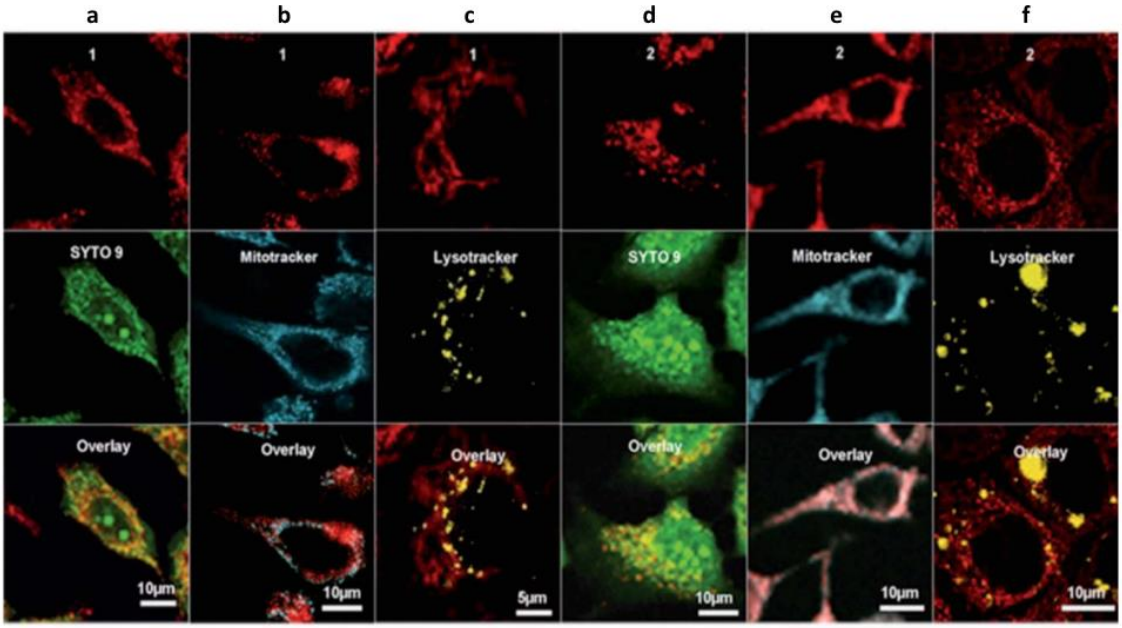

*Figure 1.30: Confocal microscopy showing cellular internalisation of **Ru8** (red), and colocalisation with a) SYTO 9, b) Mitotracker Red (blue), and c) Lysosome tracker Yellow (yellow) in MCF-7 cells. Confocal microscopy showing cellular internalisation of **Ru9** (red), and colocalisation with a) SYTO 9, b) Mitotracker Red (blue), and c) Lysosome tracker Yellow (yellow) in MCF-7 cells.[74]*

Following the success of these dinuclear ruthenium(II) complexes as cellular imaging agents the Thomas group went on investigate the bioactivity of the new complex $[(Ru(DIP)_2)_2(tpphz)]^{4+}$ (DIP = 4,7-diphenyl-1,10-phenanthroline), **Ru10**, (*Figure 1.31*).[98] By incorporating the DIP as an ancillary ligand this produced a lipophilic derivative. Similar to previous work, the complex was incubated with MCF-7 breast cancer cells, and intracellular cellular targeting was investigated by detailed co-localisation experiments. The complex was costained with the nuclear stain DAPI –(4'-6-diamidino-2phenylindole) and calnexin-specific fluorescent secondary antibody. Calnexin is a calcium-binding protein located within the endoplasmic reticulum. As **Ru10** is a lipophilic molecule it was hypothesised that it would

interact strongly with membrane structures and associate with lipophilic regions within cells. Indeed, it was reported that the lipophilic Ru^{II} MLCT luminescent complex successfully targets the lipid-dense endoplasmic reticulum in cells, where it acts as an *in cellulo* imaging agent for this organelle for confocal scanning microscopy.

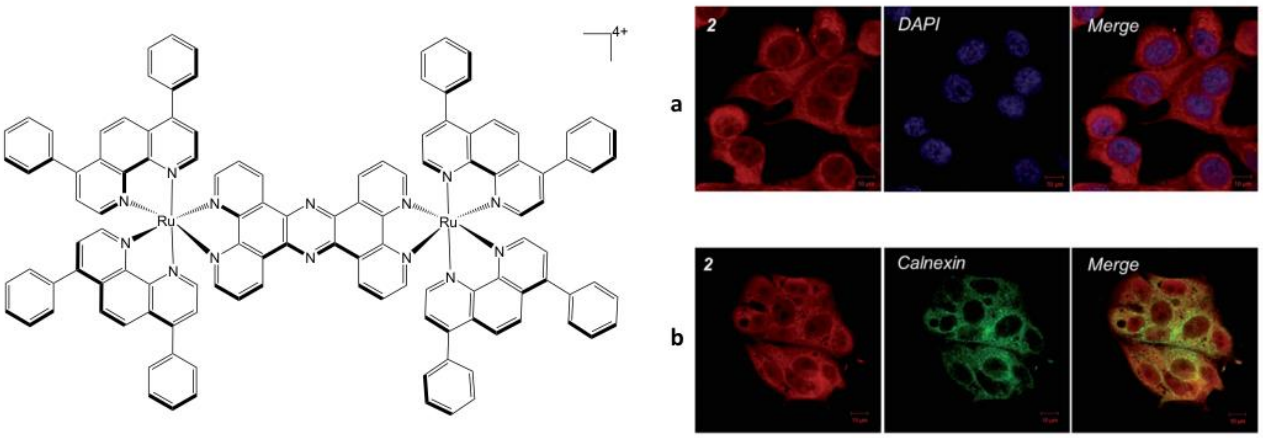

Figure 1.31: Left - Chemical structure of $[(Ru(DIP)_2)_2(tpphz)]^{4+}$ (DIP = 4,7-diphenyl-1,10-phenanthroline) ***Ru10****. Right - a) costaining of complex (red) and DAPI (blue), b) costaining of complex (red) and ER-localised calnexin protein (green).*[88]

1.1.7.4 Iridium(III) complexes for luminescent imaging

Iridium(III) complexes are considered to be one of the most versatile class of biosensing and bioimaging agents. They are attractive as new cell imaging probes because not only do they possess the characteristics suitable for imaging applications; kinetic inertness with very low rates of ligand exchange, large Stokes shifts (hundreds of nm), long luminescence lifetimes (100 ns to ms) and enhanced photostability.[99] Iridium(III) complexes, in comparison to tris-diimine ruthenium(II) complexes, possess highly tunable excitation and emission states. Ru(II) complexes have shorter lifetimes due to the thermal population of a low lying ^{3}MC state, which is non-emissive. This boarder colour tunability is a result of Ir^{III} complexes having an increased ligand-field stabalisation energy (LFSE) creating less thermally accessible non emissive ^{3}MC states.[100,101] Therefore, the two principle transitions observed in the long lived excited state Ir^{III} complexes are metal-to-ligand charge transfer (MLCT) and ligand-centred (LC) transitions. Due to the aforementioned heavy atom effect, the third-row transition metal promotes strong spin-orbit coupling, facilitating intersystem crossing to a mixed triplet state. This excited state

mixing of ^{3}LC and ^{3}MLCT creates systems where the energy gap between the lowest unoccupied molecular orbital (LUMO) and the highest occupied molecular orbital can be deliberately adjusted by structural modification of the ancillary ligands and by substituent effects (*Figure 1.32*).[102] Wavelengths (of energy) are blue shifted by electron-withdrawing substituents and red shifted by electron donating groups.[103] Electron withdrawing substituents tend to stabalise the HOMO by removing electron density from the metal, whereas electron donating has the inverse effect.[104] This means that a high number of ligand and substituent variables can be utilised to influence the nature of the excited state of Ir^{III} complexes. These different excited states render these complexes to show interesting and tunable emission wavelengths, quantum yields and lifetimes, creating a wide-range photophysical toolkit for cellular imaging.[105,106]

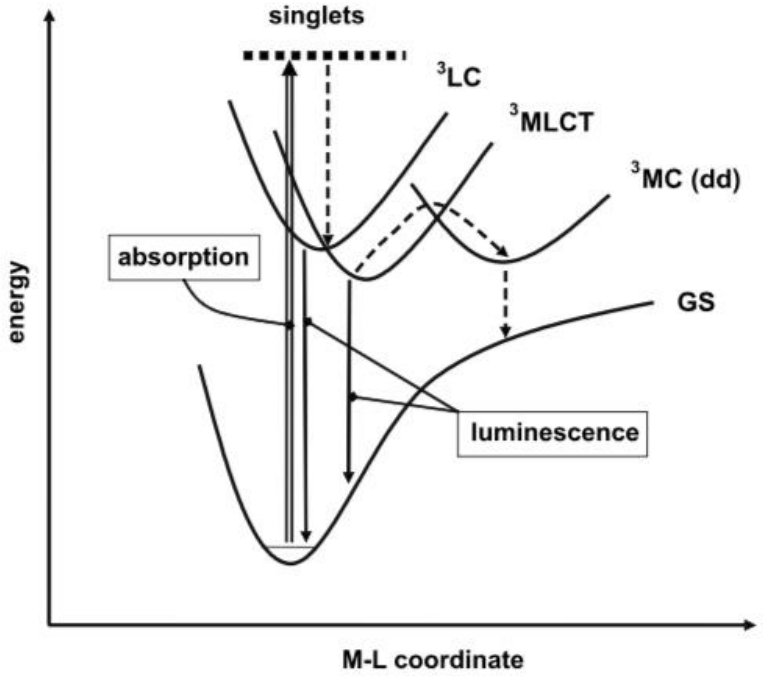

Figure 1.32: Electronic transitions involving MC, MLCT and LC excited states; the MC levels are not emissive.[102]

The first report of the application of Ir^{III} complexes in cellular imaging experiments came from Li, *et al.* in 2008 (*Figure 1.25*).[107] They reported on two phosphorescent probes based on cationic iridium complexes, which exclusively stain the cytoplasm. The synthesised complexes, $[Ir(dfpy)_2(bpy)]^+PF_6^-$ **Ir1** and $[Ir(dfpy)_2(quqo)]^+PF_6^-$ **Ir2** [dfpy = 2-(2,4-difluorophenyl)pyridine, quqo = 2-(2-quinolinyl)quinoxaline] displayed green emission (λ_{max}

= 517 nm) and red emission (λ_{max} = 623 nm) respectively. This illustrated the versatility of iridium complexes and the capability of tunable emission profiles for this function.

Li and co-workers also carried out investigations proving low cytotoxicity and reduced photobleaching making them promising candidates for the design of specific phosphorescence bioimaging agents. At the time of this report, the fluorinated units in the complexes were regarded as essential to facilitating cellular uptake as they increased the lipophilicity of the system. Subsequent work determined that cyclometallated iridium complexes are intrinsically of high enough lipophilicity. After being incubated with the breast cancer cell line, both complexes cellular uptake were examined and measured using confocal microscopy (*Figure 1.33*).

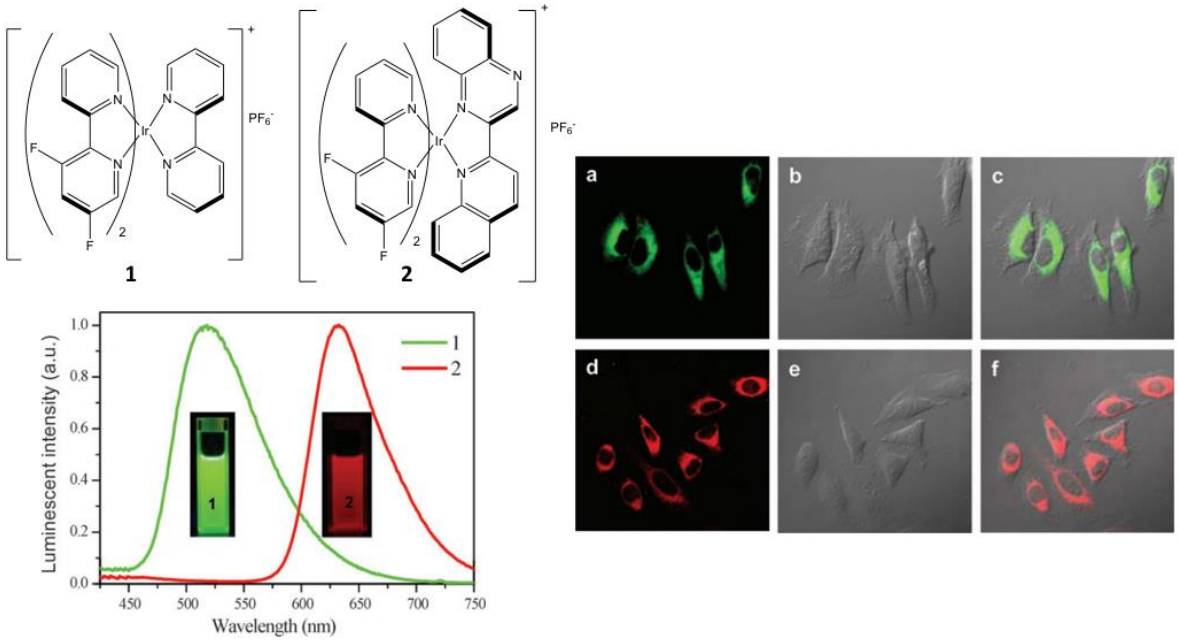

*Figure 1.33: Left (top) - Chemical structures of **Ir1** [Ir(dfpy)$_2$(bpy)]$^+$Pf6$^-$ (dfpy = 2-(2,4-difluorophenyl)pyridine) and **Ir2** [Ir(dfpy)$_2$(quqo)]$^+$PF6$^-$ (quqo = 2-(2-quinolinyl)quinoxiline). Left (bottom) – Room temperature photoluminescence spectra (λ_{ex} = 360 nm) and a photograph showing the luminescenes (under 365 nm UV excitation) of 20 μM **1** and **2** in CH_2Cl_2. Right – confocal luminescence (a and d) and brightfield images (b and e) of living Hela cells incubated with 20 μM **1** (top) or **2** (bottom) in DMSO/PBS for 10 mins at 25 ℃. Overlays of luminescence and brightfield images (c and f) for **Ir1** and **Ir2** respectfully.*[76]

Williams *et al* reported two new bis-cyclometallated iridium complexes based on $[Ir(ppy)_2(pybz)]^+$ [ppy= 2-phenyl pyridine, and pybz = 2-pyridyl-benzimidazole] **Ir3**, with one complex simply being the conjugate acid of the other **Ir4** (*Figure 1.34*).[108] The protonation of the system affects the excited state properties of the system. The intense low energy luminescence of these complexes can be discriminated from the fluorescence of H33258. Complex **Ir3** emits brightly in the green region, meanwhile complex **Ir4** is in the orange region. Within the cell the complex (which is in equilibrium between protonated and deprotonated states, depending on the pH of its surroundings) is in the predominate form of the charge neutral species. The long-lived lifetimes of these complexes were exploited in time-gated co-staining experiments with Hoechst stain.

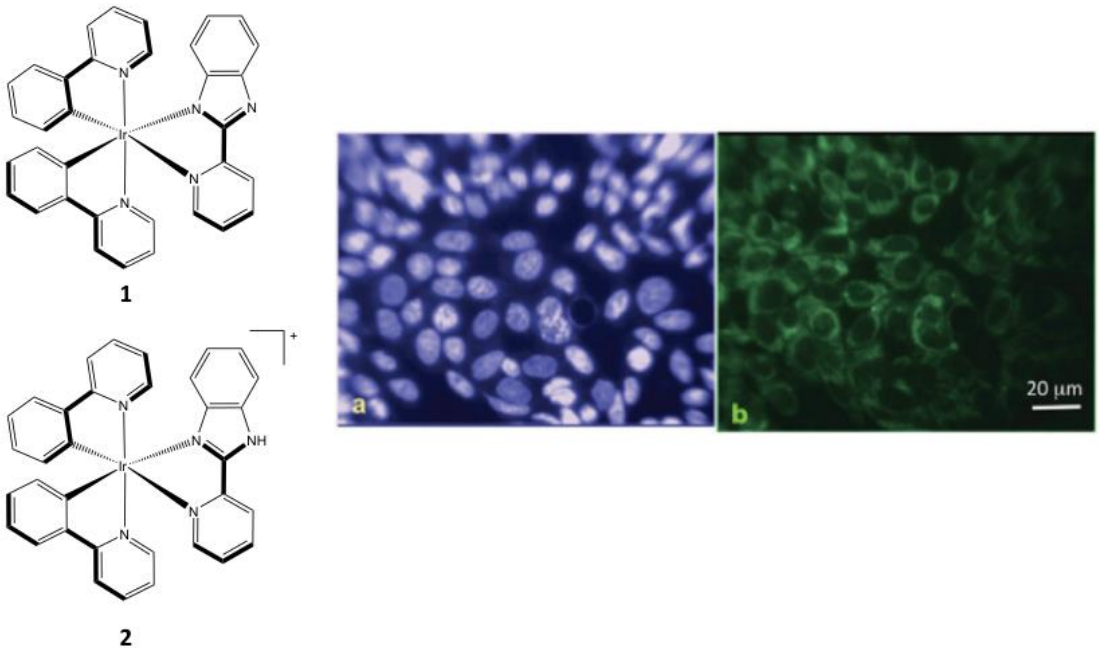

Figure 1.34: Left - Chemical structures of [Ir(ppy)2(pybz)] (pybz = 2-pyridyl-benzimidazole) ***Ir3*** *and the conjugate acid* $[Ir(ppy)2(pybzH)]^+$ ***Ir4*** *Right - Fluorescence microscopy images of live CHO (chinese hamster ovary) cells co-stained with* ***Ir3*** *(10 uM, 1 hr incubation) and Hoechst (350 nM, 5 min), using pulsed excitation at 355 nm (pulse length 4 ns). (a) no delay between laser pulse and image acquisition. (b) the image recorded after a delay of 10 ns.*[78]

In the image recorded with no time delay, bright emission in the nucleus dominates the image from the Hoechst stain. After a 10 ns time delay, emission from the Hoechst stain decays to a negligible level (3.6 ns lifetime), however the iridium complex's very long intercellular lifetime of around a microsecond, still remains clear. Thus, producing a system where it is possible to observe different subcellular sections of the same sample simply by time-gating data acquisitions.

Li *et al* investigated a non-emissive cyclometalated iridium(III) solvated complex $[Ir(ppy)_2(DMSO)_2]^+PF_6^-$ **Ir5** whose luminescence "switches-on" when inside the nuclei of living cells.[109] The non-emissive complex, without conjugation of a molecular transporter can react with histidine and histidine-rich proteins to exhibit intense emission, resulting in very quick selective lighting up of the nuclei of living cells. This novel light-switch effect is highly selective towards histidine over amino acids as shown by a series of control experiments which demonstrated that upon entering the cell the luminescence enhancement is 200-fold. Proof of preferential uptake to the nucleus was confirmed by complete intracellular colocalisation with H33528. As shown, the complex bright green spots perfectly colocalise with the blue of the Hoechst emission (*Figure 1.35*).

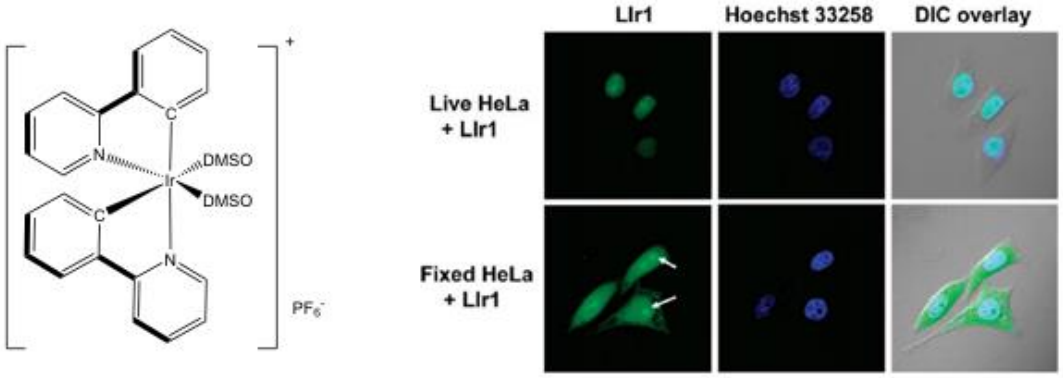

Figure 1.35: Left - Chemical structure of $[Ir(ppy)_2(DMSO)_2]^+ PF6^-$ ***Ir5****. Right: Confocal luminescence images of (top) living HeLa cells incubated with 10 μM complex in DMSO/PBS for 10 mins at 37 ℃ and then further incubated with Hoechst 33258, and (bottom) fixed HeLa cells stained with complex and Hoechst 33258 under the same conditions. Arrows point to the nucleolus of HeLa cells.[79]*

In 2013 Zhou *et al* first reported biscarbene iridium(III) complexes as living cell imaging agents.[81] The group investigated five complexes **Ir6-Ir10** with a range of ligand architectures including electronically neutral complexes containing the N^O ancillary ligand (picolate) and positively charged complexes which have a N^N ancillary ligand (2,2-bipyridyl). Alongside the variation in charge, derivatives with $–CF_3$ and –CN groups were also investigated, because of their electron-withdrawing effects and potential effects on the lipophilicity. HeLa cells were co-incubated with 20 μM iridium(III) complexes for 2 hours and luminescent images were taken using a confocal microscope. The intracellular distribution of the five complexes is mainly in the cytoplasm rather than the nucleus and the membrane. To summarise; based on

their emissive and biological properties five novel biscarbene iridium(III) complexes were utilised as multicolour cellular imaging agents (*Figure 1.36).*

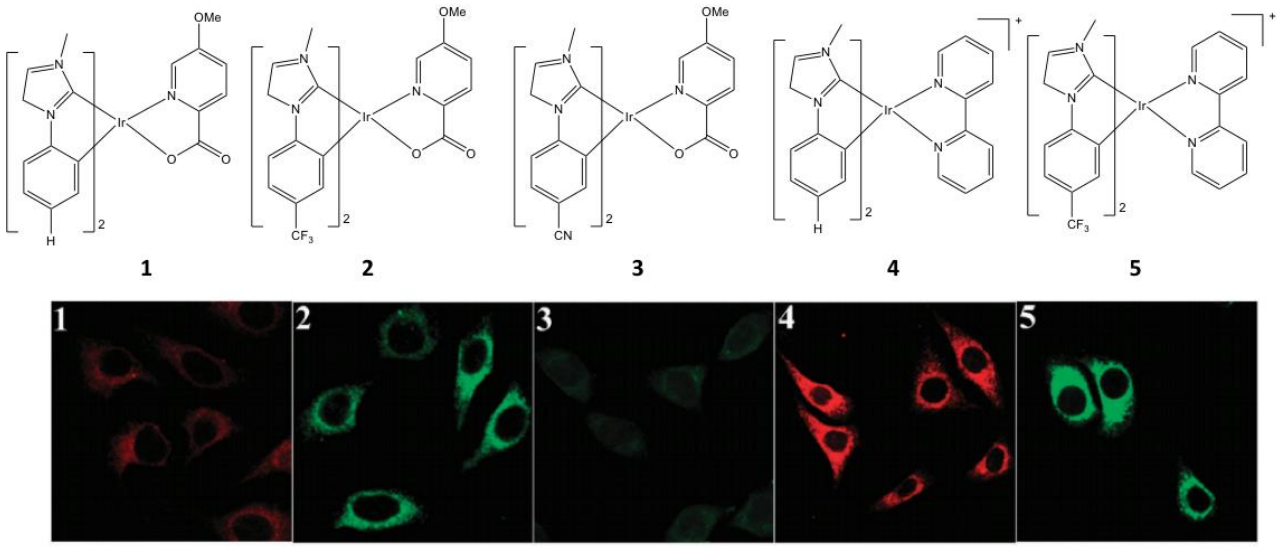

*Figure 1.36: Top - The chemical structures of the five biscarbene iridium(III) complexes used in this work **Ir6-Ir10**. Bottom - Fluorescence images of HeLa cells incubated with complexes **Ir6-Ir10** for 2 hours at 37 ℃.*[81]

Another recent example is by Li Xu and co-workers in 2017, who reported two near-infrared cyclometallated Ir^{III} complexes as mitochondrial imaging agents in living cells.[110] $[Ir(pbq\text{-}g)_2(N\text{^}N)]^+Cl^-$ (pbq-g = phenylbenzo[*g*]-quinoline; N^N = 2-(1-benzyl-1H-pyrazole-3-yl)pyridine **Ir11** and $[Ir(pbq\text{-}g)_2(N\text{^}N)]^+Cl^-$ (N^N = 2-(1-(napthalen-1-ylmethyl)-1H-pyrazol-3-yl)pyridine **Ir12** were the two NIR-emitting complexes reported (*Figure 1.37*).

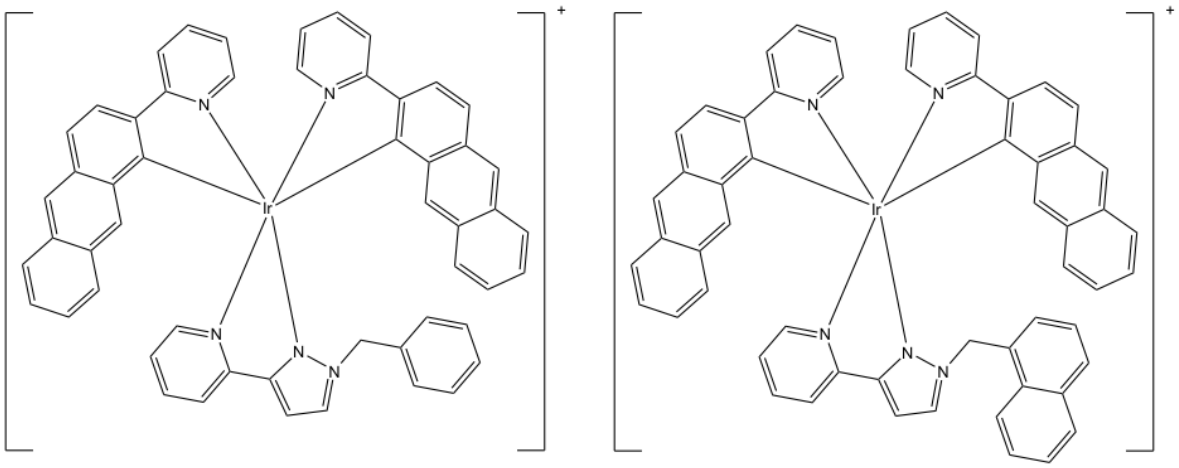

*Figure 1.37: Chemical structures of (left) $[Ir(pbq\text{-}g)_2(N\text{^}N)]^+Cl^-$ (pbq-g = phenylbenzo[g]-quinoline; N^N = 2-(1-benzyl-1H-pyrazole-3-yl)pyridine and **Ir11** (right) $[Ir(pbq\text{-}g)_2(N\text{^}N)]^+Cl^-$ (N^N = 2-(1-(napthalen-1-ylmethyl)-1H-pyrazol-3-yl)pyridine **Ir12**.*

The photophysical properties of the two complexes were investigated by UV-vis absorption and emission spectroscopy. Their MLCT emission bands were almost identical with complex 1 showing strong emission 751 nm and 2 at 750 nm. In addition, both complexes were found to possess long phosphorescent lifetimes at 442 ns **Ir11** and 456 ns **Ir12** respectfully. Co-localisation experiments were carried out to investigate cellular uptake and specificity. **Ir11**, **Ir12**, MitoTracker® Green (MTG) and DAPI dyes were used to co-label HeLa cells, and it was concluded that both the complexes selectively accumulate in the mitochondria of living cells.

As previously mentioned organic fluorescent dyes commonly suffer from photobleaching therefore, the complexes photostability within the cells were also monitored. The photostability of **Ir11, Ir12** were tested against commercially available MTG as both stained HeLa cells. Confocal microscopy images of the cells revealed longer lived emission: after 450 s the MTG intensity had decreased by 35%, whereas the iridium complexes were still emitting at 98% and 99% of the maxima suggesting much better photostability (*Figure 1.38*).

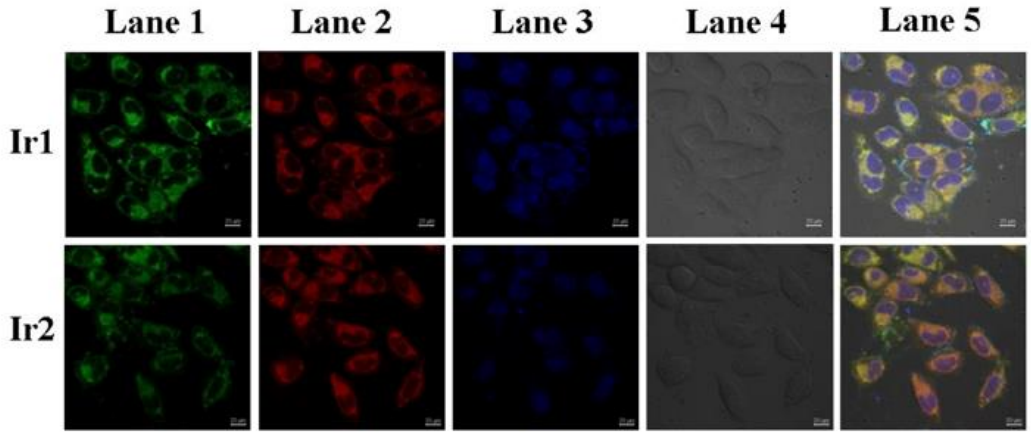

*Figure 1.38: Confocal phosphorescence images, bright field images and their overlay of living HeLa cells incubated with 20 uM of Ir1 and Ir2 inPBS for 1 hr 37 °C, Lane 1 50 nM Mitotracker Green, lane 2 confocal phosphorescence images of **Ir11-Ir12**, lane 3 confocal images of DAPI, lane 4 bright field images, lane 5 overlay of lane 1,2,3,4 and 5.*[80]

1.1.8 Project Aims

Ir^{III} complexes have recently excelled in a range of applications due to their attractive photophysical and electrochemical properties. Yet, despite the success of research associated with the molecular light-switch complex $[Ru(bpy)_2(dppz)]^{2+}$ and other analogues; Ir^{III} equivalents have yet to be developed. The aim of this thesis was to design iridium polypyridyl complexes **1-3** based on the well-characterised Ru^{II} counterparts that can reversibly bind to DNA *in vitro* (*Figure 1.38*). The luminescent properties of these complexes mean that the mode of binding and affinity to DNA could be explored. Successful preliminary work could be carried out on a selected cancer cell line to explore cellular uptake and cytotoxic activity.

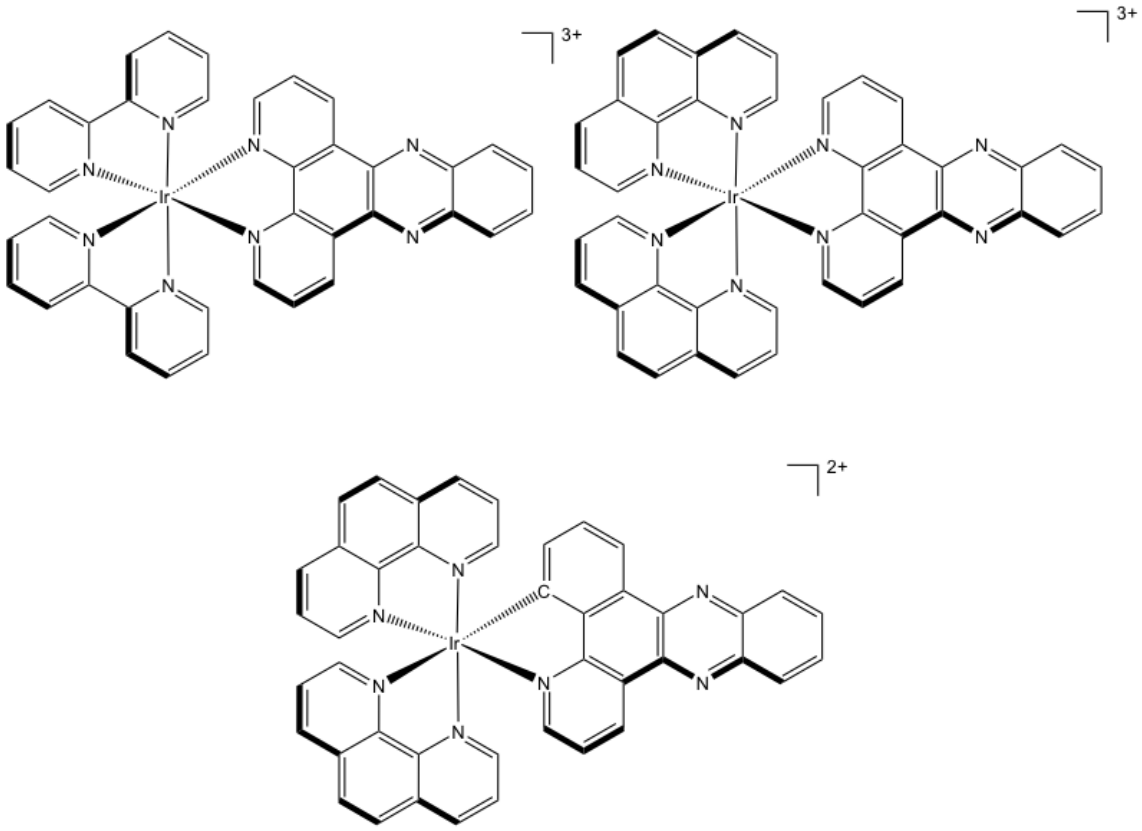

*Figure 1.38: The three target complexes; Top left: **1**, top right: **2**, bottom: **3**.*

1.1.9 References

1. B. Alberts, A. Johnson, J. Lewis, D. Morgan, M. Raff, K. Roberts and P. Walter, in *The Molecular Biology of The Cell*, Garland Science Taylor & Francis Group, 6th edn., 2015.
2. F. Crick, Central Dogma Of Molecular Biology, *Nature*, 1970, **227**, 561–563.
3. G. W. Beadle, M. Beadle, *The language of life. An introduction to the science of genetics.*, London: Victor Gollancz Ltd., 1966.
4. B. J. Strasser, *History and Philosophy of the Life Sceinces*, Stazione Zoologica Anton Dohrn, 2006.
5. L. Pauling and R. B. Corey, A Proposed Structure For The Nucleic Acids, *Proc. Natl. Acad. Sci. USA*, 1953, **39**, 84–97.
6. R. R. Sinden, DNA Structure and Function, *Academic Press*, San Diago, 1994.
7. R. E. Dickerson, H. R. Drew, B. N. Conner, R. M. Wing, A. V Fratini and M. L. Kopka, The Anatomy of A- , B- , and Z-DNA, *Science*, 1982, 475-485.
8. D. W. Ussery, DNA Structure : A- , B- and Z-DNA Helix Families, *Life Sci.*, 2002, 1–11.
9. B. Dumat, A. F. Larsen and L. M. Wilhelmsson, Studying Z-DNA and B-to Z-DNA transitions using a cytosine analogue FRET-pair, *Nucleic Acids Res.* 2016, **11,** 5-12.
10. S. Neidle, DNA minor-groove recognition by small molecules, *Nat. Prod. Rep.*, 2001, **18**, 291–309.
11. M. B. Kastan and J. Bartek, Cell-cycle checkpoints and cancer, *Nature*, 2004, **432**, 316–323.
12. B. Lippert, *Cisplatin: Chemistry and Biolochemistry of a leading anticancer drug*, John Wiley and Sons, 1999.
13. C. F. Kettering and B. Rosenberg, General Motors Cancer Research Prize Fundamental Studies With Cisplatin, *Cancer*, 1985, **55**, 2303–2316.
14. M. Fuertes, J. Castilla, C. Alonso and J. Pérez, Cisplatin Biochemical Mechanism of Action: From Cytotoxicity to Induction of Cell Death Through Interconnections Between Apoptotic and Necrotic Pathways, *Curr. Med. Chem.*, 2003, **10**, 257–266.
15. L. Strekowski and B. Wilson, Noncovalent interactions with DNA: An overview, *Mutat. Res.*, 2007, **623**, 3–13.
16. G. S. Manning, The molecular theory of polyelectrolyte solutions with applications to the electrostatic properties of polynucleotides., *Q. Rev. Biophys.*, 1978, **11**, 179–246.

17. E. Minyat, V. Ivanov, A. Kritzyn, L. Minchenkova and A. Schyolkina, Spermine and Spermidine-induces B to A transition of DNA in Solution, *J. Mol. Biol.*, 1978, **128**, 397–409.
18. a U. Khan, Y. H. Mei and T. Wilson, A proposed function for spermine and spermidine: protection of replicating DNA against damage by singlet oxygen., *Proc. Natl. Acad. Sci. U. S. A.*, 1992, **89**, 11426–7.
19. S. G. K. R, B. B. Mathew, C. N. Sudhamani and H. S. B. Naik, Mechanism of DNA Binding and Cleavage, *Biomed. Biotechnol.*, 2014, **2**, 1–9.
20. P. Workman, *New approaches in cancer pharmacology drug design adn development, Volume II*, Berlin, 1st edn., 1994.
21. L. a Marky and K. J. Breslauer, Origins of netropsin binding affinity and specificity: correlations of thermodynamic and structural data., *Proc. Natl. Acad. Sci. U. S. A.*, 1987, **84**, 4359–63.
22. J. B. Chaires, A thermodynamic signature for drug-DNA binding mode, *Biochem. Biophys.*, 2006, **453**, 26–31.
23. G. S. Manning, Counterion Binding in Polyelectrolyte Theory, *Acc. Chem. Res.*, 1979, **12**, 443–449.
24. P. Pjura, K. Grzeskowiak and R. E. Dickerson, Binding of Hoechst 33528 to the Minor Groove of B-DNA, *J. Mol. Biol.*, 1987, **197**, 257–271.
25. en.Wikipedia.org.
26. L. H. Fornander, L. Wu, M. Billeter, P. Lincoln and B. Nordén, Minor-groove binding drugs: Where is the second hoechst 33258 molecule?, *J. Phys. Chem. B*, 2013, **117**, 5820–5830.
27. B. Weisblum and E. Haenssler, Fluorometric properties of the bibenzimidazole derivative hoechst 33258, a fluorescent probe specific for AT concentration in chromosomal DNA, *Chromosoma*, 1974, **46**, 255–260.
28. L. . Lerman, Structural Considerations in the Interaction of DNA and Acridines, *J. Mol. Biol.*, 1961, **3**, 18–30.
29. B. M. Zeglis, V. C. Pierre and J. K. Barton, Metallo-intercalators and metallo-insertors, *Chem. Commun.*, 2007, **7345**, 4565.
30. C. Metcalfe and J. a Thomas, Kinetically inert transition metal complexes that reversibly bind to DNA., *Chem. Soc. Rev.*, 2003, **32**, 215–224.
31. B. J. Pages, D. L. Ang, E. P. Wright and J. R. Aldrich-Wright, Metal complex interactions with DNA, *Dalt. Trans.*, 2015, **44**, 3505–3526.

32. C. Chow and J. K. Barton, Transition Metal Complexes as Probes of Nucleic Acids, *Methods Enzymol.*, 1991, **212**, 219–242.
33. A. H. J. Wang, J. Nathans, G. Van Der Marel, J. H. Van Boom and A. Rich, Molecular structure of a double helical DNA fragment intercalator complex between deoxy CpG and a terpyridine platinum compound, *Nature*, 1978, **276**, 471–474.
34. K. W. Jennette, S. J. Lippard, G. A. Vassiliades and W. R. Bauer, Metallointercalation reagents. 2-hydroxyethanethiolato(2,2',2'-terpyridine)-platinum(II) monocation binds strongly to DNA by intercalation., *Proc. Natl. Acad. Sci. U. S. A.*, 1974, **71**, 3839–43.
35. M. Carter, M. Rodriguez and A. Bard, Voltammetric Studies of the Interaction of Metal Chelates with DNA. 2 Tris-Chelated Complexes of Cobalt(III) and Iron(II) with 1,10-Phenanthroline and 2,2'-Bipyridine, *J. Am. Chem. Soc*, 1989, **111**, 8901–8911.
36. J. Rehmann and J. Barton, 1H NMR studies of tris(phenanthroline) metal complexes bound to oligonucleotides: characterization of binding modes, *Biochemistry*, 1990, **29**, 1701–1709.
37. J. K. Barton, C. V. Kumar and N. J. Turro, DNA-Mediated Photoelectron Transfer Reactions, *J. Am. Chem. Soc.*, 1986, **108**, 6391–6393.
38. J. K. Barton, J. M. Goldberg, C. V. Kumar and N. J. Turro, Binding Modes and Base Specificity of Tris(phenanthroline)ruthenium(II) Enantiomers with Nucleic Acids: Tuning the Stereoselectivity, *J. Am. Chem. Soc.*, 1986, **108**, 2081–2088.
39. C. V. Kumar, J. K. Barton and N. J. Turro, Photophysics of Ruthenium Complexes Bound to Double Helical DNA, *J. Am. Chem. Soc.*, 1985, **107**, 5518–5523.
40. M. R. Gill, 2010.
41. J. W. Lichtman and J. A. Conchello, Fluorescence microscopy, *Nat. Methods*, 2005, **2**, 910–919.
42. A. Jablonski, Efficiency of Anti-Stokes Fluorescence in Dyes, *Nature*, 1933, **131**, 839–840.
43. P. Atikins and J. de Paula, *Atkins' Physical Chemistry*, Oxford University Press, 8th edn., 2006, 230-260.
44. J. Lakowicz, *Principles of Fluorescence Spectroscopy*, Kluwer Academic/ Plenum Publisher, 2nd edn., 1999, 34-38.
45. S. Fery-Forgues and D. Lavabre, Are Fluorescence Quantum Yields So Tricky to Measure? A Demonstration Using Familiar Stationery Products, *J. Chem. Educ.*, 1999, **76**, 1260.
46. B. Hötzer, I. L. Medintz and N. Hildebrandt, Fluorescence in nanobiotechnology:

Sophisticated fluorophores for novel applications, *Small*, 2012, **8**, 2297–2326.

47. R. Englman and J. Jortner, The energy gap law for radiationless transitions in large molecules, *Mol. Phys.*, 1970, **18**, 145–164.
48. J. Lakowicz, *Principles of Fluorescence Spectroscopy*, Springer International Publishing, 2007.
49. J. V. Caspar and T. J. Meyer, Application of the energy gap law to nonradiative, excited-state decay, *J. Phys. Chem.*, 1983, **87**, 952–957.
50. L. Hammarström, M. Abrahamsson and H.-C. Becker, Microsecond 3MLCT Excited State Lifetimes in Bis-Tridentate Ru(II)-complexes: Significant Reductions of Non-Radiative Rate Constants., *Dalt. Trans.*, 2017, 13314–13321.
51. G. A. Crosby, Spectroscopic Investigations of Excited States of Transition-Metal Complexes, *Acc. Chem. Res.*, 1975, **8**, 231–238.
52. V. J. Antonin and Z. Stanislav, Modeling of charge-transfer transitions and excited states in d6 transition metal complexes by DFT techniques, *Coord. Chem. Rev*, 2007, **251**, 258–287.
53. V. Balzani, A. Juris, M. Venturi, S. Campagna and S. Serroni, Luminescent and Redox-Active Polynuclear Transition Metal Complexes, *Chem. Rev.*, 1996, **96**, 759–834.
54. J. N. Demas and B. A. DeGraff, Design and Applications of Highly Luminescent Transition Metal Complexes, *Anal. Chem.*, 1991, **63**, 829A–837A.
55. A. E. Friedman, J. K. Barton, J. C. Chambron, J. P. Sauvage, N. J. Turro and J. K. Barton, Molecular ‘Light Switch’ for DNA: Ru(bpy)2(dppz)2+, *J. Am. Chem. Soc.*, 1990, **112**, 4960–4962.
56. E. Amouyal, A. Homsi, J. Chambron and J. Sauvage, Synthesis and Study of a mixed-ligand ruthenium (II) complex in its ground and excited states: bis(2,2’-bipyrideine)(dipyrido[3,2-a:2’,3’-c]phenazine n4n5)ruthenium(II), *J. Chem. Soc. Dalt. Trans.*, 1990, 1841–1845.
57. C. Hiort, P. Lincoln and B. Nordén, DNA Binding of Δ- and Λ-[Ru(phen)2DPPZ]2+, *J. Am. Chem. Soc.*, 1993, **115**, 3448–3454.
58. J. Andersson, L. H. Fornander, M. Abrahamsson, E. Tuite, P. Nordell and P. Lincoln, Lifetime heterogeneity of DNA-bound dppz complexes originates from distinct intercalation geometries determined by complex-complex interactions, *Inorg. Chem.*, 2013, **52**, 1151–1159.
59. C. J. Cardin, J. M. Kelly and S. J. Quinn, Photochemically active DNA-intercalating ruthenium and related complexes – insights by combining crystallography and transient

spectroscopy, *Chem. Sci.*, 2017, **8**, 4705–4723.

60. C. J. Cardin and J. P. Hall, in *DNA-Targetting Molecules as Therapeutic Agents*, ed. M. J. Waring, Royal Society of Chemistry, Volume 7 o., 2018, pp. 198–227.
61. J. P. Hall, K. O'Sullivan, A. Naseer, J. A. Smith, J. M. Kelly and C. J. Cardin, Structure determination of an intercalating ruthenium dipyridophenazine complex which kinks DNA by semiintercalation of a tetraazaphenanthrene ligand, *Proc. Natl. Acad. Sci.*, 2011, **108**, 17610–17614.
62. F. H. C. Crick and A. Klug, Kinky helix, *Nature*, 1975, **255**, 530–533.
63. H. Niyazi, J. P. Hall, K. O'Sullivan, G. Winter, T. Sorensen, J. M. Kelly and C. J. Cardin, Crystal structures of λ-[Ru(phen)2dppz]2+with oligonucleotides containing TA/TA and AT/AT steps show two intercalation modes, *Nat. Chem.*, 2012, **4**, 621–628.
64. J. K. Barton, A. T. Danishefsky and J. M. Goldberg, Tris(phenanthroline)ruthenium(II): Stereoselectivity in Binding to DNA, *J. Am. Chem. Soc.*, 1984, **106**, 2172–2176.
65. J. P. Hall, D. Cook, S. R. Morte, P. McIntyre, K. Buchner, H. Beer, D. J. Cardin, J. A. Brazier, G. Winter, J. M. Kelly and C. J. Cardin, X-ray crystal structure of rac-[Ru(phen)2dppz]2+ with d(ATGCAT)2 shows enantiomer orientations and water ordering, *J. Am. Chem. Soc.*, 2013, **135**, 12652–12659.
66. H. Song, J. T. Kaiser and J. K. Barton, Crystal structure of Δ-[Ru(bpy)2dppz]2+bound to mismatched DNA reveals side-by-side metalloinsertion and intercalation, *Nat. Chem.*, 2012, **4**, 615–620.
67. D. R. Boer, L. Wu, P. Lincoln and M. Coll, Thread insertion of a bis(dipyridophenazine) diruthenium complex into the DNA double helix by the extrusion of at base pairs and cross-linking of DNA duplexes, *Angew. Chemie Int. Ed.*, 2014, **53**, 1949–1952.
68. J. P. Hall, P. M. Keane, H. Beer, K. Buchner, G. Winter, T. L. Sorensen, D. J. Cardin, J. A. Brazier and C. J. Cardin, Delta chirality ruthenium 'light-switch' complexes can bind in the minor groove of DNA with five different binding modes, *Nucleic Acids Res.*, 2016, **44**, 9472–9482.
69. B. A. Jackson and J. K. Barton, Recognition of DNA Base Mismatches by Rhodium Intercalator, *J. Am. Chem. Soc.*, 1997, **7863**, 12986–12987.
70. G. Rossetti, P. D. Dans, I. Gomez-Pinto, I. Ivani, C. Gonzalez and M. Orozco, The structural impact of DNA mismatches, *Nucleic Acids Res.*, 2015, **43**, 4309–4321.
71. B. M. Zeglis, V. C. Pierre, J. T. Kaiser and J. K. Barton, A bulky rhodium complex bound to an adenosine-adenosine DNA mismatch: General architecture of the metalloinsertion binding mode, *Biochemistry*, 2009, **48**, 4247–4253.

72. A. Komor and J. Barton, The Path for Metal Complexes to a DNA Target, *Chem. Commun.*, 2013, **49**, 3617–3630.
73. H. Song, J. T. Kaiser and J. K. Barton, Crystal structure of Δ-[Ru(bpy)2dppz]2+bound to mismatched DNA reveals side-by-side metalloinsertion and intercalation, *Nat. Chem.*, 2012, **4**, 615–620.
74. M. Aarnio, R. Sankila, E. Pukkala, R. Salovaara, L. A. Aaltonen, A. de la Chapelle, P. Peltomoki, J.-P. Mecklin and H. J. Jarvinen, Cancer risk in mutation carriers of DNA-mismatch-repair genes, *Int. J. Cancer*, 1999, **81**, 214–218.
75. A. N. Boynton, L. Marcélis and J. K. Barton, [Ru(Me4phen)2dppz]2+, a Light Switch for DNA Mismatches, *J. Am. Chem. Soc.*, 2016, **138**, 5020–5023.
76. K. Nienhaus and G. Ulrich Nienhaus, Fluorescent proteins for live-cell imaging with super-resolution, *Chem. Soc. Rev.*, 2014, **43**, 1088–1106.
77. D. J. Stephens and V. J. Allan, Light microscopy techniques for live cell imaging, *Science (80-.).*, 2003, **300**, 82–86.
78. M. Gunkel, F. Erdel, K. Rippe, P. Lemmer, R. Kaufmann, C. Hörmann, R. Amberger and C. Cremer, Dual color localization microscopy of cellular nanostructures, *Biotechnol. J.*, 2009, **4**, 927–938.
79. V. Fernandez-Moreira, F. L. Thorp-Greenwood and M. P. Coogan, Application of d6 transition metal complexes in fluorescence cell imaging, *Chem. Commun.*, 2010, **46**, 186–202.
80. A. Diaspro, G. Chirico, C. Usai, P. Ramoino and J. Dobrucki, Photobleaching, *Handb. Biol. Confocal Microsc.*, 2006, 690–702.
81. Y. Zhou, J. Jia, W. Li, H. Fei and M. Zoug, Luminescent biscarbene iridium(III) complexes as living cell imagine agents, *Chem. Commun.*, 2013, **49**, 3230–3232.
82. D. LLoyd, M. P. Coogan and S. J. A. Pope, Novel Metal-Based Luminophores for Biological Imagine, *Reveiws Fluoresc. 2010*, 2011, 15–44.
83. R. Pellow and M. Vala, The external heavy atom effect: Theory of spin-orbit coupling of alkali and noble metals in rare gas matrices, *J. Chem. Phys.*, 1989, **90**, 5612–5621.
84. B. J. Powell, Theories of phosphorescence in organo-transition metal complexes - from relativistic effects to simple models and design principles for organic light-emitting diodes, *Coord. Chem. Rev*, 2015, **295**, 1501–1571.
85. M. P. Coogan and V. Fernández-Moreira, Progress with, and prospects for, metal complexes in cell imaging, *Chem. Commun.*, 2014, **50**, 384–399.
86. N. K. Shee, M. G. B. Drew and D. Datta, Tuning of the lowest excited states in mixed

ruthenium polypyridyl complexes having RuN cores by the conformation of the ancillary ligand. Emission from a ligand-to-ligand-charge-transfer state, *New J. Chem.*, 2016, **40**, 5002–5009.

87. C. A. Puckett and J. K. Barton, Mechanism of cellular uptake of a ruthenium polypyridyl complex, *Biochemistry*, 2009, **47**, 11711–11716.
88. C. A. Puckett and J. K. Barton, Fluorescein Redirects a Ruthenium - Octaarginine Conjugate to the Nucleus, *J. Am. Chem. Soc.*, 2009, **131**, 8738–8739.
89. D. A. Giljohann, D. S. Seferos, W. L. Daniel, M. D. Massich, P. C. Patel and C. A. Mirkin, Gold nanoparticles for biology and medicine, *Angew. Chemie Int. Ed.*, 2010, **49**, 3280–3294.
90. P. Tiwari, K. Vig, V. Dennis and S. Singh, Functionalized Gold Nanoparticles and Their Biomedical Applications, *Nanomaterials*, 2011, **1**, 31–63.
91. P. Ghosh, G. Han, M. De, C. K. Kim and V. M. Rotello, Gold nanoparticles in delivery applications, *Adv. Drug Deliv. Rev.*, 2008, **60**, 1307–1315.
92. R. B. P. Elmes, K. N. Orange, S. M. Cloonan, D. C. Williams and T. Gunnlaugsson, Luminescent ruthenium(II) polypyridyl functionalized gold nanoparticles; Their DNA binding abilities and application as cellular imaging agents, *J. Am. Chem. Soc.*, 2011, **133**, 15862–15865.
93. C. A. Puckett and J. K. Barton, Methods to Explore Cellular Uptake of Ruthenium Complexes, *J. Am. Chem. Soc*, 2007, **129**, 46–47.
94. M. R. Gill, J. Garcia-Lara, S. J. Foster, C. Smythe, G. Battaglia and J. A. Thomas, A ruthenium(II) polypyridyl complex for direct imaging of DNA structure in living cells, *Nat. Chem.*, 2009, **1**, 662–667.
95. C. Rajput, R. Rutkaite, L. Swanson, I. Haq and J. A. Thomas, Dinuclear monointercalating RuII complexes that display high affinity binding to duplex and quadruplex DNA., *Chem. Eur. J*, 2006, **12**, 4611–4619.
96. D. R. Green and J. C. Reed, Mitochondria and apoptosis, *Science*, 1998, **281**, 1309-1311.
97. X. Tian, M. R. Gill, I. Cantón, J. A. Thomas and G. Battaglia, Live Cell Luminescence Imaging As a Function of Delivery Mechanism, *ChemBioChem*, 2011, **12**, 548–551.
98. M. R. Gill, D. Cecchin, M. G. Walker, R. S. Mulla, G. Battaglia, C. Smythe and J. A. Thomas, Targeting the endoplasmic reticulum with a membrane-interactive luminescent ruthenium(ii) polypyridyl complex, *Chem. Sci.*, 2013, **4**, 4512.
99. M. S. Lowry, W. R. Hudson, R. A. Pascal and S. Bernhard, Accelerated Luminophore Discovery through Combinatorial Synthesis, *J. Am. Chem. Soc*, 2004, 14129–14135.

100. M. S. Lowry and S. Bernhard, Synthetically tailored excited states: phosphorescent, cyclometalated iridium(III) complexes and their applications., *Chem. Eur. J*, 2006, **12**, 7970–7.

101. J. Knoll and C. Turro, Control and utilization of ruthenium and rhodium metal complex excited states for photoactivated cancer therapy, *Coord. Chem. Rev*, 2015, **282**, 997–1003.

102. L. Flamigni, A. Barbieri, C. Sabatini, B. Ventura and F. Barigelletti, in *Photochemistry and Photophysics of Coordination Compounds*, eds. V. Balzani and S. Campagna, Springer, 2nd edn., 2007, pp. 145–199.

103. R. J. Watts and J. Van Houten, Effect of ligand substituents of the d-d luminescence of iridium (III) and rhodium (III) complexes of 1 , 10-phenanthroline, *Chem. Mater.*, 2002, **96**, 4334–4335.

104. M. S. Lowry, J. I. Goldsmith, J. D. Slinker, R. a Pascal, G. G. Malliaras, S. Bernhard and R. Rohl, Single-Layer Electroluminescent Devices and Photoinduced Hydrogen Production from an Ionic Iridium (III) Complex Single-Layer Electroluminescent Devices and Photoinduced Hydrogen Production from an Ionic Iridium (III) Complex, *J. Mater.*, 2005, **17**, 5712–5719.

105. K. K.-W. Lo, K. Y. Zhang and S. P.-Y. Li, Design of cyclometalated iridium(III) polypyridine complexes as luminescent biological labels and probes, *Pure Appl. Chem.*, 2011, **83**, 823–840.

106. A. Wragg, M. R. Gill, D. Turton, H. Adams, T. M. Roseveare, C. Smythe, X. Su and J. A. Thomas, Tuning the Cellular Uptake Properties of Luminescent Heterobimetallic Iridium(III)-Ruthenium(II) DNA Imaging Probes, *Chem. Eur. J.*, 2014, **20**, 14004–14011.

107. M. Yu, Q. Zhao, L. Shi, F. Li, Z. Zhou, H. Yang, T. Yi and C. Huang, Cationic iridium(iii) complexes for phosphorescence staining in the cytoplasm of living cells, *Chem. Commun.*, 2008, 2115.

108. L. Murphy, A. Congreve, L.-O. Pålsson and J. A. G. Williams, The time domain in co-stained cell imaging: time-resolved emission imaging microscopy using a protonatable luminescent iridium complex, *Chem. Commun.*, 2010, **46**, 8743.

109. C. Li, M. Yu, Y. Sun, Y. Wu, C. Huang and F. Li, A nonemissive iridium(III) complex that specifically lights-up the nuclei of living cells, *J. Am. Chem. Soc.*, 2011, **133**, 11231–11239.

110. Y. Liu, P. Zhang, X. Fang, G. Wu, S. Chen, Z. Zhang, H. Chao, W. Tan and L. Xu,

Near-infrared emitting iridium(III) complexes for mitochondrial imaging in living cells, *Dalt. Trans.*, 2017, **46**, 4777–4785.

Chapter 2
Iridium metallo-intercalators

2.0 Iridium metallo-intercalators

2.1 Introduction

Luminescent transition metal complexes are appealing for their utility in diverse applications. The performance of these complexes in such roles depends heavily on their excited state properties. Many of the photochemical and photophysical properties of molecules depend upon the kinetics of excited-state processes that occur after the absorption of a photon. Early work in this field predominantly focused on ruthenium(II) polypyridyl complexes such as $[Ru(bpy)_3]^{2+}$, and the molecular light-switch, $[Ru(bpy)_2(dppz)]^{2+}$ and its derivatives.[1–4] The excited-state chemistry of such Ru(II) complexes takes place from the triplet manifold. As deactivation of the emissive triplet metal-to-ligand charge-transfer state ^{3}(MLCT) in these complexes proceeds due to the thermal population of a non-emissive metal-centred state they can often display limited photostability and lack of luminescence tunability.[5,6] More recent studies have been focused on phosphorescent 5*d* transition metal complexes, with particular attention being paid to Ir(III). Changing the metal centre to a more stable third-row transition metal not only drastically improves the metal ligand bond stability, but also increases their photostability.[7] Iridium(III) is appealing due to its increased ligand-field stabilisation energy , synthetic versatility (it is able to form both homo- and heteroleptic complexes) and the fact that it has colour-tunable photoluminescence.[8] The two principle transitions observed in iridium(III) complexes are MLCT (electron promoted from metal *d* orbital to a ligand vacant π^* orbital) and ligand-centred (LC) transitions (electron π orbitals on one of the coordinated ligands). This is because, as a consequence of the high spin-orbit coupling constants for Ir(III) complexes, the ligand field splitting parameter, Δ is very large (ζ = 431, 1042, 3381, 3909 cm^{-1} for Fe, Ru, Os and Ir respectively).[9] This large ligand field splitting parameter causes the metal-centred (MC) levels to be pushed higher in energy so that they do not usually affect the emission properties, which are traceable back to MLCT levels or LC levels, as both of these states can be emissive (*Figure 2.1*).

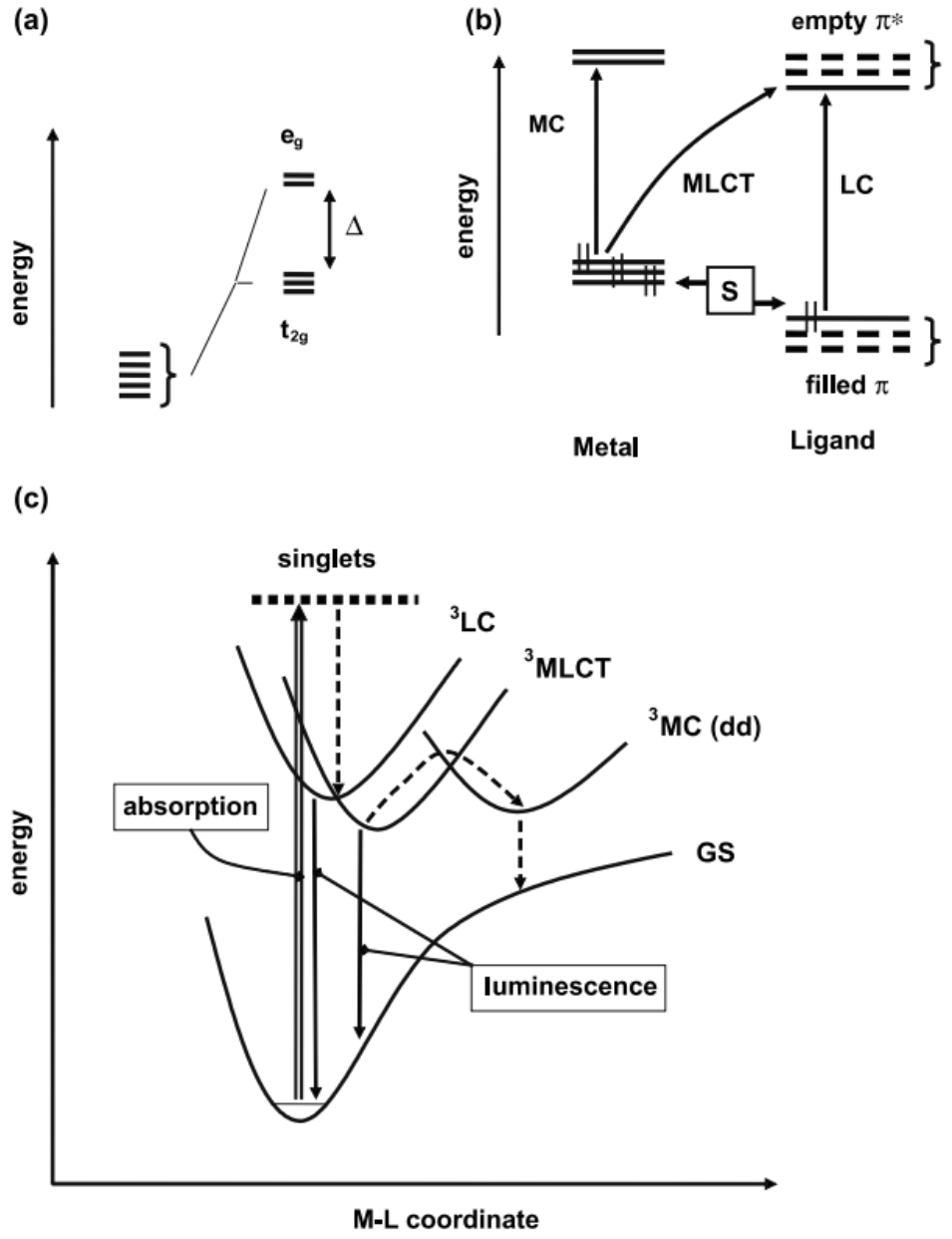

Figure 2.2: a) d-orbitals in an octahedral field; (b) orbital description of MC, MLCT and LC transitions; S is a substituent group capable of exerting electron withdrawing or releasing effects (resulting in stabalisation or destabalisation, respectively, of the energy level and the filled d and π orbitals). (c) electronic transitions involving MC, MLCT and LC states; the MC states are not emission.[10]

Due to the heavy atom effect, which induces a quantum mechanical mixing of states with different multiplicity, strong spin-orbit coupling from the iridium(III) centre facilitates intersystem crossing.[11] This emissive mixed triplet state, which usually contains contributions from both ^{3}MLCT and ^{3}LC states, can be tuned through chemical variation and structural modification of the ancillary ligands. DFT calculations have confirmed that the absorption and emission energies of the Ir(III) polypyridyl complexes can be controlled by adjusting the energy of the metal and ligand orbital; this can be accomplished simply by structural control

and/or substituent effects.[12] As expected in these complexes, in the MLCT state, the highest occupied molecular orbital (HOMO) is on the iridium metal and the lowest unoccupied molecular orbital (LUMO) is on the N-substituted ligand. In tuning this excited state, a rule of thumb is that the aryl rings mainly impact the HOMO level, while the substituents on the N-coordinated ring impact the LUMO.[13] Deliberate functionalisation of the ligands can control these levels and produce tremendous colour versatility. While changing the degree of conjugation and size of the ancillary ligands can distort/destabilise these excited states, electron effects have been proven to show a profound influence on the orbital energies. Electron-withdrawing (e.g. –F, -CF_3) and electron-donating (e.g. –$C(CH_3)_3$, -OCH_3) can be incorporated into the ligand structure. Electron withdrawing groups stabilise the HOMO by removing electron density from the metal centre, whereas electron-donating groups behave in opposite. (*Figure 2.2).*[14]

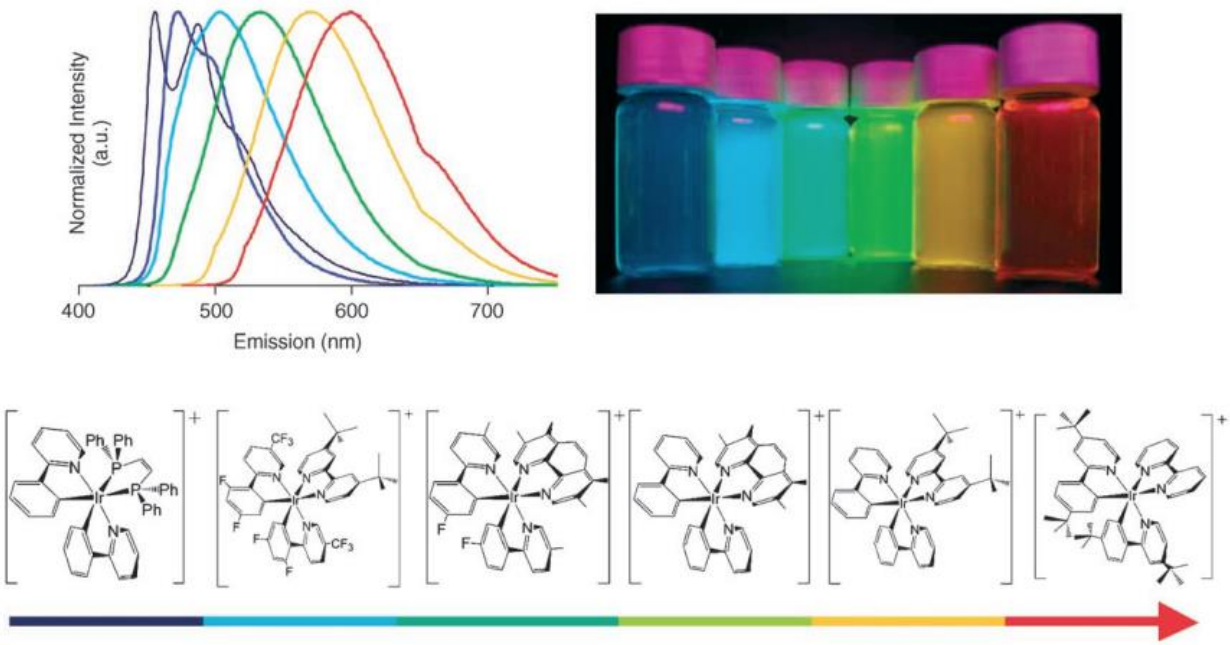

Figure 2.2: Colour versatility expressed by a series of six cationic iridium(III) luminophores. Their structures are listed in order of increasing emission wavelength (blue to red). The evolution of ^{3}LC (vibrationally structured, high energy bands) and ^{3}MLCT character (structureless, low energy bands) in the luminescence spectra are indicative of a mixed excited state.[14]

2.2 Ir-dppz complexes

Ever since the discovery of striking photophysical properties of $[Ru(bpy)_2(dppz)]^{2+}$ there has been interest in ruthenium complexes incorporating the 'dppz' unit.[4,15,16] This complex was found to be a luminescent probe for DNA, with the "light-switch" effect stemming from the intercalation of the phenazine unit. This chapter is concerned with the DNA binding properties of iridium(III) metallo-intercalators containing dppz as an intercalating ligand. These structures were chosen as iridium variants of the highly studied Ru(II) molecular light-switch parent compound. Iridium is a third-row transition metal and can form 3^+ polypyridyl complexes or lower when cyclometallated ligands are incorporated. This family of iridium complexes: $[Ir(bpy)_2(dppz)]^{3+}$ **1**, $[Ir(phen)_2(dppz)]^{3+}$ **2**, $[Ir(phen)_2(C\text{^}N\ dppz)]^{2+}$ **3** have variations of ligand with the phenanthroline and bipyridine ancillary ligands, and charge variations with non-and cyclometallated dppz units (*Figure 2.3).*

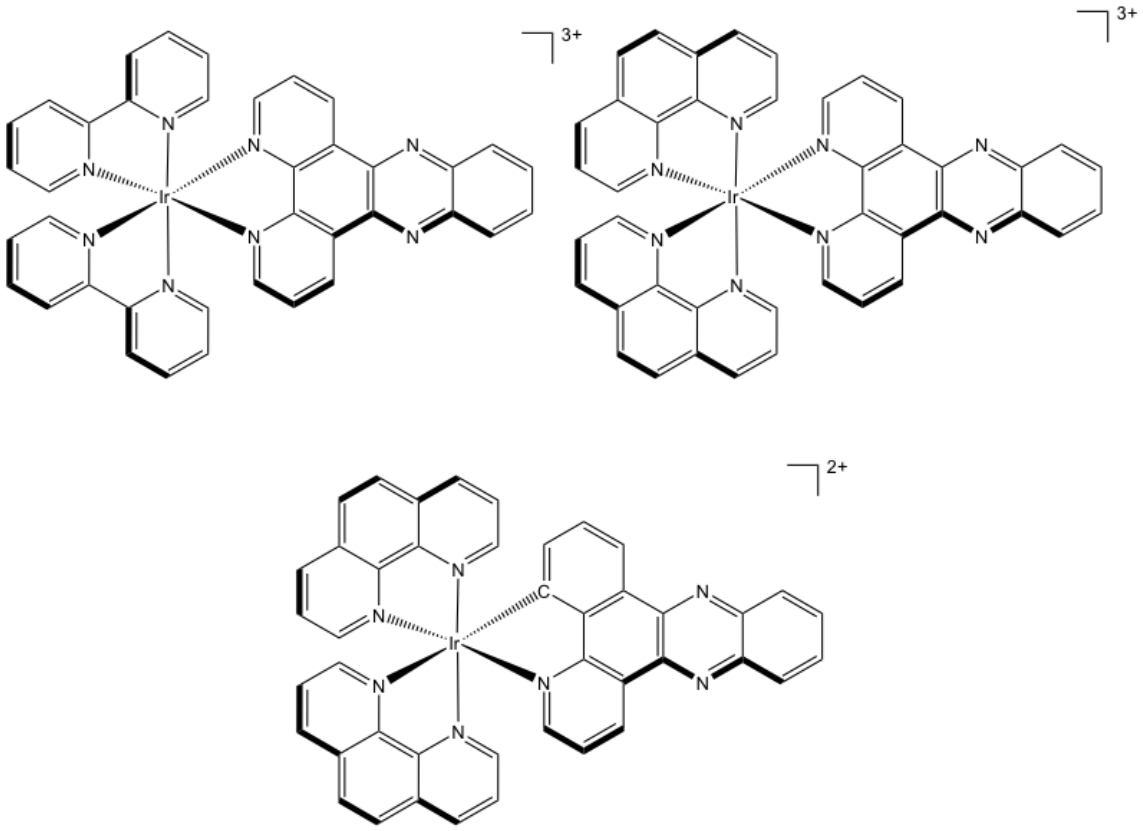

*Figure 2.3: Chemical structures of the Ir^{III} complexes in this thesis; top left – $[Ir(bpy)_2(dppz)]^{3+}$**1**; top right – $[Ir(phen)_2(dppz)]^{3+}$**2**; $[Ir(phen)_2(C\text{^}N\ dppz)]^{2+}$ **3**.*

2.2.1 Synthesis

2.2.1.1 Ligand Synthesis

The ligands dppz and cyclometallated dppz (C^N dppz) were synthesised by published procedures (*Figure 2.4*).[17,18]

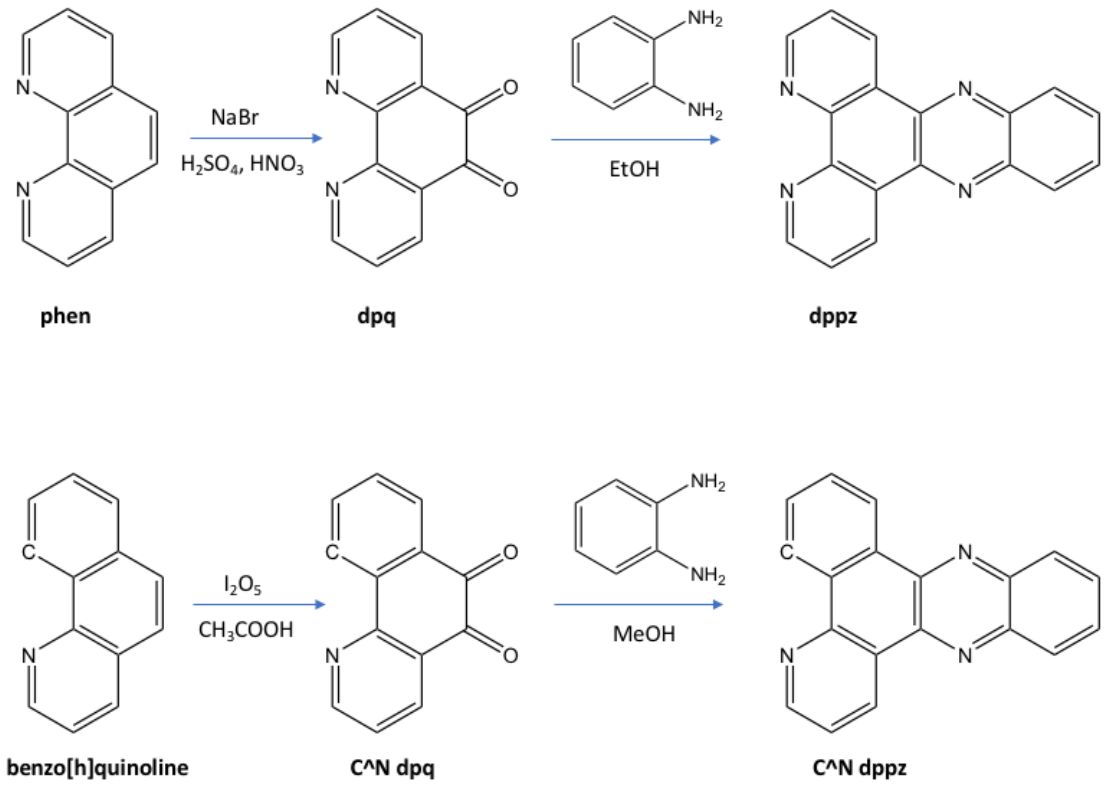

Figure 2.4: Synthesis of dppz (top) and cyclometallated dppz (bottom).

2.2.1.2 Complex Synthesis

The ligands 2,2'-bipyridine and 1,10-phenanthroline have been used extensively by inorganic chemists due to the ease with which they can chelate to most transition metals. Most of the d^6 ions in the group 8 transition metals are known to easily form tris complexes with bidentate bound bpy and phen units; $[Fe(bpy)_3]^{2+}$, $[Co(bpy)_3]^{2+}$,$[Ru(bpy)_3]^{2+}$,$[Rh(bpy)_3]^{2+}$,$[Os(bpy)_3]^{2+}$, are all well-known species.[19–23] The product formed when reacting $IrCl_3$ with either bpy is $[Ir(bpy)_2Cl_2]^+$ and not $[Ir(bpy)_3]^{3+}$. Demas *et al* synthesised the long-sought $[Ir(bpy)_3]^{3+}$ by boiling a mixture of K_3IrCl_6 hydrate in the presence of the strong oxidants potassium persulfate

and potassium bisulphate with 2,2'bipyridine.[24] Iridium is a third-row transition metal characterised by great inertness of its coordination sphere, requiring harsh conditions to substitute the chloride ligands present on the salt. The synthesis of the iridium polypyridyl complexes in this study were by a modification of the methods of Watts *et al*, and Keene/Collins *et al (Figure 2.5).*[25,26]

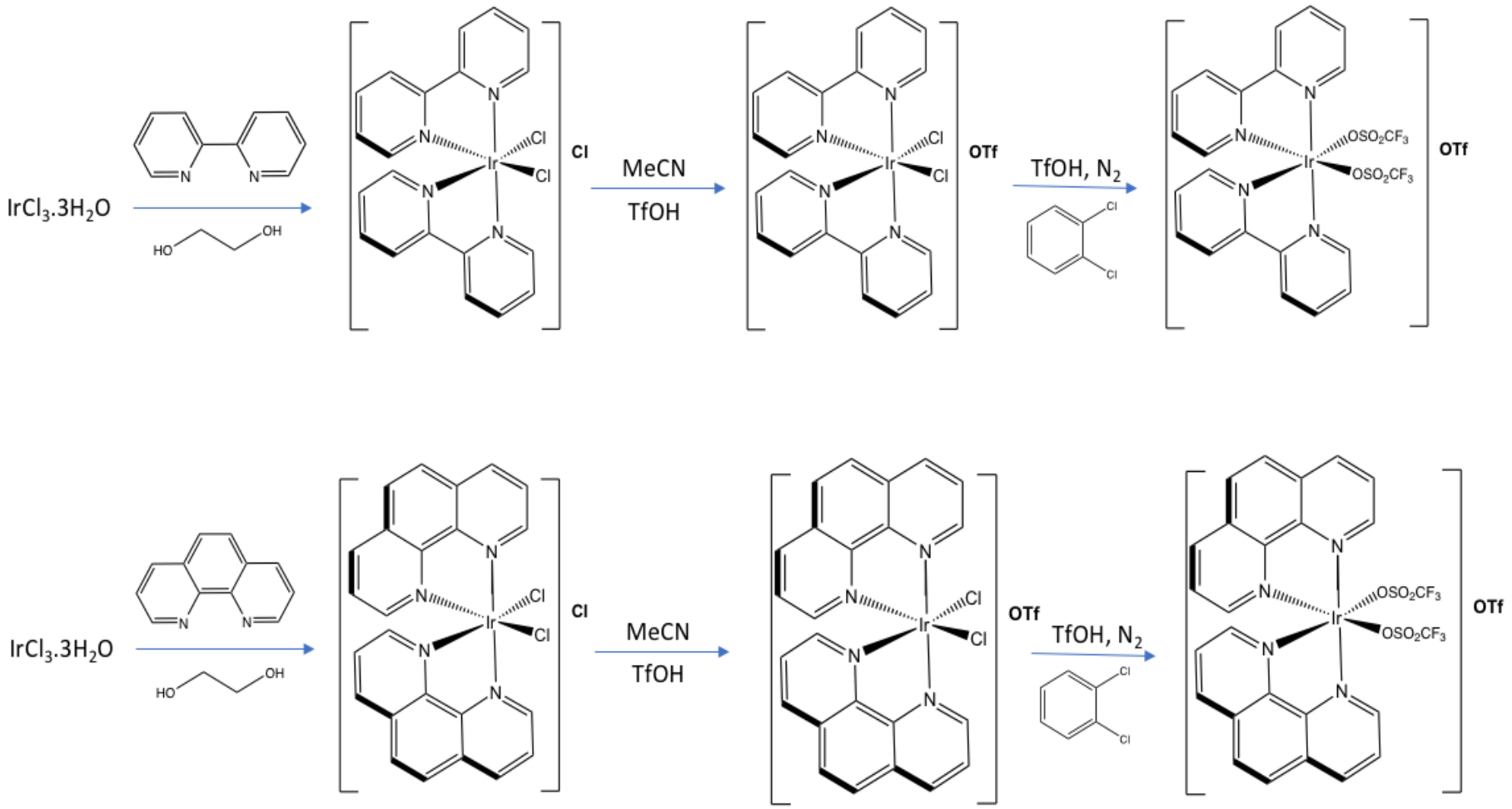

*Figure 2.5: Overall synthetic route to obtain the triflato species for complexes **1-3**.*

This multi-step synthesis is needed, as it is considerably more difficult to react iridium with ancillary ligands. First, iridium(III) trichloride hydrate was coordinated to either bidentate bipyridine or 1,10-phenanthroline units and precipitated with ammonium hexafluorophosphate to form $[Ir(bpy)_2Cl_2]PF_6$ or $[Ir(phen)_2Cl_2]PF_6$. Both bright yellow species were isolated in high yields. Instead of following a one-pot synthesis, used for more kinetically labile ruthenium analogues, the synthesis makes use of the triflato intermediate produced from triflic acid. First, the PF_6 species were converted to water-soluble chloride moieties and then these were treated with triflic acid to directly yield the triflic salt. Trifluoromethanesulfonic acid (triflic acid) has found considerable use in transition metal chemistry. Now that the complexes were in this form, the triflato species, where triflic acid groups substitute the chloride groups and coordinate directly onto the iridium centre could be produced. The attractive qualities of triflato complexes - including their high thermal stability, and the excellent leaving group properties of the $[CF_3SO_3]^-$ group - were first established by Scott and Taube.[27] The triflato group (CF_3SO_2) is one of the strongest electron-withdrawing groups known, and consequently the anion ($CF_3SO_3^-$) has found use as an excellent leaving group in nucleophilic substitution reactions in organic chemistry.[28] The lability of such complexes has provided facile route to a range of synthetically challenging iridium(III) complexes. Once prepared the triflato complexes have desirable properties such as high lability of the acid leaving group, high solubility in most polar solvents, relatively low reactivity with atmospheric moisture, and simple high yielding preparative routes from readily available reagents.[29] Due to the excellent leaving capabilities of the triflate anions, the intercalating ligand can be added to the iridium centre with the correct geometry needed for DNA intercalation. Despite containing labile triflato groups the iridium metal centre is still kinetically inert: coordination of the intercalating dppz analogues still requires long reaction times. Each complex was synthesised as their hexafluorophosphate salt and characterised by NMR and mass spectroscopy (*see experimental section).* They were converted to their water-soluble chloride salts by counter-ion metathesis. The overall reaction scheme is shown below (*Figure 2.6),* each complex synthesised in this thesis followed the same general experimental route. Only the isolated molecules and reagents used are included in the scheme. For a more detailed synthesis consult the experimental sections. For all aqueous luminescence, DNA and cellular studies the complexes were first converted to their water-soluble chloride counter-ions by counter-ion metathesis where the PF_6 salt was first dissolved in acetone and then tetrabutylammonium chloride was added to exchange the counter ion and precipitate the chloride complex. The full procedure is contained in the experimental section.

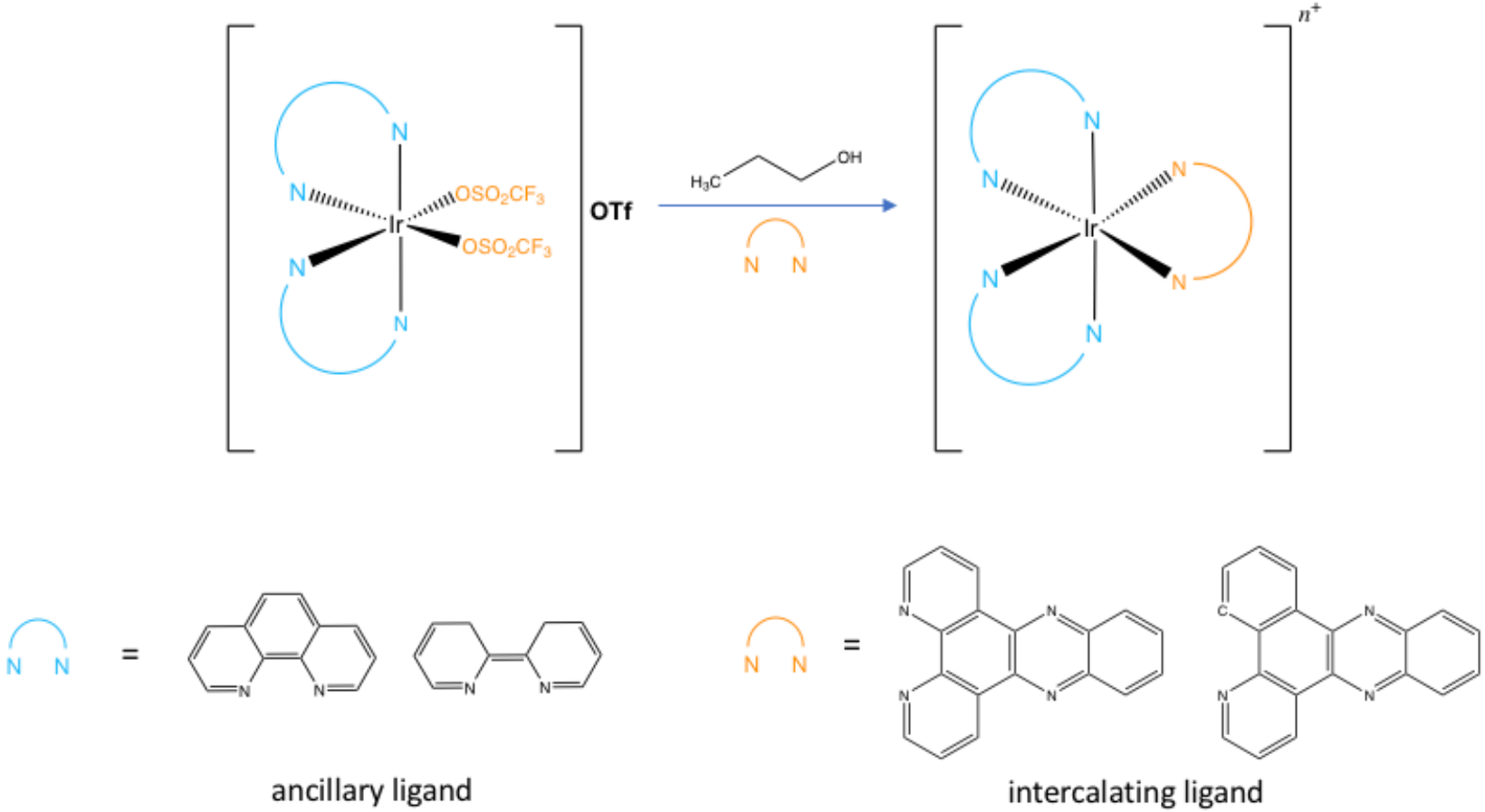

*Figure 2.6: Final synthesis step producing complexes **1-3.***

2.2.2 Photophysical Parameters

2.2.2.1 UV-Visible spectroscopic studies

The UV-Visible absorption spectra for all of the Ir-dppz complexes **1-3** were recorded in acetonitrile as hexafluorophosphate salts and in water as chloride salts at 25 °C. *Figure 2.7* below shoes the UV-visible absorbance spectra for **1-3** in water, the data from this graph is summerised in *Table 2.1*.

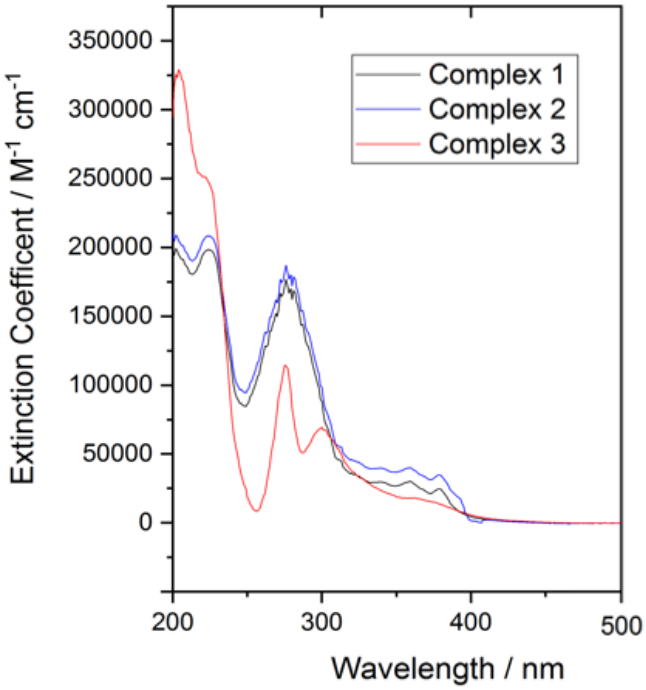

*Figure 2.7: UV-Visible spectra for the Ir-dppz complexes **1-3** as chloride salts recorded in water.*

Compound	λ_{max} **(nm)**	**ε (M^{-1} cm^{-1})**	**Assignment**
[Ir(bpy)$_2$(dppz)][Cl]$_3$	200	194000	π-π*
	240	114000	π-π*
	290	130000	π-π*
	360	44000	MLCT
	389	48000	MLCT
[Ir(phen)$_2$(dppz)][Cl]$_3$	205	254000	π-π*
	245	156000	π-π*

	295	38000	MLCT
	355	49000	MLCT
	395	40000	MLCT
[Ir(phen)$_2$(C^Ndppz)][Cl]$_2$	200	320000	π-π^*
	230	102000	π-π^*
	290	110000	π-π^*
	300	60000	π-π^*
	360	25000	MLCT

Table 2.1: UV-Visible data for Ir-dppz chloride complexes recorded in water.

The data for these complexes recorded in acetonitrile as their respective hexafluorophosphate salts is also summarised below in *Table 2.2* There is a slight shift in the MLCT bands due to a phenomenon called solvatochromism. The shift is produced by the non-redistribution of solvent molecules around the complex causing different electronic dipole moments in both the complex ground state and excited state. The MLCT absorption spectral shifts can therefore be used to determine the electric dipole moments and thus how the complex interacts with the surrounding solvent molecules. Charge transfer processes, such as MLCTs, which involve a donor and acceptor part, can strongly depend on solvent properties.[30–33] For **1-**

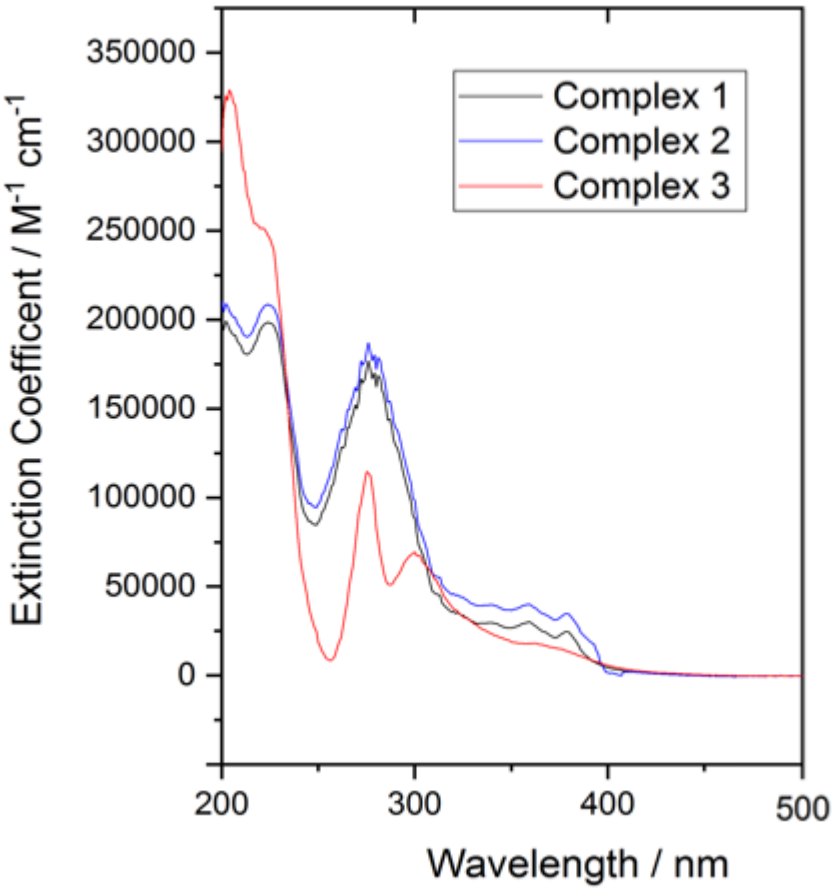

the MLCT is shifted to a slightly higher wavelength/lower energy in acetonitrile. Electronic transitions are effectively instantaneous within systems so solvent molecules have no times to rearrange upon electron transition. In the polar water solvent the excited state of **1** and **2** is slightly destabilised by the dipole moment of the water molecules, however in the less polar acetonitrile this is not present. The fact that there is more stabilisation in the excited state in acetonitrile causes the transition to appear at a lower energy.

Compound	λ_{max} **(nm)**	**ε (M^{-1} cm^{-1})**	**Assignment**
[Ir(bpy)$_2$(dppz)][PF$_6$]$_3$	201	204000	π-π*
	318	80000	π-π*
	363	38000	MLCT
	383	32000	MLCT
[Ir(phen)$_2$(dppz)][PF$_6$]$_3$	204	196000	π-π*

	226	196600	π-π^*
	275	176800	π-π^*
	361	28800	MLCT
	381	22728	MLCT
[Ir(phen)$_2$(C^Ndppz)][PF$_6$]$_2$	205	201200	π-π^*
	271	124000	π-π^*
	392	8000	MLCT

Table 2.2 UV-Visible data for Ir-dppz hexafluorophosphate complexes recorded in acetonitrile.

All of the complexes give a pale yellow/brown colour when dissolved in solution, attributed to their absorbing visible light up to 600 nm. The iridium centres are coordinated to polypyridyl ligands π-π^* transitions dominate as high-energy, short wavelength transitions of each spectra. Despite the change in counter-ions each complex possesses high energy transitions at around 205 nm and 277 nm, which are due to the phen, bpy and dppz π-π^* transitions. The complexes all have an MLCT around 390 nm, which is the highest wavelength when a cyclometallated dppz is coordinated to the metal centre, **3.** This red shift of around 10 nm is due to the phototunable nature of iridium complexes. The cyclometallated dppz unit will cause the electronic lowest unoccupied molecular orbital (LUMO) and highest occupied molecular orbital (HOMO) to shift in energy producing a red shift in absorption λ_{max}. There are many ways to achieve more pronounced colour versatility changes with iridium complexes including; deliberate functionalization of ligands through the use of substituent groups. By manipulating the electronic effects within the iridium complex, a profound influence on the orbital energies can be achieved. By incorporating electron withdrawing groups the HOMO can be stabalise by removing electron density from the metal, and electron donating groups will produce an opposing effect of HOMO destabalisation.[14]

2.2.2.2 Luminescence studies

Emission spectra of **1-3** were recorded in acetonitrile and water as hexafluorophosphate and chloride salts respectfully and the data was collected at room temperature and normalized for clarity. All of the complexes were excited at a wavelength characteristic to that of their MLCT band concluded from the UV-visible assignments made previously. The normalised spectra for each compound in acetonitrile and water, excited at 390 nm are shown below with a table

summarising all the data. Emission units are not shown and classified as arbitrary units (*Figures 2.8-2.10).*

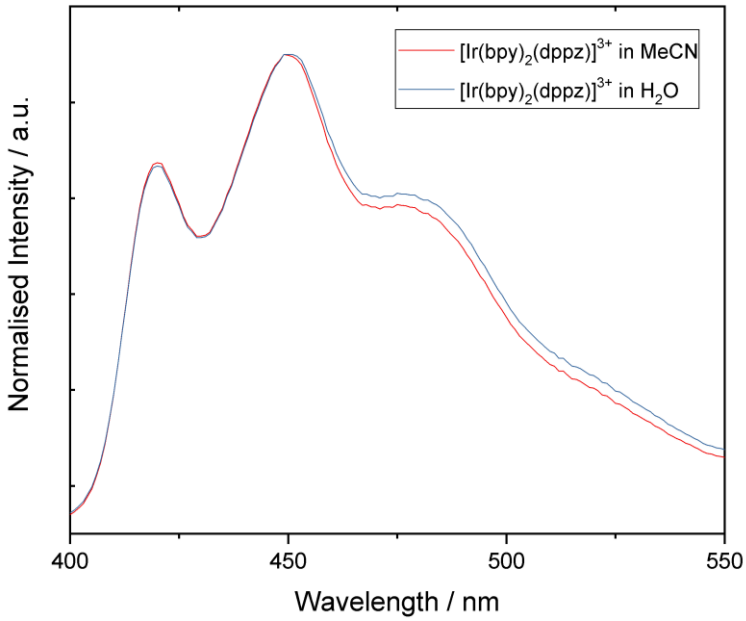

Figure 2.8: Normalised emission spectra for $[Ir(bpy)_2(dppz)]^{3+}$, ***1,*** *in acetonitrile (red) and water (blue).*

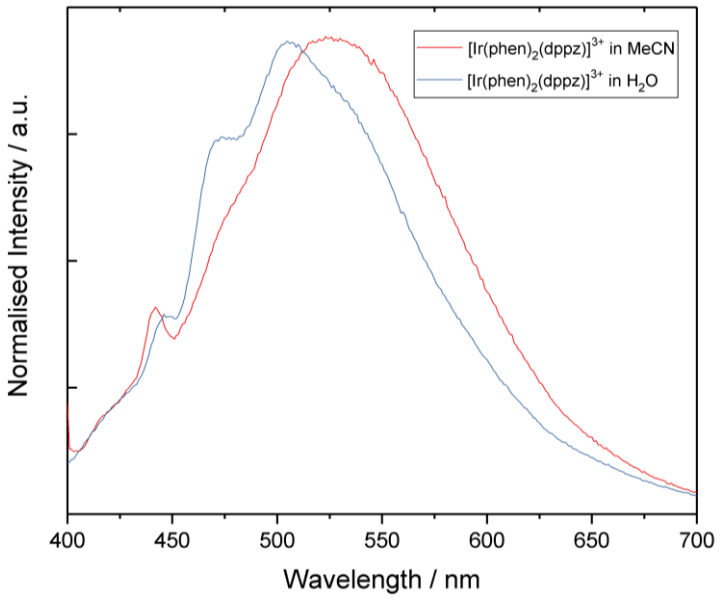

Figure 2.9: Normalised emission profile for $[Ir(phen)_2(dppz)]^{3+}$, ***2,*** *in acetonitrile (red) and water (blue).*

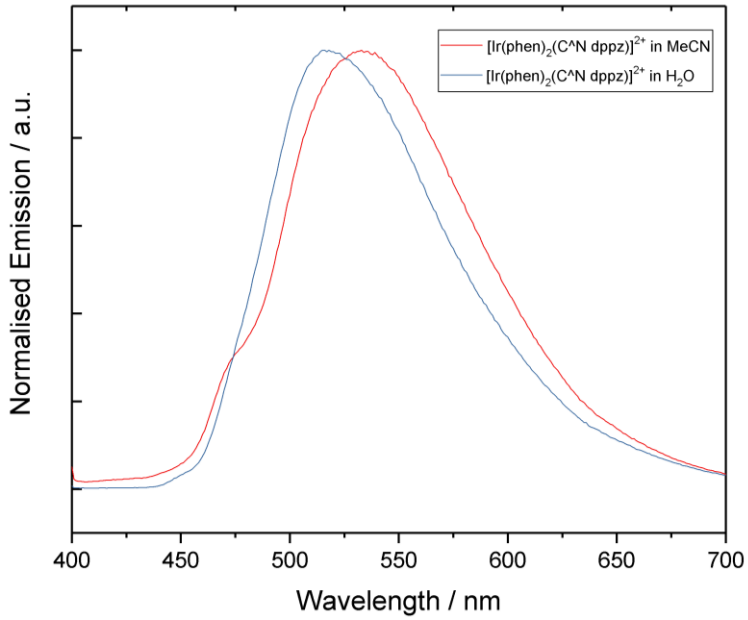

*Figure 2.10: Normalised emission profile for $[Ir(phen)_2(C^N\ dppz)]^{2+}$,**3**, in acetonitrile (red) and water (blue).*

Emission spectra were recorded in freshly distilled acetonitrile for PF_6 or double distilled water for chloride salts. The complexes, **1-3**, all share a similar emission in both solvents. All of the complexes display emission around 500 nm, shifting in λ_{max} by 2 nm between each solvent for **1**, 14 nm for **2**, and 18 nm for **3.** For complexes **2** and **3** the emission shifts to that of a higher energy in water, however for **1** this shift is negligible. The fluorescence or phosphorescence quantum yield - which is defined as the ratio of the number of emitted photons to that of absorbed photons - is one of the most fundamental and important photophysical parameters of emissive compounds. Quantum yields were measured according to the method described by Jobin Yvon for $[Ru(bpy)_3]^{2+}$.[34] Two separate standards were cross-calibrated in order to obtain reliable results.[35] These results are summerised in *Table 2.3.*

Complex	λ_{max} (nm)		φ_F		φ_F ratio
	MeCN	H_2O	MeCN	H_2O	
$[Ir(bpy)_2(dppz)]^{3+}$	449	451	4.2×10^{-3}	2.8×10^{-3}	1.50
$[Ir(phen)_2(dppz)]^{3+}$	525	511	6.6×10^{-3}	4.69×10^{-3}	1.41
$[Ir(phen)_2(C^N\ dppz)]^{2+}$	533	515	26.2×10^{-3}	15.6×10^{-3}	1.68

*Table 2.3: Summary of the maximum emission wavelengths, the quantum yield of fluorescence and ratio for **1-3** as both PF_6 salts in acetonitrile and chloride salts in water.*

The quantum yields are higher in acetonitrile for all three complexes than in water. Although the complexes do not display the light-switch effect like Ru^{II} analogies, they all have longer lifetimes in organic solvents. Complex **2** possessing the cyclometallated ligand has the largest quantum yield and is the most emissive in both acetonitrile and water.

2.2.2.3 Luminescence lifetime studies

Lifetimes were measured using a mini-tau filter-based fluorescence lifetime spectrometer which uses a time-correlated single photon counting technique. The samples can be excited at a particular wavelength using a laser with a defined pulse width, and by recording single excitation/emission events one photon at a time and a time-dependent intensity profile of the emitted light can be produced. The delay between the excitation event and the detected emission is measured over numerous single-photon cycles producing a cumulative time profile of the exponential decay curve for each complex. When fitting a dual exponential, there is one consistently short lifetime component, τ_1, and a longer lifetimes component,τ_2, with the percentage contribution always larger from the second lifetime. The quality of the bi-exponential can be monitored by the χ^2 value (*Table 2.4).* The biexponential nature of the complexes could be due to two close lying electronic states (*i.e. MLCT and π-π*).*

	H_2O (ns)				χ^2	MeCN (ns)				χ^2
	τ_1	%	τ_2	%		τ_1	%	τ_2	%	
$[Ir(bpy)_2(dppz)]^{3+}$	6.9	***41***	900	***59***	1.14	24	***22***	1350	***78***	1.17
$[Ir(phen)_2(dppz)]^{3+}$	25	***29***	740	***71***	1.22	77	***37***	1478	***63***	1.34
$[Ir(phen)_2(CN\ dppz)]^{2+}$	30	***35***	592	***64***	1.30	89	***33***	1645	***67***	1.26

*Table 2.4: Luminescent lifetimes attained from **1-3** in both water and dry acetonitrile, $[Ru(bpy)_3]^{2+}$ was used as a standard.*

2.2.2.4 Density functional theory calculations

Density functional theory (DFT) is a valuable tool for the exploration of molecular properties of biological system as it is important to understand the redistribution of electron density brought about by optical excitation. Partnering experimental excited state luminescent studies with quantum chemical calculations provides a means to explore the excited-state character of metal complexes such as; excited state character and relaxation pathways –beyond experimental observations.[36] To investigate these emission properties in more detail, DFT calculations were performed on both the S_0 state and the T_1 state of all the complexes by Prof. Anthony J. H. M. Meijer, University of Sheffield (*Figure 2.11).* DFT calculations were performed using Gaussian09, version D.01.[37] Gaussian was compiled with Gaussian-supplied versions of BLAS and ATLAS.[38,39] The B3LYP[39] functional was used throughout with the GD3 correction[40] to account for dispersion interactions, whereby it is noted that in this case the correction did not change the answers significantly compared to the bare B3LYP functional. The 6-311gG** basis set[41,42] was used on all C, N, and H. A Stuttgart-Dresden pseudopotential[41,42] was used on Ru and Ir throughout. This computational procedure was found to give good correlation with experiment in previous work.[43–47] Whilst the triplet states of the three complexes are structurally similar, they are clearly electronically different. The spin density for the T_1 state of **1** and **2** is largely concentrated on the dppz unit. In contrast, for the T_1 state of **3**, the spin density is located on the metal centre and one of the phenanthroline ancillary units. To investigate this behaviour, DFT calculations on a fourth complex $[Ir(bpy)_2(C\text{^}N\ dppz)]^{2+}$ were carried out. These further calculations confirm that the change in the excited state is a consequence of the cyclometalation, as similar to **3** the spin density is localised away from the dppz ligand onto the bipyridine units.[48] The DFT calculations explain why all three complexes do not display the DNA light-switch effect. The excited state of **1** and **2** is best described as an intraligand state localised on the dppz unit. Upon binding DNA-induced luminescence quenching is a well-studied phenomenon and indeed several metal-dppz based complexes show emissions that are quenched with polynucleotides.[49–51] In contrast, the excited state of **3** is more consistent with a high-energy MLCT transition involving a non-intercalative phenanthroline unit, which will not be quenched by water but can be redox quenched on interaction with DNA. This work shows that although the binding properties of these complexes are comparable to the parent Ru^{II} systems, the emission characteristics can be readily tuned.

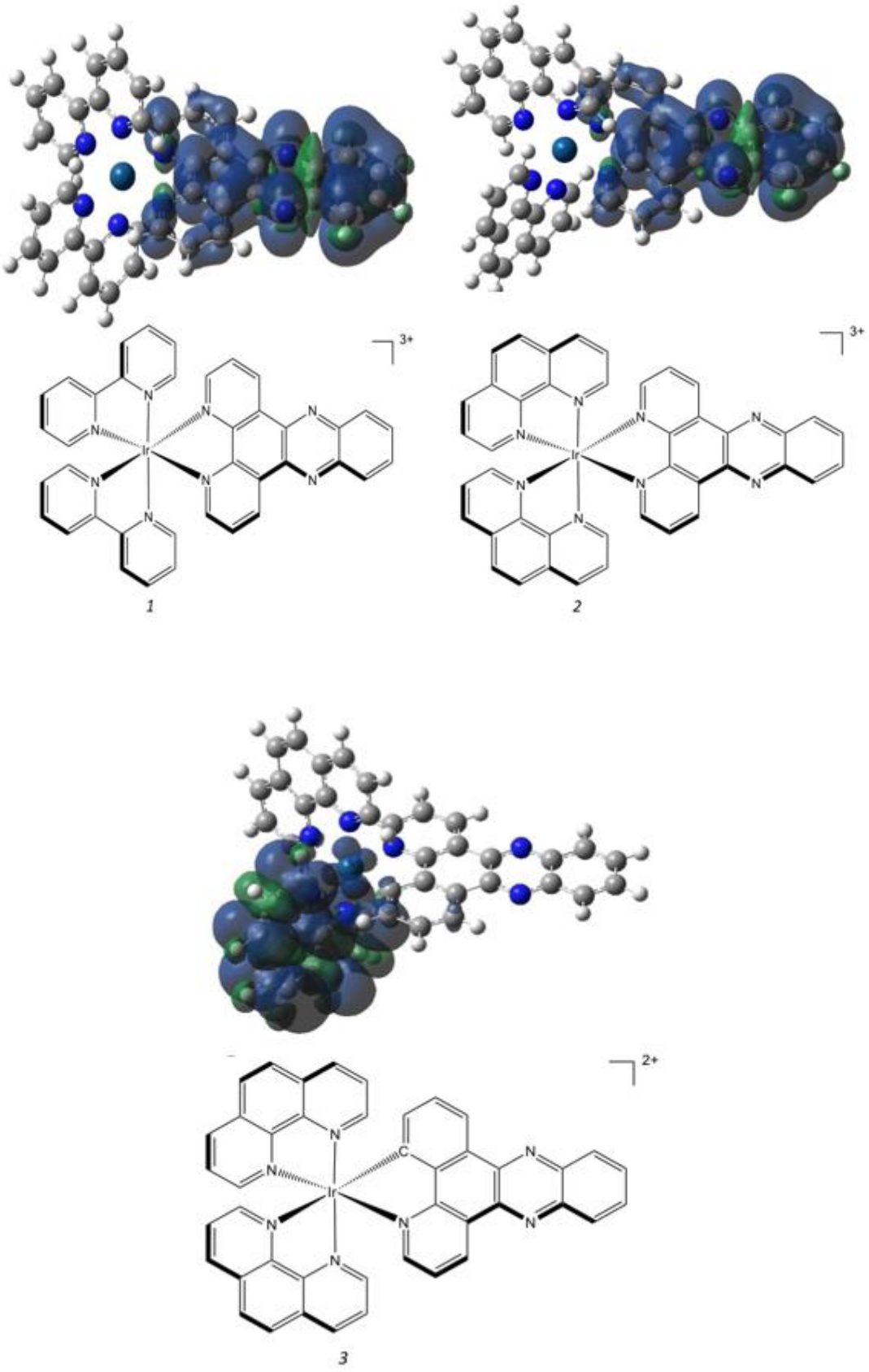

*Figure 2.11: Spin-density plots for the T_1 state of complexes **1-3**. Atom sphere colors: C = grey; H = white; N = dark blue; Ir = lighter blue.*

2.2.2.5 Singlet oxygen studies

The photophysical property of transition metal complexes known as the heavy atom effect causes fast singlet to triplet intersystem crossing. This triplet excited state can react with oxygen producing the damaging $^1O_2$, reactive oxygen species (ROS) radical in high yields.[52] Singlet oxygen is a highly reactive species which is able to oxidise many chemical entities such as cellular DNA.[53]

$$complex + light \rightarrow complex^*$$

$$complex^* + O_2 \rightarrow ROS \rightarrow DNA\ oxidative\ damage$$

Singlet oxygen is detected directly in organic solution by measurement of singlet oxygen luminescence following photo excitation of the compound at room temperature in air saturated solutions in organic solvents. The quantum yield of singlet oxygen (ϕ_Δ) is determined by comparing the initial intensity for the compounds and that of a known singlet oxygen generator standard (perinapthenone ϕ_Δ = 95% in DCM and ϕ_Δ = 100% in acetonitrile) at various power outputs, then averaged (*Equation 2.1) (Table 2.5)*:[54]

$$\frac{initial\ intensity\ of\ compound}{initial\ intensity\ of\ standard} \times standard\ \phi_\Delta\ in\ solvent = compound\ \phi_\Delta$$

Equation 2.1

Complex	Singlet oxygen yield (ϕ_Δ)
$[Ir(bpy)_2(dppz)]^{3+}$	0.48
$[Ir(phen)_2(dppz)]^{3+}$	0.56
$[Ir(phen)_2(C\text{^}N\ dppz)]^{2+}$	0.60

*Table 2.5: Singlet oxygen yield for $[Ir(bpy)_2(dppz)]^{3+}$**1**, $[Ir(phen)_2(dppz)]^{3+}$ **2**, $[Ir(phen)_2(C\text{^}N\ dppz)]^{2+}$ **3**.*

The absorption of a single photon has the capacity to generate only one molecule of singlet oxygen in an ideal situation the ϕ_Δ is expressed as an integer with a value between zero and one. A ϕ_Δ of one would correspond to a system where every single photon observed by the metal complex correlates to the generation of a singlet oxygen molecule. All of the complexes **1-3** possess long-lived luminescent triplet-state lifetimes, which promotes and enables efficient energy transfer with the triplet ground state of molecular oxygen.[55] This interaction with the ground state oxygen, results in simultaneous luminescence quenching and formation of triplet oxygen. (*Figure 2.12).* The three iridium complexes in this work produce singlet oxygen in high yields; between 40-60 %.

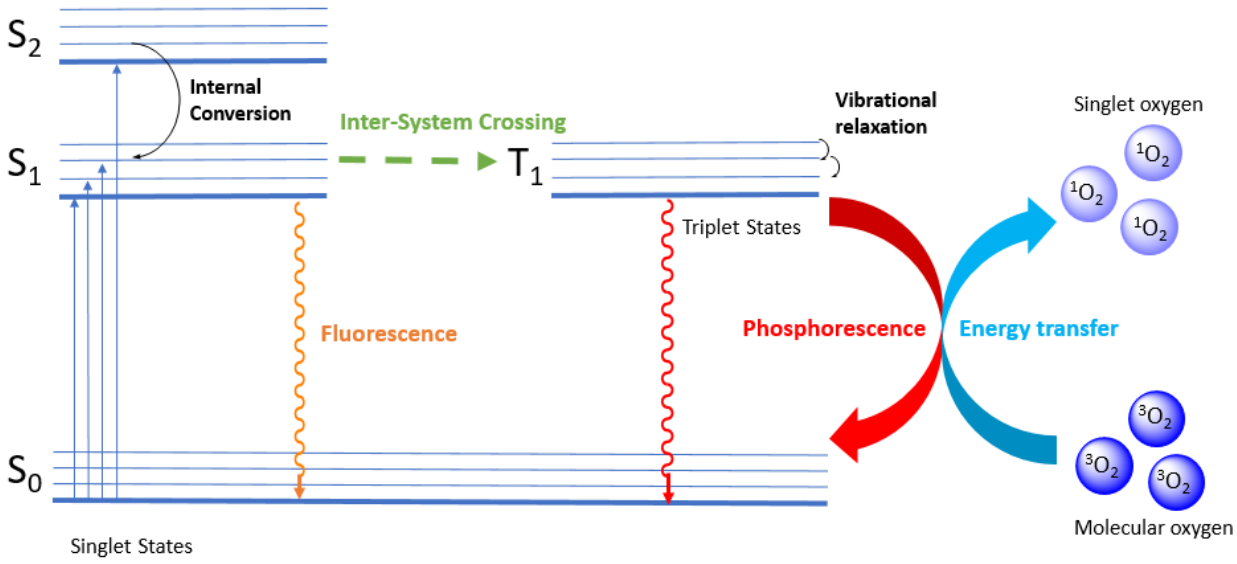

Figure 2.13 – Jablonski schematic of the triplet state of the iridium complexes interacting with molecular oxygen through an energy transfer reaction to produce the damaging singlet oxygen radical.

2.3 Conclusions and Future Work

Three novel Ir-dppz complexes (*Figure 2.13)* have been synthesised and their photophysical properties have been documented in acetonitrile and in water. Characterisation using UV-Visible studies show the presence of π-π^* and MLCT bands for all three complexes. All of which show strong π-π^* transitions around 200-300 nm and MLCT transitions around 390 nm. The highest MLCT is observed in **3** due to the incorporation of the cyclometallated dppz unit. As iridium polypyridyl complexes are susceptible to colour tunability, the incorporation of this ligand will result in a shift in LUMO/HOMO electronic levels within the complex producing a shift in MLCT. Variations in electronic distribution could be investigated by incorporating electron donating or withdrawing ligands on the polypyridyl ligands to investigate the extent of the colour tuning capabilities. Luminescence experiments were carried out for all three complexes showing them all to have maximum wavelength emissions around 500 nm in acetonitrile and water. For **2** and **3** the emission was shifted to a higher energy in water by 14 nm and 18 nm, respectfully. For **1** this shift is negligible at 2 nm. All three complexes were found to possess bi-exponential lifetimes in aqueous/ polar solvents, which produced singlet oxygen of yields 40 % and higher. Future work would include using cyclic voltammetry to determine the exact oxidation and reduction potentials. As electron transfer processes are central to the reactivity of inorganic complexes, electrochemistry is a powerful tool to investigate electron transfer kinetics.[56]

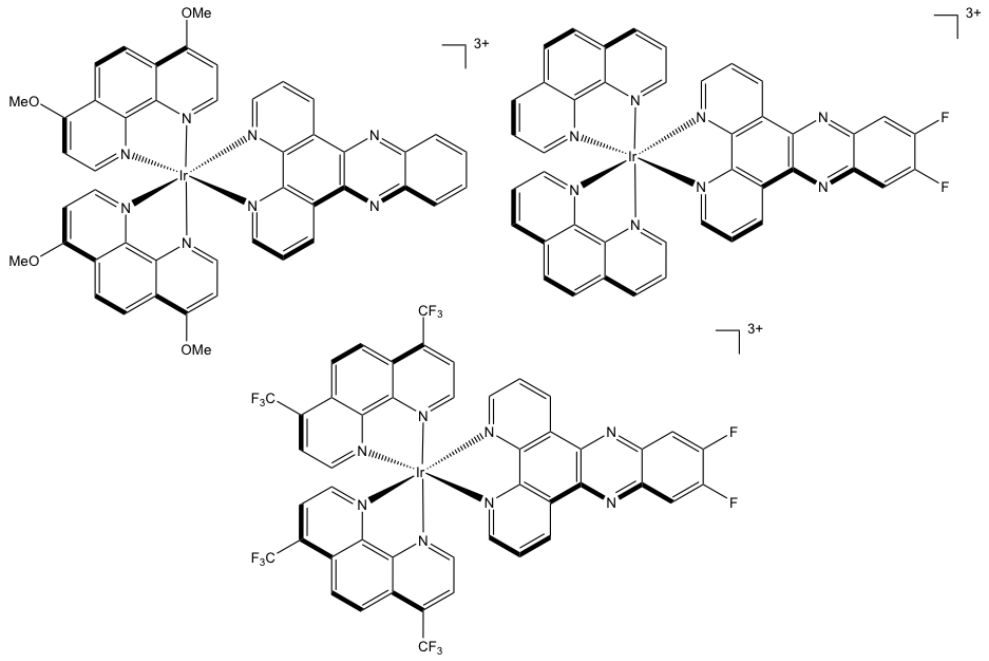

Figure 2.13: Potential future complexes to explore the electronic effects of ancillary ligands.

2.4 References

1 Y. Sun, S. N. Collins, L. E. Joyce and C. Turro, Unusual photophysical properties of a ruthenium(II) complex related to [Ru(bpy)2(dppz)]2+, *Inorg. Chem.*, 2010, **49**, 4257–4262.

2 N. H. Damrauer, Femtosecond Dynamics of Excited-State Evolution in [Ru(bpy)3]2+, *Science*, 1997, **275**, 54–57.

3 J. V. Caspar and T. J. Meyer, Photochemistry of [Ru(bpy)3]2+ Solvent Effects, *J. Am. Chem. Soc.*, 1983, **105**, 5583–5590.

4 A. E. Friedman, J. K. Barton, J. C. Chambron, J. P. Sauvage, N. J. Turro and J. K. Barton, Molecular "Light Switch" for DNA: Ru(bpy)2(dppz)2+, *J. Am. Chem. Soc.*, 1990, **112**, 4960–4962.

5 J. Knoll, B. Albani and C. Turro, New Ru(II) Complexes for Dual Photoreactivity: Ligand Exchange and 1O2 generation, *Acc. Chem. Res*, 2015, **48**, 2280–2287.

6 M. Licini and J. a. Gareth Williams, Iridium(III) bis-terpyridine complexes displaying long-lived pH sensitive luminescence, *Chem. Commun.*, 1999, 1943–1944.

7 J. D. Slinker, A. A. Gorodetsky, M. S. Lowry, J. Wang, S. Parker, R. Rohl, S. Bernhard and G. G. Malliaras, Efficient Yellow Electroluminescence from a Single Layer of a Cyclometalated Iridium Complex, *J. Am. Chem. Soc.*, 2004, **126**, 2763–2767.

8 M. S. Lowry, J. I. Goldsmith, J. D. Slinker, R. a Pascal, G. G. Malliaras, S. Bernhard and R. Rohl, Single-Layer Electroluminescent Devices and Photoinduced Hydrogen Production from an Ionic Iridium (III) Complex Single-Layer Electroluminescent Devices and Photoinduced Hydrogen Production from an Ionic Iridium (III) Complex, *J. Mater.*, 2005, **17**, 5712–5719.

9 M. Montalti, A. Credi, L. Prodi and M. Gandolfi, Tersesa, *Handbook of Photochemistry*, CRC Press, 3rd Editio., 2006.

10 L. Flamigni, A. Barbieri, C. Sabatini, B. Ventura and F. Barigelletti, *Photochemistry and Photophysiscs of Coordination Compounds: Iridium*, 2007.

11 J. C. Koziar and D. O. Cowan, Photochemical Heavy-Atom Effects, *Acc. Chem. Res.*, 1978, **11**, 334–341.

12 I. N. Mills, J. A. Porras and S. Bernhard, Judicious Design of Cationic, Cyclometalated Ir(III) Complexes for Photochemical Energy Conversion and Optoelectronics, *Acc. Chem. Res.*, 2018, **51**, 352–364.

13 I. N. Mills, J. A. Porras and S. Bernhard, Judicious Design of Cationic, Cyclometalated

Ir(III) Complexes for Photochemical Energy Conversion and Optoelectronics, *Acc. Chem. Res.*, 2018, 265-270.

14 M. S. Lowry and S. Bernhard, Synthetically tailored excited states: phosphorescent, cyclometalated iridium(III) complexes and their applications., *Chem. Eur. J*, 2006, **12**, 7970–7.

15 C. Metcalfe and J. A. Thomas, Kinetically inert transition metal complexes that reversibly bind to DNA, *Chem. Soc. Rev.*, 2003, **32**, 215.

16 M. K. Brennaman, J. H. Alstrum-Acevedo, C. N. Fleming, P. Jang, T. J. Meyer and J. M. Papanikolas, Turning the [Ru(bpy)2dppz]2+ light-switch on and off with temperature, *J. Am. Chem. Soc.*, 2002, **124**, 15094–15098.

17 W. Paw and R. Eisenberg, Synthesis, Characterization, and Spectroscopy of Dipyridocatecholate Complexes of Platinum, *Inorg. Chem.*, 1997, **36**, 2287–2293.

18 K. Kloc, J. Mlochowski and Z. Szulc, Synthesis of Azafluorenones, *J. fur Prakt. Chemie*, 1977, **319**, 959–967.

19 J. V McArdle, C. L. Coyle, H. B. Cray, G. S. Yoneda and R. a Holwerda, Kinetics studies of the oxidation of blue copper proteins by tris(1,10-phenanthroline)cobalt(III) ions., *J. Am. Chem. Soc.*, 1977, **99**, 2483–9.

20 C. T. Lin and N. Sutin, Quenching of the luminescence of the tris(2,2′-bipyridine) complexes of ruthenium(II) and osmium(II). Kinetic considerations and photogalvanic effects, *J. Phys. Chem.*, 1976, **80**, 97–105.

21 R. H. Holyer, C. D. Hubbard, S. F. A. Kettle and R. G. Wilkins, The Kinetics of Replacement Reactions of Complexes of the Transition Metals with 1,10-Phenanthroline and 2,2'-Bipyridine, *Inorg. Chem.*, 1965, **4**, 929–935.

22 T. C. Tris, R. Ii, G. A. Crosby, W. G. Perkins and D. M. Klassen, Luminescence from Transition-Metal Complexes: Tris(2,2-bipyridine)- and Tris(1,10-phenanthroline)Ruthenium(II), *J. Chem. Phys.*, 1965, **43**, 1498-1502.

23 R. A. Palmer, T. S. Piper and W. A. Noyes Laboratory, 2,2′-Bipyridine Complexes. I. Polarized Crystal Spectra of Tris(2,2′-bipyridine)copper(II), -nickel(II), -cobalt(II), -iron(II), and -ruthenium(II), *Inorg. Chem.*, 1966, **5**, 864–878.

24 C. M. Flynn and J. N. Demas, Synthesis and Luminescence of the Tris(2,2′-bipyridine)iridium(III) Ion, *J. Am. Chem. Soc.*, 1974, **96**, 1959–1960.

25 R. J. Watts, J. S. Harrington and J. V. van Houten, A Stable Monodentate 2,2'-Bipyridine Complex of Iridium(III): A Model for Reactive Intermediates in Ligand Displacement Reactions of Tris-2,2'-bipyridine Metal Complexes, *J. Am. Chem. Soc.*,

1977, **99**, 2179–2187.

26 M. Pandrala, F. Li, M. Feterl, Y. Mulyana, J. M. Warner, L. Wallace, F. R. Keene and J. G. Collins, Chlorido-containing ruthenium(ii) and iridium(iii) complexes as antimicrobial agents, *Dalt. Trans.*, 2013, **42**, 4686.

27 A. Scott and H. Taube, Complexing Tendency of Trifluoromethylsulfonate Ion as Measured Using Chromium(III), *Inorg. Chem.*, 1971, **10**, 62–66.

28 N. E. Dixon, W. G. Jackson, M. J. Lancaster, G. A. Lawrance and A. M. Sargeson, Labile (Trifluoromethanesulfonato)cobalt(III) Amine Complexes, *Inorg. Chem.*, 1981, **20**, 470–476.

29 N. E. Dixon, G. A. Lawrance, P. a Lay, A. M. Sargeson and H. Taube, in *Inorganic Syntheses: Reagents for Transition Metal Complex and Organometallic Syntheses, Volume 28*, ed. W. and Sons, 1990, pp. 70–76.

30 A. Marini, A. Muñoz-Losa, A. Biancardi and B. Mennucci, What is Solvatochromism?, *J. Phys. Chem. B*, 2010, **114**, 17128–17135.

31 D. M. Manuta and A. J. Lees, Solvatochromism of the Metal to Ligand Charge-Transfer Transitions of Zerovalent Tungsten Carbonyl Complexes, *Inorg. Chem.*, 1986, **25**, 3212–3218.

32 G. V. Loukova, A. A. Milov, V. P. Vasiliev and V. I. Minkin, Dipole moments and solvatochromism of metal complexes: principle photophysical and theoretical approach, *Phys. Chem. Chem. Phys.*, 2016, **18**, 17822–17826.

33 P. Chen and T. J. Meyer, Medium Effects on Charge Transfer in Metal Complexes, *Chem. Rev.*, 1998, **98**, 1439–1478.

34 L. Palsson and A. Monkman, A Guide to Recording Fluorescence Quantum Yields.

35 K. Suzuki, A. Kobayashi, S. Kaneko, K. Takehira, T. Yoshihara, H. Ishida, Y. Shiina, S. Oishi and S. Tobita, Reevaluation of absolute luminescence quantum yields of standard solutions using a spectrometer with an integrating sphere and a back-thinned CCD detector, *Phys. Chem. Chem. Phys.*, 2009, **11**, 9850.

36 A. Vlcek Jr. and Z. Stanislav, Modeling of charge-transfer transitions and excited states in d6 transition metal complexes by DFT techniques, *Coord. Chem. Rev*, 2007, **251**, 258–287.

37 D. J. Frisch, M. J.; Trucks, G. W.; Schlegel, H. B.; Scuseria, G. E.; Robb, M. A.; Cheeseman, J. R.; Scalmani, G.; Barone, V.; Petersson, G. A.; Nakatsuji, H.; Li, X.; Caricato, M.; Marenich, A. V.; Bloino, J.; Janesko, B. G.; Gomperts, R.; Mennucci, B.; Hratch, 2016.

38 C. R. Whaley and A. Petitet, Minimizing decelopment and maintenance costs in supporting persistently optimized BLAS, *J. Softw. Pract. Exp.*, 2005, **35**, 101–121.

39 R. C. Whaley, A. Petitet and J. J. Dongarra, Automated Emperical Optimization of Software and the {ATLAS} Project, *Parallel Comput.*, 2000, **27**, 3–35.

40 S. Grimme, J. Antony, S. Ehrlich and H. Krieg, A consistent and accurate ab initio parametrization of density functional dispersion correction (DFT-D) for the 94 elements H-Pu, *J. Chem. Phys.*, 2010, **132**, 154104-154110.

41 R. Krishnan, J. S. Binkley, R. Seeger and J. A. Pople, Self-consistent molecular orbital methods. XX. A basis set for correlated wave functions, *J. Chem. Phys.*, 1980, **72**, 650–654.

42 A. D. McLean and G. S. Chandler, Contracted Gaussian basis sets for molecular calculations. I. Second row atoms, Z=11-18, *J. Chem. Phys.*, 1980, **72**, 5639–5648.

43 J. Best, I. V. Sazanovich, H. Adams, R. D. Bennett, E. S. Davies, A. J. H. M. Meijer, M. Towrie, S. A. Tikhomirov, O. V. Bouganov, M. D. Ward and J. A. Weinstein, Structure and ultrafast dynamics of the charge-transfer excited state and redox activity of the ground state of mono- and binuclear platinum(II) diimine catecholate and bis-catecholate complexes: A transient absorption, TRIR, DFT, and electrochemical stud, *Inorg. Chem.*, 2010, **49**, 10041–10056.

44 S. P. Foxon, C. Green, M. G. Walker, A. Wragg, H. Adams, J. A. Weinstein, S. C. Parker, A. J. H. M. Meijer and J. A. Thomas, Synthesis, Characterization, and DNA Binding Properties of Ruthenium(II) Complexes Containing the Redox Active Ligand Benzo[*i*]dipyrido[3,2- *a* :2′,3′- *c*]phenazine-11,16-quinone, *Inorg. Chem.*, 2012, **51**, 463–471.

45 H. Ahmad, A. J. H. M. Meijer and J. A. Thomas, Tuning the excited state of photoactive building blocks for metal-templated self-assembly, *Chem. - An Asian J.*, 2011, **6**, 2339–2351.

46 J. B. Chaires, A thermodynamic signature for drug-DNA binding mode, *Biochem. Biophys.*, 2006, **453**, 26–31.

47 M. Pandrala, A. F. Li, A. L. Wallace, G. P. J. Steel, B. M. Ii, C. J. Autschbach and C. J. G. Collins, Iridium (III) Complexes Containing 1 , 10-Phenanthroline and Derivatives : Synthetic , Stereochemical , and Structural Studies , and their Antimicrobial Activity, *Aust. J. Chem*, 2013, **66**, 1065–1073.

48 S. Stimpson, D. R. Jenkinson, A. Sadler, M. Latham, A. Wragg, A. J. H. M. Meijer and J. A. Thomas, Tuning the excited state of water-soluble IrIII-based DNA intercalators

that are isostructural with [RuII(NN)2(dppz)] light-switch complexes, *Angew. Chemie - Int. Ed.*, 2015, **54**, 3000–3003.

49 T. Phillips, I. Haq and J. a Thomas, Water-soluble amino derivatives of free-base dppz - syntheses and DNA binding studies., *Org. Biomol. Chem.*, 2011, **9**, 3462–70.

50 T. Phillips, I. Haq, A. J. H. M. Meijer, H. Adams, I. Soutar, L. Swanson, M. J. Sykes and J. A. Thomas, DNA binding of an organic dppz-based intercalator, *Biochemistry*, 2004, **43**, 13657–13665.

51 C. Moucheron, A. Kirsch- De Masmaeker and M. Kelly, John, Photoreactions of ruthenium(II) and osmium(II) complexes with deoxyribonucleic acid (DNA), *J. Photochem. Photobiol. BBiology*, 1997, **40**, 91–106.

52 L. K. McKenzie, I. V. Sazanovich, E. Baggaley, M. Bonneau, V. Guerchais, J. A. G. Williams, J. A. Weinstein and H. E. Bryant, Metal Complexes for Two-Photon Photodynamic Therapy: A Cyclometallated Iridium Complex Induces Two-Photon Photosensitization of Cancer Cells under Near-IR Light, *Chem. - A Eur. J.*, 2017, **23**, 234–238.

53 K. Krumova and G. Cosa, Chapter I: Overview of reactive oxygen species, *Singlet Oxyg. Appl. Biosci. Nanosci. Vol. 1*, 2016, 21.

54 R. Berera, R. van Grondelle and J. T. M. Kennis, Ultrafast transient absorption spectroscopy: principles and application to photosynthetic systems, *Photosynth. Res.*, 2009, **101**, 105–118.

55 P. I. Djurovich, D. Murphy, M. E. Thompson, B. Hernandez, R. Gao, P. L. Hunt and M. Selke, Cyclometalated iridium and platinum complexes as singlet oxygen photosensitizers: Quantum yields, quenching rates and correlation with electronic structures, *Dalt. Trans.*, 2007, 3763–3770.

56 N. Elgrishi, K. J. Rountree, B. D. McCarthy, E. S. Rountree, T. T. Eisenhart and J. L. Dempsey, A Practical Beginner's Guide to Cyclic Voltammetry, *J. Chem. Educ.*, 2018, **95**, 197–206.

Chapter 3
DNA-binding studies

3.0 DNA binding studies

3.1 Introduction

The interactions of transition metal polypyridyl coordination complexes with deoxyribonucleic acid (DNA) have been extensively studied in recent years and they have been used in the design of new drugs, theranostics, and imaging agents. Previous studies revealed that subtle modification of these species can lead to substantial changes in the binding modes, location and affinities of the complexes. A complete characterisation of these DNA binding agents requires that their DNA binding modes needs to be established. In this chapter, the interactions between the iridium complexes described in the previous chapter and DNA will be reported. These complexes vary in the size of their ancillary ligands and overall charge (*Figure 3.1).*

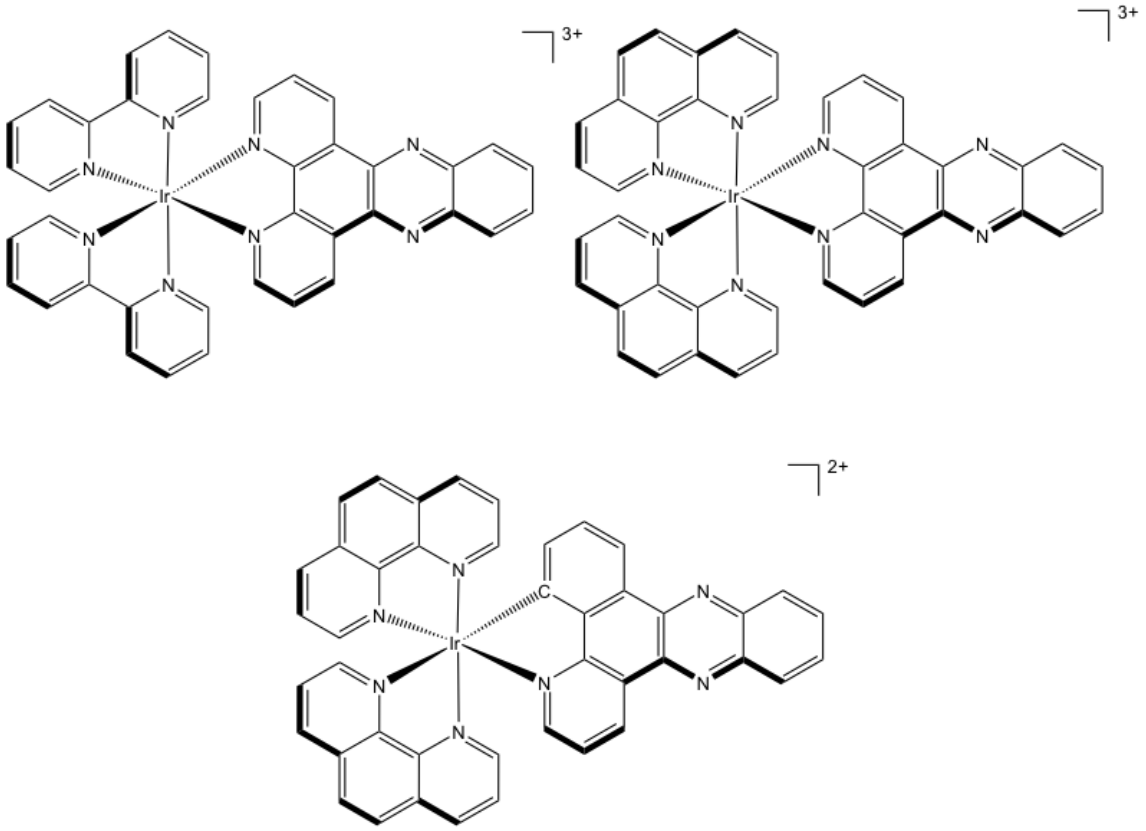

*Figure 3.1: Iridium polypyridyl complexes in this chapter. Top left – $[Ir(bpy)_2(dppz)]^{3+}$ **1**; top right – $[Ir(phen)_2(dppz)]^{3+}$ **2**; bottom – $[Ir(phen)_2(C\text{^}N\ dppz)]^{2+}$ **3.***

3.2 Analytical techniques

3.2.1 Viscosity

Viscosity is commonly perceived as resistance to pouring. It describes a fluid's resistance to flow. The intrinsic viscosity gives a measure of the effective hydrodynamic volume of a polymer in solution.[1] As described in previous chapters, when a small molecule interacts reversibly with DNA, the two most likely binding modes are intercalation or groove binding.[2] Groove binders are commonly crescent shaped, residing along the DNA helix in either the major or minor groove. Typically in this interaction the structure of the DNA helix remains unperturbed. In contrast, intercalating molecules are planar, aromatic species that slide between the nucleotide base pairs, resulting in substantial changes to the DNA structure. A partly extended DNA double helix containing the intercalated complex differs from native DNA in solution several ways; it has an increased length, and it also displays stiffening and helical unwinding.[3–5] This results in pronounced alteration of the system's hydrodynamic properties, such as viscosity. Therefore, as reported by Cohen and Eisenberg in 1969, viscosity measurements provide a simple, theoretically sound, means of distinguishing DNA binding modes.[6] In these studies the viscosity of DNA on additions of complex are compared to those of native DNA solutions. Relative viscosities for DNA in either the presence or absence of a transition metal can be calculated from the relation:

$$\eta = \frac{t - t_0}{t_0}$$

Equation 3.1

Where t is the observed time flow time of the DNA containing solution and t_0 is the flow time of the buffer alone. In the absence of X-ray crystallographic or NMR structural data, hydrodynamic data provides the most critical test for intercalative binding. The viscosity changes induced by different binding modes are summarised in *Figure 3.2*.

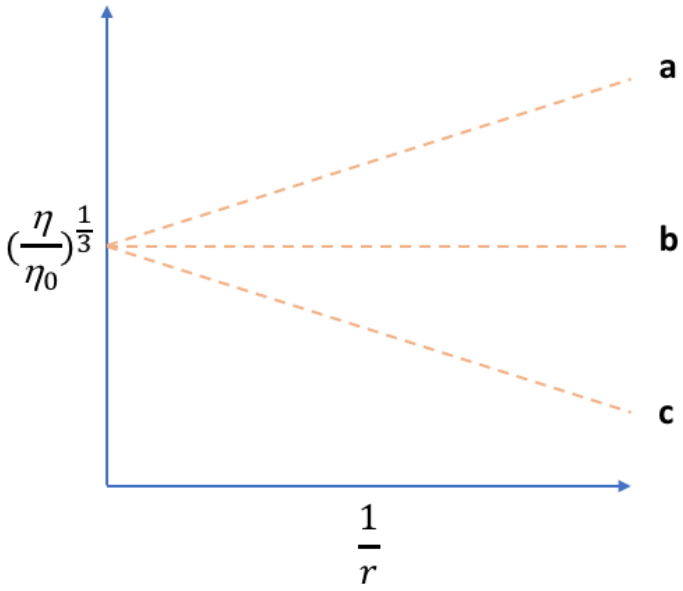

Figure 3.2: Effect of increasing amounts of bound ligand on the relative specific viscosity of DNA. Schematic showing 'a' intercalation, 'b' groove binding, 'c' binding mode that produces DNA bending/kinking. Where r = binding ratio, η = relative specific viscosity of complex and DNA, and η_0 = relative viscosity of DNA in buffer alone.

As shown in this figure, an intercalator increases the relative specific viscosity, through lengthening of the DNA double helix by insertion between the base pairs. A groove binder - which does not perturb the DNA structure upon binding - does not appreciably alter the hydrodynamic properties of the DNA viscosity. In some cases a decrease in viscosity can be observed; this is due to bending of the helix as a result of partial intercalation of species such as peptides containing aromatic amino acids as well as other aromatic cations.[7,8]

3.2 2 Luminescent DNA titrations

The most commonly used method to study transition metal complexes' interaction with DNA is absorption and luminescence spectroscopy. Coordination complexes are often visibly coloured and this property also provides a useful spectroscopic handle to follow DNA/drug interactions. The UV-vis spectra of transition metal complexes originate from various electronic transitions (intense MLCT, ligand π-π^* bands) into excited states. On binding to nucleic acids these electronic transitions are perturbed. Factors that can affect absorption spectra include protonation/deprotonation (pH), solvent polarity (dielectric constant of solvent), and orientation effects. So, as the immediate environment of a species is reflected by

their absorbance properties, this is an ideal reporter for investigating the environmental changes induced by DNA binding.[9] A simple way to determine whether an interaction takes place is to examine the modifications of the maximum of one of these bands when the nucleic acid is present in different concentrations.[9] Binding with DNA through intercalation usually results in hypochromism and bathochromism[10] and it has been assumed that the magnitude of this shifting is an indication of the strength of the metal-DNA system. These changes occur due to stacking interactions between the fused aromatic rings of the ligand and the base pairs of the DNA. If the binding mode is intercalation, the π^* orbitals of the intercalated ligand can overlap with the π orbitals of the DNA base pairs, decreasing the transition energy resulting in bathochromism. The coupling π orbital is partially filled by electrons, such an intercalative interaction results in the decrease in transition probabilities causing a decrease in absorption, hypochromism.[11] Similar to UV-vis spectra, luminescence spectroscopy can be used to investigate the binding events between a transition metal complex and DNA. Steady state luminescence measurements can be carried out to monitor the changes in emission intensities for metal complexes in the presence of varying concentrations of DNA.[11] The intensity of the MLCT band can be monitored using this method. Given the common preferential charge transfer onto the extended intercalating ligand, the luminescence of the bound complex can provide a sensitive reporter of its environment.[12] If DNA is titrated into a known concentration of binding substrate solution, the shift in any given band is proportional to the fraction of the complex bound to the DNA. Therefore the fraction of complex bound (χ) can be calculated in the case of luminescence spectroscopy by monitoring these specific changes:

$$\chi = \frac{I_{obs} - I_f}{I_b - I_f}$$

Equation 3.2

Where I_f is the emission of the free complex, I_b is the emission of the fully bound complex and I_{obs} is the emission at a given point. To determine the binding constant more accurately, it is important to ensure that saturation binding has occurred. Using this information, a binding curve can be created if χ is plot against the mixing ratio, R ([DNA]/[Drug]) (*Figure 3.3*).[13]

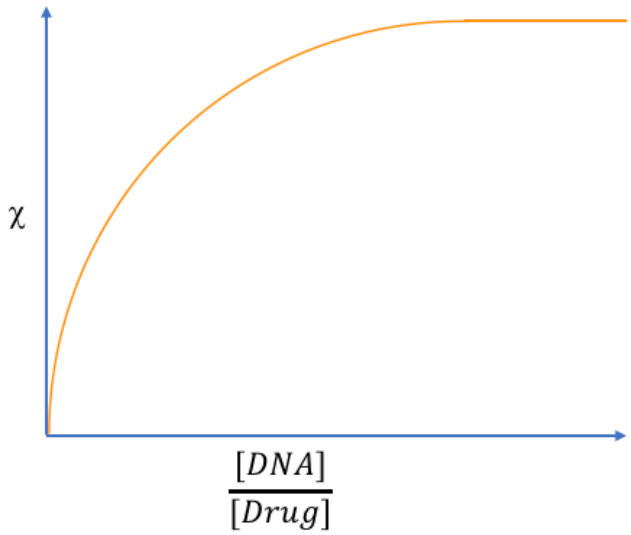

Figure 3.3: Example of a binding curve to show saturation binding.

The concentration of bound complex (C_b) can then be calculated by knowing the initial concentration of complex (C_i) and the fraction bound (χ):

$$C_b = \chi \, . \, C_i$$

Equation 3.3

C_f is the concentration of free complex[7]:

$$C_i = C_f + C_b$$

Equation 3.4

Rearranging to make C_f the subject gives the following equation:

$$C_f = C_i - C_b$$

Equation 3.5

The binding ratio can then be calculated, as the concentrations of bound and free drug at any given time can be found:

$$r = \frac{C_b}{[DNA]}$$

Equation 3.6

Primary data like this is often used to construct a Scatchard plot, in which the degree of binding saturation versus the free ligand concentration is produced by plotting r/C_f vs. r. In this plot, the slope yields the intrinsic equilibrium binding constant K_i and the intercept gives a value for the number of ligand binding sites, n:[14,15]

$$\frac{r}{C_f} = K_i(n - r)$$

Equation 3.7

The Scatchard equation is a traditional method of analysing equilibrium ligand binding data. The equation is based on the assumptions that all ligands are identical, the activity (chemical, biological) will not be altered except by binding, and all sites of each set are discrete and equivalent.[16] In the case of DNA binding is slightly more complicated. Small molecules interacting with DNA can be divided into two classes characterised by "specific" and "non-specific" binding. The classical Scatchard model is for species showing specific binding, expressing an overwhelming affinity for one, or a very few, particular base sequences on certain DNA molecules, meaning that a simple Scatchard plot would only be valid if a ligand binds to one repeating unit of the lattice. When a ligand binds over an extended lattice site complications occur leading to an inaccurate Scatchard analysis of the system. For example, since DNA is an isotropic lattice most ligand binding sites overlap. Therefore, at any degree of binding saturation the number of free binding sites depends not only on the number of ligands already bound, but the distribution of these bound ligands on the lattice. When this type of binding occurs, instead of a linear Scatchard plot, a curvature arises. Therefore, due to the overlap of potential binding sites, binding data and parameters cannot be treated in a linear fashion. Quantitative analysis of such data can be performed by nonlinear least squares fitting to the simple neighbour exclusion model of McGhee and von Hippel (Equation 3.5).[17,18]

$$\frac{r}{C_f} = K(1 - nr).\left[\frac{(1 - nr)}{1 - (n - 1)r}\right]^{n-1}$$

Equation 3.8

This equation was derived assuming an infinite lattice, however real macromolecules are not infinite and end effects will arise. To minimize the error associated with this effect, experimental data between 30-90% bound drug is usually fitted.[19]

3.2.3 Gel Electrophoresis

Upon binding, transition metal complexes can undergo chemical reactions at the binding site. Commonly, photo-induced DNA cleavage can occur when redox reactions involving the generation of reactive oxygen species, ROS occur. Gel electrophoresis can be used to measure any DNA damage caused by ROS generation as these species can lead to damage, cleavage or scission. Gel electrophoresis is the most effective analytical technique to separate DNA fragments from varying sizes from 100 bp to 25 kb.[20] Agarose gel is a polysaccharide isolated from seaweed consisting of repeating agarobiose (L- and D-galactose) subunits. The gelation process forms cross links within the polymer, which determine the pore size characteristicS of the gels molecular sieving properties. Under physiological conditions, phosphate groups in the phospho-sugar backbone of DNA are negatively ionised forming a large polyanion; therefore, when DNA is loaded into pre-cast wells within the gel, and placed in an electric field, these polyanions will migrate to the positive electrode (anode) (*Figure 3.4*). The electrophoretic migration rate of DNA through agarose gels depends on the following parameters; size of the DNA molecules, concentration of the agarose gel, voltage applied, conformation of the DNA, and the buffer used for the electrophoresis.[21] DNA has a uniform mass/charge ratio, meaning that when DNA sequences migrate through the agarose gel they will be separated by size (smaller fragments travelling quicker and further than larger species in the agarose gel when the electric field is applied).[22]

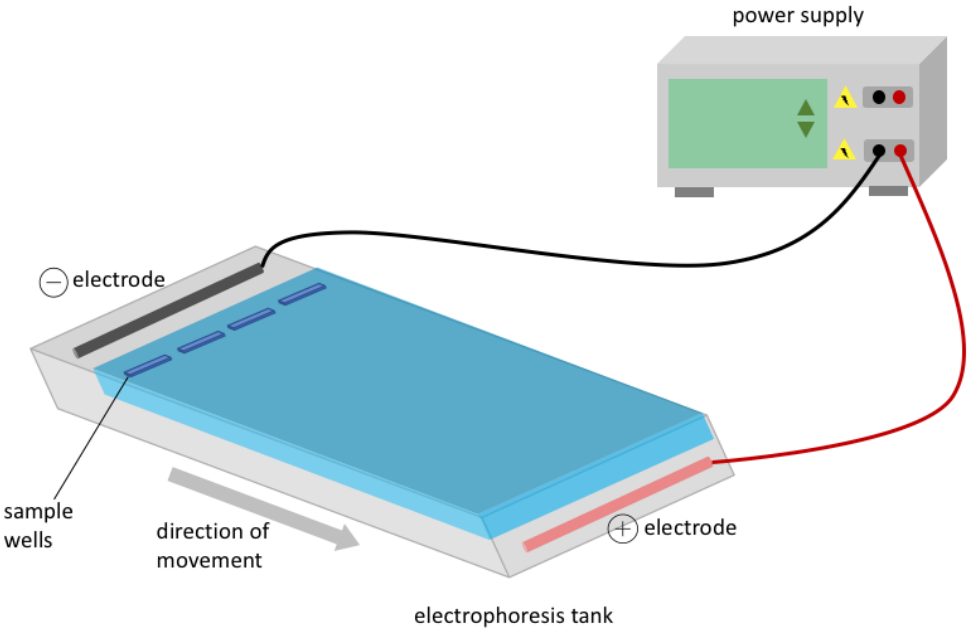

Figure 3.4: Schematic of the equipment set up for DNA gel electrophoresis. A gel sits within a tank of buffer, DNA samples are placed in wells at one end of the gel and an electrical current is passed across the gel. The negatively charged DNA migrates towards the positive electrode and can be separated by size.

3.2.4 Atomic Force Microscopy

Atomic force microscopy (AFM) has three main functions; force measurement, imaging and manipulation. It is a microscopy technique that uses a sharp probe to trace a sample surface at nanometre-resolution. One of the great benefits of AFM is its ability to measure at multiple spatial scales with excellent resolutions. Combining AFM with optical microscopy creates a powerful tool, exploiting capabilities to image live processes with chemical specificity. For biological applications, its key advantage is its ability to visualise substructure of single molecules and molecular processes in aqueous physiological environments.[23] This near-atomic resolution is useful for imaging the structure and conformational changes of nucleic acids such as supercoiled, kinked and looped DNA.[24] As biological molecules are usually delicate and soft, it is a great challenge to image such samples without damage, therefore a gentle tapping mode approach has to be taken. In tapping mode, the probe-sample separation is modulated as the probe scans, minimising frictional forces present when the probe is constantly in contact with the surface (*Figure 3.5*), thus increasing resolution and reducing sample damage.[25] Tapping mode AFM can be used to investigate DNA binding modes. Elongation of the phosphate backbone can be monitored through AFM by measuring the contour length before

and after complex incubation, so this technique provides a method to directly image. [26]

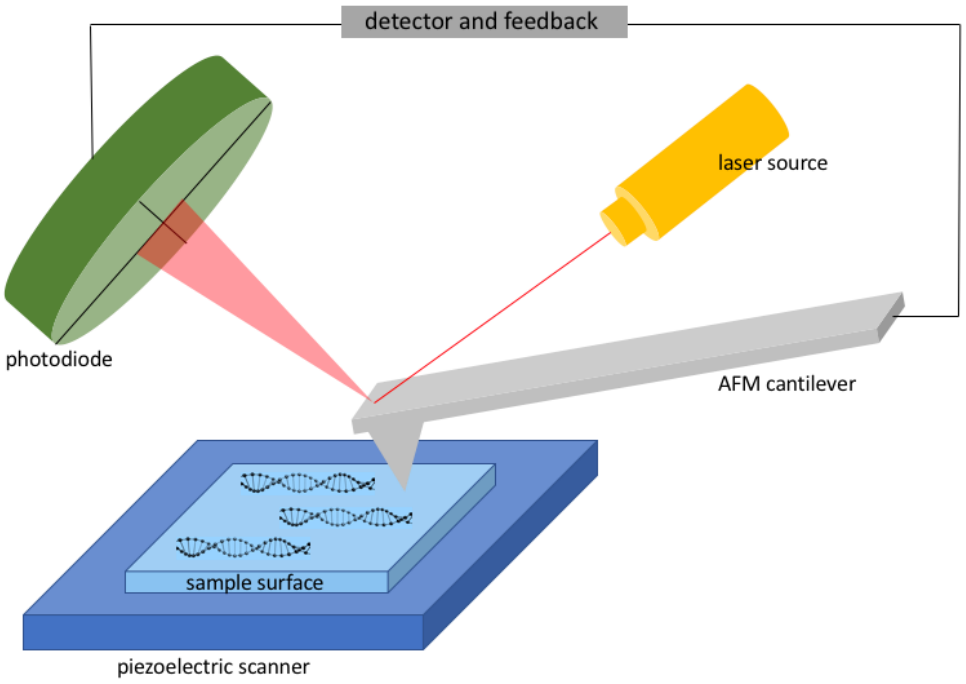

Figure 3.5: Typical AFM schematic for surface imaging of DNA persistance length in tapping mode.

3.3 DNA binding studies of iridium complexes

The following studies formed the basis of the paper: "S. Stimpson *et al*, Tuning the excited state of water-soluble Ir^{III}-based DNA intercalators that are isostructural with $[Ru^{II}(NN)_2(dppz)]$ light-switch complexes, *Angew. Chem.*, 2015, **127**, 3043-3046"

3.3.1 Viscosity

Viscosity studies were carried out with Ethidium bromide and Hoechst 33258 as controls. Ethidium bromide is a known intercalator, which causes an increase in viscosity, whilst Hoechst 33258 is a groove binder that does not increase viscosity of DNA solutions (*Figure 3.6*). [27,28]

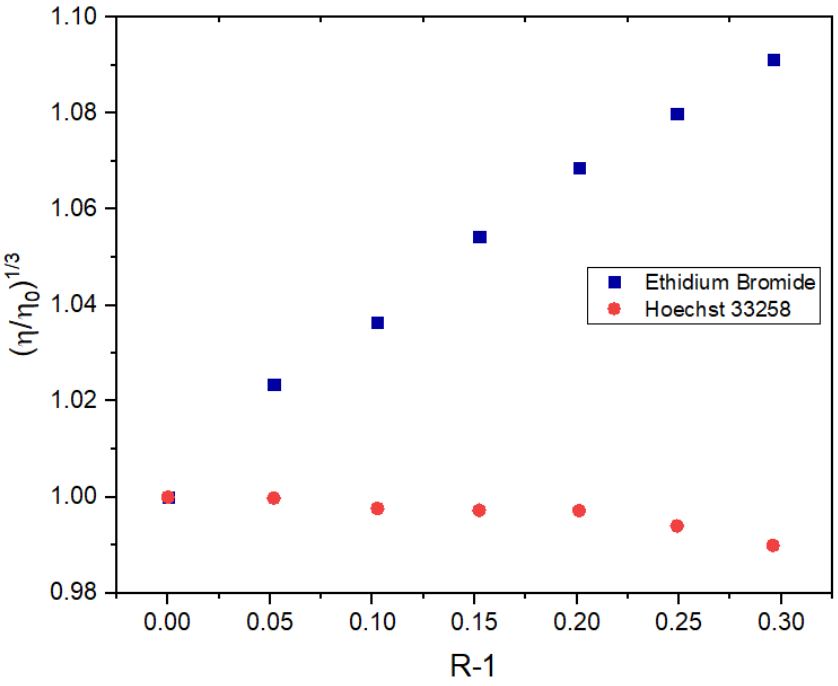

Figure 3.6: A plot of relative viscosity $(\eta/\eta_0)^{1/3}$ of CT-DNA versus R. (R = ([DNA]/[Ligand])$^{-1}$ upon addition of Ethidium Bromide (■) and Hoechst 33258 (●). Experimental conditions in all cases: 5mM Tris, 25 mM NaCl, pH 7.4 at 27 ℃.

3.3.2 Viscosity studies of Ir-dppz complexes effect on DNA

The relative viscosities of the complexes $[Ir(bpy)_2(dppz)]^{3+}$ **1**, $[Ir(phen)_2(dppz)]^{3+}$ **2**, and $[Ir(phen)_2(C^N\ dppz)]^{2+}$ **3** with CT-DNA are shown below (*Figure 3.7).*

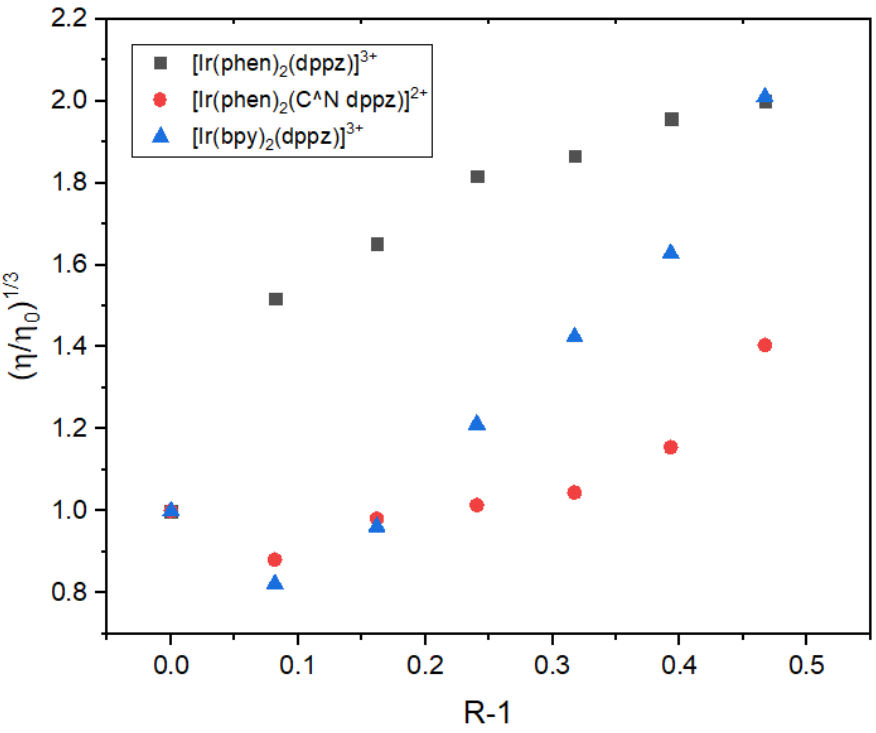

*Figure 3.7: A plot of relative viscosity $(\eta/\eta_0)^{1/3}$ of CT-DNA versus R. (R = ([DNA]/[complex])$^{-1}$ upon addition of **1** (▲), **2** (■), and **3** (●). Experimental conditions: 5 mM Tris, 25 mM NaCl, pH 7.4 at 27 ℃.*

All three complexes show a positive increase in relative specific viscosity, changes that are indicative of intercalative binding. Both complexes **1** and **2** possess a +3 charge and induce a larger relative viscosity change compared to dicationic **3.** It seems, because the electrostatic contribution to association with the polyanionic backbone of DNA for the tricationic complexes is higher than the dication, the higher charged complexes associate with the DNA more closely.[29] Of the tricationic species, the complex with the largest increase in relative viscosity has larger phenanthroline ancillary ligands. Complexes **1** and **3** initially induce a negative charge in relative viscosity, suggesting that, at low complex loading, non-intercalative interactions are occurring, a phenomenon that has been observed before for ruthenium(II) based systems.[30] An initial surface interaction is observed followed by the classical intercalative mode at higher complex concentrations.[31]

3.3.3 Luminescence titrations

Having established that all three complexes do interact with DNA through intercalation, their binding properties were further parameterised through luminescent titrations. Considerable attention has been given to ruthenium(II) complexes which contain the dipyridophenazaine ligand.[12,31–34] As mentioned previously, compared to the parent phenanthroline unit, this ligand has an extended aromatic surface area, driving intercalative interactions with DNA resulting in the light-switch effect. The iridium complexes in this study all contain the intercalating units dppz or the cyclometallated dppz analogue so it was of great interest to investigate their luminescent behaviour upon DNA binding. In this context, the interactions of complexes **1-3** with double stranded CT-DNA were investigated using emission titrations.

3.3.3.1 $[Ir(bpy)_2(dppz)]^{3+}$ Luminescence studies

Complex, **1** was excited at 390 nm and the variation in its structured band at ~ 475 nm on incremental additions of CT-DNA was recorded. In contrast to the isostructural Ru^{II}(dppz) analogues, **1** is emissive in water and addition of DNA produces a substantial reduction in steady state luminescence (*Figure 3.8).*

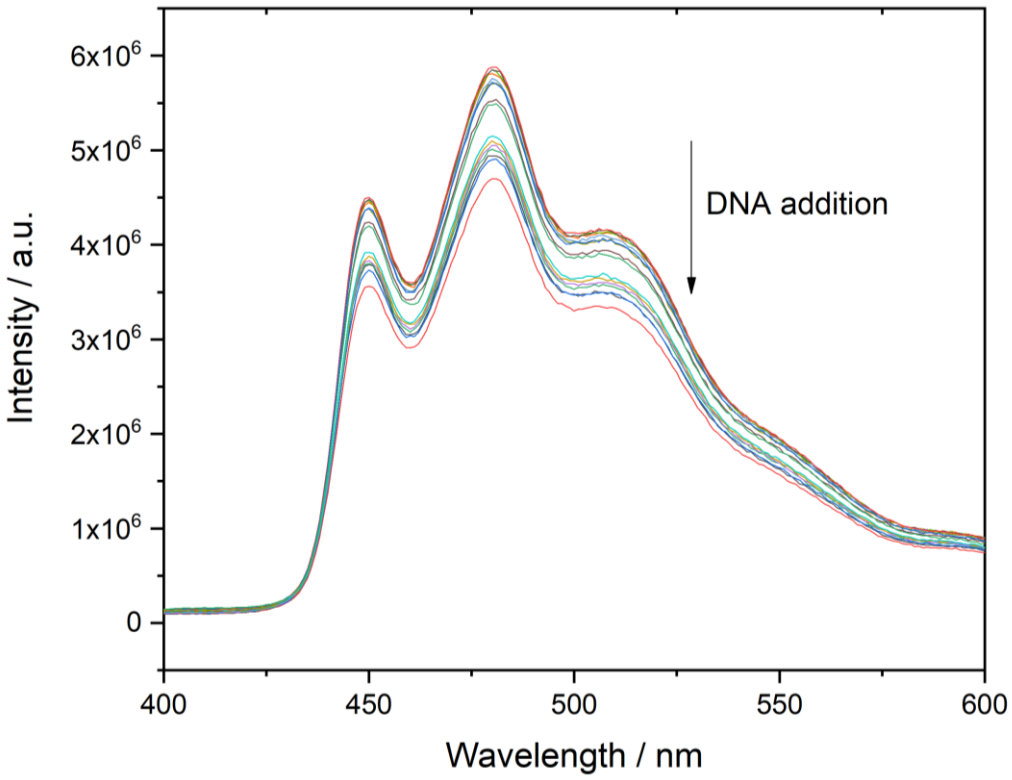

Figure 3.8: Luminescent titration of 16.4 mM CT-DNA into a solution of 59 μM of $[Ir(bpy)_2(dppz)]^{3+}$ in 5 mM tris buffer, 25 mM NaCl, pH 7.4, at 27 ℃.

The maximum emission wavelength (λ_{max}) is 480 nm giving a 5 nm hyperchromic blue shift in luminescence. The DNA-induced emission decrease is ≈ 19%. The non-linear Scatchard plot can be fitted to the commonly employed McGhee Von Hippel for non-cooperative binding to produce binding parameters summarised in *Table 3.1*.

3.3.3.2 $[Ir(phen)_2(dppz)]^{3+}$ Luminescence studies

Similar to **1**, upon addition of CT-DNA in aqueous conditions, the luminescence of the MLCT of $[Ir(phen)_2(dppz)]^{3+}$ also decreases. The structured emission of **2** shows a maximum at 500 nm, which is blue shifted by 10 nm from the spectrum of the free complex. There is also an overall decrease of approximately 20% in luminescence with successive additions of CT-DNA (*Figure 3.9).*

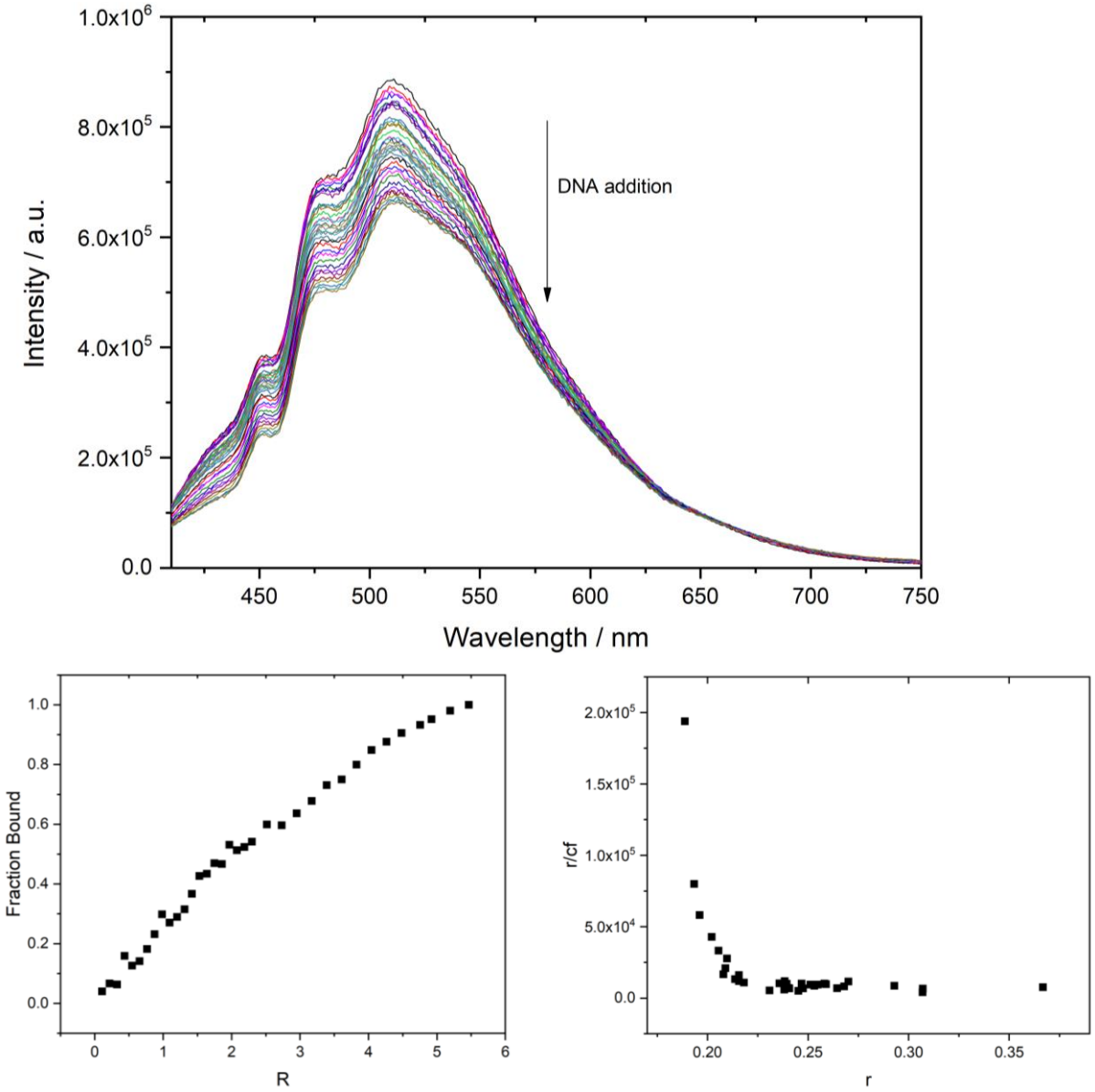

*Figure 3.9 : Top - Luminescent titration of 16.4 mM CT-DNA into a solution of 59 μM of $[Ir(phen)_2(dppz)]^{3+}$ in 5 mM tris buffer, 25 mM NaCl, pH 7.4, at 27℃. Bottom left – binding curve obtained from luminescent titrations of CT-DNA into **2**, where r = [DNA]/[complex]. Bottom right – non-linear Scatchard plots for the luminescent titrations.*

The titration data was fitted using the McGhee Von Hippel binding model to obtain the binding constant and number of sites associated with this interaction summarised in *Table 3.1.*

3.3.3.3 $[Ir(phen)_2(C^N\ dppz)]^{2+}$ Luminescence studies

Similar to the previous iridium complexes, the luminescence of **3** upon CT-DNA addition decreases substantially. The complex has a maximum emission of 521 nm, which displays a 7 nm hyperchromic blue shift upon addition of DNA. The DNA-induced emission decrease is much larger for **3** (~35%) compared to **1** and **2.** Binding saturation was achieved, and fits to the McGhee Von Hippel model, produced a binding constant and site size for the binding event (*Figure 3.10) (Table 3.1).*

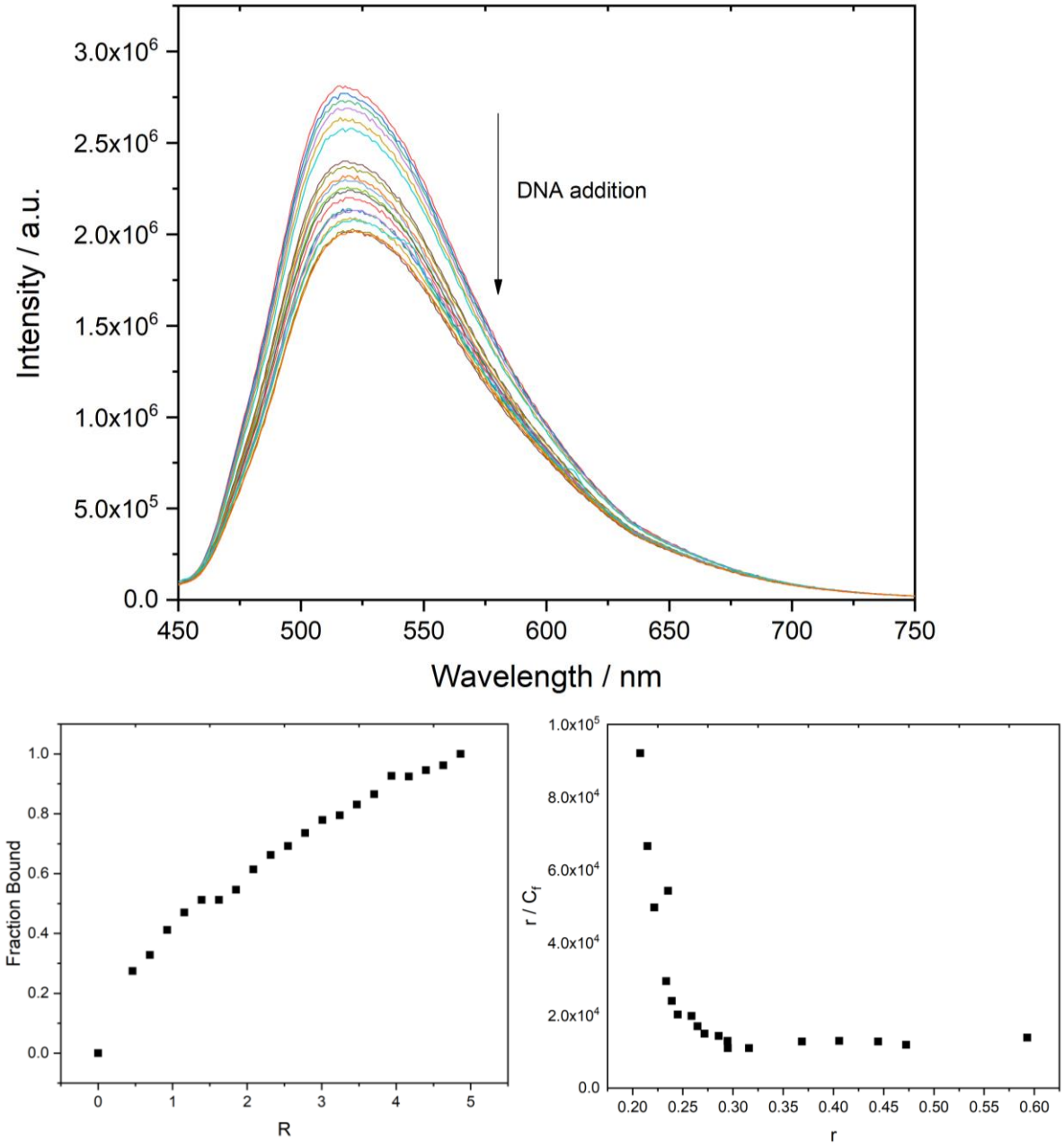

*Figure 3.10: Top - Luminescent titration of 16.4 mM CT-DNA into a solution of 59 μM of $[Ir(phen)_2(C^N\ dppz)]^{2+}$ in 5 mM tris buffer, 25 mM NaCl, pH 7.4, at 27°C. Bottom left – binding curve obtained from luminescent titrations of CT-DNA into **3**, where r = [DNA]/[complex]. Bottom right – non-linear Scatchard plots for the luminescent titrations.*

The table below displays the parameters obtained from the McGhee Von Hippel fits to the luminescence-based titration data.

Complex	λ_{max} (nm) (aqueous)	λ_{max} (nm) (CT-DNA)	Binding affinity, K_b [M^{-1}]	Site size, n, (base pairs)
$[Ir(bpy)_2(dppz)]^{3+}$	475	480	$1.8x10^6$	2.0
$[Ir(phen)_2(dppz)]^{3+}$	500	505	$2.9x10^6$	4.1
$[Ir(phen)_2(C^N\ dppz)]^{2+}$	514	521	$2.7x10^6$	2.4

*Table 3.1: CT-DNA binding parameters for complexes **1-3** including emission λ_{max} values, and from a MVH fit of binding data, K_b and n.*

These results are consistent with the interplay of two contributing factors to DNA binding. All three complexes bind to DNA with affinities of similar magnitude. The decreased charge of complex **3** decreases electrostatic interactions of the complex with DNA. However, previous studies have shown that electrostatics are not necessarily a major contribution to the thermodynamics of the intercalative interaction, which is largely driven by hydrophobic and electronic effects. Intercalating molecules distort the DNA but show favourable net enthalpy values.[35] The favourable base pair stacking interactions lost upon intercalation are regained by the formation of base pair-drug stacking. Another significant observation is that the intrinsic binding constants determined for **1-3** are similar to that of $[Ru(bpy)_2(dppz)]^{2+}$ ($K_b = 4x10^6\ M^{-1}$), unlike previously reported Ir^{III}(dppz) systems which are usually two orders of magnitude smaller.[36] Similar to results in the literature, DNA induced changes in the emission spectra of **1-3** show sharp decreases in intensities.[37,38] The decrease in intensity of the high-energy luminescence of **1-3** on addition of DNA is particularly striking and is suggestive of redox quenching by nucleobase sites in DNA. All three complexes also produce singlet oxygen in high yields. The excited state of the metal complexes can interact with oxygen producing the energetically active singlet oxygen - this is through a process called triplet-triplet annihilation. The MLCT of the complexes produces a long-lived triplet excited state species, which can interact with triplet-state oxygen, producing highly reactive singlet oxygen. Singlet oxygen has a non-radical and electrophilic character meaning it can induce oxidative reactions with biological macromolecules.[39] This damage can occur within nucleic acids, by reactions with the nucleotide bases or phosphate backbone, which ultimately often leads to cleavage of DNA strands. Such cleavage has the potential to cause a substantial decrease in the luminescent behaviour of metallo-intercalators.[40,41]

3.3.3.4 Quenching of Ir emission by guanosine- 5'- monophosphate

Apart from the generation of ROS such as singlet oxygen, a second process can deactivate the excited state of DNA bound complex; the photo-induced redox reaction between the complex and nucleobases sites.[42] Chemists have used spectroscopic tools to monitor these photoinduced electron transfer reactions which may be mediated by the π-stacked array formed by the aromatic overlap of the intercalated ligand and the DNA base pairs.[43] The DNA helix contains a π-stacked collection of heterocyclic bases and it has been hypothesised for some time that this could be a medium for the migration of charge over considerable molecular distances, serving as a molecular wire.[44] The oxidation potentials for guanine, adenine, cytosine, and thymine are 1,29, 1.42, 1.6, 1.7 V respectfully, indicating that guanine is the most easily oxidised constituent of the polynucleotide chain of DNA and thus these bases are usually the ultimate sites of redox damage.[45] Generally speaking redox quenching can occur during the excited state of a complex by collisions, or by the formation of complexes in the ground state leading to two types of quenching; dynamic (collision) and static (complex forming). Due to the oxidation potentials discussed above, within DNA this phenomena is observed primarily at guanine (G) out of all the nucleotide bases as it is the most easily oxidised.[46] Thus, the guanine base is oxidised and the metal complex is simultaneously reduced. Information about emission lifetime and excited state deactivation by introducing quenchers and their rates can be investigated using Stern-Volmer kinetics. In this description; k_f, is the rate of emission, k_{nr} rate of non-radiative processes, and k_q the rate of quenching where M* is an excited molecule:

$$\frac{\partial[M^*]}{\partial t} = I_{abs} - (k_f + k_{nf} + k_q[Q])[M^*]$$

Equation 3.6

An important quantity for the determination of different reaction rate constants is the emission quantum yield ϕ:

$$\phi = \frac{number\ of\ emitted\ photons}{number\ of\ absorbed\ photons} = \frac{rate\ of\ emission}{rate\ of\ absorption}$$

Equation 3.7

The ratio of the quantum yield is equal to the ratio of observed emission intensities and lifetimes with and without the quencher molecules. This produces the final result also known as the Stern-Volmer equation producing a graph where the rate of quenching can be calculated from (*Figure 3.11)*:

$$\frac{\phi_0}{\phi} = \frac{I_0}{I} = \frac{\tau_0}{\tau} = 1 + k_q\,\tau_0[Q]$$

Equation 3.8

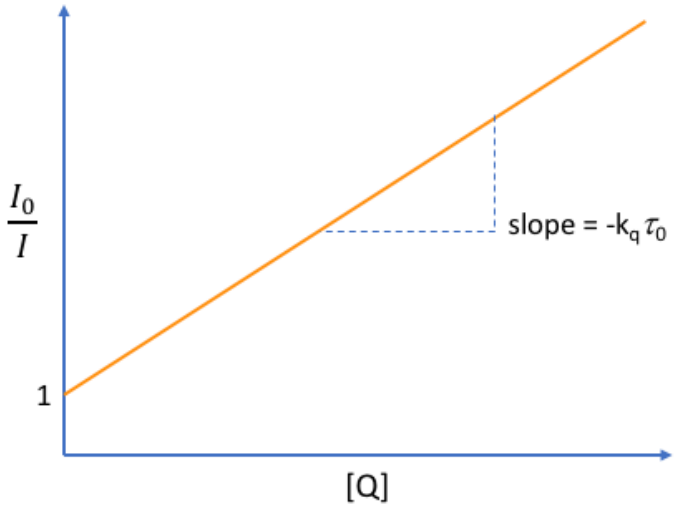

Figure 3.11: Schematic of a Stern-Volmer plot used to calculate the rate of quenching.

The quenching of the excited state of iridium complexes by photoredox processes can be monitored by addition of guanine monophosphate (GMP) using these Stern-Volmer relationships. Therefore, the emission profiles of aqueous solutions of **1-3** upon successive additions of GMP were monitored. As the luminescence of each of the complexes decreases upon addition of CT-DNA, it is assumed that the high-energy MLCT excited states of all the complexes are capable of photo-oxidising guanine. As **1-3** strongly luminesce in water, without possessing light-switch behaviour, it is possible that a photo-induced proton-coupled electron transfer can occur with GMP. In the following section the analysis of the photochemistry of **1-3** is presented.

3.3.3.3.5 $[Ir(bpy)_2(dppz)]^{3+}$ - Quenching by guanosine -5'-monophosphate

The emission of **1** in aqueous solution is quenched by guanosine monophosphate. The luminescence quenching rate constant, determined by the measurement of emission intensities with various GMP concentrations in air-saturated solutions at room temperature in water, using Stern-Volmer kinetics was calculated as 1.25 $x10^{10}$ $dm^3mol^{-1}s^{-1}$ (*Figure 3.12).* This figure indicates **1** is quenched by GMP at an order of magnitude higher rate compared to Ru^{II} analogues; for example, $[Ru(TAP)_2(dppz)]^{2+}$ possesses a GMP quenching rate of $kq = 1.7 \times 10^9$ $dm^3mol^{-1}s^{-1}$.[47,48] This data suggest that the complex is a potent photo-oxidising agent.

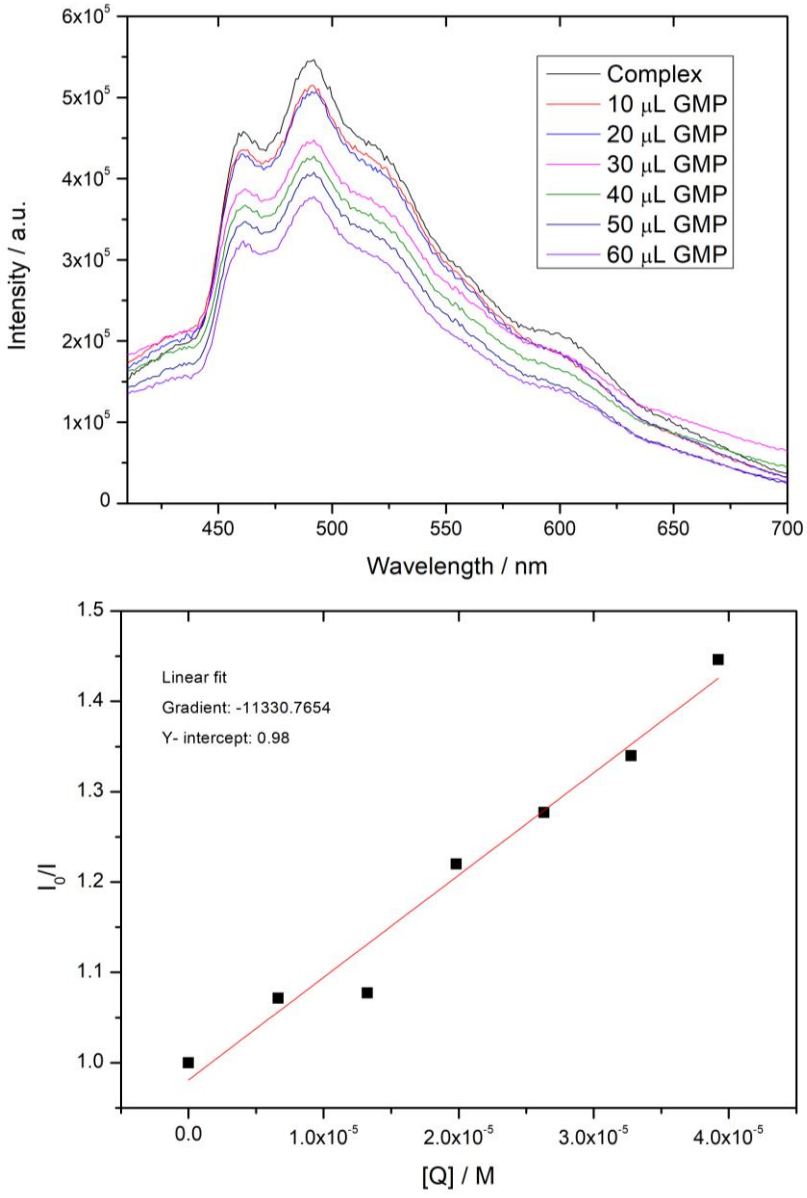

*Figure 3.12: Top - Emission intensity of 50μM $[Ir(phen)_2(dppz)]^{3+}$ upon successive addition ofs 2 mM guanosine monophosphate. Bottom - A Stern-Volmer plot of the integrated intensity of **1** versus concentration of quencher to determine the quenching rate.*

3.3.3.3.6 $[Ir(phen)_2(dppz)]^{3+}$ - Quenching by guanosine -5'-monophosphate

Similar to **1**, upon addition of GMP the emission intensity of **2** decreases, in air saturated solutions at room temperature. Using Stern-Volmer kinetics the rate of quenching was calculated to be 2.78 $x10^{10}$ $dm^3mol^{-1}s^{-1}$ (*Figure 3.13).*

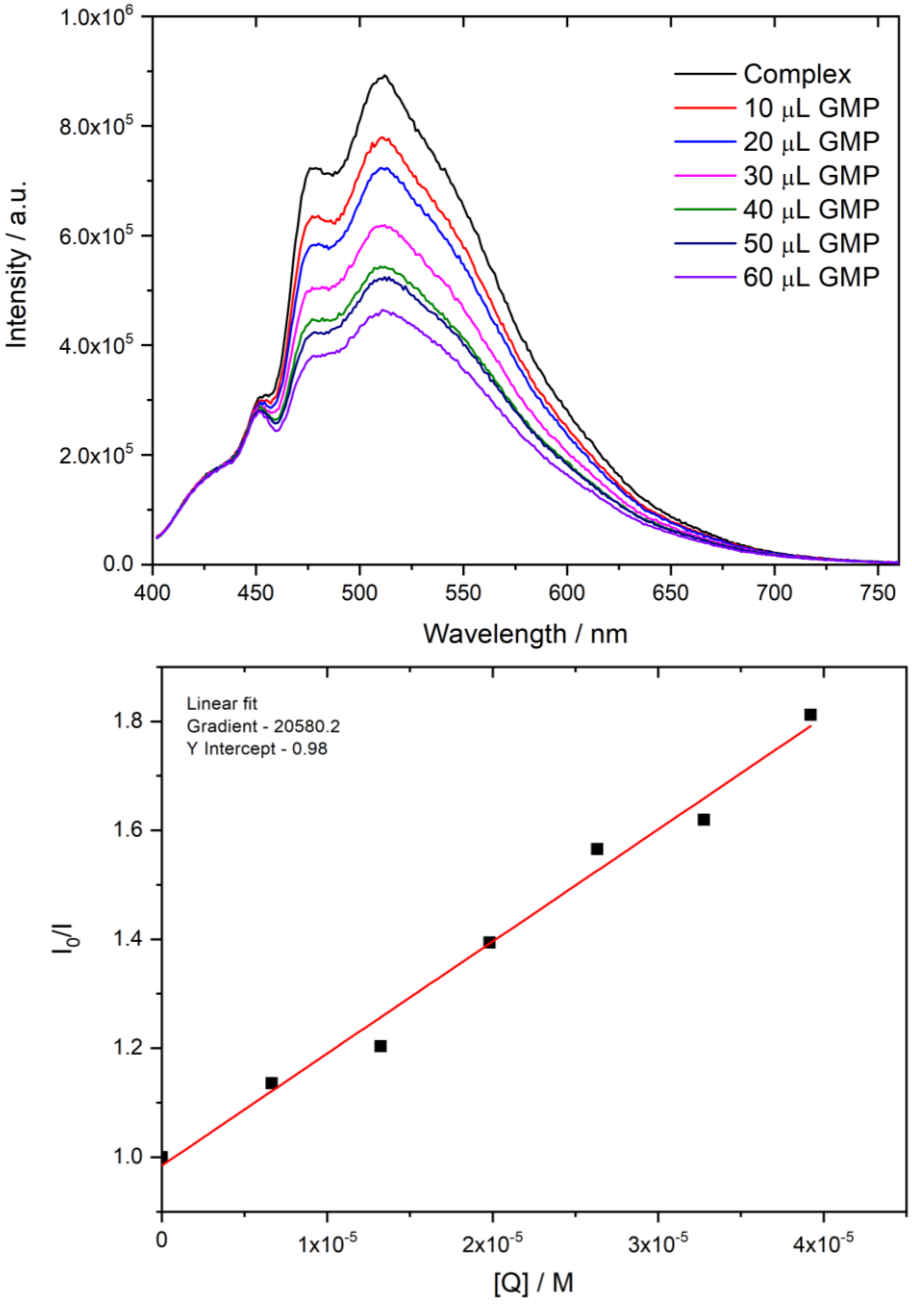

*Figure 3.13: Left - Emission intensity of 50µM $[Ir(phen)_2(dppz)]^{3+}$ upon successive addition of 2 mM guanosine monophosphate. Right - A Stern-Volmer plot of the integrated intensity of **2** versus concentration of quencher to determine the quenching rate.*

3.3.3.7 $[Ir(phen)_2(C^Ndppz)]^{2+}$ - Quenching by guanosine-5'monophosphate

The emission of **3** was quenched upon addition of increasing concentrations of GMP, in air-saturated solutions at room temperature. Using Stern-Volmer kinetics the quenching rate constant was calculated to be 7.62 x10^9 $dm^3mol^{-1}s^{-1}$ (*Figure 3.14).*

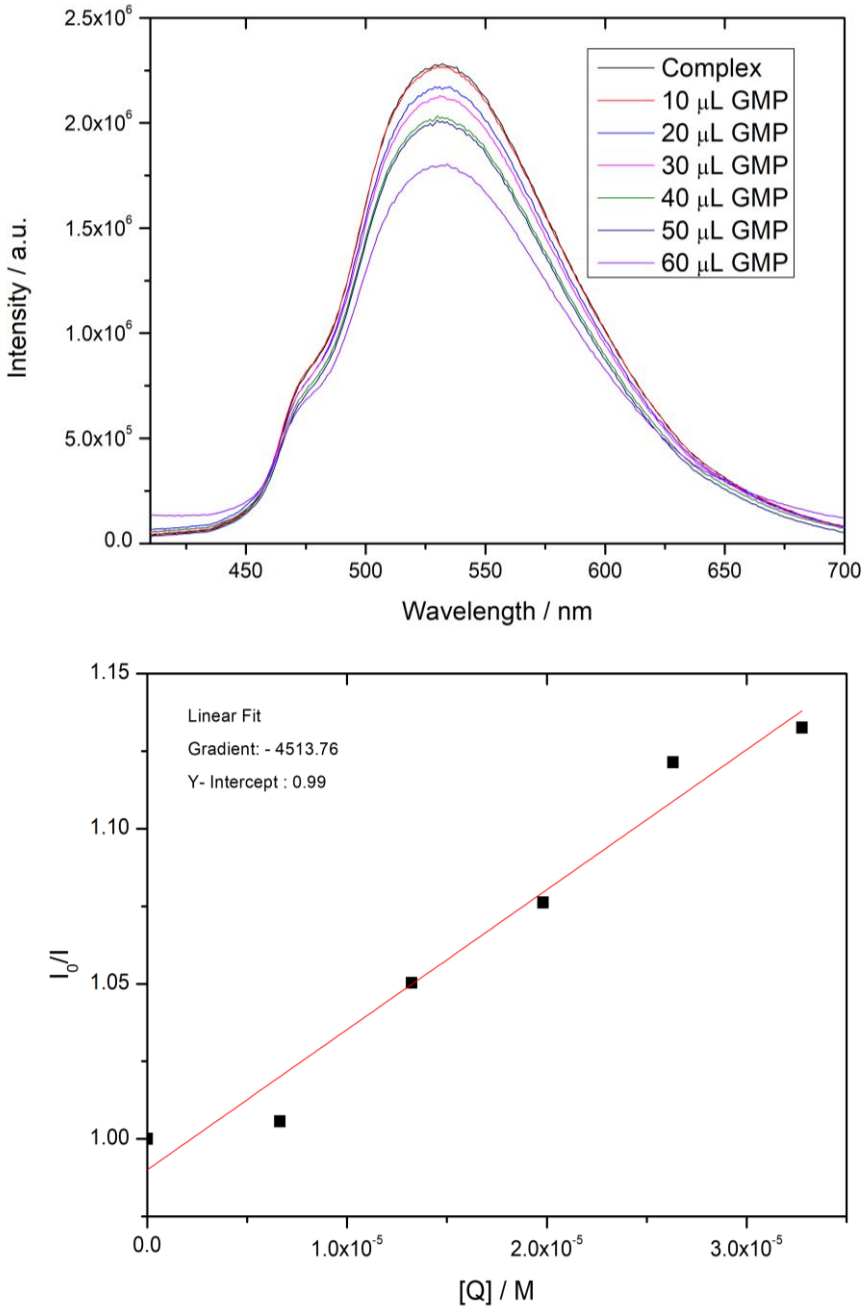

*Figure 3.14: Top - Emission intensity of 50μM $[Ir(phen)_2(dppz)]^{3+}$ upon successive addition of 2 mM guanosine monophosphate. Bottom - A Stern-Volmer plot of the integrated intensity of **3** versus concentration of quencher to determine the quenching rate.*

The emission intensities of all three complexes decrease with successive additions of guanosine monophosphate. **1** and **2** have the largest quenching constants, of 1.25 $x10^{10}$ $dm^3mol^{-1}s^{-1}$ and 2.78 $x10^{10}$ $dm^3mol^{-1}s^{-1}$ respectively, and **3** has a quenching constant that is almost a third lower than the highest rate (7.62 $x10^9$ $dm^3mol^{-1}s^{-1}$). All these values are higher than similar ruthenium analogues, indicating that all three are potent photo-oxidizing agents. The reason that the GMP quenching rate for **3** is slightly smaller than **1** and **2** could be due to differences in electronic distribution in the excited states. DFT calculations show that for **1** and **2**, the electronic distribution on the triplet state is localised on the intercalating dppz unit, whereas for **3** the electron density of the triplet state is shifted onto the ancillary phenanthroline units (*Figure 3.15).* This re-assignment of electron density due to the incorporation of a cyclometallating dppz species could be the cause of the change in the quenching constants. As these are all intercalating species, as determined by viscosity experiments, if the excited state is localised on the dppz unit then excited state photo-redox processes may happen more readily if – as seems likely - the GMP stacks onto this ligand rather than the less extended ancillary ligand.

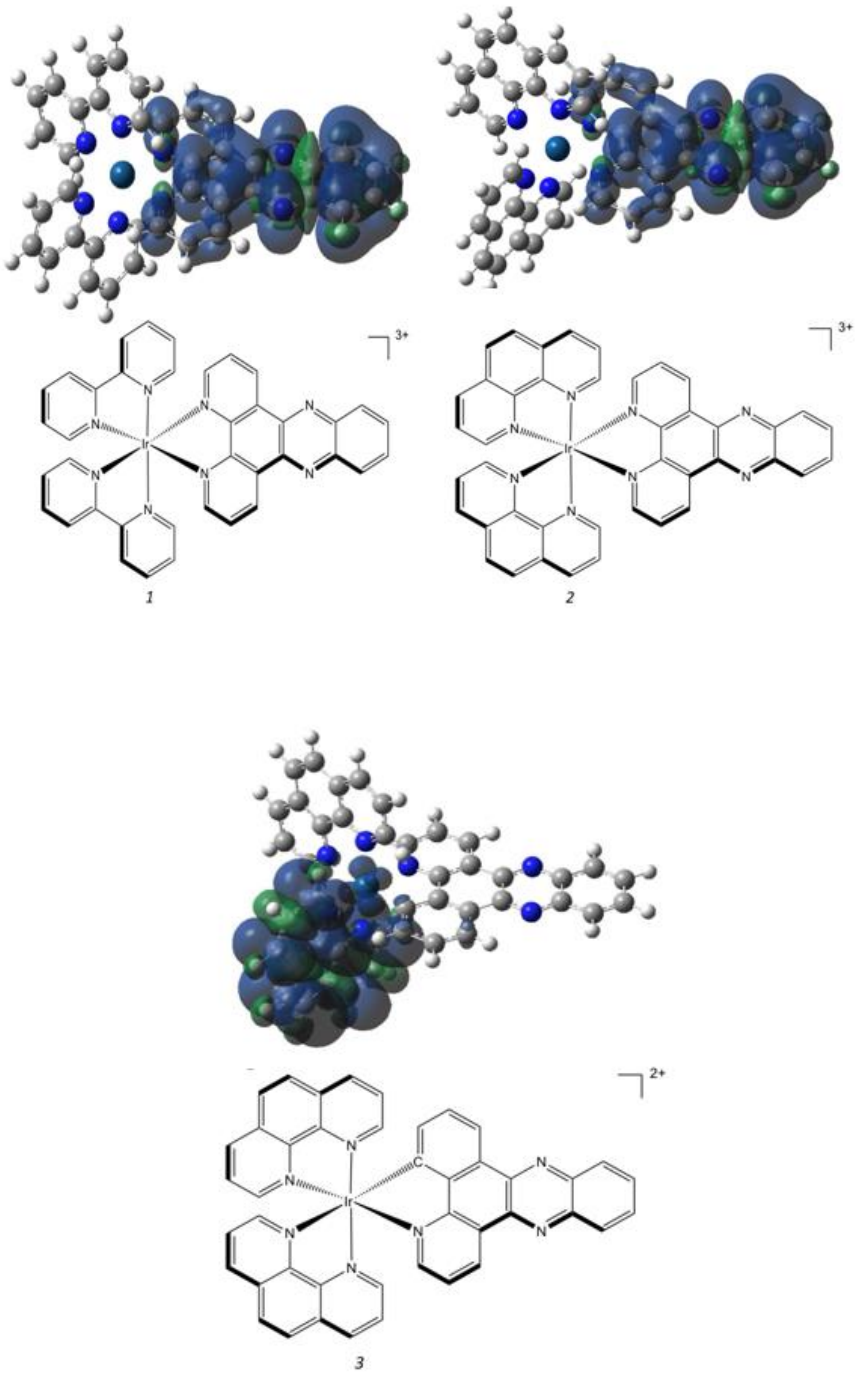

Figure 3.15: Spin-density plots for the T1 state of complexes 1-3. Atom sphere colors: C = gray; H = white; N = dark blue; Ir = lighter blue

3.3.4 Gel electrophoresis

There is substantial and continuing interest in DNA endonucleolytic cleavage reactions that are caused by metal-ions.[49–51] Agarose gel electrophoresis is the most commonly used method for the size-and shape -based separation of DNA molecules, including plasmid DNA. Besides their size, the electrophoretic mobility of the DNA fragments using this technique is significantly affected by their shape. Superhelically packed circular plasmid DNA has a very compact structure, this smaller hydrodynamic size results in an increased electrophoretic mobility in comparison to linear DNA. When one of the strands is cut, this leads to unravelling to adopt a much more relaxed circular form; an elastic band is a relevant analogy. Upon further scission, the plasmid DNA will adopt a linear confirmation. As this structure is not globular it can travel more quickly than the single strand break form through the agarose gel (*Figure 14).* The photonuclease activity of **1-3** were studied using supercoiled pBR322 in Tris-HCl/NaCl under illuminated conditions (365 nm, 125 mV, 10 minutes exposure) (*Figure 3.16).*[52]

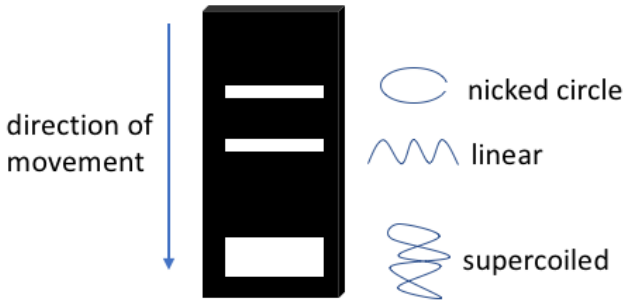

Figure 3.16: Schematic showing the different types of plasmid DNA produced after photocleavage and how they separate using gel electrophoresis.

3.3.4.1 $[Ir(bpy)_2(dppz)]^{3+}$ Gel electrophoresis studies

The photocleaving activity of $[Ir(bpy)_2(dppz)]^{3+}$, **1**, was monitored by agarose gel electrophoresis. In the figure below (*Figure 3.17)* moving right to left; lane 1 corresponds to untreated plasmid pBR322, lane 2 – 4 are plasmid DNA with increasing concentration of **1**. As the concentration of **1** increases the distance travelled through the gel by the DNA becomes less. There is evidence of photocleavage here; as the concentration of **1** increases the leading band on the gel disappears. The second band becomes increasingly bright in comparison. The drop in intensity/overall brightness suggests that the plasmid DNA is getting cleaved into faster

migrating sections. The photocleavage mechanism of **1** was investigated by running a follow-up gel with various promotors/inhibitors of various photochemical processes such as singlet oxygen production, hydroxyl-radical formation, and electron transfer (*Figure 18).*[53–56]

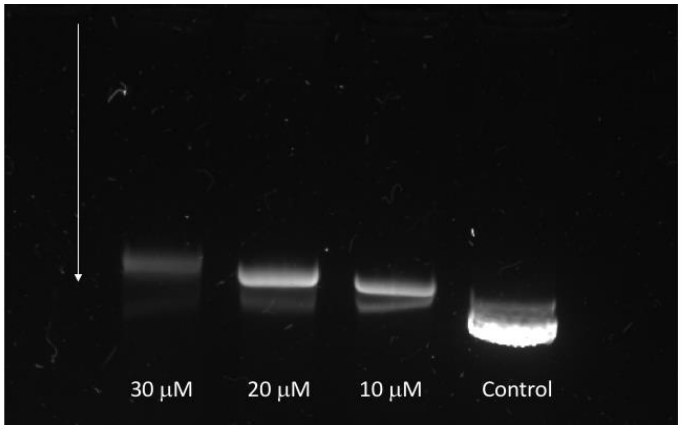

*Figure 3.17: Photocleavage of supercoiled pBR322 DNA by $[Ir(bpy)_2(dppz)]^{3+}$, **1**, + in illuminated conditions (365 nm, 126 mV, 10 minutes exposure) in 50 mM Tris-HCl buffer. (Right to left) Lane 1 DNA control; Lane 2 DNA + complex (10 μM); lane 3 DNA + complex (20 μM); lane 4 DNA + complex (30 μM). Gel ran at 100 mV for 25 minutes.*

As can be seen from *Figure 3.18* below there is no significant cleavage in the dark, this confirms that light is necessary for nuclease activity The plasmid DNA migrates at a slower pace through the agarose gel when irradiated in the presence of various inhibitors. The most photocleavage activity occurs in lane 3, in the presence of D_2O, a species that potentiates the activity of singlet oxygen due to an increased lifetime. This effect is only slight and does not rule out the possibility of photocleavage by other means of other reactive oxygen species, however **1** has a singlet oxygen quantum yield of 48% which would be consistent with ROS cleavage.

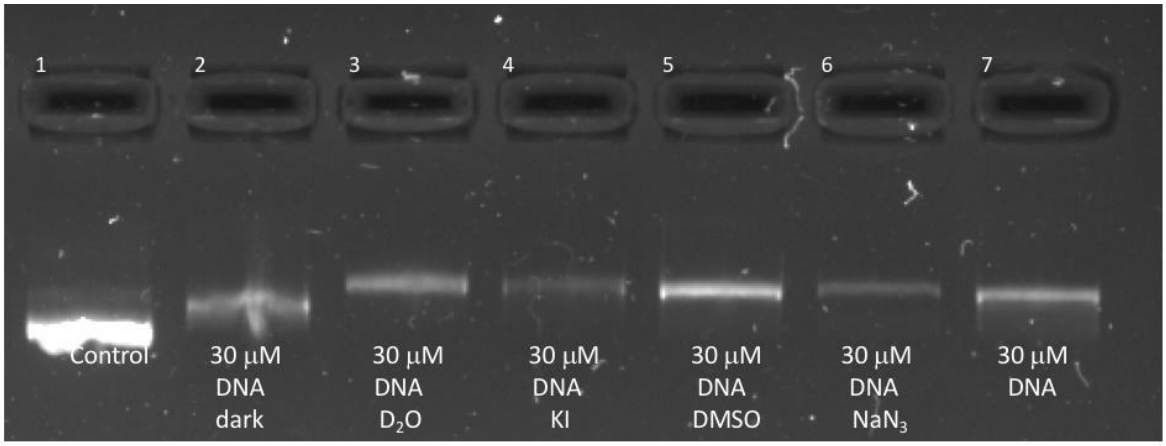

*Figure 3.18: Photocleavage of supercoiled pBR322 (3μg) and $[Ir(bpy))_2(dppz)]^{3+}$ **1** under illuminated conditions 365 nm, 126 mV, 10 minutes exposure) in 50 mM Tris-HCl buffer. Lane 1, DNA control; lane 2, DNA + complex (30 μM) in the dark; lane 3, DNA + complex (30 μM) + D_2O; lane 4, DNA + complex (30 μM) + KI; lane 5, DNA + complex (30 μM) + DMSO; lane 6, DNA + complex (30 μM) + NaN_3; lane 7, DNA + (30 μM). Gel ran for 40 minutes at 70 mV.*

3.3.4.2 $[Ir(phen)_2(dppz)]^{3+}$ Gel electrophoresis studies

The photocleaving activity of $[Ir(phen)_2(dppz)]^{3+}$, **2**, was monitored by agarose gel electrophoresis (*Figure 3.19).*

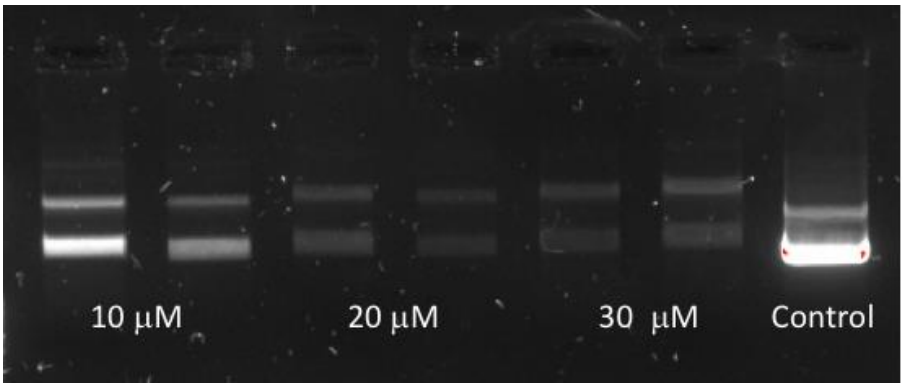

*Figure 3.19: Photocleavage of supercoiled pBR322 DNA by $[Ir(phen)_2(dppz)]^{3+}$, **2**, in illuminated conditions (365 nm, 126 mV, 10 minutes exposure) in 50 mM Tris-HCl buffer. (Left to right) Lane 1-2 DNA + complex (10 μM); lane 2-3 DNA + complex (20 μM); lane 3-4 DNA + complex (30 μM); lane 5 DNA control lane. Gel ran at 100 mV for 20 minutes.*

The figure above shows the cleavage of plasmid DNA at different concentrations of complex. The increase in concentration causes an increase of cleavage of the DNA. The mechanism of photocleavage was explored through further experiments involving pBR322 and a range of different inhibitors (*Figure 3.20).*

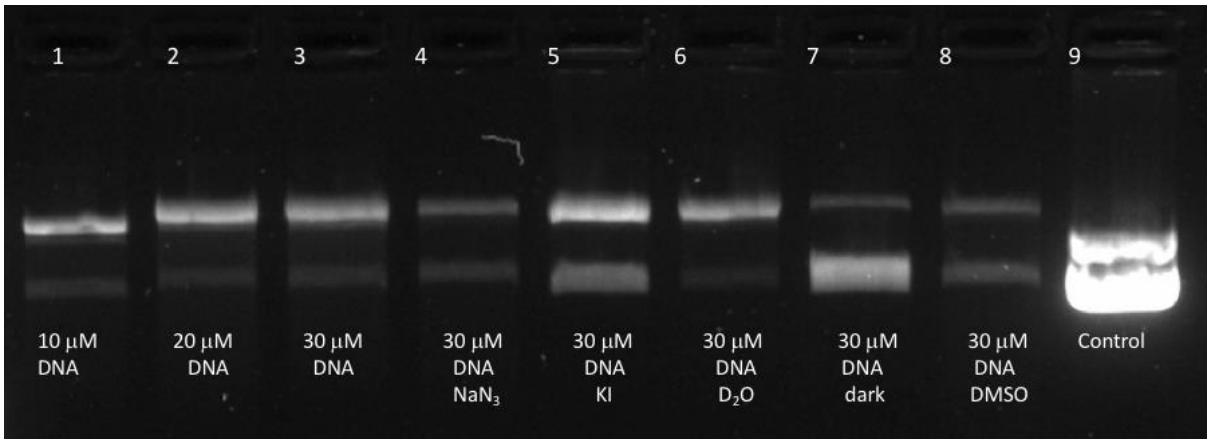

Figure 3.20: Photocleavage of supercoiled pBR322 (3μg) and $[Ir(phen)_2(dppz)]^{3+}$ under illuminated conditions 365 nm, 126 mV, 10 minutes exposure) in 50 mM Tris-HCl buffer. Lane 1 DNA + complex (10 μM); lane 2, DNA + complex (20 μM); Lane 3, DNA + complex (30 μM); lane 4 DNA + complex (30 μM) + NaN_3; lane 5 DNA + complex (30 μM) + KI; lane 6 DNA + complex (30 μM) + D_2O; lane 7 DNA + complex (30 μM) in the dark; lane 8 DNA + complex (30 μM) + DMSO; lane 9 DNA control. Gel ran at 40 mins at 70 mV.

There is no significant cleavage in the dark, this confirms that light is necessary for nuclease activity. Hydroxyl (OH^-) scavengers such as potassium iodide and DMSO do seem to inhibit plasmid cleavage, DMSO to a lesser extent but it is likely that OH^- radicals are involved in the cleavage here. Photoinduced cleavage was confirmed to be via the singlet oxygen radical by the experiments with sodium azide and D_2O. Sodium azide is an $^1O_2$ quencher and D_2O potentiates the activity of the radical due to an increased lifetime. The maximum photocleavage activity was monitored in D_2O and KI confirming that the mechanism of DNA damage is caused by both the reactive oxygen species OH^- and $^1O_2$. **2** was found to produce singlet oxygen in a high yield of 56%, matching these results.

3.3.4.3 $[Ir(phen)_2(C^N\ dppz)]^{2+}$ Gel electrophoresis studies

The photocleavage activity of $[Ir(phen)_2(dppz)]^{3+}$, **3**, was monitored by agarose gel electrophoresis (*Figure 3.21).*

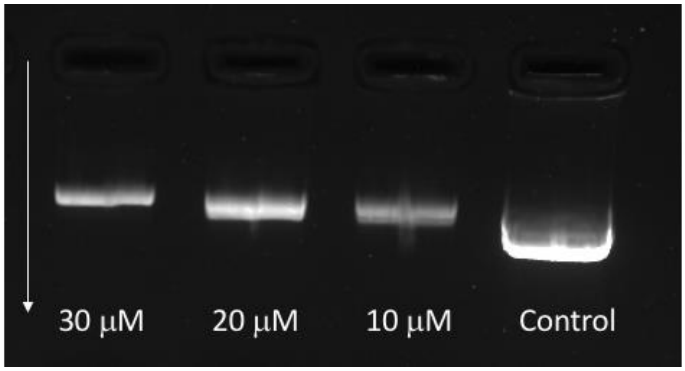

*Figure 3.21: Photocleavage of supercoiled pBR322 DNA by $[Ir(phen)_2(C^N\ dppz)]^{3+}$, **3**, + in illuminated conditions (365 nm, 126 mV, 10 minutes exposure) in 50 mM Tris-HCl buffer. (Right to left) Lane 1 DNA control; Lane 2 DNA + complex (10 μM); lane 3 DNA + complex (20 μM); lane 4 DNA + complex (30 μM). Gel ran at 100 mV for 25 minutes.*

From referring to the figure above there is no significant evidence of DNA cleavage here, and the effect observed is similar to one observed *via* a gel mobility shift assay.[57,58] An electrophoretic mobility shift assay is a technique used to study DNA-drug interactions. Complex **3** has been proven by viscosity and AFM experiments to intercalate within DNA. This effect increases the shape/size of the plasmid DNA, causing it to migrate slower/less in within the gel. As well as altering the size, intercalation of **1** would change the overall charge of the system, altering the field electric effect on the plasmid DNA. As the concentration increases of **3** this effect becomes greater as more intercalative interactions our occurring within the plasmid DNA. If there was cleavage occurring, nicked forms of the plasmid would be visible, in this case they are not present. To investigate further if any photocleavage activity is occurring, a second gel experiment was run incorporating a range of inhibitors and a control lane in the dark (*Figure 3.22).*

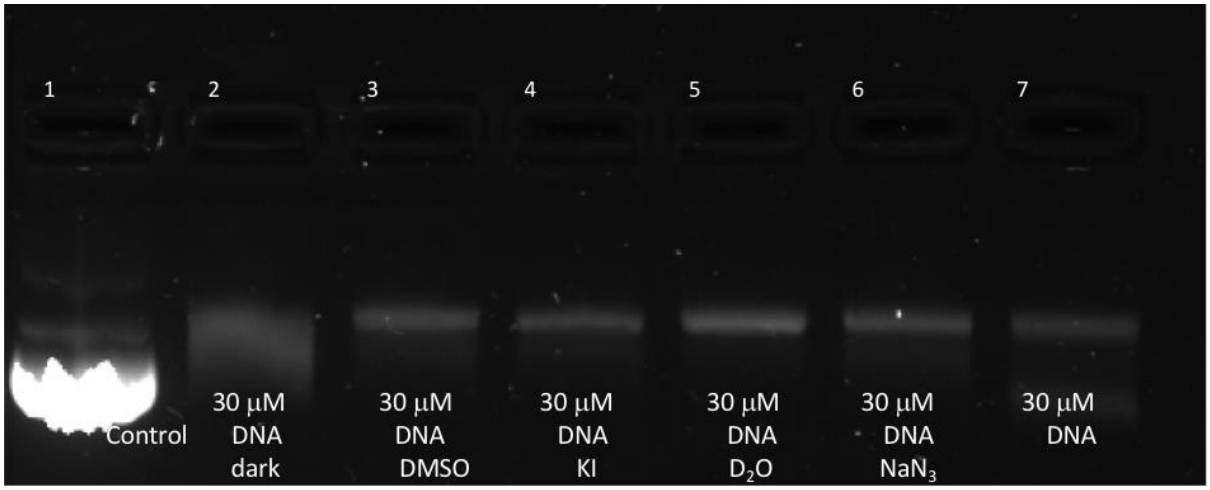

*Figure 3.22: Photocleavage of supercoiled pBR322 (3μg) and $[Ir(phen)_2(C^N\ dppz)]^{3+}$ **3** under illuminated conditions 365 nm, 126 mV, 10 minutes exposure) in 50 mM Tris-HCl buffer. Lane 1, DNA control; lane 2, DNA + complex (30 μM) in the dark; lane 3, DNA + complex (30 μM) + DMSO; lane 4, DNA + complex (30 μM) + KI; lane 5, DNA + complex (30 μM) + D_2O; lane 6, DNA + complex (30 μM) + NaN_3; lane 7, DNA + (30 μM). Gel ran for 40 minutes at 70 mV.*

The gel above shows no photocleavage for **3** and is therefore inconclusive. This experiment was repeated three times and the same result was obtained. Each of the lanes migrate at a similar rate with no formation of nicked or linear plasmid DNA (which is evidence of photocleavage). These results insinuate that the complex can directly damage guanine sites (due to previous quenching experiments with GMP) however does not cleave DNA *via* singlet oxygen generation like **1** and **2**. DFT calculations indicate that for complexes **1** and **2** the excited state is localised on the dppz unit, whereas for **3** the electron density is shifted onto the ancillary phenanthroline units. As the only real difference between the complexes is that the phenanthroline based excited state of **3** is not directly intercalated within the DNA, it seems this may be responsible for this striking observation, Although this does seem unlikely. Further experiments will need to be carried out to resolve this issue completely.

3.3.5 AFM Studies

AFM studies were carried out to measure the length of DNA in the presence of the iridium complexes to determine any intercalative binding modes. The DNA was synthesised by a polymerase chain reaction method to produce all lengths at 230 bp for clarity. The DNA contour length was measured using AFM tapping mode in the presence of **1-3** along with two known intercalators $[Ru(phen)_2(dppz)]^{2+}$ and $[Ru(phen)_2(dppn)]^{2+}$ (dppn = benzo[i]dipyrido[3,2-a:2',3'-c]phenazine) as a reference (*Figure 3.23) (Table 3.2).*

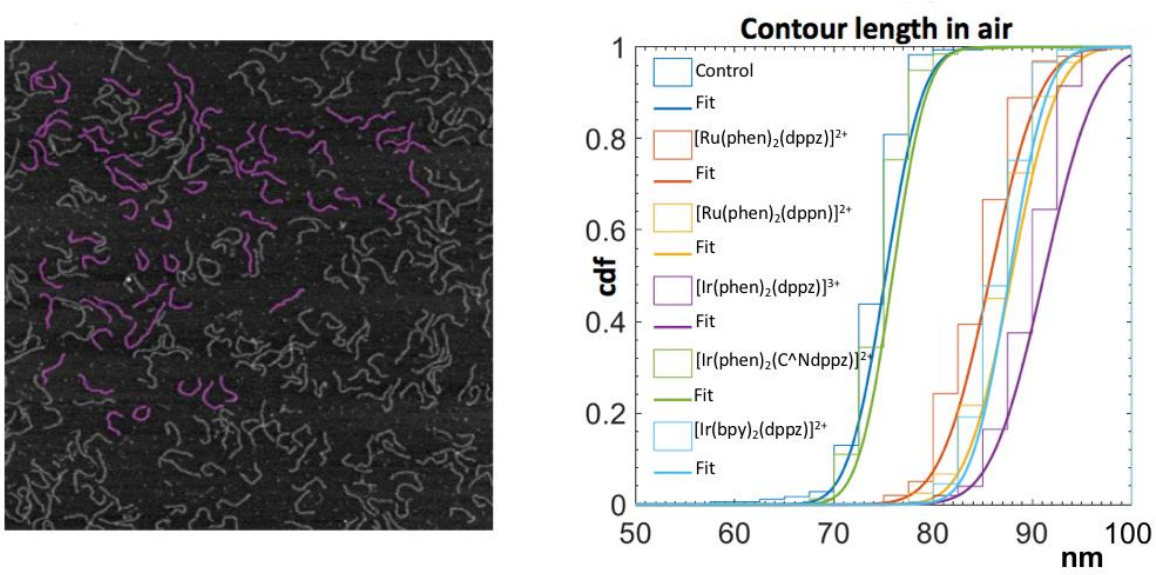

Figure 3.23: Left – AFM image produced highlighting the DNA strands incubated with $[Ir(phen)_2(dppz)]^{3+}$. Right – graph showing the changes in contour length after incubation with the various iridium and ruthenium complexes. Table below – showing the number of molecules the contour length was averaged over and the overall change.

Complex	DNA contour length (nm) (Number of Molecules)
Control	75.21 (178)
$[Ru(phen)_2(dppz)]^{2+}$	85.77 (99)
$[Ru(phen)_2(dppn)]^{2+}$	87.91 (120)
$[Ir(phen)_2(dppz)]^{3+}$	91.18 (155)
$[Ir(phen)_2(C^N\ dppz)]^{2+}$	75.90 (256)
$[Ir(bpy)_2(dppz)]^{3+}$	87.70 (178)

*Table 3.2: The contour length of CT-DNA after incubation with **1-3** and two known intercalators $[Ru(phen)_2(dppz)]^{2+}$ and $[Ru(phen)_2(dppn)]^{2+}$.*

In-air AFM can provide static snapshots of the reactions that involve DNA.[59] The results from the AFM are consistent with the previous viscosity results. The contour length of DNA is increased in the order $[Ir(phen)_2(dppz)]^{3+}$ > $[Ir(bpy)_2(dppz)]^{3+}$ > $[Ir(phen)_2(C\text{^}N\ dppz)]^{2+}$. The relative viscosities of the DNA/complex systems also behave in this manner and follow this trend. This provides further evidence for the hypothesis that overall charge is the primary driving force for the intercalation of the complexes, as opposed to the steric bulk of the ancillary ligands attached. Both controls have the same phenanthroline ancillary units however, one possesses an intercalating unit with one more ring on the phenazine. The AFM results show that the length of the planar aromatic section does not affect the intercalation rate drastically. Also agreeing with overall charge being the motivation behind the binding event.

3.3.6 Transient Absorption Spectroscopy

Transition metal complexes as we know, have been broadly used in photochemistry based on their versatility in light absorption, excited state redox properties as well as chemical tunability. A major goal in chemistry is to quantitatively probe chemical bonding dynamics at the molecular level. Recent advances in experimental ultra-fast spectroscopy provide methods to probe excited electronic and nuclear structures, and photophysical relaxation processes of metal complexes.[60] Important physical and chemical properties of a material are determined by the electronic redistribution caused by photoexcitation. Transient absorption spectroscopy provides a way to measure and understand the sequence of events and intramolecular excited state processes occurring in the processes (*Figure 3.24).*

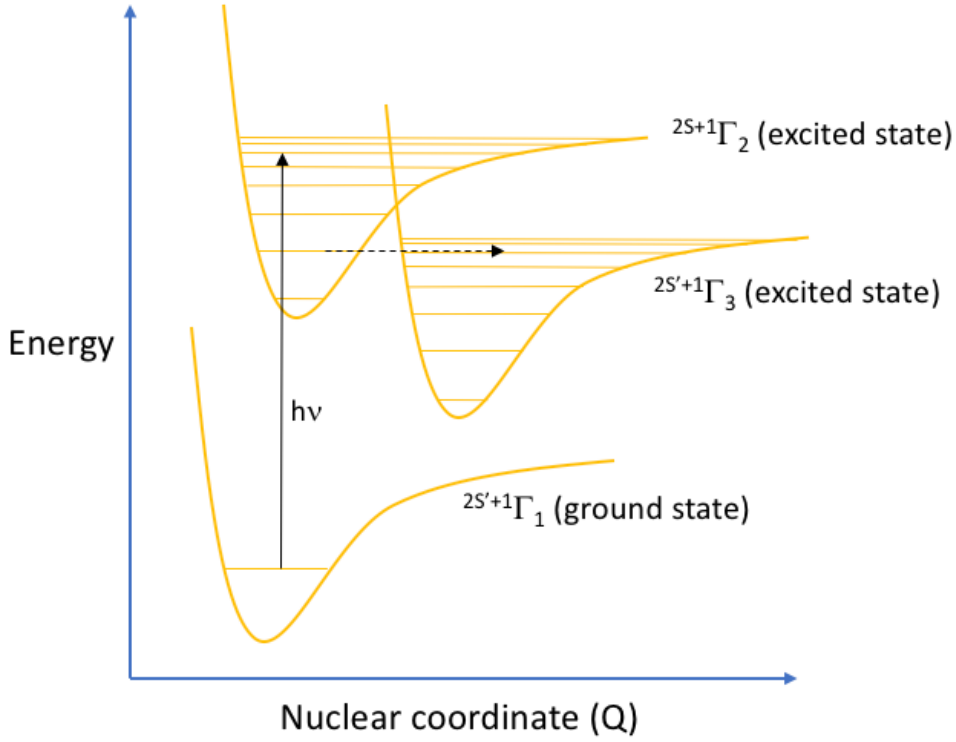

Figure 3.24: Generalised potential energy surface for excited state evolution in transition metal complexes. Initial excitation from the ground state ($^{2S+1}\Gamma_1$, where S denotes spin state) to the higher lying excited sate ($^{2S+1}\Gamma_2$) is followed by relaxation to the lower-energy surface ($^{2S'+1}\Gamma_3$).

In transition metal complexes, due to efficient spin-orbit coupling, the lowest excited state is usually a triplet state, which is populated within ~100 fs. The triplet excited state is relatively long-lived (hundreds of nanoseconds or longer and excited states are potentially important in this study.[61] It is therefore important to characterise their properties through transient absorption, TA, spectroscopy.

TA is a pump-probe method: a sample is excited using a short laser pulse, after a delay another laser pulse is used to measure how the absorption of the sample was altered by the first pulse (*Figure 3.25).* The time between these two laser pulses can be varied so as to monitor the entire time-dependence of the absorption change. After the excitation of a molecule, a different absorption spectrum will appear, which will then decay back to the ground state; this decay can be either directly to the ground state, or through some intermediate excited states – the exact nature of the decay will be clear from changes in spectral shape with time. These data will allow us to establish if there is one or several excited states involved in the decay of the initially populated excited state; and what are the lifetime(s) of all the states involved. By making use of ultrafast spectroscopy, it is possible to follow the process of energy dissipation in real time and to determine photophyscial mechanisms occurring upon the complex's interactions with DNA.

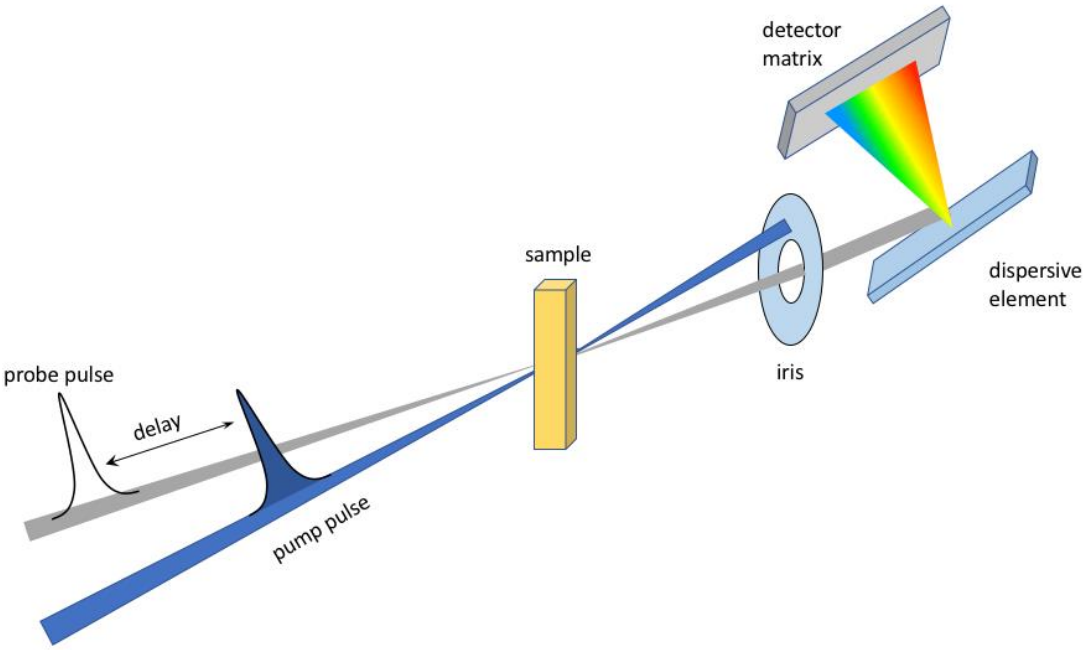

Figure 3.25: Schematic of the transient absorption laser setup. The idea of pump-probe experiment: pump pulse excited the sample, and probe is used to measure the transmittance. The variable time delay between pump and probe pulses provides the time dependence of the absorption signal.[35]

Luminescence methods are, of course, invaluable for the study of most "bright" excited states, but generally do not provide information on other species. The advantage of transient absorption measurements is that they report on any short lived species formed all the way down to the femtosecond domain, meaning that the evolution of non-emissive states and dark states can be investigated.[35]

This type of pump-probe spectroscopy was first described by Norrish and Porter in 1949, but massively developed in the 60's due to the revolution in high power lasers.[62] A transient absorption spectra will record the difference in absorbance (ΔA) at each wavelength of the transient species present and that of the ground state.[63] The spectra produced are therefore characteristic of the excited state. It is a well-known fact that the photophysical properties of intercalating complexes, such as the Ru^{II}-dppz light-switch complexes, change dramatically upon DNA binding. The photophysics of $[Ru(bpy)_2(dppz)]^{2+}$ and $[Ru(phen)_2(dppz)]^{2+}$ were investigated in aqueous solutions and in mixtures of acetonitrile and water by transient absorption and emission spectroscopies by Olsen *et al.* It was shown that the light-switch mechanism involves two steps: in H_2O solution the lifetimes of the "dark" MLCT (MLCT") excited state is 250 ps (hence no emission was detected, and the state is called "dark"), whereas no decay of the "bright" excited state (MLCT') could be observed on the ps timescale when the complex was either in the organic solvent acetonitrile or bound to DNA. In aqueous solution the MLCT" state was formed with a lifetime of 3 ps from the other state.[64] As outlined previously in this thesis, complexes with the flat, extended dppz unit are known to interact with double stranded DNA by intercalation. During this binding event the emission of the complex can be quenched, especially in the presence of guanine bases. Recent advances in the use of transient absorption allowed scientists to study both the excited states and reaction intermediates of metal complexes interacting with DNA. Kelly *et al* reported transient absorption measurements on the photooxidising complex $[Ru(TAP)_2(dppz)]^{2+}$ (TAP – 1,4,5,8-tetraazaphanthrene).[65] Complexes containing two TAP ligands have been proven by previous studies to photooxidise DNA.[66] Transient absorption spectroscopy of the unbound complex $[Ru(TAP)_2(dppz)]^{2+}$ under 400 nm excitation showed the bleaching of the MLCT band at 460 nm, and a formation of a broad transient centered at 600 nm. When the complex is bound to guanine-containing DNA, there is a formation of a new species absorbing at 510 nm (*Figure 3.26).* These new species were found to be the reduced Ru complex.

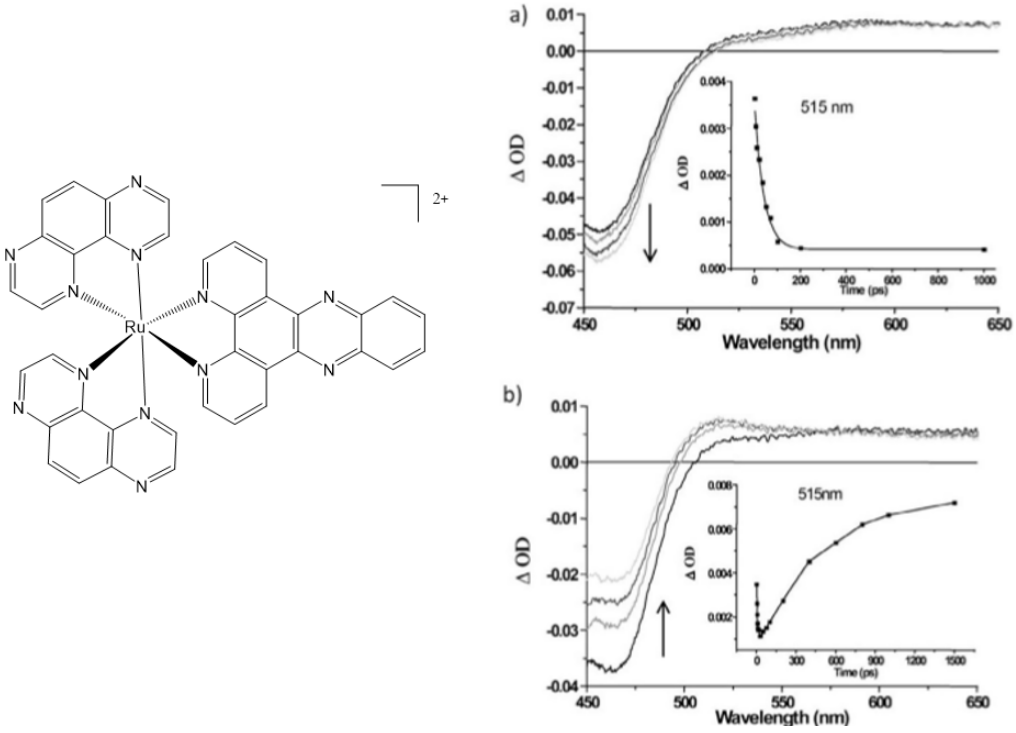

Figure 3.26: Left - chemical structure of $[Ru(TAP)_2(dppz)]^{2+}$. Right - Ps-TA of rac-$[Ru(TAP)_2(dppz)]^{2+}$ (8.58×10^{-5} M) in 10 mm aqueous phosphate buffer (a) in absence and (b) in presence of Guanine-containing DNA (1.78 mM nucelotide). Specta displayed from 10 to 1000 ps (a) and 100 to 1500 ps (b). Insets: kinetics at 515 nm.[65]

These results are of relevence for this work because complexes **1-3** all showed quenhing with 5-GMP, and therefore could behave in a similar manner to $[Ru(TAP)_2(dppz)]^{2+}$.

3.3.6.1 Transient absorption spectroscopy of Ir-dppz complexes

Following the use of transient absorption spectroscopy in studying the Ru^{II} complexes described in the previous section, work was focused into probing the excited state of complexes **1-3** both with and without CT-DNA. The ultrafast transient absorption setup used was a commercial detection instrument (Helios, Ultrafast Systems) with tunable excitation (*See experimental section for full laser set-up).* As seen previously in this chapter, the complexes in this study are all emissive in aqueous solutions (unlike their molecular light switch Ru^{II} analogues), and upon DNA binding the MLCT emission is quenched substantially. The aim of carrying out transient absorption on **1-3** is to fully understand the photophysical properties of these complexes, to detect "dark" states, and to reveal the electron transfer processes in controlling their photochemical behavior with nucleic acids. The excited state absorption spectra of **1-3** with and without DNA are shown in (*Figure 3.27).*

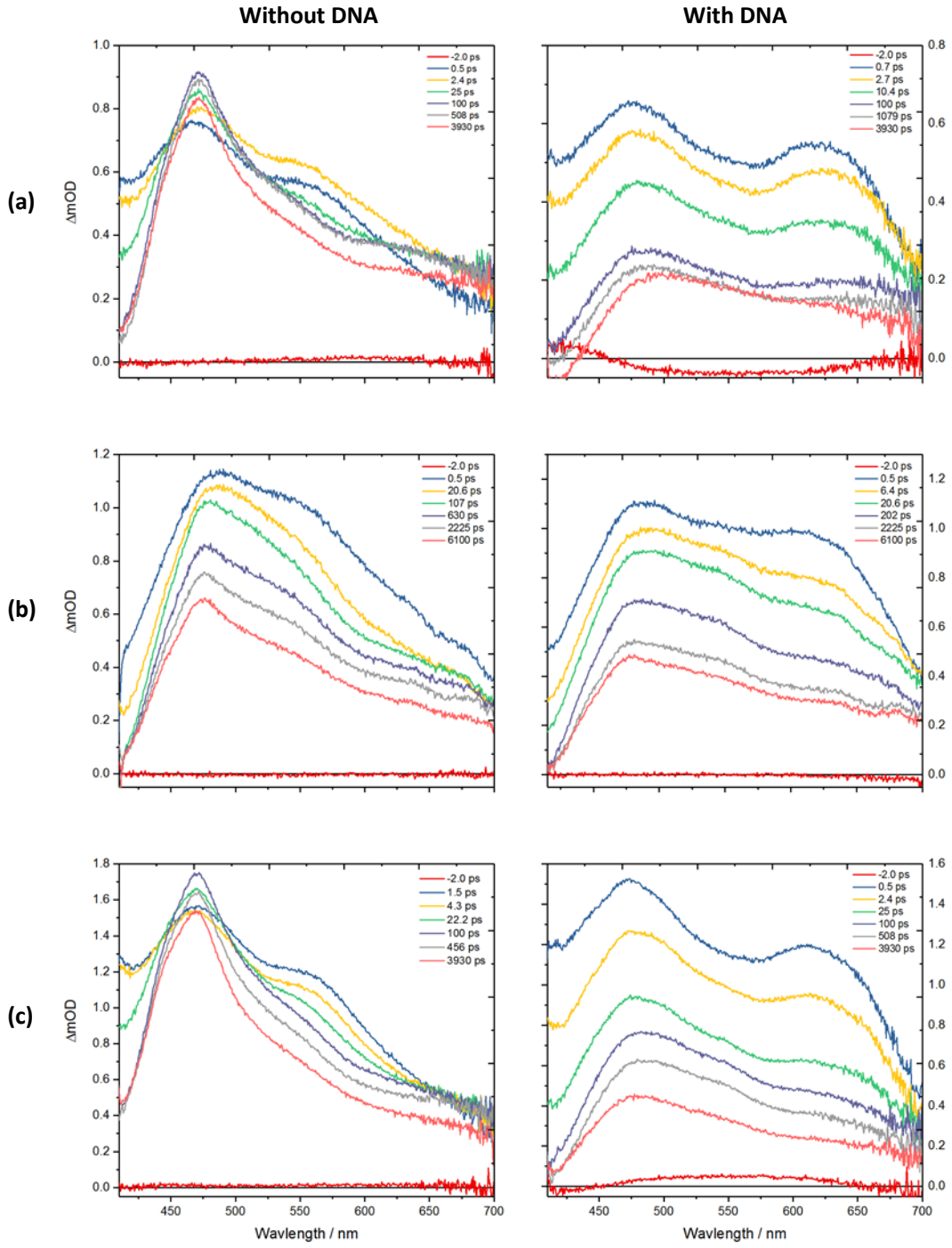

*Figure 3.27: (a) Left - ps-TA of **1** (OD = 0.4 at 455 nm), right – **1** in the presence of 10 mM CT-DNA in phosphate buffer solution, pH = 7.4. (b) ps-TA of **2** (OD = 0.2 at 455 nm), right – **2** in the presence of 10 mM CT-DNA in phosphate buffer solution, pH = 7.4. (c) ps-TA of **3** (OD = 0.2 at 455 nm), right – **3** in the presence of 10 mM CT-DNA in phosphate buffer solution, pH = 7.4.*

Complexes **1-3** all behave similarly under 400 nm excitation in aqueous solutions: in the absence of DNA, there is a maximum of ~ 470 nm which decreases over time, whilst upon interaction with CT-DNA a second absorption maximum, at 620 nm, is observed. It is

hypothesised that these observations are consistent with a redox electron transfer process occurring between the excited states of **1-3** and the guanine bases of the DNA strands. A similar process has been reported by the photooxiding $[Ru(TAP)_2(dppz)]^{2+}$ complex.[65] The global kinetic analysis is fully consistent with this interpretation (*Figure 3.28)*, and shows that there is a very short decay component in the presence of the DNA, and a long decay component which has the same lifetime as that of complexes **1-3** without DNA.

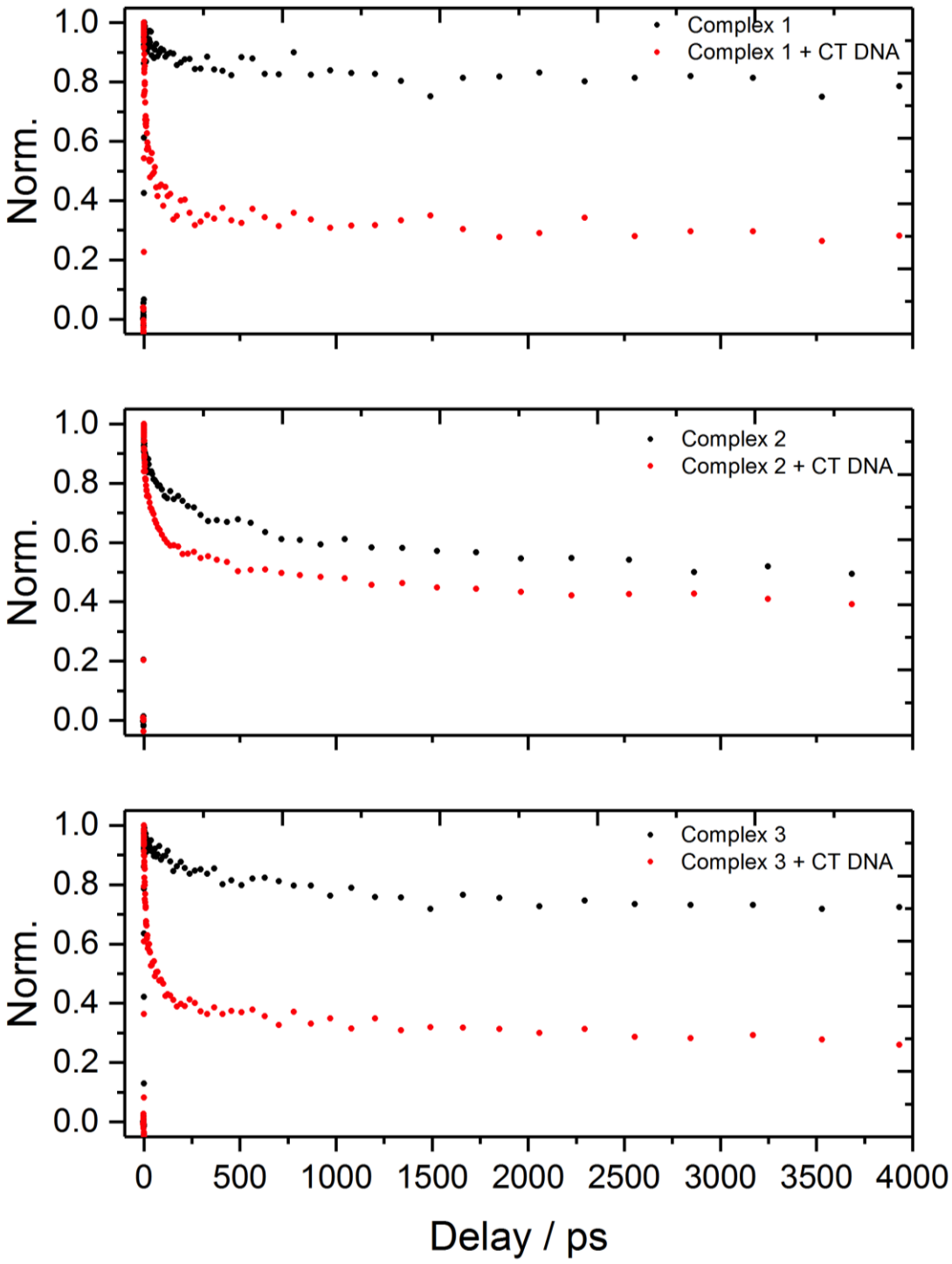

*Figure 3.28: Global kinetics of the transient absorption spectra. Top – **1** (●) without DNA, (●) with DNA. Middle- **2**, **1** (●) without DNA, (●) with DNA, Bottom – **3** **1** (●) without DNA, (●) with DNA.*

The decay kinetics of the complexes in the presence of DNA are quite different to those of the complexes in solution. When the complex is intercalated in the DNA there is a rapid decay of transient absorption, dominated by the lifetime of ~ 9 ps. Whereas, in the free solution, the

excited state has a lifetime in excess of >80 ps. This is consistent with rapid electron transfer from the guanine to the excited state. This decay is accompanied by the growth of the new species with a characteristic strong absorption band at ~ 620 nm. Results in the literature indicate isostructural Cr(III)-dppz complexes behave in a similar manner, however there is no generation of electron transfer products suggesting that there is a rapid back reaction.[67,68] More detailed kinetics of **1**-**3** with/without DNA at the important wavelengths of 472 nm and 624 nm (the maximum wavelengths of the transient species generated can be found in *Figures 3.29-3.31*.

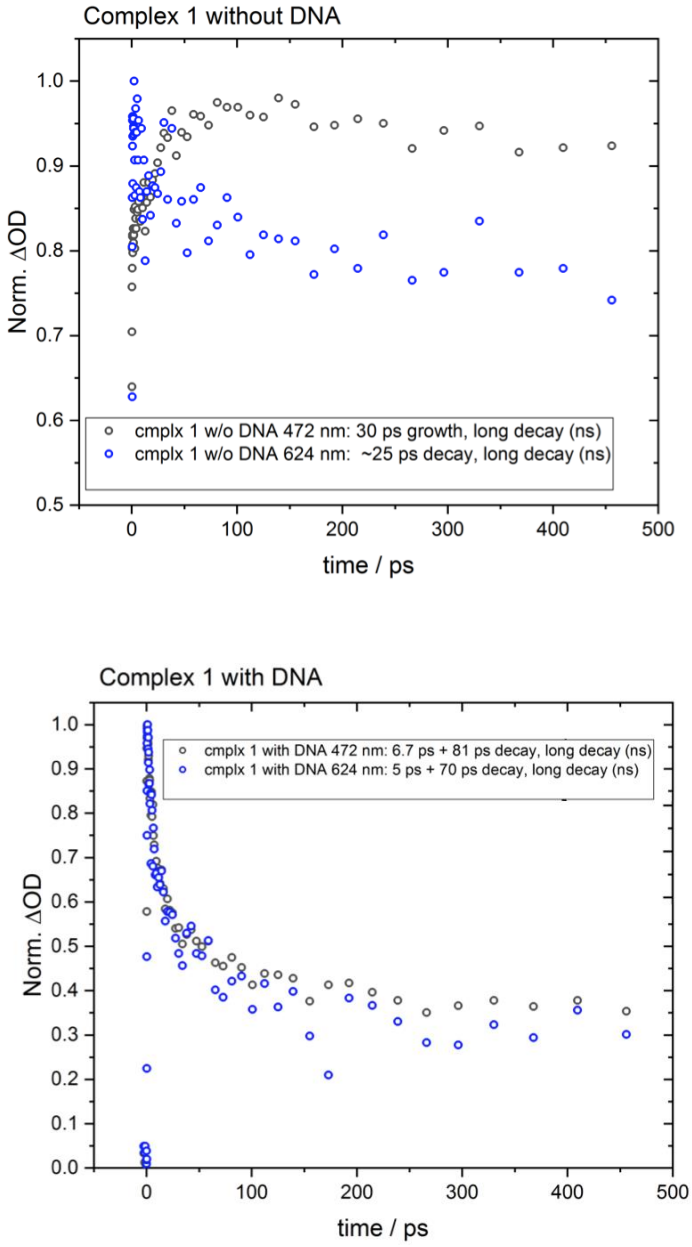

*Figure 3.29: Detailed kinetics of the transient species generated. Top – **1** without DNA (○) at 472 nm, (○) at 624 nm. Bottom – **1** in the presence of DNA (○) at 472 nm, (○) at 624 nm.*

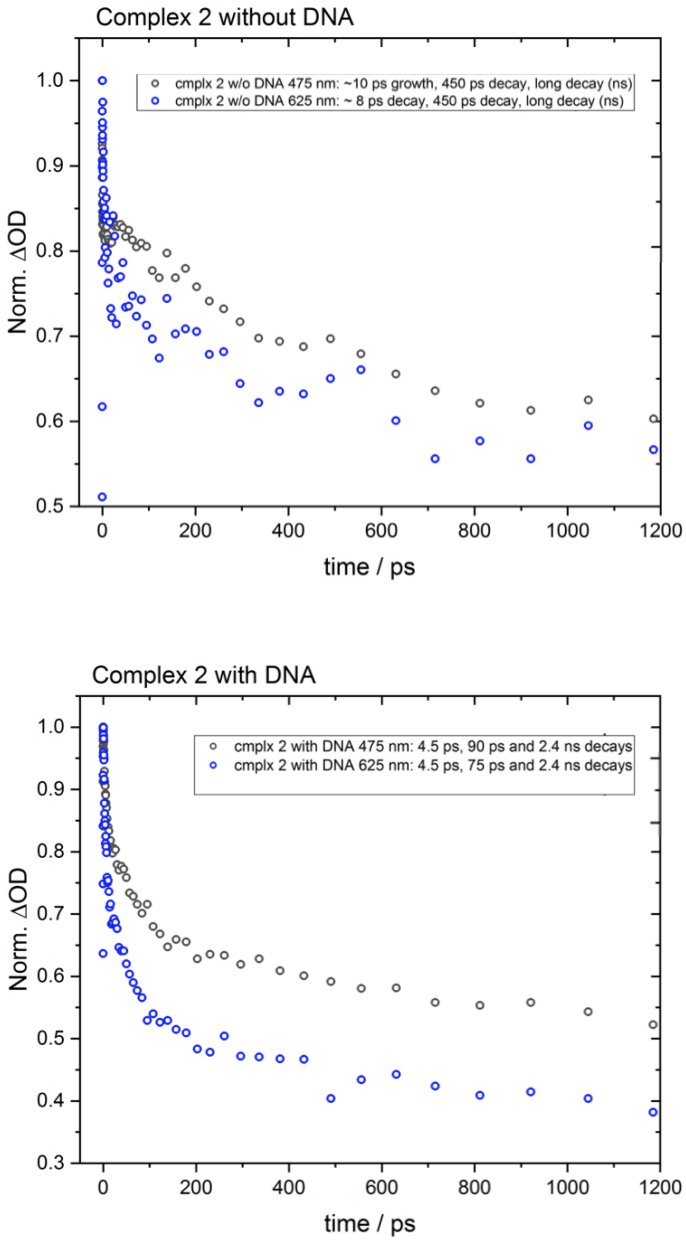

*Figure 3.30: Detailed kinetics of the transient species generated. Top – **2** without DNA (○) at 475 nm, (○) at 625 nm. Bottom – **2** in the presence of DNA (○) at 475 nm, (○) at 625 nm.*

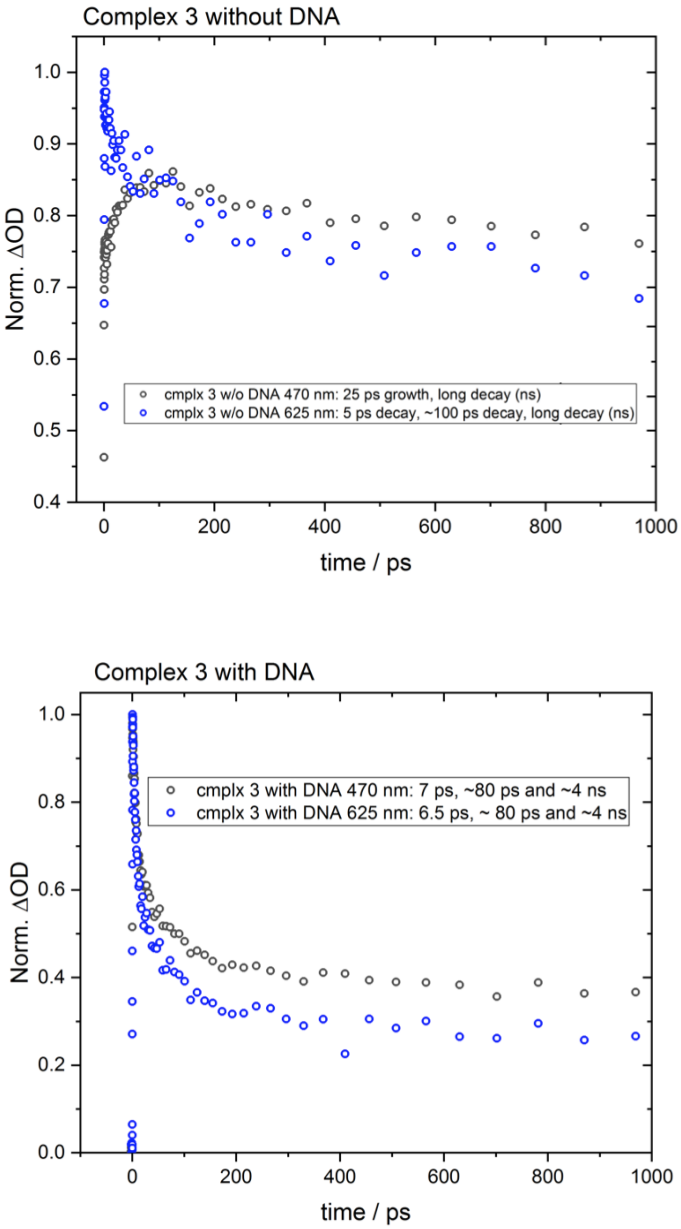

*Figure 3.31: Detailed kinetics of the transient species generated. Top – **3** without DNA (○) at 470 nm, (○) at 625 nm. Bottom – **3** in the presence of DNA (○) at 470 nm, (○) at 625 nm.*

The transient absorption data indicate that all three complexes do interact with DNA upon irradiation, and appear to generate radical anions. Therefore these results confirm that all three complexes are capable of directly photo-damaging DNA.

3.4 Conclusions and future work

The DNA binding properties of iridium compounds $[Ir(bpy)_2(dppz)]^{2+}$, $[Ir(phen)_2(dppz)]^{3+}$ and $[Ir(phen)_2(C\text{^}N\ dppz)]^{2+}$ were investigated in this chapter. All of these complexes possess a dppz or dppz analogue ligand and should therefore interact with DNA with interesting photophysical properties. Initial hydrodynamic studies concluded that all three complexes did indeed interact with DNA *via* an intercalative manner. This was proven by an increase in the relative specific viscosity with successive additions of each complex to CT-DNA. Further higher resolution investigations of DNA binding modes were carried out using tapping mode AFM. By measuring the persistence length of DNA chains 230 bps after incubation with the complexes, it was proven again that the mode of biding was through intercalation. The extent of the DNA lengthening of each complex was comparable to the results obtained through the viscosity experiments, in the order of $[Ir(phen)_2(dppz)]^{3+} > [Ir(bpy)_2(dppz)]^{3+} > [Ir(phen)_2(C\text{^}N\ dppz)]^{2+}$. Future endeavours in this area could be to use tapping mode AFM in liquid conditions to image interactions of the complexes with DNA. Simply because AFM in liquid has both yielded the highest resolution to monitor binding events and conformational changes in real time.

Due to the Ir(dppz) unit, it might be thought that the iridium complexes would behave in a similar manner to the isostructural Ru^{II}(dppz) analogues, and display a DNA light-switch effect. In fact, all three complexes displayed an opposite effect: their MLCT emission decreases upon addition of CT-DNA. DFT theoretical calculations of the singlet and excited state triplet states explain why the light-switch effect is not shown. $[Ir(bpy)_2(dppz)]^{3+}$ and $[Ir(phen)_2(dppz)]^{3+}$ excited states are best described as intraligand states located on the dppz unit which are emissive in water. Taken together, the data indicates that **1** and **2** are not only capable of sensitizing singlet oxygen but can also cause DNA damage through photo-induced redox processes involving nucleobase sites. Complex **3** appears to be slightly different, its excited state involves charge transfer between the Ir^{III} metal centre and one of the ancillary phenanthroline units. This high-energy MLCT transition is not quenched by water, and judging by the plasmid cleavage experiments, is not cleaving DNA despite being the most efficient singlet oxygen generator- further investigations need to be carried out to explain this result. DNA-induced luminescent quenching is a well-studied phenomenon, with work showing that complexes containing organic-based intercalators are strongly oxidising and capable of directly oxidising G sites. This quenching is mainly due to electron transfer from photo-oxidised

quinine sites, however can also involve adenine sites, depending on the redox potentials.[69–71] As well as spectrophotometric experiments there is scope to use cyclic voltammetry to determine binding interactions with DNA. The electrochemical behaviour of the iridium complexes in the absence and presence of DNA can be measured. If there is a dramatic shift in both the cathodic and anodic peak potential it can be deduced that the complexes have the ability to bind into DNA. The net shift in the potential can be used to estimate the equilibrium constants for the binding of the complexes to DNA.[72]

To create a complete thermodynamic profile of the interaction of these metal complexes with DNA could be investigated using isothermal titration calorimetry. This technique directly measures the heat that is either released or absorbed during a biomolecular binding events, enabling accurate determinations of binding constants, enthalpy (ΔH), and entropy (ΔS).

Further investigations into the decrease in luminescence of the complexes upon titration of DNA were undertaken. Titration experiments with guanosine monophosphate confirm that quenching displaying Stern-Volmer kinetics occurs, as a result of redox chemistry between the metal complex and guanine sites. A future experiment could be to use the metallo-intercalators **1**-**3** to introduce a photo-excited hole into the DNA helix at a specific site, using a linker, in order to evaluate oxidative damage to the strand from a distance. Barton *et al* document this well; by using piperidine, the oxidative damage site can be changed into a cleavage site, ejecting the damaged guanine base. This approach can be used to monitor the extent of oxidative damage as a result of "hole migration" along the DNA π-stack.[73,74]

Gel electrophoresis investigated possible photocleavage mechanisms of plasmid DNA and indicated that for complexes **1** and **2** singlet oxygen radicals promote the cleavage of DNA. To confirm this gel electrophoresis under an argon atmosphere to monitor any photocleavage mechanisms in an oxygen free environment should be carried in the future. Therefore, work on this issue could determine how much of each effect is contributing to the DNA damage. Partition cleavage experiments in hypoxic conditions *etc*.

Given the well-established tunable nature of the excited states of polypyridyl Ir^{III} complexes, the potential of these systems and their derivatives for a range of applications, including as sensitisers for photodynamic therapy, is clearly apparent. In summary, the three complexes

associate with DNA in cell free conditions. However binding to demonic CT-DNA in saline buffer at approximately 27 °C is different to physiological cellular conditions. The next chapter will investigate the possibilities of intracellular interactions.

3.5 References

1 R. L. Scruggs and P. D. Ross, Viscosity study of DNA, *Biopolymers*, 1964, **2**, 593–609.

2 C. Metcalfe and J. A. Thomas, Kinetically inert transition metal complexes that reversibly bind to DNA, *Chem. Soc. Rev.*, 2003, **32**, 215.

3 L. . Lerman, The structure of the DNA-Acridine complex, *Biochemistry*, 1963, **49**, 94–102.

4 L. Lerman, Structural Considerations in the Interaction of DNA and Acridines, *J. Mol. Biol.*, 1961, **3**, 18–30.

5 R. B. Macgregor, R. M. Clegg and T. M. Jovin, Viscosity Dependence of Ethidium-DNA Intercalation Kinetics, *Biochemistry*, 1987, **26**, 4008–4016.

6 G. Cohen and H. Eisenberg, Viscosity and sedimentation study of sonicated DNA–proflavine complexes, *Biopolymers*, 1969, **8**, 45–55.

7 S. Satyanarayana, J. C. Dabrowiak and J. B. Chaires, Neither Δ-nor Δ-Tris(phenanthroline)ruthenium(II) Binds to DNA by Classical Intercalation, *Biochemistry*, 1992, **31**, 9319–9324.

8 L. Kapicak and E. J. Gabbay, Topography of nucleic acid helixes in solutions. XXXIII. Effect of aromatic cations on the tertiary structures of deoxyribonucleic acid, *J. Am. Chem. Soc.*, 1975, **97**, 403–408.

9 A. Hofmann, *Methods of Molecular Analysis in the Life Sciences*, 2014.

10 T. Topală, A. Bodoki, L. Oprean and R. Oprean, Experimental techniques employed in the study of metal complexes-DNA -interactions, *Farmacia*, 2014, **62**, 1049–1061.

11 N. Sohrabi, Binding and UV/Vis spectral investigation of interaction of Ni(II) piroxicam complex with calf thymus deoxyribonucleic acid (Ct-DNA): A thermodynamic approach, *J. Pharm. Sci. Res.*, 2015, **7**, 533–537.

12 A. E. Friedman, J. K. Barton, J. C. Chambron, J. P. Sauvage, N. J. Turro and J. K. Barton, Molecular “Light Switch” for DNA: Ru(bpy)2(dppz)2+, *J. Am. Chem. Soc.*, 1990, **112**, 4960–4962.

13 S. R. Byrn and G. D. Dolch, Analysis of Binding of Daunorubicin and Doxorubicin to DNA Using Computerized Curve-Fitting Procedures, *J. Pharm. Sci. Res.*, 1978, **67**, 688–693.

14 G. Scatchard, the Attractions of Proteins for Small Molecules and Ions, *Ann. N. Y. Acad. Sci.*, 1949, **51**, 660–672.

15 X. Qu and J. B. Chaires, Analysis of Drug-DNA Binding Data, *Methods Enzymol.*, 2000, **321**, 353–369.

16 H. G. Weder, J. Schildknecht, R. A. Lutz and P. Kesselring, Determination of binding parameters from Scatchard plots. Theoretical and practical considerations., *Eur. J. Biochem.*, 1974, **42**, 475–481.

17 J. D. McGhee and P. H. von Hippel, Theoretical Aspects of DNA-protein Interactions: Co-operative and Non-cooperative Binding of Large Ligands to a One-dimensional Homogeneous Lattice, *J. Mol. Biol.*, 1974, **86**, 469–489.

18 P. H. von Hippel and J. D. McGhee, DNA-Protein Interactions, *Annu. Rev. Biochem.*, 1972, **41**, 231–300.

19 A. Valazquez-Campoy, Ligand binding to one-dimensional lattice-like macromolecules: Analysis of the McGhee-von Hippel theroy implemented in isothermal titration calorimetry, *Anal. Biochem.*, 2006, **348**, 94–104.

20 N. C. Stellwagen, Electrophoresis of DNA in agarose gels, polyacrylamide gels and in free solution, *Electrophoresis*, 2010, **30**, 1–14.

21 S. Surzycki, in *Basic Techniques in Molecular Biology*, Springer, 2000.

22 R. B. Helling, H. M. Goodman and H. W. Boyer, Analysis of endonuclease R-EcoRI fragments of DNA from lambdoid bacteriophages and other viruses by agarose-gel electrophoresis., *J. Virol.*, 1974, **14**, 1235–44.

23 A. L. B. Pyne and B. W. Hoogenboom, *Imaging DNA Structure by Atomic Force Microscopy*, Humana Press, New York, NY, 2016.

24 H. G. Hansma, R. L. Sinsheimer, M. Li and P. K. Hansma, Atomic force microscopy of single- and double-stranded DNA, *Nucleic Acids Res.*, 1992, **20**, 3585–3590.

25 P. K. Hansma, J. P. Cleveland, M. Rademacher and D. Walters, Tapping mode atomic force microscopy in liquids, *Appl. Phys Lett*, 1994, **64**, 1738.

26 T. Berge, N. S. Jenkins, R. B. Hopkirk, M. J. Waring, J. M. Edwardson and R. M. Henderson, Structural perturbations in DNA caused by bis-intercalation of ditercalinium visualised by atomic force microscopy., *Nucleic Acids Res.*, 2002, **30**, 2980–6.

27 K. E. Reinert, DNA stiffening and elongation caused by the binding of ethidium bromide, *Biochim. Biophys.*, 1973, **319**, 135–139.

28 D. Suh and J. B. Chaires, Criteria for the mode of binding of DNA binding agents., *Bioorg. Med. Chem.*, 1995, **3**, 723–8.

29 S. Stimpson, D. R. Jenkinson, A. Sadler, M. Latham, D. A. Wragg, A. J. H. M. Meijer and J. A. Thomas, Tuning the Excited State of Water-Soluble Ir III -Based DNA

Intercalators that are Isostructural with [Ru II (NN) 2 (dppz)] Light-Switch Complexes, *Angew. Chemie Int. Ed.*, 2015, **127**, 3043–3046.

30 T. Biver, C. Cavazza, F. Secco and M. Venturini, The two modes of binding Ru(phen)2(dppz)2+ to DNA: Thermodynamic evidence and kinetic studies, *J. Inorg. Biochem.*, 2007, **101**, 461–469.

31 H. D. Stoeffler, N. B. Thorntor, S. L. Temkin and K. S. Schanze, Unusual Photophysics of a Rhenium(I) Dipyridophenazine Complex in Homogenous Solution and Bound to DNA, *J. Am. Chem. Soc.*, 1995, **117**, 7119–7128.

32 M. G. Walker, V. Gonzalez, E. Chekmeneva and J. A. Thomas, Temperature-switched binding of a RuII(dppz)/DNA light-switch complex, *Angew. Chemie - Int. Ed.*, 2012, **51**, 12107–12110.

33 Y. Jenkins, J. K. Barton, A. E. Friedman and N. J. Turro, Characterization of Dipyridophenazine Complexes of Ruthenium(II): The Light Switch Effect as a Function of Nucleic Acid Sequence and Conformation, *Biochemistry*, 1992, **31**, 10809–10816.

34 C. Hiort, P. Lincoln and B. Nordén, DNA Binding of Δ- and Λ-[Ru(phen)2DPPZ]2+, *J. Am. Chem. Soc.*, 1993, **115**, 3448–3454.

35 R. Berera, R. van Grondelle and J. T. M. Kennis, Ultrafast transient absorption spectroscopy: principles and application to photosynthetic systems, *Photosynth. Res.*, 2009, **101**, 105–118.

36 S. Schäfer and W. S. Sheldrick, Coligand tuning of the DNA binding properties of half-sandwich organometallic intercalators: Influence of polypyridyl (pp) and monodentate ligands (L = Cl, (NH2)2CS, (NMe2)2CS) on the intercalation of (η5-pentamethylcyclopentadienyl)-iridium(III)- dipyrid, *J. Organomet. Chem.*, 2007, **692**, 1300–1309.

37 K. K. W. Lo, C. K. Chung and N. Zhu, Nucleic acid intercalators and avidin probes derived from luminescent cyclometalated iridium(III)-dipyridoquinoxaline and -dipyridophenazine complexes, *Chem. - A Eur. J.*, 2006, **12**, 1500–1512.

38 Y. M. Chen, A. G. Zhang and K. Z. Wang, Cyclometalated iridium(III) complex of 6-hydroxydipyrido[3,2-a:2′, 3′-c]phenazine: Synthesis, and acid-base and avid DNA binding properties, *Appl. Organomet. Chem.*, 2011, **25**, 521–529.

39 L. F. Agnez-Lima, J. T. A. Melo, A. E. Silva, A. H. S. Oliveira, A. R. S. Timoteo, K. M. Lima-Bessa, G. R. Martinez, M. H. G. Medeiros, P. Di Mascio, R. S. Galhardo and C. F. M. Menck, DNA damage by singlet oxygen and cellular protective mechanisms, *Mutat. Res. - Rev. Mutat. Res.*, 2012, **751**, 15–28.

40 M. B. Fleisher, K. C. Waterman, N. J. Turro and J. K. Barton, Light Induced Cleavage of DNA by Metal Complexes, *Inorg. Chem.*, 1986, **25**, 3551–3552.

41 H. K. Saeed, P. J. Jarman, S. Archer, S. Sreedharan, I. Q. Saeed, L. K. Mckenzie, J. A. Weinstein, N. J. Buurma, C. G. W. Smythe and J. A. Thomas, Homo- and Heteroleptic Phototoxic Dinuclear Metallo-Intercalators Based on RuII(dppn) Intercalating Moieties: Synthesis, Optical, and Biological Studies, *Angew. Chemie - Int. Ed.*, 2017, **56**, 12628–12633.

42 C. V. Kumar, J. K. Barton and N. J. Turro, Photophysics of Ruthenium Complexes Bound to Double Helical DNA, *J. Am. Chem. Soc.*, 1985, **107**, 5518–5523.

43 M. R. Arkin, E. D. A. Stemp, S. Coates Pulver and J. K. Barton, Long-range oxidation of guarnine by Ru(III) in duplex DNA, *Chem. Biol.*, 1997, **4**, 389–400.

44 Y. A. Berlin, A. L. Burin and M. A. Ratner, DNA as a molecular wire, *Superlattices Microstruct.*, 2000, **28**, 241–252.

45 S. Steenken, J. P. Telo, H. M. Novais and L. P. Candelas, One-Electron-Reduction Potentials of Pyrimidine Bases, Nucleosides, and Nucleotides in Aqueous Solution. Consequences for DNA Redox Chemistry, *J. Am. Chem. Soc.*, 1992, **114**, 4701–4709.

46 E. D. A. Stemp, M. R. Arkin and J. K. Barton, Oxidation of Guanine in DNA by Ru (phen)2(dppz)3+ Using the Flash-Quench Technique, *J. Am. Chem. Soc*, 1997, **2**, 2921–2925.

47 I. Ortmans, B. Elias, J. M. Kelly, C. Moucheron and A. Kirsch-DeMesmaeker, [Ru(TAP)2(dppz)]2+: a DNA intercalating complex, which luminesces strongly in water and undergoes photo-induced proton-coupled electron transfer with guanosine-5'-monophosphate., *Dalton Trans.*, 2004, **2**, 668–676.

48 C. J. Cardin, J. M. Kelly and S. J. Quinn, Photochemically active DNA-intercalating ruthenium and related complexes – insights by combining crystallography and transient spectroscopy, *Chem. Sci.*, 2017, **8**, 4705–4723.

49 F. Gao, H. Chao, F. Zhou, Y.-X. Yuan, B. Peng and L.-N. Ji, DNA interactions of a functionalised ruthenium(II) mixed-polypyridyl complex [Ru(bpy)2(ppd]2+, *J. Biol. Inorg. Chem.*, 2006, **100**, 1487–1494.

50 M. Mariappan, R. Alagarsamy, A. P. Panneerselvam, A. Veerappan, S. Rajendran and J. Arunachalam, Synthesis, solvatochromism, photochemistry, DNA binding, photocleavage, cytotoxicity and molecular docking studies of a ruthenium(II) complex bearing photoactive subunit, *J. Photochem. Photobiol. A Chem.*, 2018, **356**, 617–626.

51 K. R. Wyland, E. E. Hoffman and A. Jain, DNA interaction studies and photoinduced

ligand exchange kinetics of a sterically strained ruthenium(II) complex, *Inorganica Chim. Acta*, 2017, **454**, 62–66.

52 M. G. Walker, P. J. Jarman, M. R. Gill, X. Tian, H. Ahmad, P. A. N. Reddy, L. McKenzie, J. A. Weinstein, A. J. H. M. Meijer, G. Battaglia, C. G. W. Smythe and J. A. Thomas, A Self-Assembled Metallomacrocycle Singlet Oxygen Sensitizer for Photodynamic Therapy, *Chem. - A Eur. J.*, 2016, **22**, 5996–6000.

53 J. K. Thomas, Rates of reaction of the hydroxyl radical, *Trans. Faraday Soc.*, 1965, **61**, 702.

54 P. L. Popham and a Novacky, Use of Dimethyl Sulfoxide to Detect Hydroxyl Radical during Bacteria-Induced Hypersensitive Reaction., *Plant Physiol.*, 1991, **96**, 1157–1160.

55 M. Bancirova, Sodium azide as a specific quencher of singlet oxygen during chemiluminescent detection by luminol and Cypridina luciferin analogues, *Luminescence*, 2011, **26**, 685–688.

56 P. R. Ogilby, Singlet oxygen: there is indeed something new under the sun, *Chem. Soc. Rev.*, 2010, **39**, 3181.

57 R. L. A. Furlan, L. M. Garrido, G. Brumatti, G. P. Amarante-Mendes, R. A. Martins, M. C. R. Facciotti and G. Padilla, A rapid and sensitive method for the screening of DNA intercalating antibiotics, *Biotechnol. Lett.*, 2002, **24**, 1807–1813.

58 V. Scott, A. R. Clark and K. Docherty, The Gel Retardation Assay, *Methods Mol. Biol.*, 1994, **31**, 339–347.

59 A. L. B. Pyne and B. W. Hoogenboom, in *Chromosome Architecture*, Humana Press, New York, NY, 2016, pp. 61–71.

60 H. A and R. C, *Structure and Bonding*, Springer International Publishing, 2016.

61 J. K. McCusker, Femtosecond absorption spectroscopy of transition metal charge-transfer complexes, *Acc. Chem. Res.*, 2003, **36**, 876–887.

62 R. G. W. Norrish and G. Porter, *Nature*, 1949, 164, 658–658.

63 R. Bonneau, J. Wirz and A. D. Zuberbuhler, Methods for the analysis of transient absorbance data (Technical Report), *Pure Appl. Chem.*, 1997, **69**, 979–992.

64 E. J. C. Olson, D. Hu, a Ho, a M. Jonkman, M. R. Arkin, E. D. a Stemp, J. K. Barton and P. F. Barbara, First Observation of the Key Intermediate in the " Light-Switch " Mechanism of [Ru (phen) 2 dppz] 2 +, *J. Am. Chem. Soc.*, 1997, **7863**, 11458–11467.

65 P. M. Keane and J. M. Kelly, Transient absorption and time-resolved vibrational studies of photophysical and photochemical processes in DNA-intercalating polypyridyl metal

complexes or cationic porphyrins, *Coord. Chem. Rev.*, 2018, **364**, 137–154.

66 J. M. Kelly, D. J. McConell, C. OhUigin, A. B. Tossi, A. Kirsch-De Mesmaeker, A. Masschelein and J. Nasielski, Ruthenium polypyridyl complexes; Their interaction with DNA and their role as sensitizers for its photocleavage, *J.Chem.Soc.Chem.Commun.*, 1987, 1821–1823.

67 S. J. Devereux, P. M. Keane, S. Vasudevan, I. V. Sazanovich, M. Towrie, Q. Cao, X. Z. Sun, M. W. George, C. J. Cardin, N. A. P. Kane-Maguire, J. M. Kelly and S. J. Quinn, Study of picosecond processes of an intercalated dipyridophenazine Cr(iii) complex bound to defined sequence DNAs using transient absorption and time-resolved infrared methods, *Dalt. Trans.*, 2014, **43**, 17606–17609.

68 M. Wojdyla, J. A. Smith, S. Vasudevan, S. J. Quinn and J. M. Kelly, Excited state behaviour of substituted dipyridophenazine Cr(iii) complexes in the presence of nucleic acids, *Photochem. Photobiol. Sci.*, 2010, **9**, 1196–1202.

69 D. A. McGovern, A. Selmi, J. E. O'Brien, J. M. Kelly and C. Long, Reduction of dipyrido-[3,2-a:2′,3′-c]-phenazine (dppz) by photolysis in ethanol solution, *Chem. Commun.*, 2005, 1402–1404.

70 T. Phillips, I. Haq, A. J. H. M. Meijer, H. Adams, I. Soutar, L. Swanson, M. J. Sykes and J. A. Thomas, DNA binding of an organic dppz-based intercalator, *Biochemistry*, 2004, **43**, 13657–13665.

71 T. Phillips, C. Rajput, L. Twyman, I. Haq and J. A. Thomas, Water-soluble organic dppz analogues - Tuning DNA binding affinities, luminescence, and photo-redox properties, *Chem. Commun.*, 2005, **44**, 4327–4329.

72 X. Lu, K. Zhu, M. Zhang, H. Liu and J. Kang, Voltammetric studies of the interaction of transition-metal complexes with DNA, *J. Biochem. Biophys. Methods*, 2002, **52**, 189–200.

73 D. B. Hall, R. E. Holmlin and J. K. Barton, *Nature*, 1996, 382, 731–735.

74 M.-H. Chung, H. Kiyosawa, E. Ohtsuka, S. Nishimura and H. Kasai, DNA strand cleavage at 8-Hydoxyguanine residues by hot piperidine treatment, *Biochem. Biophys. Res. Commun.*, 1992, **188**, 1–7.

Chapter 4
Cellular studies

4.0 Cellular studies

4.1 Introduction

The clinical success of the serendipitously discovered cisplatin stimulated the search for new metal complexes. Compared to small organic molecules, metal-based complexes offer several advantages as therapeutics. As mentioned in previous chapters, ancillary ligands can be modified to affect sterics, lipophilicity and overall charge. Such structural/electronic changes can alter the selectivity and reactivity of the metal complex to fit a particular function or biological target. Phosphorescent metal complexes in particular possess advantages that make them excellent candidates for sensing or imaging probes; they generally possess photophysical properties that are sensitive to the microenvironment, alongside a significant Stokes shift that prevents self-quenching and allows clear excitation and high resolutions.

Since most cells are transparent and largely colourless, detailed studies within cells could not commence until a way to highlight them was discovered. Luminescent probes were found to provide infinite contrast providing higher sensitivity to cellular imaging. This area of research then developed toward the design of optical probes to highlight specific intracellular structures with high specificity. The majority of current commercial optical probes rely on simple emission intensities to locate target structures.[1–3]

More recently, the concept of personalised medicine has emerged as a promising way to target unmet challenges in medicine. Patients are separated into different groups with treatments being tailored to the individual patient based on their predicted response.[4] In this context, the term “theranostic” was coined by Funkhouser in 2002 which encompasses both therapy and diagnostic imaging.[5] Theranostic agents therefore deliver therapeutic drugs and diagnostic imaging agents within the same entity.

The antitumor properties of ruthenium complexes have received much attention in recent years as, relative to cisplatin and its derivatives, some show enhanced pharmacological profiles toward platinum-resistant cell lines.[6] Ruthenium, being a group 8 transition-metal (the so-called platinum group), was originally studied to ameliorate cisplatin off-target toxicity and potency. Studies found that ruthenium complexes can often accumulate in neoplasmic tissue,

whilst there was an absence of significant haematological toxicity in normal tissues.[7] Both *in vivo* and *in vitro* research has also demonstrated that Ru-based anticancer complexes can bind to transferrin, which plays a crucial role in drug metabolism and transport to target area.[8] Octahedral ruthenium(III) complexes are relatively inert towards ligand substitution, however upon reduction to ruthenium(II) complexes a more reactive species is generated. As cancer cells are rapidly growing in comparison to healthy cells an environment with less oxygen is created. This increased metabolic rate produces a lower pH, and a more reducing environment around the developing tumour. This provides a way of administering ruthenium(III) anti-cancer agents in their less active forms, acting as a prodrug to deliver the therapeutic to cancerous areas.[9] Finally, some ruthenium complexes have been found to combat secondary metastasis as opposed to the primary tumour.[10] Examples of the first ruthenium complexes to make it to clinical trials are ([Him][transRuCl$_4$(DMSO)(im)], im = imidazole), KP1019, and ([Hind][trans-[RuCl$_4$(ind)$_2$], ind = indazole), which are classical cytotoxics, and NAMI-A, an anti-metastatic therapeutic (*Figure 4.1).*

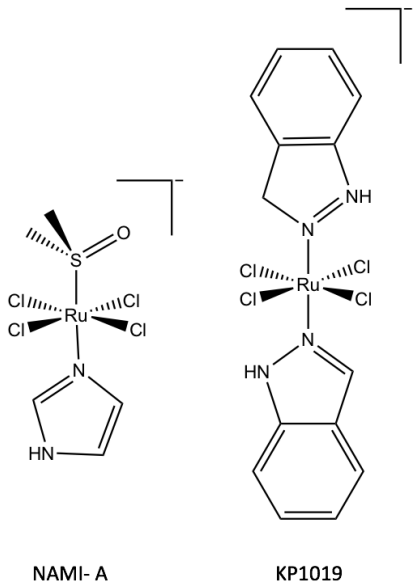

Figure 4.1: Chemical structures of ruthenium complexes in clinical trials. Left: NAMI-A [Him][transRuCl$_4$(DMSO)(im)]. Right: KP1019 ([Hind][trans-[RuCl$_4$(ind)$_2$]

Complexes such as NAMI and KP1019 were only the beginning in the newly emerging field of ruthenium anti-cancer agents. Many Ru(II) complexes containing polypyridyl ligands have been assayed and shown to display interesting preclinical properties, particularly due to their photophysical properties. Their long-lived metal-to-ligand charge-transfer (MLCT) shows

emission at wavelengths in the visible to near-infrared region, different to the excitation wavelength, resulting in deep penetration of the tissue. The large Stokes shift allows light scattering to be minimised, and their long lived excited state can either help determination of cellular localisation, or maximise the energy transfer processes to a biological target. This creates scope for complexes to become theranostic by nature. By simple structural modification of the ancillary ligands, both the photophysical and pharmacologic properties can be tuned. For example, in view of these properties Carlos, *et al.* studied the cytotoxicity and antitumor activity of a new Ru(II) series of complexes with the general formula *cis*-$[Ru(L\text{-}L)_2(L)_2]^{2+}$ where L-L = 2,2-bipyridine (bpy) and 1,10-phenanthroline (phen) and L = imidazole (ImH) , 1-methylimidazole (1MeIm), and histamine (Him) (*Figure 4.2)*. The binding interactions of these complexes with human serum albumin (HSA), the most abundant protein in blood plasma, was investigated using various techniques such as isothermal scanning calorimetry (ITC), circular dichroism (CD) and diffusion ordered spectroscopy (DOSY) experiments. The complexes were also assayed *in vitro* for cell proliferation inhibitory activity in human colon and ovarian tumours. The collected results showed that the complexes all bound weakly to HSA, indicating that a cytotoxic mechanism contributed to inhibition of cell proliferation, whilst maintaining specific cellular localisation.[6]

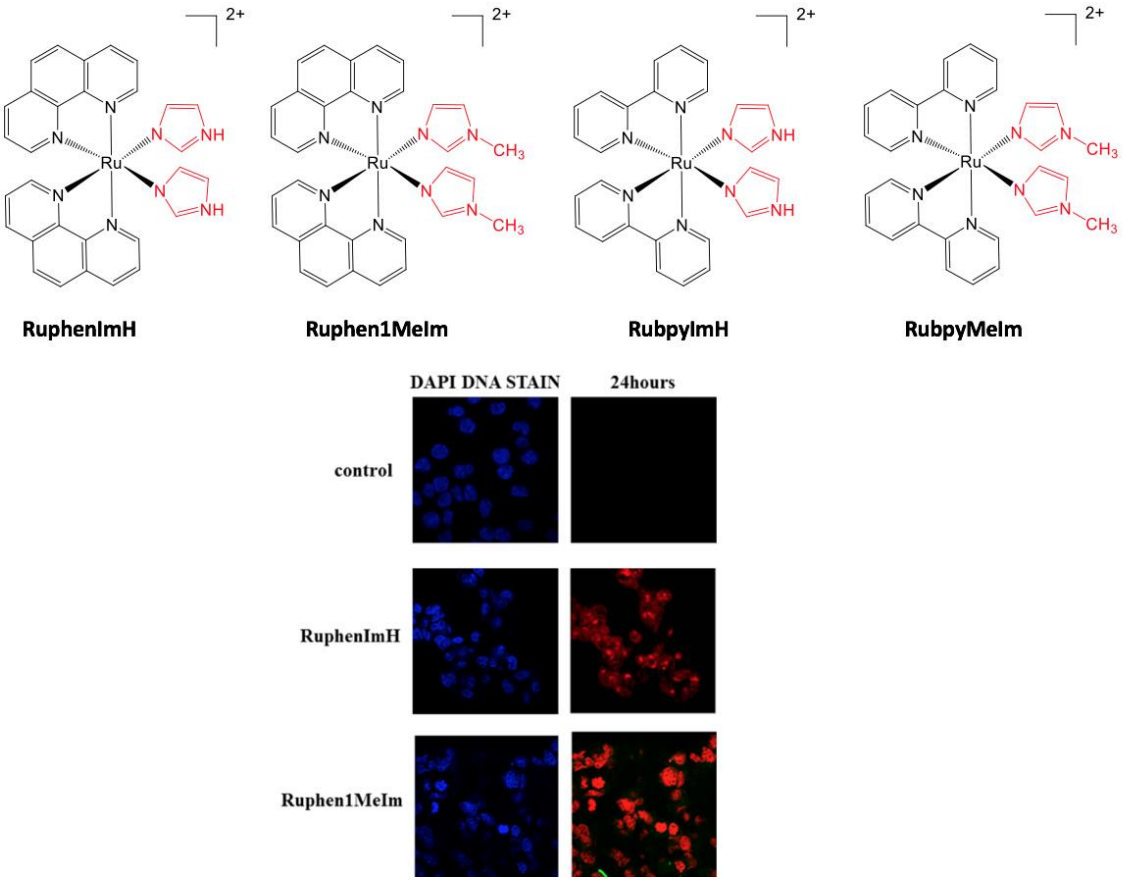

*Figure 4.2: Top: Chemical structures of the Ru^{II} complexes in this study (left to right) $[Ru(phen)_2(ImH)_2]^{2+}$, $[Ru(phen)_2(MeIm)_2]^{2+}$, $[Ru(bpy)_2(ImH)_2]^{2+}$, and $[Ru(bpy)_2(MeIm)_2]^{2+}$. Bottom: Fluorescent confocal imaging for complexes **RuphenImH** and **Ruphen1MeIm** in the HCT116 cell line.*

The complexes showed high uptake in HCT116 cells, detected by confocal microscopy. The inhibition of cell proliferation in ovarian tumor A2780 and the human colon cancer cell line HCT116 were evaluated and the complexes were found to be more cytotoxic than cisplatin.

Ever since it was discovered that the cationic ruthenium complex $[Ru(bpy)_2(dppz)]^{2+}$ functions as a molecular light-switch for DNA, there has been great interest in the binding properties of polypyridyl complexes of d^6 octahedral ions, to function as highly sensitive molecular probes.[11–13] These complexes offer rich photophysical and photochemical properties, expanding their utility beyond chemical recognition. As the cellular uptake characteristics of small molecules which interact with DNA are critical to their application as therapeutic, diagnostic or imaging agents, research began focusing on exploring cellular uptake of the molecular light-switch and similar complexes, particularly as these ruthenium complexes have well described synthetic routes, high stability, and luminescence activity making them

attractive candidates for cellular studies. It was found that the classic and structurally simplest $[Ru(bpy)_2(dppz)]^{2+}$, and $[Ru(phen)_2(dppz)$ were unable to permeate the cells due to their low lipophilicity. Work carried out by the Barton group showed that cellular uptake was facilitated by increasing the lipophilicity of the complex $[Ru(DIP)_2(dppz)]^{2+}$(*Figure 4.3)*.[14] There are various methods to examine cellular accumulation of these complexes: as they are frequently luminescent, facile characterisation can occur through fluorometry, confocal microscopy and flow cytometry, whilst inductively coupled plasma mass spectrometry (ICP-MS) can directly measure ruthenium concentrations.[14]

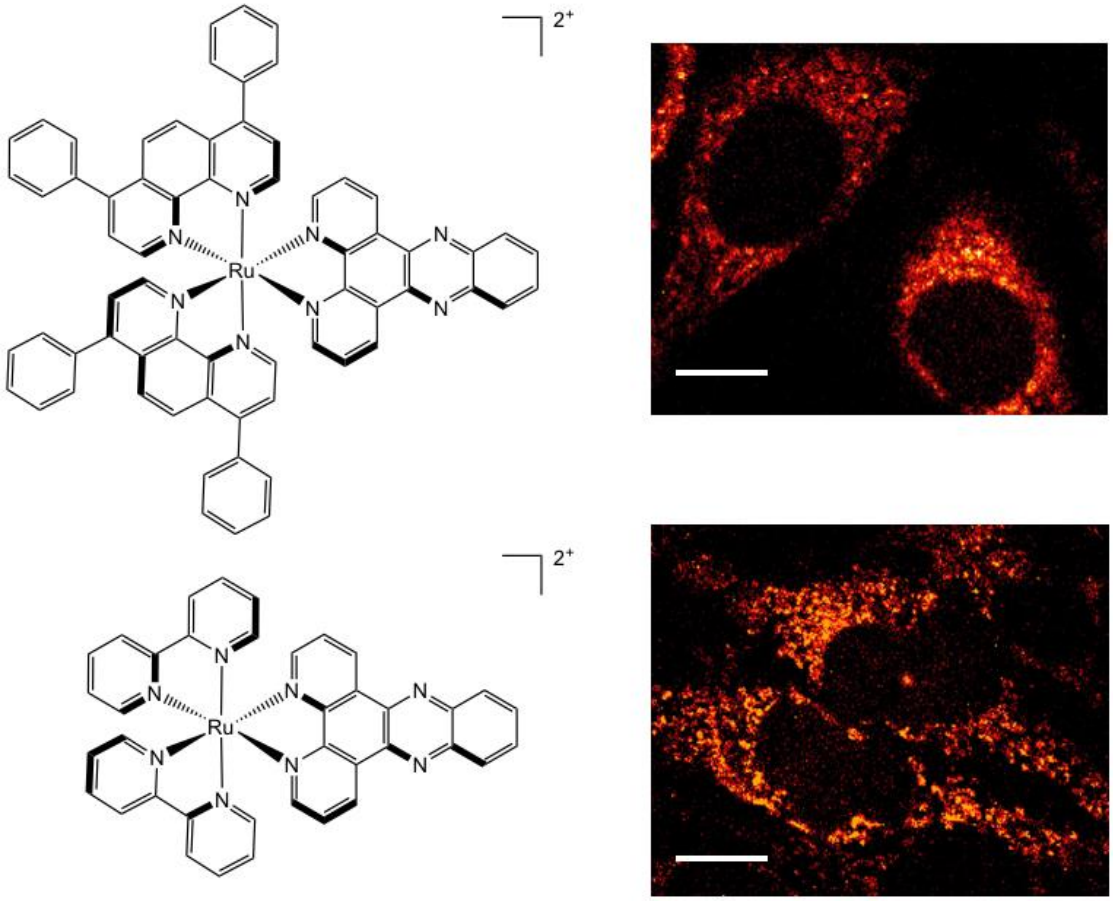

Figure 4.3: The lipophilic complex of [Ru(DIP)2(dppz)]2+ is observed inside HeLa cells at lower concentrations and shorter times (top, 5 μM for 2 h) than $[Ru(bpy)_2(dppz)]^{2+}$ (bottom, 20 μM for 72 h). Structures of the complexes are shown at the left, scale bars are 10 μm.[14]

4.2 Iridium polypyridyl complexes

While ruthenium-based anticancer agents have attracted significant attention in the realm of inorganic medicinal chemistry, over the past decade or so, iridium complexes have received increasing attention in therapeutic and bioanalytical applications.[15] Due to their large Stokes shifts (more than 100 nm), long luminescence lifetimes (100 ns to 1 ms), and enhanced photostabilities (less photobleaching), iridium(III) complexes are extremely attractive in the bioimaging field.[16] With all this in mind, and the increased phototunability of iridium complexes, it was only logical to investigate cellular activity. Iridium complexes are also very promising alternatives to platinum-based metallo-anticancer drugs, as demonstrated by the groups of Meggers and Sadler.[17,18]

4.2.1 Live cell imaging of Ir-dppz complexes

Since the previous chapter has shown that the newly synthesised complexes bind to DNA with high affinity through an intercalative manner, their cellular uptake can, potentially, be measured by luminescent microscopy. Therefore MCF-7 human breast cancer cell lines were incubated with each of the iridium complexes **1-3** and cellular uptake was examined using CLSM (confocal laser scanning microscopy) and widefield microscopy. In each individual case, the Ir(III) complex was excited at 390 m, using a He-Ne laser and the luminescence emission at 500-600 nm was recorded. These luminescent properties mean that each Ir-dppz complex has a Stokes shift of >150 nm, which is a considerable advantage in an imaging context. This cell line was chosen because they are easy to handle, exhibit a relatively high degree of homogeneity, and provide a quick growth rate of cell replication. To scope the properties of the complexes a range of concentrations and staining times were monitored using confocal microscopy. Images courtesy of Dr. Caroline Glover and Dr. Sree Sreedharan.

4.2.2 $[Ir(bpy)_2(dppz)]^{3+}$ cellular uptake

As shown by *Figure 4.4* below, trial and error showed that incubation of MCF-7 cells with **1** (200 µM, 24 hours) displays *in cellulo* luminescence in live cells.

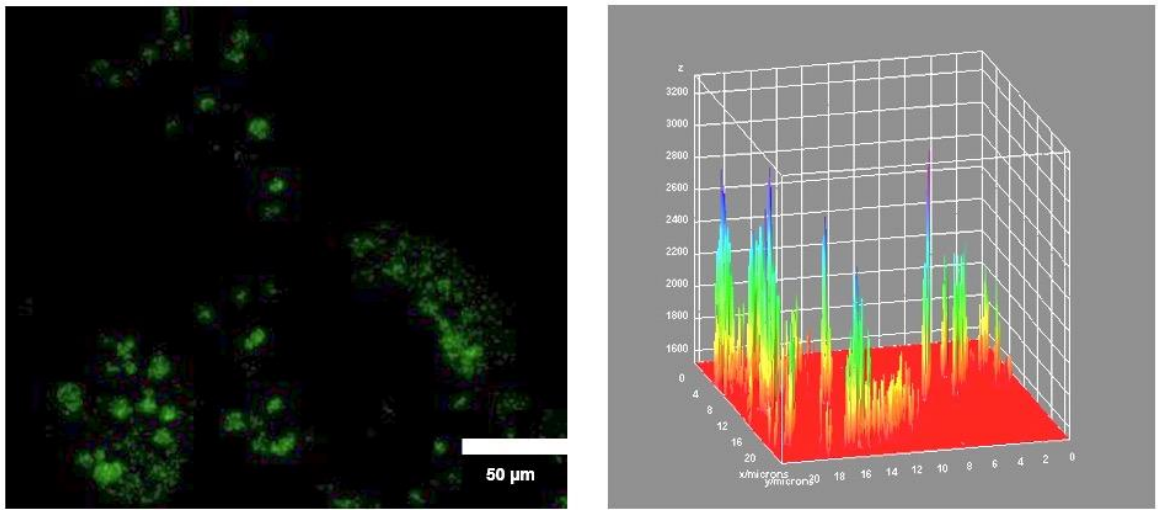

*Figure 4.4: Left - wide field microscopy luminescence emission of MCF-7 cells incubated with **1** (200 µM, 24 hours). Right – an intensity map of the cellular uptake.*

Although research has been largely focussed on the development of metal complexes as cellular probes, direct imaging of DNA with ruthenium systems have had limited success. The Ru^{II} molecular light-switch complex which is isostructural, and similar analogues to **1**, displays no/ poor live cellular uptake due to limited cell permeability. In order to facilitate cellular uptake of such complexes, more lipophilic ligands or hormone/peptide conjugates had to be incorporated.[14,19,20]

4.2.3 $[Ir(phen)_2(dppz)]^{3+}$ cellular uptake

As shown in *Figure 4.5* incubation of MCF-7 cells with **2** (400 µM, 24 hours) appears to display more distinct luminescence in CLSM imaging of live cells.

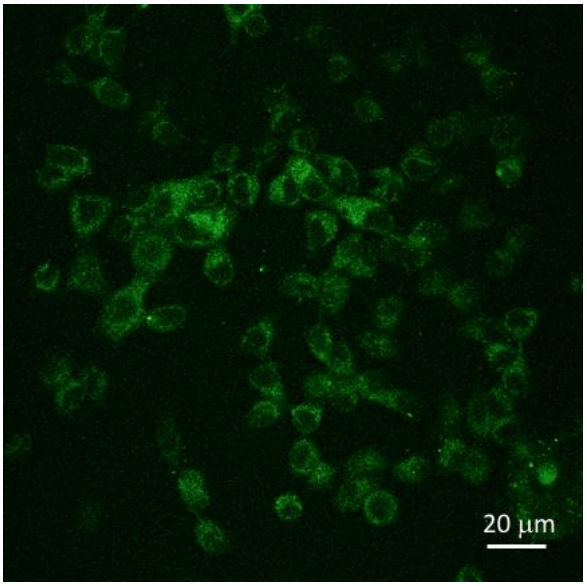

*Figure 4.5: Confocal microscope image of MCF-7 cell lines stained with **2** (400 µM, 24 hours).*

Comparing *Figures 4.4* and *4.5* shows **2** has an increased cellular uptake within live MCF-7 cell lines. This could be due to the incorporation of the phenanthroline ligands creating an increased lipophilic character, promoting cell permeation. Lipophilicity is one of the most influential factors in the biological activity of a species The affinity for a lipophilic environment facilitates the transport of membranes through cellular membranes.[21] Although the incorporation of phenanthroline ligands would increase the size of the complex, the increase in lipophilicity must promote more cellular uptake.

4.2.4 $[Ir(phen)_2(C^N\ dppz)]^{2+}$

As shown in *Figure 4.6*, incubation of MCF-7 cells with **3** (400 μM, 24 hours) also results in intracellular luminescence.

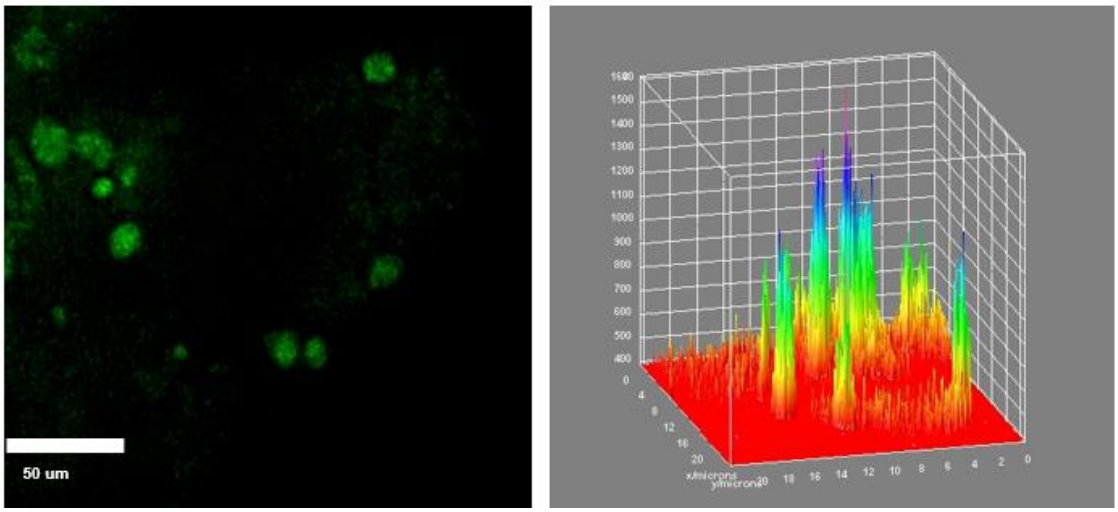

*Figure 6: Left - wide field microscopy luminescence emission of MCF-7 cells incubated with **3** (200 μM, 24 hours). Right – an intensity map of the cellular uptake.*

Complex **3** is indeed taken up by the live MCF-7 cell line, but provides less intense staining than **1** and **2**. This is unusual as the dicationic complex has a lower electronic charge than the other complexes and would be expected to be more lipophillic. Future work could investigate the exact mode of cellular uptake for all three of the complexes in this study.

4.2.5 Co-localisation experiments

The location and physiological effects of a complex can be closely related. So, after these complexes were found to be successfully taken up by the cells, attention was drawn to determining their sub-cellular location using colocalisation studies. One of the most common applications of emission microscopy is to compare the subcellular distributions of two luminescently labelled molecules.[23] Colocalisation refers to the observation of spatial overlap between two (or more) fluorescent labels and is conveniently measured by the Pearson's correlation. This is the measure of strength of the linear relationship between two variables and is referred to as the correlation coefficient. This is a quantitative statistical measure of colocalisation based in the pixel-intensity correlation of two fluorescent channels.[24]

4.2.6 $[Ir(bpy)_2(dppz)]^{3+}$ colocalisation experiments

Co-staining MCF-7 cells with the commonly used organelle stains Mitotracker red and Lysotracker red, indicated that **1** showed a preferential uptake into lysosomes (*Figures 4.7* and *4.8*). Complex **1** produced Pearson coefficients of 0.21 with mitochondria and 0.96 with lysosomes.

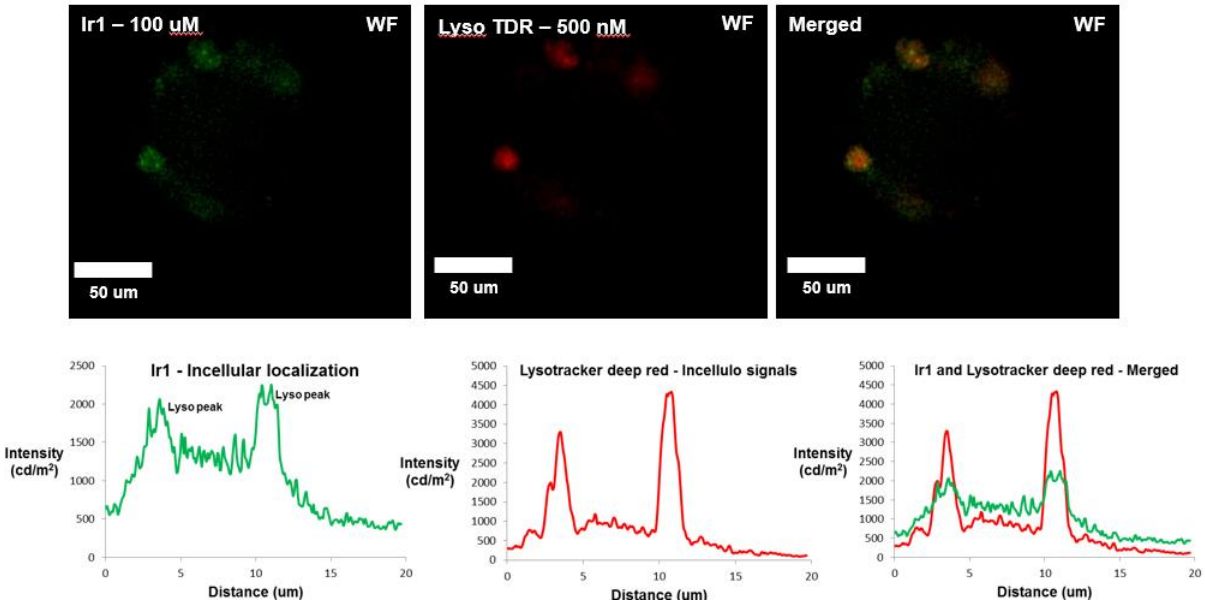

*Figure 4.7: Top (left to right) – wide field luminescence microscopy images of **1** (100 µM, 24 hrs), Lysotracker Red (500 nM, 30 minutes), and overlay of both images (P= 0.96). Bottom (left to right) – Luminescence intensity graphs of **1**, Lysotracker Red, and an overlay of the two.*

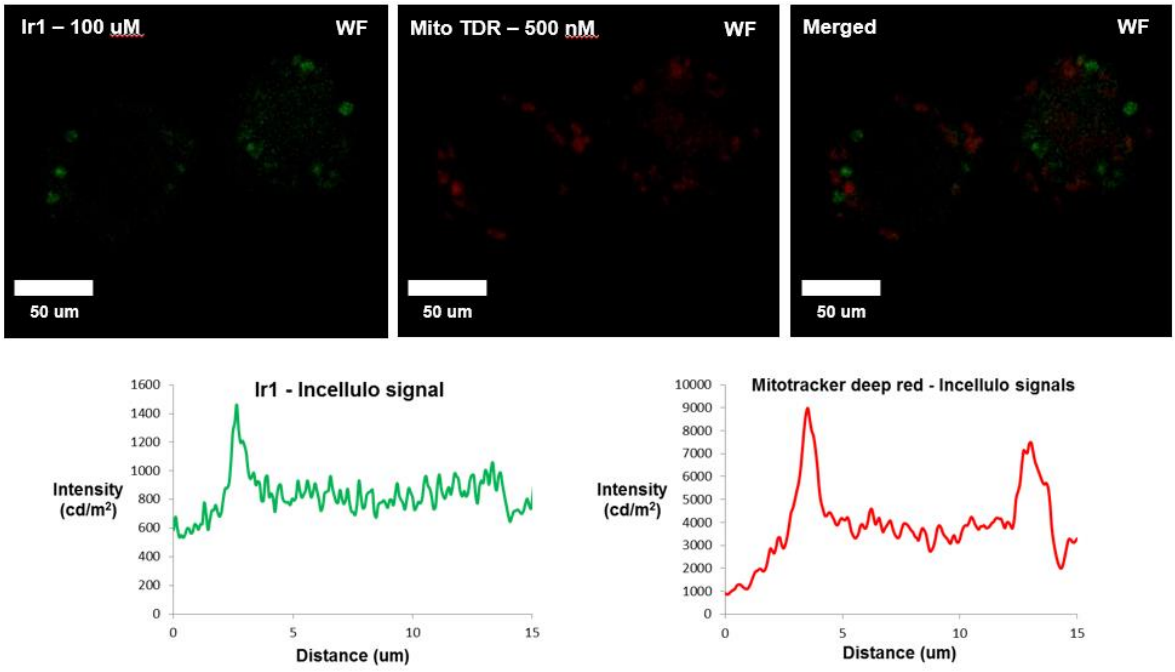

*Figure 4.8: Figure 7: Top (left to right) – wide field luminescence microscopy images of **1** (100 µM, 24 hrs) Mitotracker Red (500 nM, 30 minutes), and overlay of both images (P=0.21). Bottom (left to right) – Luminescence intensity graphs of **1** and Mitotracker Red.*

4.2.7 $[Ir(phen)_2(dppz)]^{3+}$ colocalisation experiment

Through similar experiments the location of $[Ir(phen)_2(dppz)]^{3+}$ was shown to be within the mitochondria. An example of colocalisation experiment with Mitotracker Red is seen in the image below (*Figure 4.9).*

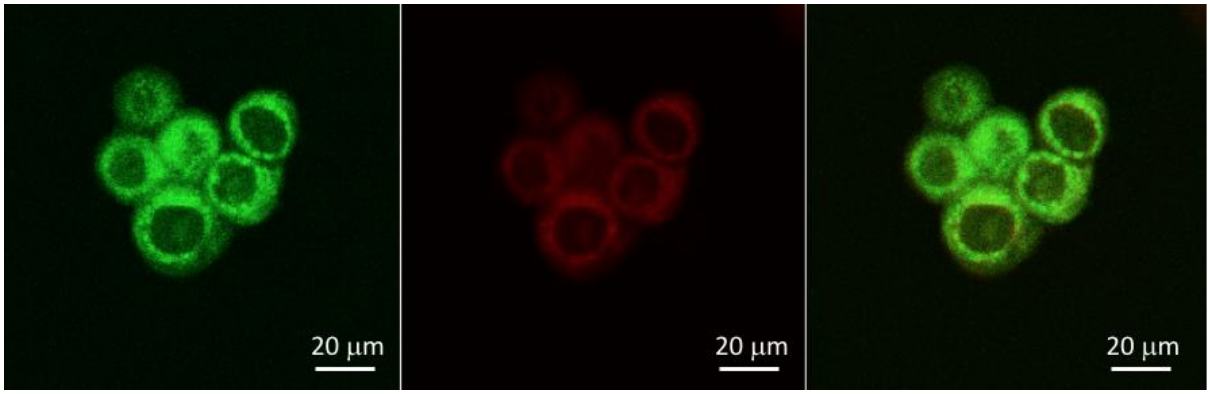

*Figure 4.9: Confocal microscope image of MCF-7 cells stained with left – **2** (400 μM, 1 hr), middle – 100 nM of Mitotracker Red® for 15 minutes, right – an overlay of both images with a Pearson's colocalisation coefficient = 0.93.*

No further colocalisation experiments were carried out as this provided a Pearson's correlation coefficient of 0.93.

4.2.8 $[Ir(phen)_2(C^N\ dppz)]^{2+}$ colocalisation experiments

Finally co-staining MCF-7 cells with the commonly used organelle stains Mitotracker red, Lysotracker red, indicated that **3**, like 1, showed preferential uptake into the lysosomes (*Figures 4.10* and 4.*11).* Complex **3** produced Pearson coefficients of 0.18 with mitochondria and 0.97 with lysosomes.

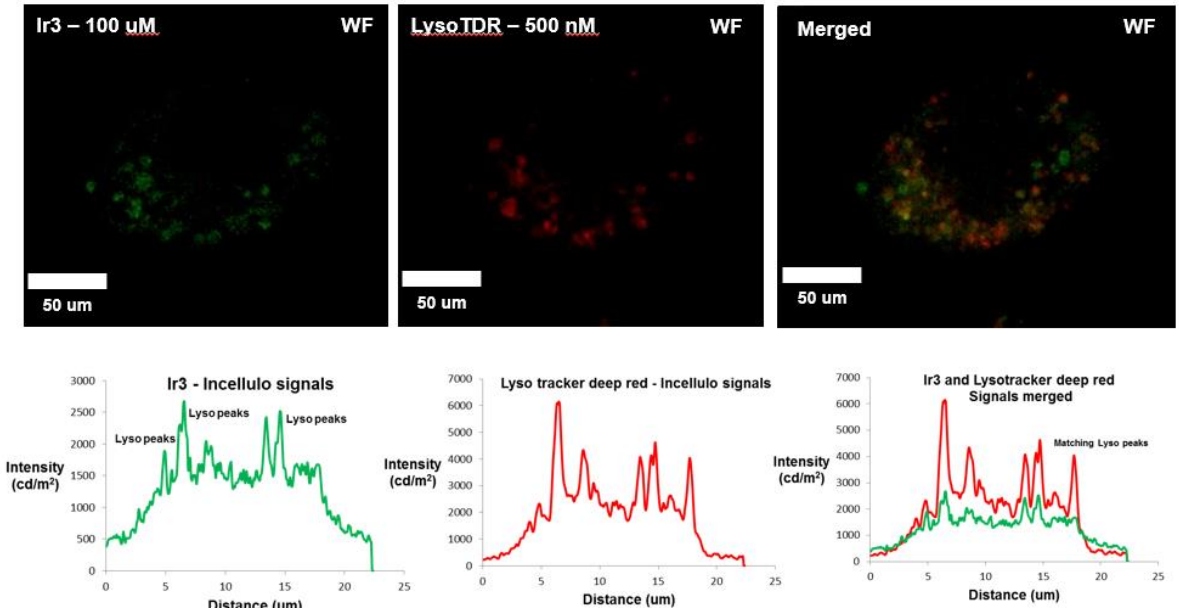

*Figure 4.10: Top (left to right) – wide field luminescence microscopy images of **3** (100 µM, 24 hrs), Lysotracker Red (500 nM, 30 minutes), and overlay of both images (P= 0.97). Bottom (left to right) – Luminescence intensity graphs of **3**, Lysotracker Red, and an overlay of the two.*

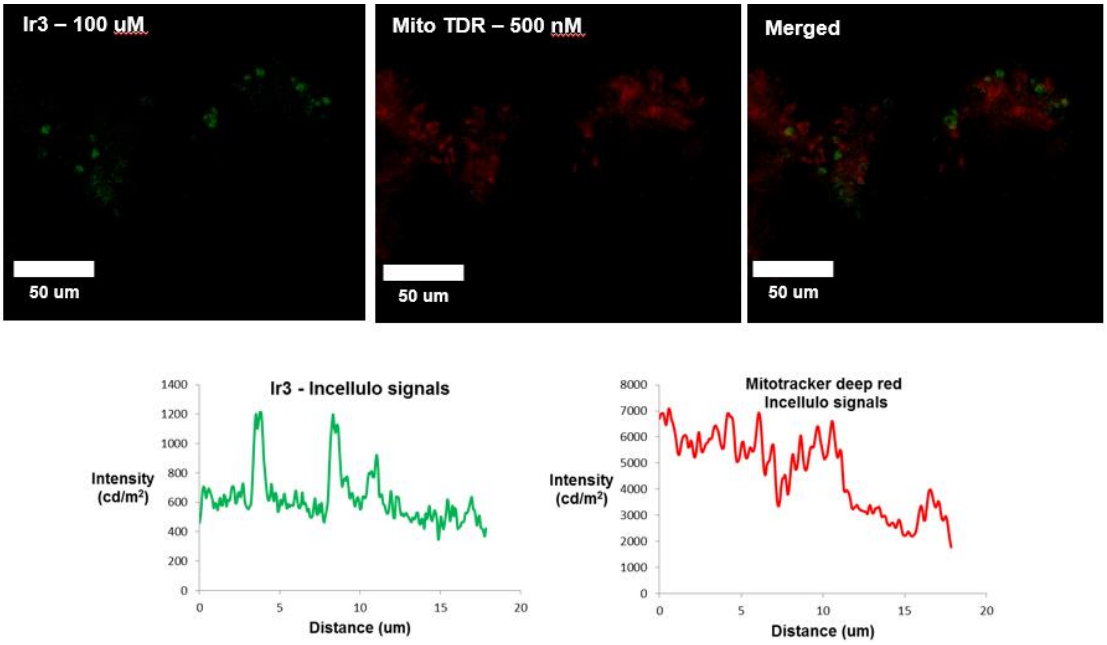

*Figure 4.11: Figure 7: Top (left to right) – wide field luminescence microscopy images of **3** (100 µM, 24 hrs) Mitotracker Red (500 nM, 30 minutes), and overlay of both images (P=0.18). Bottom (left to right) – Luminescence intensity graphs of **3** and Mitotracker Red.*

From the above experiments it is clear that all three complexes **(1-3)** are up taken by MCF-7 human breast cancer cell line. Although the complexes are structurally similar, from the colocalisation data produced, they enter different subcellular location. **1** and **3** are lysosome stains and poor mitochondria stains, with **2** being a mitochondria stain. Although the complexes appear structurally similar, previous DFT calculations prove that their electronic properties differ. From comparing all images obtained it can be concluded that the mitochondrial stain **2** is taken up more readily than **1** and **3** by the MCF-7 cell line. This seems to be due to the increased lipophilicity of the ancillary ligands .

4.3 Inductively coupled mass spectrometry (ICP-MS)

To investigate the intracellular accumulation of **2** within MCF-7 cells inductively coupled mass spectrometry (ICP-MS) analysis of metal content was used after treatment of 400 μM complex concentrations for 4 and 24 hours (*Figure 4.12).* This was carried out in serum and serum free conditions to monitor any uptake changes, as previous research showed that the absence of serum proteins greatly altered the cytotoxicity of compounds of interest by increasing the level of cellular uptake.[25] The metal concentration within the MCF-7 cells were calculated by taking the initial concentration of iridium in μg L^{-1} from the sample submitted. From the known volume, relative molecular mass of the iridium complex and the chemical structure of the complex the total number of moles could be calculated. The intracellular concentration could then be obtained by applying the number of moles to the previously determined number and volume of cells per sample, presented in mmol L^{-1}.

The uptake of **2** into MCF-7 cell line occurred relatively rapidly with approximate intracellular concentration of 200 μM after 4 hours, only increasing to 250 μM after 24 hours. Without serum present, there is an increased uptake with intracellular concentrations of 235 μM and 447 μM after 4 and 24 hours respectfully (*Figure 4.13).* Standard cell culture media are commonly supplemented with animal serum as a source of nutrients. Serum albumin proteins are likely candidates in live cell culture serum to interact with metal complexes. This protein-metal coordination complex interaction has been suggested to impair the cellular uptake and therefore its potency.[26] This provides an explanation as to why the increase in intracellular concentration is observed in serum free conditions because this interaction is not present. Time restraints prevented further studies with **1** and **3**.

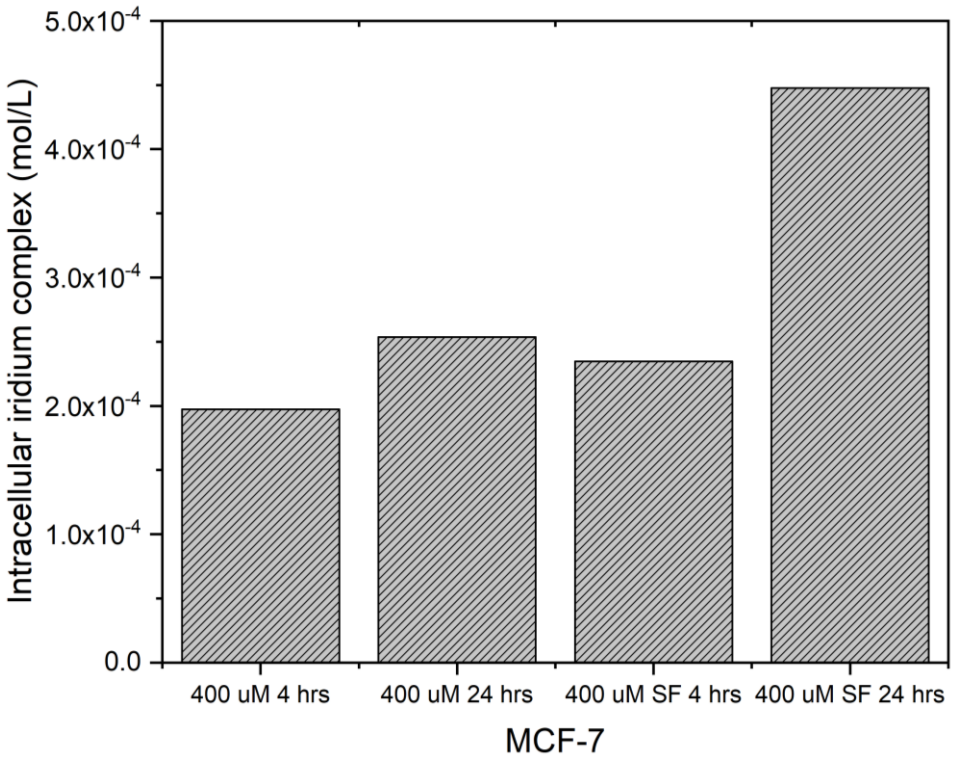

Figure 4.12: Intracellular concentration of $[Ir(phen)_2(dppz)]^{3+}$.

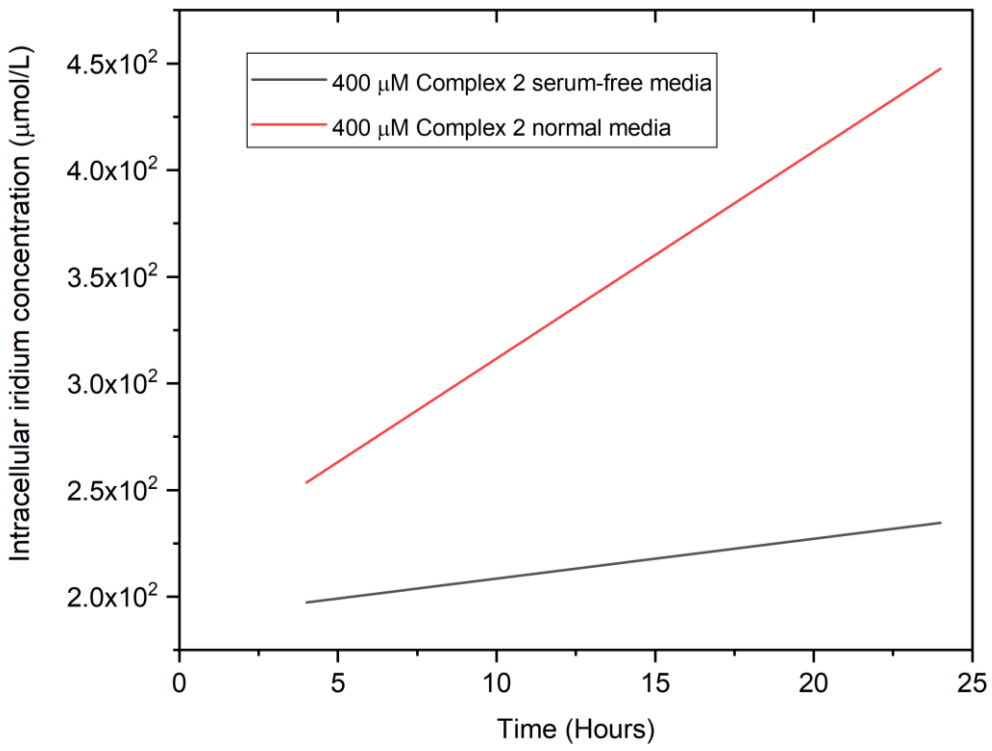

*Figure 4.13: Graph showing the increase in intracellular concentration of **2** in serum free conditions vs normal media.*

4.4 Cytotoxicity Studies

As **2** binds to DNA with a high affinity and seems to be taken up by MCF-7 human breast cancer cells more readily than complexes **1** and **3**, due to time restraints, this complex was the only candidate to undergo a full cytotoxicity assessment.

4.4.1 IC_{50} Determination

A commonly used reference for cytotoxicity is the half maximal inhibitory concentration, the IC_{50} value, which is required to inhibit cellular processes in half of the treated population. The most common experimental technique to determine cell viability is via an MTT assay (3-(4,5-dimethylthiazol-2-yl)-2,5-diphenyltetrazolium bromide, a tetrozole) assay. This is a colourimetric assay that measures only metabolically active cells[27] that relies on the ability of mitochondrial dehydrogenase enzymes to convert the tetrazole to a purple formazan precipitate. This colour change intensity can therefore be measured using multiwell scanning spectrophotometers. The tetrazolium ring is cleaved in active mitochondria, and so the reaction only occurs in living cells.[27] The level of MTT cleavage by viable cells is directly proportional to the number of cells as a function of time. Thus, any increase or decrease in viable cell number can be detected by measuring formazan concentration with a plate reader. The ease, sensitivity, rapidity, and low cost have made the MTT method one of the most widely used assays for measuring acute cytotoxic effects of compounds.[28] The general purpose of the MTT assay is to measure viable cells in relatively high throughput (96-well plates), without the need for elaborate cell counting (*Figure 4.14).*

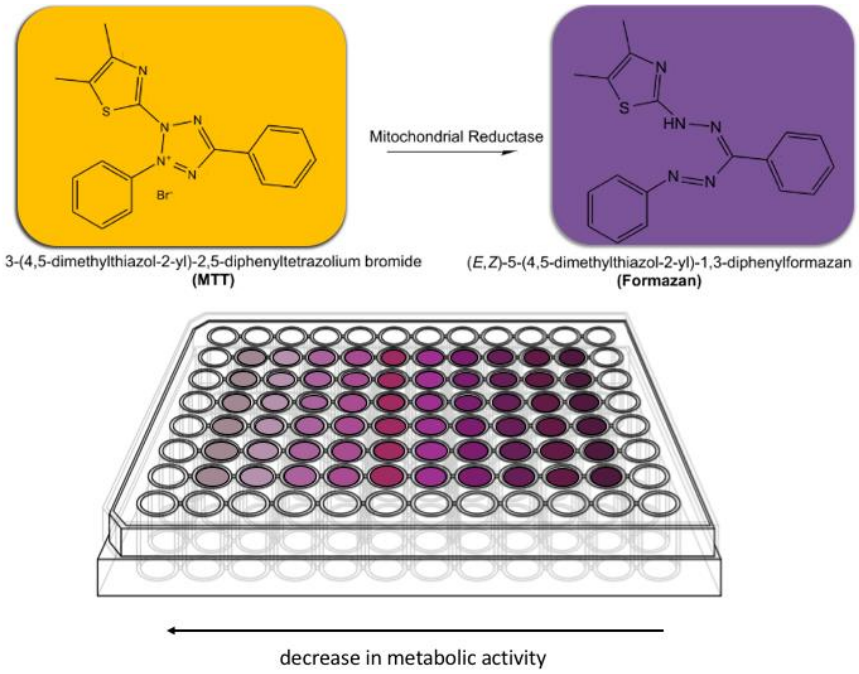

Figure 4.14: Top – conversion of yellow MTT to the purple formazan. Bottom – schematic of a 96-well plate MTT assay showing differing cell viabilities. The more toxic a complex the less colour is observed. The IC_{50}^{-} of the complex can be determined by measuring the amount of formazan present with a spectrophotometer followed by subsequent calculations.

As in the imaging studies, the MCF-7 cell line was used as this is one of the most studied human breast cancer cell lines, and previous results from this line have had a fundamental impact upon breast cancer research and patient outcomes.[25] A 48 hour MTT assay was carried out to determine the IC_{50} value of the activity of **2** against the cell line MCF-7. To ensure experimental techniques were in line with literature methods cisplatin was employed as a positive control with the results from the following procedures showed below (*Figure 4.15*). The IC_{50} value for cisplatin against MCF-7 was calculated, *via* interpolation of the curve, as 10 µM, this value is in line with previous literature values.[26] The IC_{50} value for **2** was calculated alongside cisplatin as 177µM showing no significant cytotoxicity towards the MCF-7 breast cancer cell line.

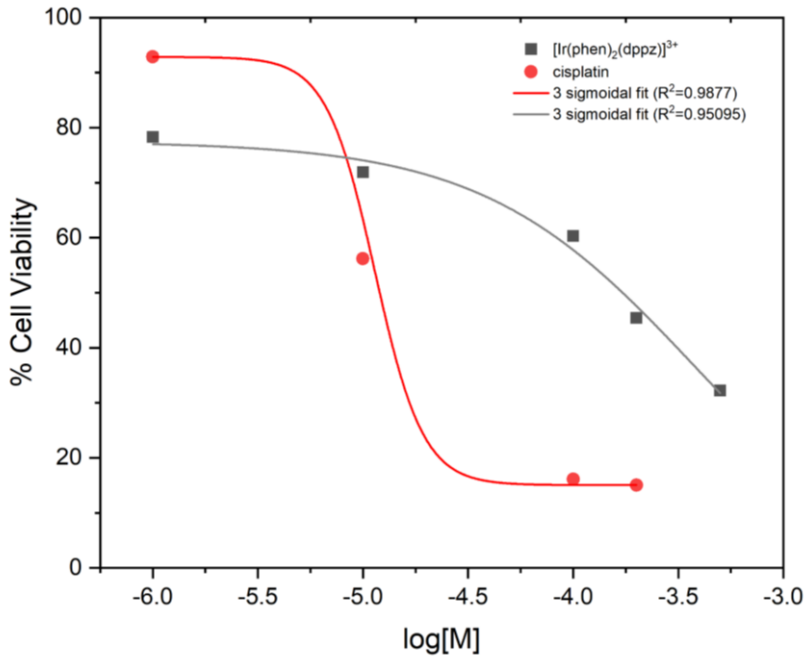

Figure 4.15: Graph showing IC_{50} values of $[Ir(phen)_2(dppz)]^{3+}$ and cisplatin on MCF-7 cell lines for 48 hours.

Compound	Exposure time (hrs)	IC_{50} (μM)
$[Ir(phen)_2(dppz)]^{3+}$	**48**	**177**
Cisplatin	**48**	**10**

4.5 Phototoxicity Studies

Chapter 3 showed that the Ir^{III} complexes associate with CT-DNA through intercalation, and irradiation of the complexes in the presence of the plasmid DNA pBR322 resulted in the cleavage of the supercoiled form (I) to the nicked form (II). Follow up determination of the photocleavage mechanisms showed that this was due to the production of the highly damaging singlet oxygen radical. Increased phototoxic activity of such complexes is highly attractive for photosensitizers for photodynamic therapy (PDT). Photodynamic therapy involves administration of a photosensitizing agent (prodrug), which can be activated by light of a specific wavelength resulting in irreversible photodamage to tumour tissues.[29] These photosensitizer complexes induce cellular and tissue effects on irradiation in an oxygen-dependant manner by transferring energy from light to molecular oxygen to generate a reactive

oxygen species (ROS).[30] As PDT relies on light activation to convert the nontoxic sensitizer into a toxic species, there needs to be a large difference between light-induced and dark cytotoxicity. This can be calculated from the IC_{50} in the dark divided by the IC_{50} in the dark, this is called the phototoxic index (PI), and can be graded into mild, moderate, or severe (*Table 4.1*).[31]

	Phototoxicity index
Absent phototoxicity	<1.4
Mild	1.3-3.0
Moderate	>3.0-6.0
Severe	>6.0

As **2** has a singlet oxygen yield of 0.56, has proven to cleave plasmid DNA upon photoradiation, and localises within the mitochondria of live cells, there is a high chance that this compound will become more phototoxic to cells after subsequent radiation.

4.5.1 Light Irradiation Source Apparatus

The apparatus used to record phototoxicity measurements was a custom made device contained within an empty computer base unit consisting of a broadband illumination source. This device was referred to as the Light Irradiation Source Apparatus (LISA) (*Figure 4.16*).

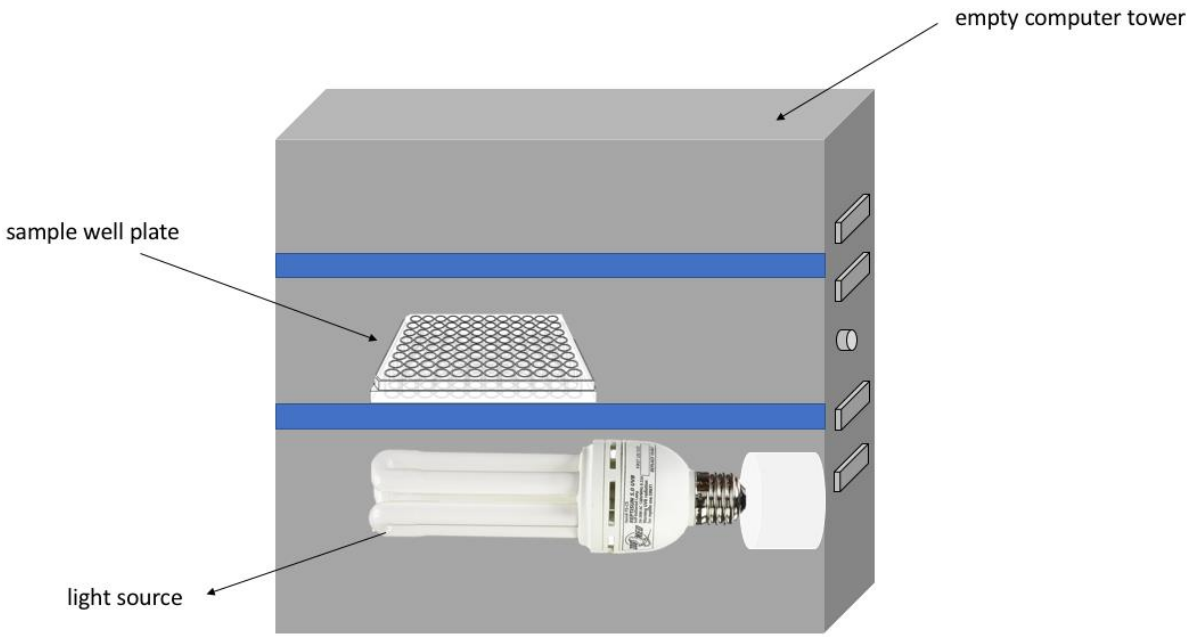

Figure 4.16: Schematic of the device used to measure phototoxicity: Light Irradiation Source Apparatus (LISA).

The same protocol was carried out for phototoxicity measurements as the IC_{50} determination mentioned previously. However, to investigate the toxicity after timed light irradiation of differing lengths four separate plates were employed. After 24 hours incubation of the cancer cell line with the complex, three plates underwent timed exposures in the LISA while a dark control remained in the incubator throughout. Each plate was placed into the device for 5, 15, or 30 minutes to monitor the variation of toxicity due to the increase of light exposure. The dark control was essential to provide a direct comparison standard assessing any phototoxicity upon irradiation. Untreated control wells were used in all the experiments to serve the purpose of delineating maximum cell viability. To prevent any damaging effects of the radiation alone to result in false positive results of increased phototoxicity of the compounds. Using the optimised protocol the activity of $[Ir(phen)_2(dppz)]^{3+}$ against MCF-7 cell lines was investigated using a concentration range of 1 – 200 µM, resulting in the effect shown below (*Figure 4.17*).

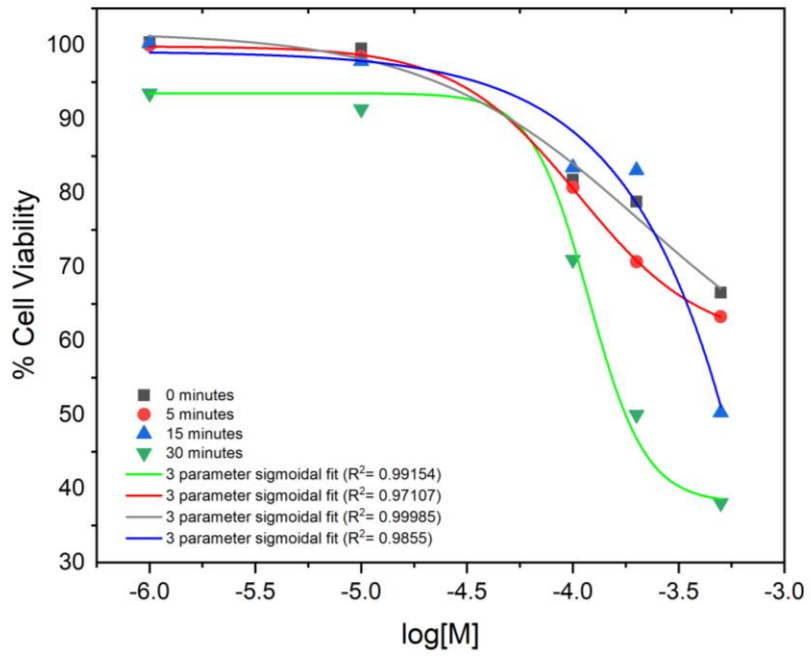

Figure 4.17: Graph showing the effect of light exposure to cytotoxicity of $[Ir(phen)_2(dppz)]^{3+}$.

Exposure Time (mins)	IC_{50} (μM)
0	--
5	--
15	316
30	100

An increase in exposure to light causes a decrease in cell viability, and phototoxicity. Bearing in mind that the compound has an IC_{50} value of 177 μM in the dark for 48 hours it is not highly cytotoxic to begin with. Here using this optimised protocol, the MTT assay is only 24 hours. For the time slots of 0 and 5 minutes, the compound does not reduce the cell viability to 50 % or less, meaning an IC_{50} value is unable to be calculated. There is a noticeable difference in the activity between 0 and 30 minutes exposure time, with the complex becoming more cytotoxic with irradiation.

4.6 Summary and Future Work

As the cell-free DNA binding studies confirmed the interaction of **1**-**3** with both CT- and plasmid- DNA, attention was turned to cellular studies. A crucial aspect for any proposed live cell applications is the cellular uptake and internalisation properties. Not only was it found that all of the complexes were successfully taken up by live MCF-7 breast cancer cell line, from sublocalisation investigations they were found to display differing cellular distributions. Complexes **1** and **3** were found to stain lysosomes preferentially, with complex **2** targeting the mitochondria. This was interesting as the well-known and studied Ru^{II} analogues, which are isostructural to this compound do not interact with cells. Staining with complex **2** produced higher intracellular concentration, produced the brightest microscopy images. Due to time constraints, only this complex was chosen to investigate cytotoxicity/phototoxicity properties.

Once it was known to successfully internalize within cells its toxicity was investigated through MTT assay both in the light and after exposure to a light source. Complex $\mathbf{2}^{+}$ showed little cytotoxicity in the dark; a 48 hour MTT assay resulted in an IC_{50} of 177 μM – which is high compared to classically cytotoxic cisplatin (IC_{50} = 10 μM). As previous DNA studies showed the complex to photocleave DNA during gel electrophoresis experiments, attention was then drawn to whether or not cytotoxicity increased upon photoirradiation. Results from the phototoxicity experiments showed that after longer irradiation times cell viability decreases, proving some phototoxicity activity.

Cellular uptake can be affected by alteration of the cellular media conditions. It was known that metal complexes can interact with serum albumin, reducing cytotoxic activity by decreasing cellular uptake. Inductively coupled mass spectrometry on **2** showed that in serum-free conditions, between a 4 hour and 24-hour testing period, there was a great increase in iridium content within cells. This is in contrast to in-serum conditions, where the intracellular concentrations remained steady with the experimental window. Follow up work in this area would be to carry out phototoxicity assays in completely serum free conditions. An increase in cellular uptake could cause an increase in both cytotoxicity and phototoxicity.

The cellular uptake, toxicity and phototoxicity properties of the remaining iridium complexes included in this thesis; $[Ir(bpy)_2(dppz)]^{3+}$ and $[Ir(phen)_2(C\text{^}N\ dppz)]^{2+}$ should also be

completed. It will be very interesting to investigate the cytotoxicity and phototoxicity of **3** as this complex was proven to produce the highest levels of the damaging singlet oxygen radical, but does not appear to cause large amounts of DNA damage in cell free conditions.

4.7 References

1. N. Rusk, The fluorescence microscope, *Nat. Cell Biol*, 2009, S8–S9.
2. D. L. Ma, H. Z. He, K. H. Leung, D. S. H. Chan and C. H. Leung, Bioactive luminescent transition-metal complexes for biomedical applications, *Angew. Chemie - Int. Ed.*, 2013, **52**, 7666–7682.
3. J. A. Thomas, Optical imaging probes for biomolecules : an introductory perspective, *Chem. Soc. Rev.*, 2015, **44**, 4494–4500.
4. J. T. Kumar S, Theranostics: A Way of Modern Medical Diagnostics and the Role of Chitosan, *J. Mol. Genet. Med.*, 2014, **09**, 1–5.
5. J. Funkhouser, Reintroducing pharma: Theranositc revolution, *Curr. Drug Discov. 2*.
6. C. R. Cardoso, M. V. S. Lima, J. Cheleski, E. J. Peterson, T. Venâncio, N. P. Farrell and R. M. Carlos, Luminescent ruthenium complexes for theranostic applications, *J. Med. Chem.*, 2014, **57**, 4906–4915.
7. G. Sava, S. Zorzet, T. Giraldi, G. Mestroni and G. Zassinovich, Antineoplastic activity and toxicity of an organometallic complex of ruthenium(II) in comparison with cis-PDD in mice bearing solid malignant neoplasms, *Eur. J. Cancer Clin. Oncol.*, 1984, **20**, 841–847.
8. W. Guo, W. Zheng, Q. Luo, X. Li, Y. Zhao, S. Xiong and F. Wang, Transferrin serves as a mediator to deliver organometallic ruthenium(II) anticancer complexes into cells, *Inorg. Chem.*, 2013, **52**, 5328–5338.
9. S. P. Fricker, *Medicinal organometallic chemistry*, 2011, vol. 55.
10. R. Gagliardi, G. Sava, S. Pacor, G. Mestroni and E. Alessio, Antimetastatic action and toxicity on healthy tissues of Na[trans-RuCl4(DMSO)Im] in the mouse, *Clin. Exp. Metastasis*, 1994, **12**, 93–100.
11. A. E. Friedman, J. K. Barton, J. C. Chambron, J. P. Sauvage, N. J. Turro and J. K. Barton, Molecular “Light Switch” for DNA: Ru(bpy)2(dppz)2+, *J. Am. Chem. Soc.*, 1990, **112**, 4960–4962.
12. M. R. Gill and J. A. Thomas, Ruthenium(ii) polypyridyl complexes and DNA—from structural probes to cellular imaging and therapeutics, *Chem. Soc. Rev.*, 2012, **41**, 3179.
13. A. C. Komor and J. K. Barton, The path for metal complexes to a DNA target, *Chem. Commun.*, 2013, **49**, 3617.
14. C. A. Puckett and J. K. Barton, Methods to explore cellular uptake of ruthenium

complexes, *J. Am. Chem. Soc.*, 2007, **129**, 46–47.

15. D. L. Ma, D. S. H. Chan and C. H. Leung, Group 9 organometallic compounds for therapeutic and bioanalytical applications, *Acc. Chem. Res.*, 2014, **47**, 3614–3631.
16. C. Jin, J. Liu, Y. Chen, R. Guan, C. Ouyang, Y. Zhu, L. Ji and H. Chao, Cyclometalated iridium(III) complexes as AIE phosphorescent probes for real-time monitoring of mitophagy in living cells, *Sci. Rep.*, 2016, **6**, 1–13.
17. A. Wilbuer, D. H. Vlecken, D. J. Schmitz, K. Kräling, K. Harms, C. P. Bagowski and E. Meggers, Ein Iridium-Komplex mit antiangiogenen Eigenschaften, *Angew. Chemie*, 2010, **122**, 3928–3932.
18. Z. Liu, I. Romero-Canelõn, B. Qamar, J. M. Hearn, A. Habtemariam, N. P. E. Barry, A. M. Pizarro, G. J. Clarkson and P. J. Sadler, The potent oxidant anticancer activity of organoiridium catalysts, *Angew. Chemie - Int. Ed.*, 2014, **53**, 3941–3946.
19. K. K. W. Lo, T. K. M. Lee, J. S. Y. Lau, W. L. Poon and S. H. Cheng, Luminescent biological probes derived from ruthenium(II) estradiol polypyridine complexes, *Inorg. Chem.*, 2008, **47**, 200–208.
20. U. Neugebauer, Y. Pellegrin, M. Devocelle, R. J. Forster, W. Signac, N. Moran and T. E. Keyes, Ruthenium polypyridyl peptide conjugates: Membrane permeable probes for cellular imaging, *Chem. Commun.*, 2008, **2**, 5307–5309.
21. E. Rutkowska, K. Pająk and K. Jóźwiak, Lipophilicity - Methods of determination and its role in medicinal chemistry, *Acta Pol. Pharm. - Drug Res.*, 2013, **70**, 3–18.
22. C. A. Puckett, R. J. Ernst and J. K. Barton, Exploring the cellular accumulation of metal complexes, *Dalt. Trans.*, 2010, **39**, 1159–1170.
23. K. W. Dunn, M. M. Kamocka and J. H. McDonald, A practical guide to evaluating colocalization in biological microscopy, *Am J Physiol Cell Physiol*, 2011, **300**, 723–742.
24. B. Moser, B. Hochreiter, R. Herbst and J. A. Schmid, Fluorescence colocalization microscopy analysis can be improved by combining object-recognition with pixel-intensity-correlation, *Biotechnol. J.*, , DOI:10.1002/biot.201600332.
25. A. V. Lee, S. Oesterreich and N. E. Davidson, MCF-7 Cells - Changing the Course of Breast Cancer Research and Care for 45 Years, *J. Natl. Cancer Inst.*, 2015, **107**, 1–4.
26. J. O. Suberu, I. Romero-Canelón, N. Sullivan, A. A. Lapkin and G. C. Barker, Comparative cytotoxicity of artemisinin and cisplatin and their interactions with chlorogenic acids in MCF7 breast cancer cells, *ChemMedChem*, 2014, **9**, 2791–2797.
27. T. Mosmann, Rapid colorimetric assay for cellular growth and survival: Application to proliferation and cytotoxicity assays, *J. Immunol. Methods*, 1983, **65**, 55–63.

28. J. van Meerloo, G. J. L. Kaspers and J. Cloos, in *Cancer Cell Culture*, Humana Press, New York, NY, 2nd edn., 2011, pp. 237–261.
29. Q. Dougherty, T.J., Gomer, C.J., Henderson, B.W., Jori, G., Kessel, D., Korbelik, M., Moan, J., Peng, Photodynamic therapy, *J. Natl. Cancer Inst.*, 1998, **90**, 889–905.
30. D. E. J. G. J. Dolmans, D. Fukumura and R. K. Jain, Photodynamic therapy for cancer, *Nat. Rev. Cancer*, 2003, **3**, 375–380.
31. H. W. Lim, H. Honigsmann and L. M. Hawk John, *Photodermatology*, CRC Press, 2007.

Chapter 5
Conclusions and future work

5.0 Conclusions

The studies presented in this thesis have produced interesting results that span the interface of chemistry and cell biology. Three novel iridium polypyridyl complexes were synthesises *via* an optimised synthetic route. UV-Visible and luminescence experiments exploring their photophysical properties were achieved showing that all three complexes could be photoexcited at around 390 nm, displaying consequential emissions around 500 nm. All three complexes, as expected, have long luminescent lifetimes due to the heavy atom effect: as iridium is a third row transition metal, the excited state originated from a formally forbidden electronic transition, producing long-lived lifetimes. All three complexes (**1**-**3**) have lifetimes in aqueous media, of 900 ns, 740 ns, 592 ns respectively, which increase when in an organic solvent environment; 1350 ns, 1478 ns, and 1645 ns, respectively. It seems the excited state of each of these complexes may be deactivated by interaction with the water molecules *via* hydrogen bonding. Density functional theoretical calculations were used to investigate the nature of the triplet excited state manifold in greater detail. For complexes **1** and **2**, the triplet excited-state, as expected, is largely on the dppz unit, whereas **3** that incorporates a cyclometalated dppz analogue, the spin density in the triplet state is localised onto an ancillary phenanthroline unit. Further DFT experiments on another complex $[Ir(bpy)_2(C\text{^}N\ dppz)]^{2+}$ produced similar behaviour, showing that this effect is due to the presence of a cyclometalated ligand. Previous and current work produced within the Thomas group has shown that resolved enantiomerically pure solutions of Ru^{II} polypyridyl complexes show differing biophysical and molecular properties; *i.e.* DNA binding affinities and cellular uptake. Chiral separation was attempted on all three complexes using chiral chromatography however was only successful for **2**. Unlike their ruthenium counter-parts, iridium complexes are pale in nature, some column visibility problems occurred (*see experimental section).*

Following the inorganic synthesis, cell free studies were carried out to establish any interaction with DNA. As there are three reversible binding modes with DNA (electrostatic, groove binding, and intercalation), viscosity measurements provided an experimentally sound way of distinguishing between these modes, as an increase in specific relative viscosity suggest binding through an intercalative manner. This is a consequence of the planar, aromatic unit of the metal complex residing between two nucleotide base pairs within the double helix. As a result, the viscosity of the system increases – which is not observed with groove binding or

electrostatic interactions. **1-3** all were found to bind to DNA through an intercalative manner. Collaborative work using Atomic Force Microscopy to measure the length of DNA in the presence of **1-3** also determined intercalative binding, consistent with previous viscosity data.

As these complexes are isostructural and similar to Ru^{II} DNA light-switch analogies, their photophysical behaviour upon DNA binding was investigated. In contrast to Ru^{II} complexes, addition of CT-DNA to aqueous solutions of **1-3** results in a substantial decrease in steady state luminescence. Fits of this data to the commonly employed McGhee Von Hippel model for non-cooperative binding yields the binding constants of **1-3**; 1.8 $x10^6$ M^{-1}, 2.9 $x10^6$ M^{-1}, and 2.7 $x10^6$ M^{-1}, r respectively. Strikingly, this data reveals that although **3** has a lower cationic charge, all complexes have almost identical binding affinities. Another significant observation is that, unlike previously reported Ir^{III} (dppz) systems, these affinities are highly comparable to the high affinities of Ru^{II}- based analogues.

The decrease in the steady-state luminescence of **1-3** upon addition of DNA could be consequence of redox quenching. Oxidative damage of DNA is most common at guanine residues due to the high oxidative potential of this base relative to cytosine, thymine and adenine. After successive additions of guanosine-5'-monophosphate (a nucleotide used as a monomer in RNA) to aqueous solutions of **1-3**, the luminescence of each complex decreased. Stern-Volmer kinetics showed that the excited states of all three complexes are quenched by guanosine-5'-monophospate at rates comparable to photo-oxidising agents (**1-3** 1.25 $x10^{10}$ $dm^3mol^{-1}s^{-1}$, 2.78 $x10^{10}$ $dm^3mol^{-1}s^{-1}$, 7.62 $x10^9$ $dm^3mol^{-1}s^{-1}$, respectfully). The photonuclease activity of **1-3** were investigated using supercoiled plasmid DNA. Initial gels simply investigating the effect of increasing the concentration of the complexes showed that for **1-3** the plasmid DNA migrated more slowly through the gel with increasing concentration. On irradiation, complexes **1** and **2** also produced photo-oxidation products that cleaved the plasmid DNA, producing scissions in the supercoiled structure. For **3** no photo-cleavage species were observed on the gel. All three complexes were found to both quench guanosine monophosphate, and produce singlet oxygen (with yields >40 %). DFT calculations on **1** and **2** show a triplet state localised on the dppz unit, whereas **3** has electronic density shifted onto the phenanthroline ancillary ligand. The different energies of the excited states between the complexes perhaps explains why **1** and **2** have photocleavage abilities after intercalation, but **3** does not. This is a matter for future studies.

As it was found that the luminescence of **1-3** was quenched during the intercalation of the dppz unit. Transient absorption spectroscopy provided a way to measure the intramolecular excited state processes. The kinetics of the complexes in the presence of DNA were quite different to that of the free complexes **1-3** in solution. When the complexes are intercalated in the DNA there is a rapid decay of excited states observed by transient absorption, dominated by species of lifetimes ~9 ps. Whereas in free solution the excited state has a lifetime in excess of > 80 ps. These results are consistent with expected rapid election transfer from the guanine bases of the DNA to the excited state.

The interdisciplinary nature of this investigation resulted in preliminary cell imaging and assays being conducted. Isostructural Ru^{II} –dppz based systems have little or no cellular uptake, surprisingly all three complexes were taken up within MCF-7 breast cancer cells. Successive co-localisation experiments using both confocal and wide-field microscopy techniques concluded that the complexes could be used as specific organelle stains. **1** and **3** were predominately localised within the lysosomes, and **2** was readily taken up by the mitochondria. As these are organelles have crucial roles within the cells, highlighting their structure and monitoring their function is of great importance in cell biology. The images produced using **2** as a molecular stain were of a higher quality than **1** and **3**. MTT assays on complex **2** revealed that it is not toxic in the dark, however subsequent phototoxicity measurements proved that with increased irradiation times the iridium complex became more toxic. Further investigations using ICP-MS revealed increased cellular uptake in serum free conditions suggesting the complex has a protein target in serum media.

5.1 Future work

Following the clinical success of platinum anticancer drugs much interest has been in the design of metal-based anticancer drugs. The drawbacks of these platinum species include severe toxicity and resistance. Attention has been driven towards new metallo drugs, such as iridium complexes, which possess attractive phototunability properties producing a tool kit to design specific drug targeting species. Complex **2** was localised in the mitochondria of MCF-7 breast cancer cells during preliminary experiments in this thesis.. Further studies into structural modification of iridium polypyridyl complexes to fine-tune not only the emission properties, but the cellular uptake levels and intercellular localisation also to explore the field of Ir^{III} theranostic agents deeper.

Chapter 6
Experimental

6.0 Experimental

6.1 Materials and Equipment

6.1.1 Chemicals

All chemicals and solvents were purchased from commercial sources and were used as supplied unless stated otherwise. Iridium complexes were treated as toxic

6.1.2 Nuclear Magnetic Resonance (NMR) Spectroscopy

^{1}H NMR spectra were recorded on a Bruker AM250 machine working in Fourier transform mode. The following abbreviations are used in the annotation of ^{1}H spectra: s = singlet, d = doublet, dd = doublet of doublets, t = triplet and m = multiplet.

6.1.3 Mass Spectrometry (MS)

Fast-atom bombardment (FAB) mass spectra (MS) were recorded on a Kratos MS80 mass spectrometer working in positive ion mode.

6.1.4 UV-Visible Absorption Spectroscopy

All UV-Visible spectra were recorded on a thermos regulated Varian-Carey Bio-300 UV-Visible spectrometer, using quartz cells of 10 mm path length at 25 °C. Spectra were baseline corrected using Cary Win UV software and were diluted accordingly to give readings between 0.2 and 1.0 absorbance units.

6.1.5 Luminescence Spectroscopy

Luminescence spectra were recorded on a thermos regulated Jobin-Yvon FluoroMax-3 spectrophotometer operating in luminescence wavelength scan mode at 25 °C, with excitation and emission slit widths at 5 nm.

6.2 DNA Binding Studies

6.2.1 Buffer Preparation

TRIS buffer (pH 7.4) was prepared using Trizma HCl (Tris(hydroxymethyl)aminomethane base at 5 mM concentrations in 25 mM NaCl. Trizma HCl and NaCl were measured into a volumetric flask and dissolved in deionised water (Millipore HPLC grade). The pH was adjusted using dilute HCl and additional water to achieve the correct volume. Buffer solutions were passed through a 0.2 micron Millipore filter and stored in a sterile glass bottle in the fridge at 4 °C.

6.2.2 DNA Preparation

Calf Thymus DNA (CT DNA) was purchased from Sigma-Chemicals as the lyophilised solid sodium salt and used without any further purification. An average length of 200-300 base pairs was achieved by using a modified preparation by Chaires *et* al.[1] Stock solutions of CT-DNA were prepared by dissolving ~100 mgs of the solid material in 20 mL of tris buffer (5 mM Tris, 25 mM NaCl) and dialysed in tris buffer overnight in the refrigerator. The stock solution was sonicated in an ice bath for a total of 30 minutes using a Soniprep 150 ultrasonic disintegrator, fitted with a 19 mm diameter probe. Five-minute periods of sonication were used, followed by 5 mins of cooling. The purity of the DNA samples were quantified using conventional absorbance measurements by measuring the ratio of contaminants to DNA; with $A_{260}/A_{280} > 1.9$ indicating a protein free sample. The concentration of the resulting solutions were also determined per base pair (bp) by UV spectroscopy using $\varepsilon_{260} = 13200\ M^{-1}cm^{-1}$ for CT-DNA.

6.2.3 Agarose Gel Electrophoresis

Agarose powder (0.8 g) was dissolved in TAE (40 mM Tris-acetate, 1 mM EDTA) (100 mL) and heated autoclaved sterile glass bottle in the microwave for 30 seconds on/off until all dissolved and the solution was bubbling through. This solution was left to cool to room temperature and poured into a casting gel tray with a comb in place. SYBR™ safe DNA gel stain (3 μL) was added to the gel, which was left to solidify for 20-30 minutes. Once fully

solidified the comb was carefully removed ready for sample loading. Solutions made up to 30 mL with 5 μL, 336 ng/μL supercoiled pBR322 DNA were mixed with DNA gel Loading Dye (concentrated 6X) (6 μL) and using gilson pipettes equipped with longer tips the samples could be loaded into the wells. Gels were typically run at 100 mV for 20 mins however to achieve greater sample separation at 70 mV for 40 minutes. DNA was visualised using a Bio-Rad Chemidoc imaging system.

6.2.4 Photocleavage experiments using gel electrophoresis[2]

50 μL solutions of $[Ir(phen)_2(dppz)]^{3+}$ in tris buffer to concentrations of choice (*i.e.* 10 μM, 20 μM, 30 μM) were made up in the dark. Solutions were irradiated for 10 minutes using a M365L2 ThorLabs 365 LED (365 nm, 125 mW). The solutions were wrapped in foil after irradiation, loaded on the gel, and visualised using a Bio-Rad Chemidoc imaging system. To investigate the photocleavage mechanism the DNA cleavage reactions were performed in the presence of various external additives such as DMSO (4 μL), D_2O (4 μL), NaN_3 (4 μL, 200 μM), and KI (4 μL, 200 μM) for the mechanistic studies.

6.2.5 Viscometry

Viscometry experiments were performed on a 1 mL Cannon-Manning semi-micro viscometer (size 50) immersed in a thermostated water bath. The temperature was maintained within ± 0.1 °C using a dual coil system. The concentration of CT-DNA in the viscometer was kept at 50 μM bp^{-1}. Buffer solutions were allowed to stand in the viscometer for 1 hour before readings were taken. After the addition of CT-DNA the solution was left to equilibrate for 30 minutes. After each addition of the analyte to the system an equilibrium time of 20 mins was allowed before the flow times were recorded. After each addition the solution was drawn through the viscometer and mixed under vacuum 5 times before being left to equilibrate to ensure the solution was homogeneous. Times were recorded in triplicate to within 0.1 second of each other and averaged.

6.2.6 Luminescence Titrations

Luminescence titrations were carried out in a thermos regulated Jobin-Yvon FluoroMax-3 spectrophotometer.3 mL of tris buffer was loaded into a 10 mm path length luminescence cuvette and was allowed to equilibrate at 25 °C before a background reading was taken. A volume of buffer was removed and replaced the same volume of a stock solution of complex of 59 μM in the cuvette. After equilibration, the emission spectrum of the solution was recorded at 390 nm. 2 μL of a concentration stock of CT-DNA (16.4 mM) was added to the cuvette and mixed 10 times to ensure homogeneity. After leaving the sample to equilibrate for 5 minutes the emission spectrum was recorded. This procedure was repeated until the emission spectra became constant (approx. 20 DNA additions).

6.2.7 Singlet oxygen yield measurement

Singlet oxygen measurements were obtained by Dr. Luke McKenzie and Dylan Pritchard. Singlet oxygen was detected directly in an organic solution by measurement of singlet oxygen luminescence (λ_{max} ~1275 nm) following photoexcitation of the compound at 25 °C in air saturated dichloromethane (DCM) or acetonitrile. The yield of the formation of $^1O_2$, $\phi(^1O_2)$ was determined by measuring its phosphorescence intensity using an optically matched solution of phenalenone as a reverence sensitiser.[3]

6.2.8 Transient absorption spectroscopy

Experiment carried out with the help of Alexander Auty. The ultrafast transient absorption setup used, was comprised of a commercial detection instrument (Helios, Ultrafast Systems) and the following laser system. A Ti:Sapphire regenerative amplifier (Spitfire ACE PA-40, Spectra-Physics) provided 800 nm, 1.2 mJ pulses (40 fs fwhm, 10 kHz, 1.2mJ). A Ti:Sapphire oscillator provided 800 nm seed pulses (25 fs fwhm, 84 MHz) for the amplifier (Mai Tai, Spectra-Physics). Two Nd:YLF lasers (Empower, Spectra-Physics) were used to pump the amplifier. Sample excitation was provided by doubling a portion of the 800 nm output, in a β-barium borate crystal within a commercially available doubler/tripler (TimePlate, Photop Technologies), yielding 400 nm pulses. White light, supercontinuum, probe pulses were generated in situ using a portion of the Ti:Sapphire amplifier output, focused onto a CaF_2 (340 – 720 nm) crystal or a Sapphire crystal (460 – 850 nm, 850 – 1450 nm), allowing for the

generation of light spanning 340 nm – 1450 nm. Detection was performed by CMOS and InGAS sensors for UV/vis and near IR grating-dispersed spectra, respectively. The pump and probe polarisations were set to a magic angle geometry. Complex solutions all had an optical density of 0.4 at 455 nm with an addition of 220 μL of 10 mM DNA with 10 minute incubation time.

6.3 Synthesis

6.3.1 1,10-phenanthroline-5,6-dione

$(DPQ)^4$

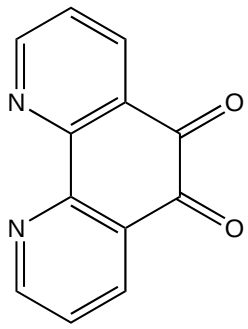

1,10-phenanthroline (5.4 g, 30 mmol) was dissolved in 60% concentrated sulphuric acid (70 mL). After dissolution solid potassium bromate (5.51 g, 33 mmol) was added slowly in batches over the course of an hour. This mixture was stirred at room temperature for 20 hours, and then poured over ice. The solution was neutralised to pH 7 using a saturated solution of sodium hydroxide. The solution was filtered, extracted with dichloromethane and evaporated to dryness. The crude produce was recrystallised from methanol and dried *in vacuo* to yield a bright yellow solid.

Mass (Yield): 2.9 g, (54 %).

TOF MS ES+ ***m/z:*** 211 $[MH^+]$.

^{1}H NMR (400 MHz, $CDCl_3$): d_H 9.14 (dd, J = 4.7, 1.9 Hz, 2H), 8.53 (dd, J = 8.1, 1.8 Hz, 2H), 7.61 (dd, J = 7.8, 4.8 Hz, 2H).

6.3.2 Benzo[h]quionline-5,6-dione

(C^N DPQ)[5]

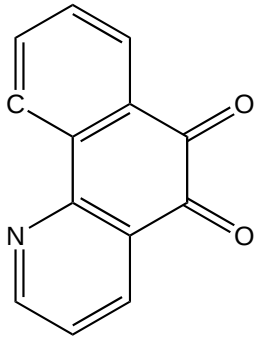

Benzo[h]quionline (1.04 g, 5.80 mmol) and iodine pentoxide (2.01 g, 6.00 mmol) were carefully dissolved in glacial acetic acid (30 mL). The solution was refluxed for 2 hours, left to cool, and filtered through a sinter. The acid was removed *under vacuo* to give a dark purple solid. The solid was washed with toluene and the solvent removed under *vacuo* and this process was repeated until the removed toluene was colourless. The crude product was recrystallised with ethanol yielding the pure product as orange crystals.

Mass, (Yield): 0.61 g, (59 %).

TOF MS ES+ *m/z:* 209 [MH^+].

^{1}H NMR (400 MHz, $CDCl_3$): δ_H 8.90 (dd, J = 4.7, 1.9 Hz, 1H), 8.71 (dd, J = 8.1, 0.8 Hz, 1H), 8.42 (dd, J = 7.8, 1.8 Hz, 1H), 8.22 (dd, J = 7.8, 1.1 Hz, 1H), 7.87 – 7.76 (m, 1H), 7.59 (td, J = 7.6, 1.2 Hz, 1H), 7.43 (dd, J = 7.9, 4.7 Hz, 1H).

6.3.3 Dipyrido[3,2-a:2',3'-*c*]phenazine

(dppz)[6]

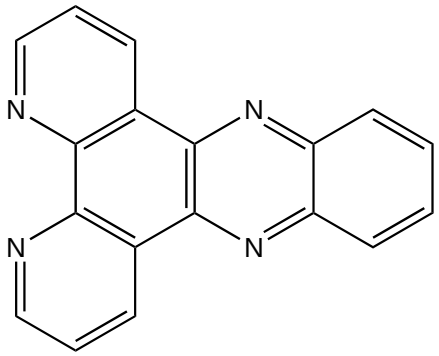

1,10-phenanthroline-5,6-dione (1.20 g, 5.70 mmol) and *o*-phenyldiamine (0.62 g, 5.74 mmol) were refluxed in ethanol (70 mL) for 2 hours. After cooling the solvent was removed *under vacuo* and the resulting crude product was recrystallised from ethanol. The crystals were collected and washed with ice cold water to produce the pure sandy coloured product.

Mass (Yield): 0.65 g (54 %)

TOF MS ES+ *m/z:* 283 [MH^+], 321 [MK^+]

^{1}H NMR (400 MHz, DMSO): δ_H = 9.50 (dd, J = 8.1 Hz, 1.8 Hz, 2H), 9.21 (dd, J = 4.4 Hz, 1.8 Hz, 2H), 8.37 (dd, J = 6.5 Hz, 3.4 Hz, 2H), 8.06 (dd, J = 6.5 Hz, 3.4 Hz, 2H), 7.94 (dd, J = 8.1 Hz, 4.4 Hz, 2H).

6.3.4 Benzopyrido[3,2-*a*:2',3'-*c*]phenazine

(C^N dppz)[5]

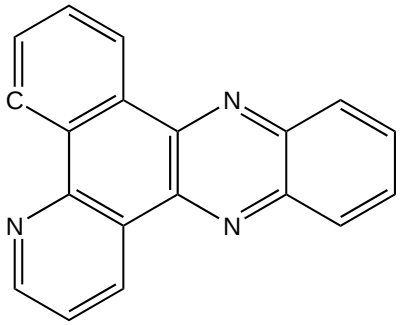

Benzo[h]quinolone (1.05 g, 3.75 mmol) and *o*-phenyldiamine (0.4 g, 3.75 mmol) were suspended in methanol (70 mL) and refluxed for 40 minutes. The solution was left to cool to forming a sandy precipitate. The crude product was collected by vacuum filtration, washed with 1:100 ethanol:water, and recrystallised from ethanol to yield pure product.

Mass (Yield): 0.60 g, (82 %).

TOF MS ES+ *m/z:* 282 [MH^+].

^{1}H NMR (400 MHz, TFA): δ_H = 9.60 (dd, J = 8.1 Hz, 1.8 Hz, 1H), 9.42 - 9.29 (m, 1H), 9.08 (dd, J = 4.5 Hz, 1.8 Hz, 1H), 8.42 – 8.26 (m, 2H), 7.96 – 7.80 (m, 4H), 7.69 (dd, J = 8.1 Hz, 4.5 Hz, 1H).

6.3.5 $[Ir(bpy)_2Cl_2][PF_6]$[7,8,9]

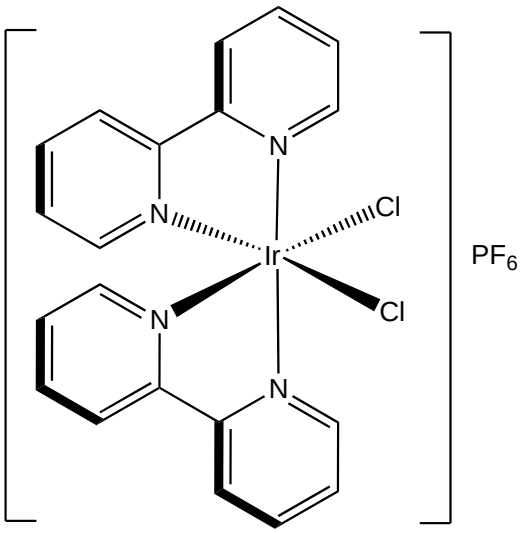

Iridium trichloride(III)hydrate (3.00 g, 10.0 mmol) and 2,2'-bipyridine (2.62 g, 16.8 mmol) were suspended in an ethylene glycol (70 mL) and water (5 mL) solution and heated under reflux for 21 hours. After cooling, addition of ammonia hexafluorophosphate salt gave rise to a bright orange precipitate. The product was collected by vacuum filtration and dried in *vacuo*.

Mass (Yield): 2.00 g (60 %).
TOF MS ES+ *m/z:* 575 $[M^+]$.

6.3.6 $[Ir(bpy)_2Cl_2][Cl]$

Counter ion metathesis

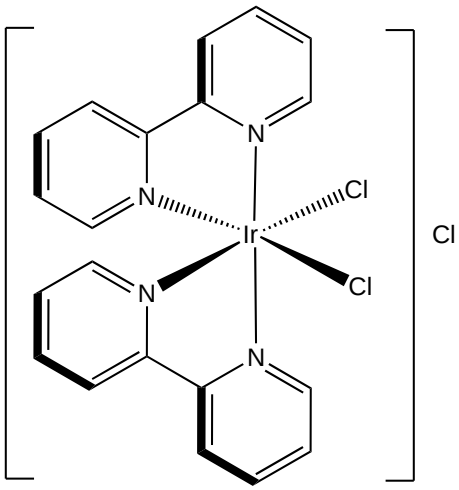

$[Ir(bpy)_2Cl_2][Pf_6]$ (1.00 g, 1.39 mmol) was dissolved in acetone. Excess tetrabutylammonium chloride was suspended in 10 mL of acetone. This saturated solution was slowly poured into the reaction mixture giving an instant precipitation of an orange solid. This was left in the fridge for 2 hours to yield maximum precipitation and collected by vacuum filtration. The product was dried under vacuum.

Mass (Yield): 0.89 g (89 %).
TOF MS ES+ ***m/z:*** 575 $[M^+]$.

6.3.7 $[Ir(bpy)_2Cl_2][OTf]$

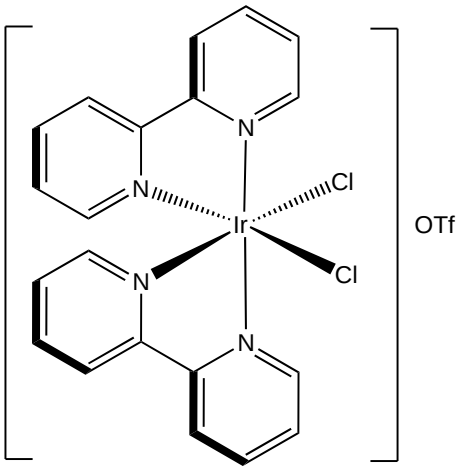

$[Ir(bpy)_2Cl_2][Cl]$ (1.05 g, 1.59 mmol) was suspended in acetonitrile (200 mL) with stirring. Triflic acid (0.7 mL, 7.9 mmol) was carefully added dropwise to the solution to give dissolution; the solution was stirred for 1 hour at room temperature. The volume of solvent was reduced under vacuum to ~25 % and the solution was placed in the freezer overnight to give a bright orange precipitate. This was collected by vacuum filtration yielding $[Ir(bpy)_2Cl_2][OTf]$.

Mass (Yield): 0.73 g, (69 %).

TOF MS ES+ ***m/z:*** 575 $[M^+]$.

6.3.8 $[Ir(bpy)_2(SO_3CF_3)_2][OTf]$

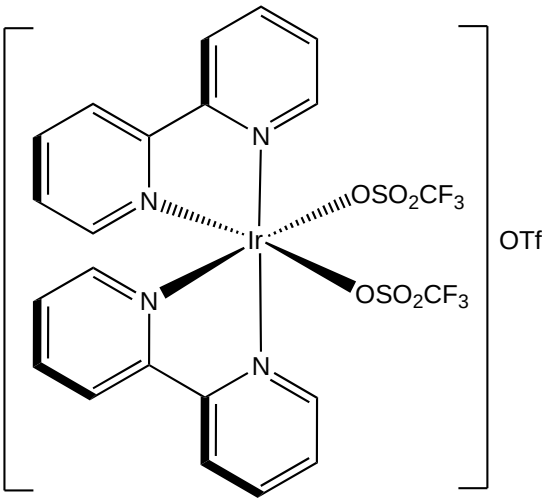

Under a nitrogen atmosphere $[Ir(bpy)_2Cl_2][OTf]$ (0.63 g, 0.66 mmol) was suspended in 1,2-dichlorobenxene (10 mL) with stirring. Triflic acid (1.4 mL, 15.80 mmol) was carefully added dropwise to give white fumes and dissolution of the solid. The reaction solution was a heterogeneous two-phase green/yellow liquid which was refluxed for 3 hours. The solution was allowed to cool to room temperature and decanted into ice cold diethyl ether (30 mL) to give a precipitation of a green solid. The reaction mixture was cooled in the fridge overnight to give further precipitation. The reaction mixture was centrifuged for 10 minutes 10,000 rpm to collect $[Ir(bpy)_2(SO_3CF_3)][OTf]$ as a pale green solid.

Mass (Yield): 0.38 g, (60 %).

TOF MS ES+ ***m/z:*** 802 $[M^+]$.

6.3.9 $[Ir(bpy)_2(dppz)][PF_6]_3$

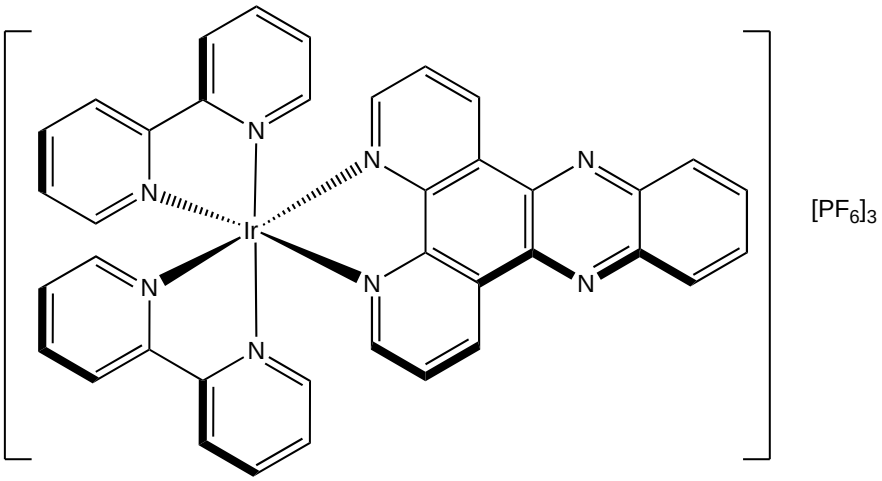

$[Ir(bpy)_2(SO_3CF_3)_2][OTf]$ (0.90 g, 0.73 mmol) and dppz (0.185 g, 0.73 mmol) were suspended in isopropanol (110 mL) with stirring and refluxed for 120 hours. The solvent was removed under vacuum yielding a dark brown solid. Deionised water (30 mL) was added to the solid followed by the addition of excess ammonium hexafluorophosphate to give instant precipitation of a brown solid which was collected by vacuum filtration to give $[Ir(bpy)_2(dppz)][PF_6]_3$

Mass (Yield): 0.62 g, (68 %).

TOF MS ES+ ***m/z:*** 1091 $[M^+]$, 931 $[M^{2+}]$, 262 $[M^{3+}]$.

^{1}H NMR (400 MHz, MeCN): δ_H = 8.89 (dd, J = 7.5 Hz, 1.5 Hz, 4H), 8.78 (dd, J = 8.1 Hz, 1.8 Hz, 2H), 8.59 (dd, J = 4.4 Hz, 1.8 Hz, 2H), 8.46 (dd, J = 7.5 Hz, 1.5 Hz, 4H), 7.80 (dd, J = 6.5 Hz, 3.4 Hz, 2H), 7.63-7.57 (m, 10 H), 7.09 (dd, J = 8.1 Hz, 4.4 Hz, 2H).

6.3.10 $[Ir(phen)_2Cl_2][PF_6]$

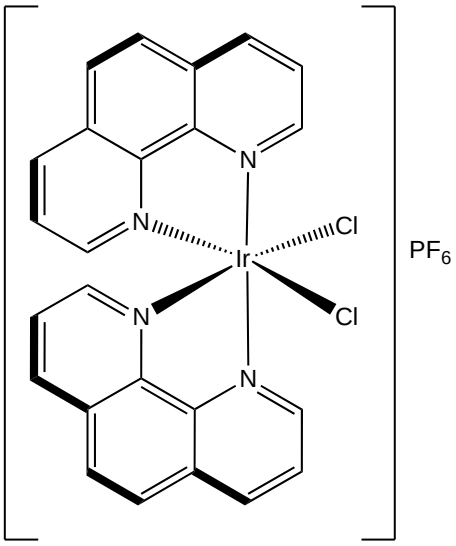

Iridium trichloride(III)hydrate (3.00 g, 10.0 mmol) and 1,10-phenanthroline (3.024 g, 16.8 mmol) were suspended in an ethylene glycol (70 mL) and water (5 mL) solution and heated under reflux for 21 hours. After cooling, addition of ammonia hexafluorophosphate salt gave rise to a bright orange precipitate. The product was collected by vacuum filtration and dried in *vacuo*.

Mass (Yield): 5.52 g, (60 %).
TOF MS ES+ *m/z:* 623 $[M^+]$.

6.3.11[Ir(phen)$_2$Cl$_2$][Cl]

Counter-ion metathesis

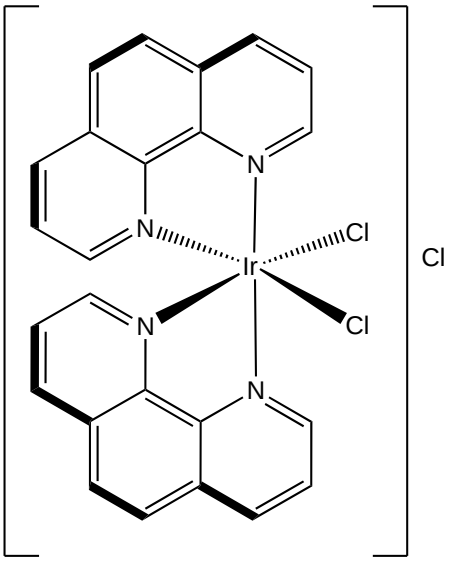

[Ir(phen)$_2$Cl$_2$][Pf$_6$] (1.00 g, 1.33 mmol) was dissolved in acetone. Excess tetrabutylammonium chloride was suspended in 10 mL of acetone. This saturated solution was slowly poured into the reaction mixture giving an instant precipitation of an orange solid. This was left in the fridge for 2 hours to yield maximum precipitation and collected by vacuum filtration. The product was dried under vacuum.

Mass (Yield): 0.89 g, 77%

TOF MS ES+ *m/z:* 623 [M$^+$]

6.3.12 $[Ir(phen)_2Cl_2][OTf]$

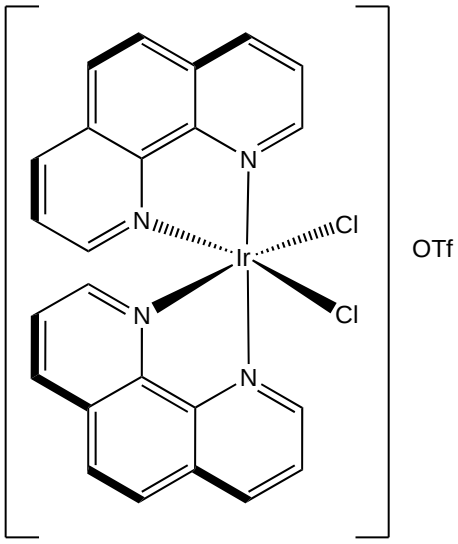

$[Ir(phen)_2Cl_2][Cl]$ (1.22 g, 1.59 mmol) was suspended in acetonitrile (200 mL) with stirring. Triflic acid (0.7 mL, 7.9 mmol) was carefully added dropwise to the solution to give dissolution; the solution was stirred for 1 hour at room temperature. The volume of solvent was reduced under vacuum to ~25 % and the solution was placed in the freezer overnight to give a bright orange precipitate. This was collected by vacuum filtration yielding $[Ir(phen)_2Cl_2][OTf]$.

Mass (Yield): 0.75 g, (61 %).
TOF MS ES+ ***m/z:*** 623 $[M^+]$

6.3.13 $[Ir(phen)_2(SO_2CF_3)_2][OTf]$

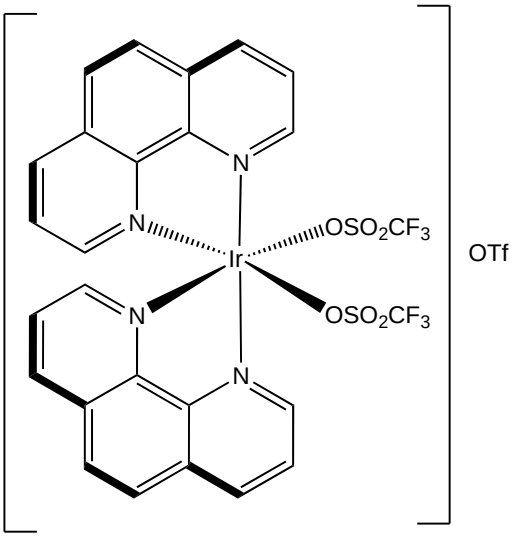

Under a nitrogen atmosphere $[Ir(phen)_2Cl_2][OTf]$ (0.65 g, 0.66 mmol) was suspended in 1,2-dichlorobenxene (10 mL) with stirring. Triflic acid (1.4 mL, 15.80 mmol) was carefully added dropwise to give white fumes and dissolution of the solid. The reaction solution was a heterogeneous two-phase green/yellow liquid which was refluxed for 3 hours. The solution was allowed to cool to room temperature and decanted into ice cold diethyl ether (30 mL) to give a precipitation of a green solid. The reaction mixture was cooled in the fridge overnight to give further precipitation. The reaction mixture was centrifuged for 10 minutes 10,000 rpm to collect $[Ir(phen)_2(SO_3CF_3)][OTf]$ as a pale green solid.

Mass (Yield): 0.61 g, (74 %).
TOF MS ES+ ***m/z:*** 850 $[M^+]$.

6.3.14 $[Ir(phen)_2(dppz)][PF_6]_3$

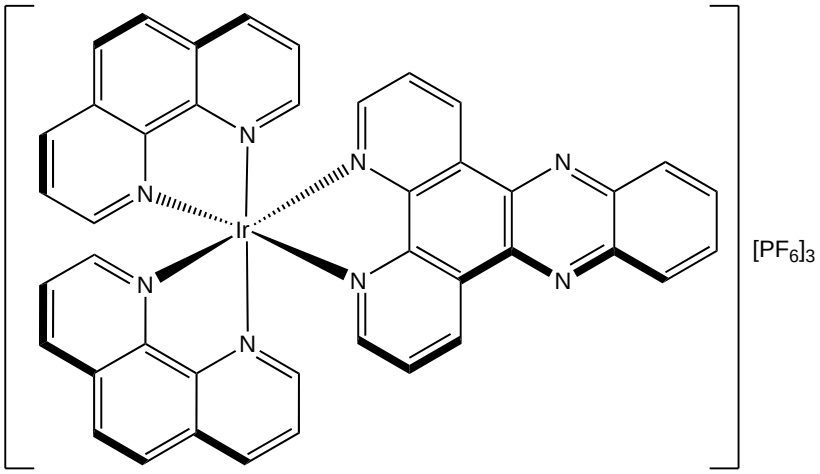

$[Ir(phen)_2(SO_3CF_3)_2][OTf]$ (0.729 g, 0.73 mmol) and dppz (0.185 g, 0.73 mmol) were suspended in isopropanol (110 mL) with stirring and refluxed for 120 hours. The solvent was removed under vacuum yielding a dark brown solid. Deionised water (30 mL) was added to the solid followed by the addition of excess ammonium hexafluorophosphate to give instant precipitation of a brown solid which was collected by vacuum filtration to give $[Ir(phen)_2(dppz)][PF_6]_3$.

Mass (Yield): 1.023g, 79 %

TOF MS ES+ ***m/z:*** 1154 $[M^+]$, 504 $[M^{2+}]$, 284 $[M^{3+}]$

^{1}H NMR (400 MHz, MeCN): δ_H 10.13 (dd, J= 8.1 Hz, 1.8 Hz, 2H), 9.10 (dd, 4H), 8.80 (dd, J = 4.4 Hz, 1.8 Hz, 2H), 8.65 (dd, J = 6.5 Hz, 3.4 Hz), 8.61 (s, 4H), 8.42 (dd, J = 6.5 Hz, 3.4 Hz, 2H), 8.30-8.22 (m, 6H), 8.24 (dd, J = 6.5 Hz, 3.4 Hz), 3.03 (m, 4H).

6.3.15 $[Ir(phen)_2(C\hat{}N\ dppz)][PF_6]_2$

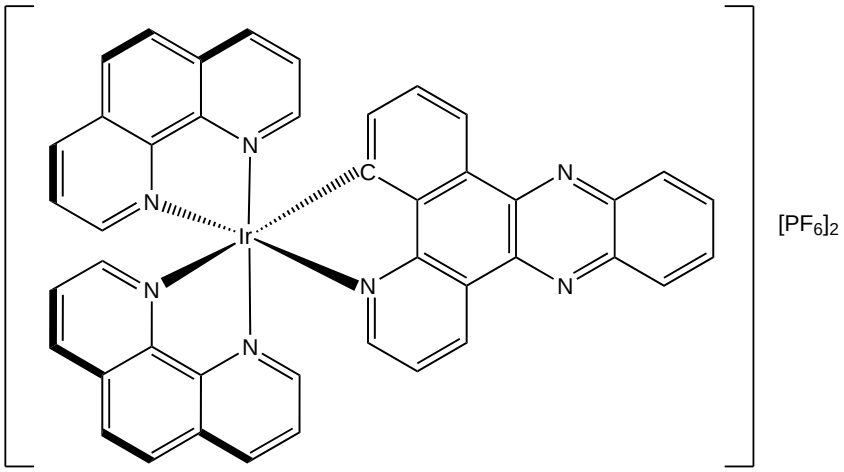

$[Ir(phen)_2(SO_3CF_3)_2][OTf]$ (0.729 g, 0.73 mmol) and C^N dppz (0.205 g, 0.73 mmol) were suspended in isopropanol (110 mL) with stirring and refluxed for 120 hours. The solvent was removed under vacuum yielding a dark brown solid. Deionised water (30 mL) was added to the solid followed by the addition of excess ammonium hexafluorophosphate to give instant precipitation of a brown solid which was collected by vacuum filtration to give $[Ir(phen)_2(C\hat{}N$ dppz)$][PF_6]$.

Mass (Yield): 0.32g, 32 %

TOF MS ES+ ***m/z:*** 1008 $[M^+]$, 504 $[M^{2+}]$

^{1}H NMR (400 MHz, MeCN): δ_H (400 MHz, CD_3CN) 9.98 (dd, J = 8.1 Hz, 1.8 Hz, 2H), 8.75 (dd, 2H), 8.70 (m, 2H), 8.57 (dd, J = 6.5 Hz, 3.4 Hz, 2H), 8.49 (dd, J = 6.5 Hz, 3.4 Hz, 2H), 8.38 (m, 2H), 8.25 (dd, J = 6.5 Hz, 3.4 Hz, 2H), 8.16 (m, 2H), 7.84 (m, 2H), 7.77 (m, 2H), 7.71 (m, 2H), 7.56 (m, 2H)

6.3.15 Anion Metathesis

All complexes were synthesised as their hexafluorophosphate salts and characterised as such unless otherwise stated. This was achieved using 10 molar equivalents of aqueous ammonium hexafluorophosphate. In cases where complexes were required as their water-soluble chloride derivatives, the compounds were dissolved in the minimum amount of acetone and converted by counter-ion metathesis using acetone solutions of tetrabutylammonium chloride (10 molar equivalencies). This resulted in precipitation of the desired chloride product which was collected by centrifugation for 10 minutes at 10,000 rpm and dried *in vacuo*.

6.3.16 Chiral Separation

Octahedral coordination, being the most frequent geometry for metallic centres, is the most studied with regard to the topographical stereochemistry.[10] A chiral object is one that does not coincide with its mirror image, producing enantiomorphs (a prototypical natural example of enantiomorph is the human hand).[11] The special relationship between a metal centre and three bidentate ligands can take on the shape of a left-handed or right-handed propeller, called enantiomers. A pair of enantiomers are physically and chemically indistinguishable by most techniques in achiral environments. They possess identical melting points, boiling points, and spectroscopy properties such as NMR, IR and UV. The way to measure the separation of enantiomers is by monitoring the effect on the plane of polarized light. Without separation, the synthesised metal complexes will be a racemic mixture with 50/50 of each enantiomer having no effect on the plane of polarized light. If separated, the enantiomerically pure compounds separated the plane of polarized light in equal and opposite directions. This is measured using a technique called circular dichroism.[12] The work carried out in this was part of a collaboration with Professors Richard Keene and Grant Collins at the University of New South Wales, Canberra, Australia. A general chromatographic technique for the separation of complexes **1-3** was investigated. Chiral column chromatography incorporates a chiral stationary phase to conventional column chromatography. The enantiomers present in the analyte will have different affinities to the chiral stationary phase and will therefore elute at two different times. In these studies, SP-Sephadex C-25 was chosen as the cation exchange support in comparison to the classical polystyrene resins. Sephadex is a cross-linked dextran matrix containing strongly acidic propanesulfonate groups. The cationic metal complexes are adsorbed on to the anionic stationary-phase and the separation is achieved by ion-exchange using an eluting

electrolytic solution (*Figure 1*). This technique has been used in previous work in the separation of ruthenium(II) complexes containing polypyridyl complexes, but it has not been widely applied to iridium (III) counterparts.[13–15] Separation was attempted for all three iridium complexes in this thesis, however success was only obtained with **3**. The first attempt to separate **3** was to use sodium dibenzoyltatrate, however this produced severe band spreading when the complex was loaded onto the column. Since the eluent is the salt of a carboxylic acid (tartaric acid) it has a $pK_a = 4.5$, causing protonation of the dppz nitrogens which have a $pK_a = 5$. This protonation causes variations in the charge of the complex, which causes band spreading. To overcome this the second attempt to separate **3** a buffered solution of sodium camphor sulfonate was used as the eluent. This prevented protonation with successive band spreading from occurring and promoted the successful separation of $[I(phen)_2(dppz)]^{3+}$. Following the isolation of the bands by precipitation as the hexafluorophosphate salts, the resolution of the individual enantiomers Λ-(+) and Δ-(-)-$[Ir(phen)_2(dppz)][PF_6]_3$ was confirmed by circular dichroism (CD) measurements (*Figure 7*).

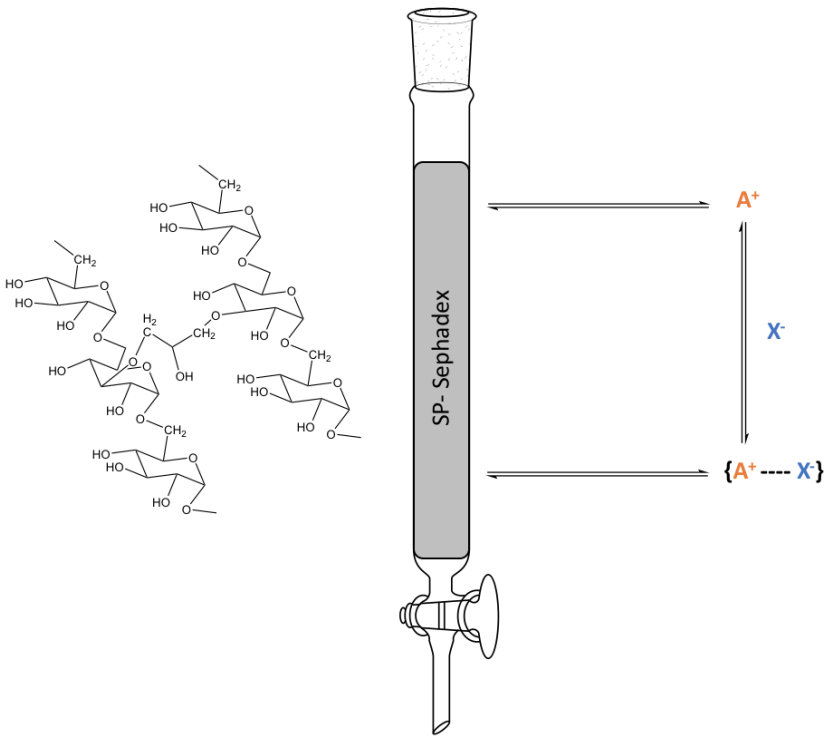

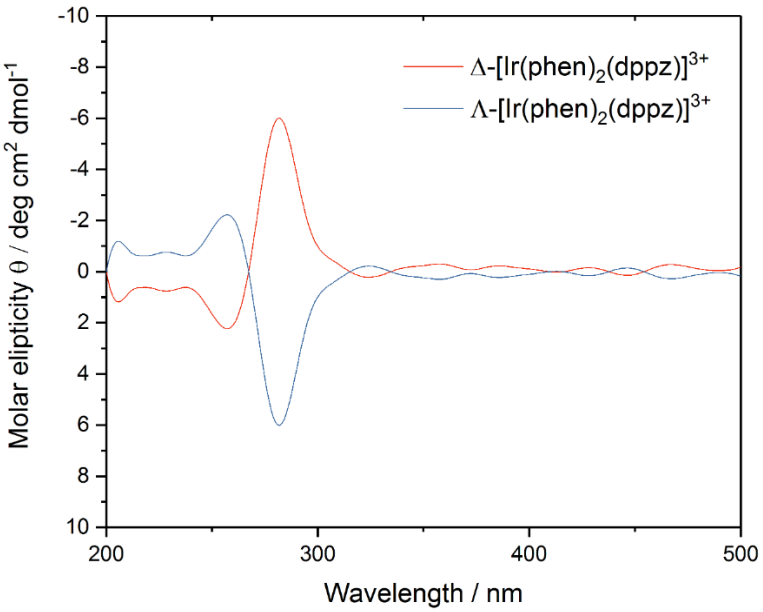

Figure 1: Top - Schematic of a Sephadex chiral column with the cation A^+ being adsorbed onto the Sephadex column being eluted with an electrolyte X^-. Bottom – Circular Dichroism spectra of Δ- (red) and Λ-(blue) $[Ir(phen)_2(dppz)]^{3+}$ ***2****.*

As **2** was successfully resolved, future work could investigate the photophysical and *in vitro* DNA binding activity and *in vivo* cellular experiments of the different enantiomers. An experimental route could also be optimised for the other complexes in this study, and similar analogies in the literature.

6.4 Cellular Studies

6.4.1 Complex Preparation

Stock solutions were made up in phosphate buffered saline (PBS) with sonication and gentle heating to aid dissolution at a high concentration, followed by sterile filtration with a 0.2 μm filter.

6.4.2 Cell Culture

MCF-7 cell lines were cultured in RPMI-1640 medium. All growth medium was supplemented by 2 mM L-Glutamine, 100 IU mL^{-1} penicillin, 100 μg mL^{-1} streptomycin and 10% v/v foetal bovine serum (FBS). Cultures were routinely subcultured using trypsin (0.1% v/v PBS) at 80-90% confluency and used between passage numbers 5-30.

6.4.3 IC_{50} values MTT assays

MTT (3-(4,5-dimethylthiazol-2-yl)-2,5-diphenyltetrazolium bromide) was used to determine the cell viability upon treatment with varying concentrations of the complex. In the mitochondria of living cells MTT is reduced to a purple formazan product by reductive enzymes. The amount of formazan can be quantified by absorbance between 500-600 nm and a comparison between untreated and exposed cells. Cell cultures were grown on 48 well plates at a seeding density of 50,000 cells per well and allowed to grow for 24 hours before treatment with a complex of various concentrations (maintaining a ration of 10 % PBS/H_2O: 90 % medium throughout all solutions). In triplicate for the given incubation time of 24 or 48 hours. Solutions were removed and the cells were incubated with MTT (0.5 mg mL^{-1} dissolved in PBS) for 30 – 40 minutes. The MTT was removed and the formazan product eluted using acidified isopropanol (110 μL/well). This eluted mixture was transferred to a 96 well plate were 100 μL/well was added. Absorbance was measured using a spectrophotometer (540 nm, referenced at 640 nm). An average absorbance for each concentration was calculated and cell viability was determined as a percentage of the untreated negative control wells (10 % PBS/water: 90% medium, average of triplicate. The data was plotted in a graph of concentration against cell viability to produce a curve from which the IC_{50} could be estimated by interpolation.

6.4.5 Light Irradiation Source Apparatus (LISA)

The apparatus used to illuminate the samples was a custom build device featuring a broadband illumination source fully contained in an empty computer base unit, referred to as the Light Irradiation Source Apparatus (LISA). The technical specifications of the bulb contained within are as follows *(Table 1).*

Product Code	**871691**
International Model Number	HC01080i
Description	CFL 80W E40 Integrated Clusterlite
Watts	80W
Cap	E40
Operating Hours	15000
Colour Temp	4000K
Lumens	5400 lm
Dimming	No
Dimensions (length x diameter)	256 mm x 80 mm

Table 6.1: Specification of the bulb contained within the irradiation apparatus.

6.4.6 Phototoxicity Experiments

Cell cultures were grown on four 48 well plates at a seeding density of 50,000 cells per well and allowed to grow for 24 hours. The cells were treated with complex (solubilised in and maintained at 10 % PBS/water: 90 % medium throughout all solutions) of a 1 – 500 μM concentration range, in triplicate, and incubated for 24 hours. All complex solution (and control media) was removed from the cells and replaced with regular growth medium 30 minutes prior to radiation. One of the four well plaines remained in the incubator whilst the other three were exposed to the LISA for the duration of 5, 15, or 30 minutes before being incubated for a further 24 hours after light treatment. All media was removed and the cells incubated with MTT (0.5 mg mL^{-1} dissolved in PBS) for 30 – 40 minutes. The MTT was removed and formazan product eluted using acidified isopropanol (120 μL/well), the solution (100 μL) was transferred to a 96 well plate for the absorbance to be quantified by spectrophotometer (540 nm, referenced at

640 nm). An average absorbance for each concentration was calculated and cell viability was determined as a percentage of the untreated negative control wells (10 % PBS/water: 90% medium, average of triplicate). Data was plotted in a graph of concentration against cell viability to produce a curve from which the IC_{50} could be derived by interpolation for each well plate exposed to the various illumination times.

6.4.7 Imaging experiments

MCF7 cells were seeded on cover slips (22 mm X 22 mm, 170 ± 5 µm square Cover glasses) placed in six well plates in RPMI 1640 culture medium containing (10% FBS and 1% Penicillin Streptomycin) for 24 hours at 37°C, 5% CO_2. After 24 hours when 70% confluency was achieved the cells were washed with RPMI 1640 culture medium then the cells were treated with Ir1 or Ir3 (50 µM or 100 µM or 200 µM) for 24 hours. Cells were then washed thrice with culture medium. The cells were then washed again with Phosphate buffer saline (2 times). After carrying out the live cell uptake of the complexes, the cells were fixed with 4% paraformaldehyde for 20 minutes and then washed thrice with PBS and then the cover slips were mounted using mounting medium (Vectashield h-1000).The coverslips were then sealed using nail varnish and the sample were then imaged - wide field fluorescence microscopy using the wide field mode of OMX-SIM.

6.4.8 Colocalisation experiment

The Colocalisation studies were carried out by using Mito Tracker Deep red or Lyso Tracker Deep Red according to the planned experiment. MCF7 cells were seeded on cover slips (22 mm X 22 mm, 170 ± 5 µm square cover glasses) placed in six well plates in RPMI 1640 culture medium containing (10% FBS and 1% Penicillin Streptomycin) for 24 hours at 37°C, 5% CO_2. After 24 hours when 70% confluency was achieved the cells were washed with RPMI culture medium then the cells were treated with 100 µM Ir1 or Ir3 for 24 hours, the culture medium is then aspirated, the cells were then washed with culture medium (2 times), PBS (2 times), then the cells were incubated with 500 nM (Mito Tracker Deep Red or Lyso Tracker Deep Red, depending on the specific planned experiment) for 30 minutes and washed twice with culture media (RPMI 1640), the cells were then washed thrice with culture medium and washed again with PBS twice, the cells were then fixed with 4% paraformaldehyde for 20 minutes and then washed thrice with PBS and then the cover slips were mounted using mounting medium

(Vectashield h-1000). The coverslips were then sealed using nail varnish and the sample were then imaged - Wide field fluorescence microscopy using the wide field mode of OMX-SIM.

6.4.9 Single colour imaging

The complexes were excited at 405 nm and the emission was collected between 500 nm and 550 nm (FITC channel of wide field mode of OMX-SIM). The Wide field imaging conditions were employed for the cellular uptake studies of the complexes featuring MCF7 cells. The Wide field microscopy conditions maintained include, thickness of the Z stack (Sections 40 to 100), section spacing (0.250 to 0.500), and thickness of the sample (8 to 15).

6.4.10 Colocalization (Multi colour imaging)

The complexes were excited at 405 nm and the emission was collected between 500 nm to 550 nm (FITC channel). Mito Tracker Deep Red or Lyso Tracker Deep Red (depending on the planned experiment) was excited at 644 nm and the emission was collected >660 nm(Far red channel). The colocalization experiments were carried out using the same microscopy conditions as mentioned for single colour experiments using the wide field mode of OMX-SIM.

6.5 References

1 J. B. Chaires, N. Dattagupta and D. M. Crothers, Studies on Interaction of Anthracycline Antibiotics and Deoxyribonucleic Acid: Equilibrium Binding Studies on Interaction of Daunomycin with Deoxyribonucleic Acid, *Biochemistry*, 1982, **21**, 3933–3940.

2 M. G. Walker, P. J. Jarman, M. R. Gill, X. Tian, H. Ahmad, P. A. N. Reddy, L. McKenzie, J. A. Weinstein, A. J. H. M. Meijer, G. Battaglia, C. G. W. Smythe and J. A. Thomas, A Self-Assembled Metallomacrocycle Singlet Oxygen Sensitizer for Photodynamic Therapy, *Chem. - A Eur. J.*, 2016, **22**, 5996–6000.

3 N. M. Shavaleev, H. Adams, J. Best, R. Edge, S. Navaratnam and J. A. Weinstein, Deep-red luminescence and efficient singlet oxygen generation by cyclometalated platinum(II) complexes with 8-hydroxyquinolines and quinoline-8-thiol, *Inorg. Chem.*, 2006, **45**, 9410–9415.

4 W. Paw and R. Eisenberg, Synthesis, Characterization, and Spectroscopy of Dipyridocatecholate Complexes of Platinum, *Inorg. Chem.*, 1997, **36**, 2287–2293.

5 K. Kloc, J. Mlochowski and Z. Szulc, Synthesis of Azafluorenones, *J. fur Prakt. Chemie*, 1977, **319**, 959–967.

6 J. E. Dickeson and L. A. Summers, Derivatives of 1,10-Phenanthroline-5,6-quinone, *Aust. J. Chem.*, 1970, **23**, 1023–1027.

7 M. Pandrala, F. Li, M. Feterl, Y. Mulyana, J. M. Warner, L. Wallace, F. R. Keene and J. G. Collins, Chlorido-containing ruthenium(ii) and iridium(iii) complexes as antimicrobial agents, *Dalt. Trans.*, 2013, **42**, 4686.

8 N. YOSHIKAWA, J. SAKAMOTO, T. MATSUMURA-INOUE, H. TAKASHIMA, K. TSUKAHARA, N. KANEHISA and Y. KAI, Electrochemical and Phosphorescent Properties of New Ir(III) Complexes Coordinated by Various Bipyridine Derivatives, *Anal. Sci.*, 2004, **20**, 711–716.

9 R. J. Watts, J. S. Harrington and J. V. van Houten, A Stable Monodentate 2,2'-Bipyridine Complex of Iridium(III): A Model for Reactive Intermediates in Ligand Displacement Reactions of Tris-2,2'-bipyridine Metal Complexes, *J. Am. Chem. Soc.*, 1977, **99**, 2179–2187.

10 A. Mohamadou and A. Haudrechy, A Simple Method for Drawing Chiral Mononuclear Octahedral Metal Complexes, *J. Chem. Educ.*, 2008, **85**, 436.

11 F. R. Keene and J. C. Chambron, in *Chirality in Supramolecular Assemblies: Causes*

and Consequences, John Wiley & Sons Ltd, 2016, pp. 1–43.

12 H. Kobayashi, H. Matsuzawa, Y. Kaizu and A. Ichida, Resolution and Circular Dichroism of the Optical Isomers of Tris(2,4-pentanedionato)ruthenium(III), *Inorg. Chem.*, 1987, **26**, 4318–4323.

13 T. J. Rutherford, M. G. Quagliotto and F. Richard Keene, Chiral [Ru(pp)2(CO)2]2+ Species (pp = Bidentate Polypyridyl Ligand) and Their Use in the Stereoselective Synthesis of Ligand-Bridged Dinuclear Complexes, *Inorg. Chem.*, 1995, **34**, 3857–3858.

14 T. J. Rutherford, P. a. Pellegrini, J. Aldrich-Wright, P. C. Junk and F. R. Keene, Isolation of Enantiomers of a Range of Tris(bidentate)ruthenium(II) Species Using Chromatographic Resolution and Stereoretentive Synthetic Methods, *Eur. J. Inorg. Chem.*, 1998, **1998**, 1677–1688.

15 N. C. Fletcher, P. C. Junk, D. A. Reitsma and F. R. Keene, Chromatographic separation of stereoisomers of ligand-bridged diruthenium polypyridyl species, *J. Chem. Soc. Trans.*, 1998, **2**, 133–138.

Angewandte
Communications

DNA Intercalators

DOI: 10.1002/anie.201411346

Tuning the Excited State of Water-Soluble Ir^{III}-Based DNA Intercalators that are Isostructural with $[Ru^{II}(NN)_2(dppz)]$ Light-Switch Complexes**

*Sasha Stimpson, Dan R. Jenkinson, Andrew Sadler, Mark Latham, Dr Ashley Wragg, Anthony J. H. M. Meijer, and Jim A. Thomas**

Abstract: *The synthesis of two new Ir^{III} complexes which are effectively isostructural with well-established $[Ru(NN)_2(dppz)]^{2+}$ systems is reported (dppz = dipyridophenazine; NN = 2,2′-bipyridyl, or 1,10-phenanthroline). One of these Ir^{III} complexes is tricationic and has a conventional N_6 coordination sphere. The second dicationic complex has a N_5C coordination sphere, incorporating a cyclometalated analogue of the dppz ligand. Both complexes show good water solubility. Experimental and computational studies show that the photoexcited states of the two complexes are very different from each other and also differ from their Ru^{II} analogues. Both of the complexes bind to duplex DNA with affinities that are two orders of magnitude higher than previously reported Ir(dppz)-based systems and are comparable with Ru^{II}(dppz) analogues.*

DNA has a vital role in life; as outlined in the "central dogma of molecular biology" it stores and transmits the genetic blueprints for structure and function in all living organisms. For this reason, molecules that target DNA have been intensively researched.

In this context, and inspired by the serendipitous discovery and subsequent clinical success of the potent anticancer agent cisplatin,[1,2] research into metal complexes that interact with DNA has burgeoned. More recently this work has been extended to yield an array of transition-metal-based nucleic acid probes as, because of an attractive combination of well-defined coordination geometries and substitution chemistry as well as distinctive electrochemical and photophysical properties, they are almost perfect candidates for such a role.[3–7]

Luminescent and photoreactive d^6 metal-ion-based complexes that intercalate into DNA have been particularly well-studied,[8–11] leading, inter alia, to the now well-characterized DNA light-switch effect exemplified by $[Ru(NN)_2(dppz)]^{2+}$ (where NN = 2,2′-bipyridyl (bipy), or 1,10-phenanthroline (phen), and dppz = dipyridophenazine).[12]

Concurrently, the coordination chemistry of another d^6 metal ion, Ir^{III}, has been rapidly developing. Polypyridyl Ir^{III} complexes are finding a range of applications, largely because their photoexcited states are much more tunable than their Ru^{II}-based analogues.[13–15] However, whilst such systems have been investigated as therapeutics[16,17] and as cell probes,[18] their use in these applications is often restricted as because of their relatively low charge, cyclometalated Ir^{III} complexes display poor inherent water solubility and DNA binding affinities. For example, several Ir^{III}(dppz) systems incorporating cyclometalated ancillary ligands have been previously reported, but these complexes display relatively low DNA binding affinities ($\approx 10^4\,M^{-1}$) compared to their Ru^{II}(dppz) analogues ($> 10^6\,M^{-1}$).[19,20]

As part of a program to develop metal-complex-based bioprobes with targeted binding properties and attractive photophysical/imaging properties, we set out to synthesize water-soluble, Ir^{III}-based metallointercalators that are isostructural analogues of the parent $[Ru(phen)_2(dppz)]^{2+}$ system. By adapting previously reported synthetic methods,[21,22] this has led to the preparation of the tricationic complex **1** (Scheme 1). We also investigated coordination of

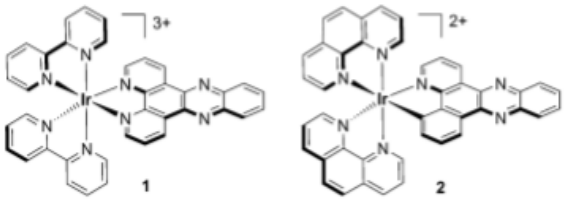

Scheme 1. Structures of complexes **1** and **2** prepared in this study.

appropriate Ir^{III} moieties to the potentially cyclometalating dppz analogue benzopyridophenazine (bppz). Surprisingly, although this ligand has been reported before,[23] this is the first time its use in the construction of a DNA binding system has been investigated. In fact, to our knowledge this study provides the first example of its use in coordination chemistry.

While attempts to synthesize the dicationic analogue of **1** using bppz were unsuccessful, the closely related complex **2**, incorporating the $Ir^{III}(phen)_2$ moiety, was isolated in reasonable yields. The complexes were synthesized as hexafluoro-

[*] S. Stimpson, D. R. Jenkinson, A. Sadler, Dr. M. Latham, D. A. Wragg, Dr. A. J. H. M. Meijer, Dr. J. A. Thomas
Department of Chemistry
University of Chemistry, Sheffield (UK)
E-mail: james.thomas@sheffield.ac.uk

[**] We are grateful for the support provided for this project by the EPSRC Molecular Scale Engineering DTC. A license for the OpenEye tools, obtained via the free academic licensing program, is gratefully acknowledged.

Supporting information for this article, including details of syntheses, computational procedures, UV/Vis absorption spectra, computational analyses, and additional references, is available on the WWW under http://dx.doi.org/10.1002/anie.201411346.

phosphate salts and then converted into chlorides by counter-ion metathesis; in this form both complexes were highly water soluble.

A comparison of the optical properties of **1** and **2** shows the effects of cyclometalation on the Ir^{III} center. The UV/Vis absorption spectra of both complexes (Figure S1 in the Supporting Information) show high-energy bands below $\lambda = 300$ nm that are assigned to ligand-centered $\pi \rightarrow \pi^*$ transitions. While complex **1** shows a "double-humped" structured band centered at approximately $\lambda = 360$ nm that is characteristic of a coordinated dppz ligand, complex **2** displays a broad, featureless absorption shoulder centered at $\lambda = 350$ nm that extends out beyond $\lambda = 400$ nm. Differences in the emission properties of the two complexes are more striking.

Unlike their Ru(dppz) analogues, both complexes are emissive in water (Figure 1). Photoexcitation of complex **1** results in an emission band with clear vibronic structure with

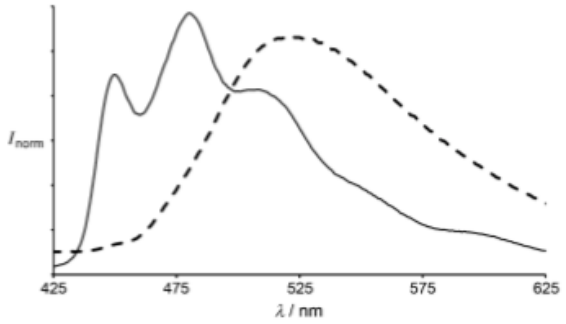

Figure 1. Normalized emission spectra of complexes **1** (solid line) and **2** (dashed line) in water.

a maximum emission centered at $\lambda = 479$ nm. In contrast, excitation of **2** results in a broad featureless emission centered at $\lambda = 522$ nm. These observations are in line with previous studies demonstrating that the energy and nature of emissive states in polypyridyl Ir^{III} complexes are modulated through coordination to cyclometalated ligands, and suggest that the excited state of **2** has a much greater MCLT (metal-to-ligand charge transfer) character than that of **1**.

To investigate these emission properties in more detail, DFT calculations were performed on both the S_0 state and the T_1 state of both **1** and **2** as well as on the bipy equivalent of **2** (**2′**).

Structurally, **1** and **2** are very similar as are **1** and **2′**. Indeed, **1** is also very similar to its Ru^{II} analogue (Tanimoto coefficient 0.997; see the Supporting Information for overlays). Interestingly, the frontier orbitals of **1** and **2** (particularly the virtual orbitals) are different (see the Supporting Information). Whereas the highest occupied molecular orbital (HOMO) of **1** is solely located on the dppz ligand, the HOMO of **2** has a significant contribution from the Ir^{III} center. Consistent with the experimental data, the calculated UV/Vis absorption spectrum of **1** and **2** (Figure S4) also shows that the absorption spectrum of **2** extends further into the lower energy region of the spectrum. Furthermore, whilst the two triplet states are structurally similar, they are

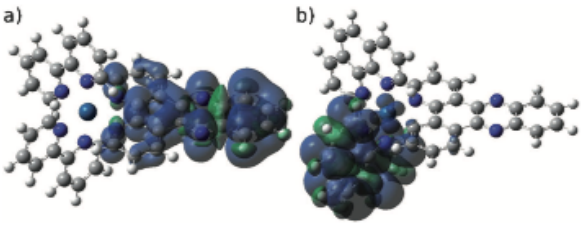

Figure 2. Spin-density plots for the T_1 state of complexes **1** (a) and **2** (b). Atom sphere colors: C = gray; H = white; N = dark blue; Ir = lighter blue.

clearly electronically different. As is shown in Figure 2, the spin density for the T_1 state of **1** is largely concentrated on the dppz unit. In contrast, for the T_1 state of **2** the spin density is located on the metal center and one of the phen units. Calculations on **2′** confirm that the change in excited state is a consequence of the cyclometalation, as for **2′** the spin density is also localized away from the dppz ligand. Calculation of the complete emission spectrum of both **2** and **1** was not possible with our current resources, but the 0–0 transition for **1** was calculated to be at $\lambda = 596.6$ nm, whereas the 0–0 emission for **2** is calculated at $\lambda = 475.3$ nm. For **1**, the calculated transition appears to be in reasonable agreement with the experimental data, whereas for **2** the calculated transition lies at higher energy than the experimental value.

Given that the two complexes are cationic and incorporate ligands with extended aromatic surfaces, the interaction of **1** and **2** with DNA was then investigated. It is well established that many complexes containing the Ru^{II}(dppz) moiety produce increases in relative viscosity on progressive addition to aqueous solutions of DNA[24] and this response is one of the clearest general diagnostics for an intercalative interaction.[25] Consequently, the effect of **1** and **2** on the viscosity of solutions of calf-thymus DNA (CT-DNA) was investigated.

As shown in Figure 3, both complexes induce significant positive viscosity changes that are indicative of intercalative binding. Interestingly, both complexes also initially induce a negative change in relative viscosity suggesting that, at low complex loading, non-intercalative interactions are occurring, a phenomenon that has been suggested before for Ru^{II}(dppz)-based systems.[26] However, it is also clear that complex **1** causes larger changes than **2**.

It seems likely that this effect may be due to the difference in charge between the two systems; the electrostatic contribution to association with the polyanionic backbone of DNA for the tricationic complex **1** should be higher than that of dicationic **2**, thus bringing about a closer association, although the influence of the different ancillary ligands may also be a factor. Having established that **1** and **2** do interact with DNA, their binding properties were further parameterized through luminescent titrations.

In stark contrast to their isostructural Ru^{II}(dppz) analogues, addition of CT-DNA to aqueous solutions of **1** or **2** results in a substantial decrease in steady-state luminescence (Figure 4). Although both complexes display a similar 5 nm blue shift in luminescence, the DNA-induced emission

[6] M. A. Jakupec, M. Galanski, V. B. Arion, C. G. Hartinger, B. K. Keppler, *Dalton Trans.* **2008**, 183 – 194.
[7] N. P. E. Barry, P. J. Sadler, *Chem. Commun.* **2013**, *49*, 5106 – 5131.
[8] K. E. Erkkila, D. T. Odom, J. K. Barton, *Chem. Rev.* **1999**, *99*, 2777 – 2796.
[9] B. M. Zeglis, V. C. Pierre, J. K. Barton, *Chem. Commun.* **2007**, 4565 – 4579.
[10] C. Metcalfe, J. A. Thomas, *Chem. Soc. Rev.* **2003**, *32*, 215 – 224.
[11] M. R. Gill, J. A. Thomas, *Chem. Soc. Rev.* **2012**, *41*, 3179 – 3192.
[12] A. E. Friedman, J. C. Chambron, J. P. Sauvage, N. J. Turro, J. K. Barton, *J. Am. Chem. Soc.* **1990**, *112*, 4960 – 4962.
[13] M. S. Lowry, W. R. Hudson, R. A. Pascal, S. Bernhard, *J. Am. Chem. Soc.* **2004**, *126*, 14129 – 14135.
[14] M. S. Lowry, S. Bernhard, *Chem. Eur. J.* **2006**, *12*, 7970 – 7977.
[15] S. Ladouceur, E. Zysman-Colman, *Eur. J. Inorg. Chem.* **2013**, 2985 – 3007.
[16] D. Herebian, W. S. Sheldrick, *J. Chem. Soc. Dalton Trans.* **2002**, 966 – 974.
[17] Z. Liu, I. Romero-Canelón, B. Qamar, J. M. Hearn, A. Habtemariam, N. P. E. Barry, A. M. Pizarro, G. J. Clarkson, P. J. Sadler, *Angew. Chem. Int. Ed.* **2014**, *53*, 3941 – 3946; *Angew. Chem.* **2014**, *126*, 4022 – 4027.
[18] K. K.-W. Lo, M.-W. Louie, K. Y. Zhang, *Coord. Chem. Rev.* **2010**, *254*, 2603 – 2622.
[19] K. K.-W. Lo, C.-K. Chung, N. Zhu, *Chem. Eur. J.* **2006**, *12*, 1500 – 1512.
[20] F. Shao, B. Elias, W. Lu, J. K. Barton, *Inorg. Chem.* **2007**, *46*, 10187 – 10199.
[21] M. Pandrala, F. Li, L. Wallace, P. J. Steel, B. Moore II, J. Autschbach, J. G. Collins, F. R. Keene, *Aust. J. Chem.* **2013**, *66*, 1065 – 1073.
[22] S. Soman, J. C. Manton, J. L. Inglis, Y. Halpin, B. Twamley, E. Otten, W. R. Browne, L. De Cola, J. G. Vos, M. T. Pryce, *Chem. Commun.* **2014**, *50*, 6461 – 6463.
[23] K. Kloc, J. Mlochowski, Z. Szulc, *J. Prakt. Chem.* **1977**, *319*, 959 – 967.
[24] P. Waywell, V. Gonzalez, M. R. Gill, H. Adams, A. J. H. M. Meijer, M. P. Williamson, J. A. Thomas, *Chem. Eur. J.* **2010**, *16*, 2407 – 2417.
[25] S. Satyanarayana, J. C. Dabrowiak, J. B. Chaires, *Biochemistry* **1992**, *31*, 9319 – 9324.
[26] T. Biver, C. Cavazza, F. Secco, M. Venturini, *J. Inorg. Biochem.* **2007**, *101*, 461 – 469.
[27] J. D. J. McGhee, P. H. P. von Hippel, *J. Mol. Biol.* **1974**, *86*, 469 – 489.
[28] J. B. Chaires, *Arch. Biochem. Biophys.* **2006**, *453*, 26 – 31.
[29] D. Řeha, M. Kabeláč, F. Ryjáček, J. Šponer, J. E. Šponer, M. Elstner, S. Suhai, P. Hobza, *J. Am. Chem. Soc.* **2002**, *124*, 3366 – 3376.
[30] S. E. Patterson, J. M. Coxon, L. Strekowski, *Bioorg. Med. Chem.* **1997**, *5*, 277 – 281.
[31] T. Phillips, I. Haq, A. J. H. M. Meijer, H. Adams, I. Soutar, L. Swanson, M. J. Sykes, J. A. Thomas, *Biochemistry* **2004**, *43*, 13657 – 13665.
[32] T. Phillips, I. Haq, J. A. Thomas, *Org. Biomol. Chem.* **2011**, *9*, 3462 – 3470.
[33] V. W.-W. Yam, K. K.-W. Lo, K.-K. Cheung, R. Y.-C. Kong, *J. Chem. Soc. Chem. Commun.* **1995**, 1191 – 1193.
[34] H. D. Stoeffler, N. B. Thornton, S. L. Temkin, K. S. Schanze, *J. Am. Chem. Soc.* **1995**, *117*, 7119 – 7128.